Extending the precision and efficiency of the all-electron full-potential linearized augmented plane-wave density-functional theory method

Gregor Michalicek

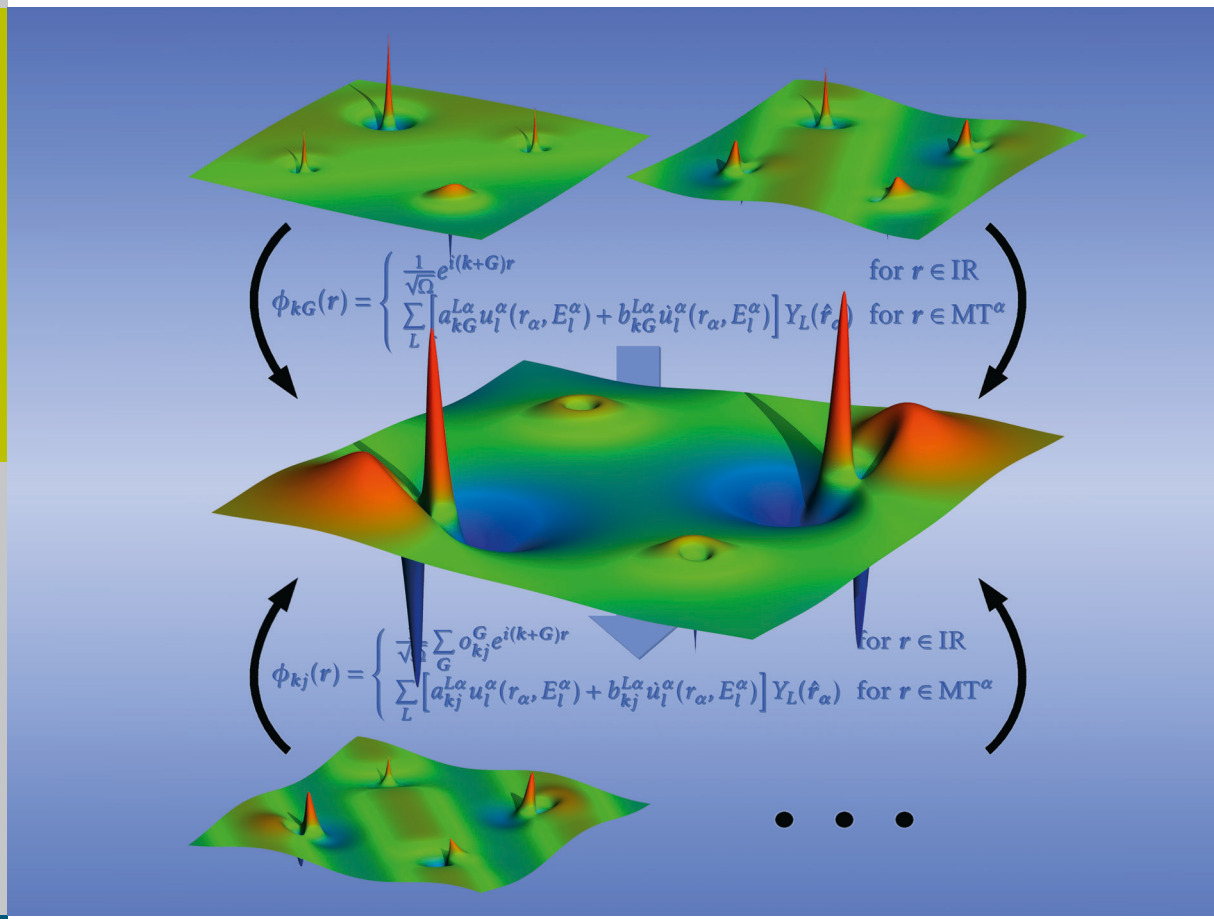

Schlüsseltechnologien / Key Technologies
Band / Volume 102
ISBN 978-3-95806-031-9

JÜLICH FORSCHUNGSZENTRUM

Schriften des Forschungszentrums Jülich
Reihe Schlüsseltechnologien / Key Technologies Band / Volume 102

Forschungszentrum Jülich GmbH
Peter Grünberg Institute (PGI)
Quantum Theory of Materials (PGI-1 / IAS-1)

Extending the precision and efficiency of the all-electron full-potential linearized augmented plane-wave density-functional theory method

Gregor Michalicek

Schriften des Forschungszentrums Jülich
Reihe Schlüsseltechnologien / Key Technologies Band / Volume 102

ISSN 1866-1807 ISBN 978-3-95806-031-9

Bibliographic information published by the Deutsche Nationalbibliothek.
The Deutsche Nationalbibliothek lists this publication in the Deutsche Nationalbibliografie; detailed bibliographic data are available in the Internet at http://dnb.d-nb.de.

Publisher and Distributor: Forschungszentrum Jülich GmbH
Zentralbibliothek
52425 Jülich
Tel: +49 2461 61-5368
Fax: +49 2461 61-6103
Email: zb-publikation@fz-juelich.de
www.fz-juelich.de/zb

Cover Design: Grafische Medien, Forschungszentrum Jülich GmbH

Printer: Grafische Medien, Forschungszentrum Jülich GmbH

Schriften des Forschungszentrums Jülich
Reihe Schlüsseltechnologien / Key Technologies, Band / Volume 102

D 82 (Diss. RWTH Aachen University, 2014)

ISSN 1866-1807
ISBN 978-3-95806-031-9

The complete volume is freely available on the Internet on the Jülicher Open Access Server (JuSER) at www.fz-juelich.de/zb/openaccess.

Abstract

Density functional theory (DFT) is the most widely-used first-principles theory for analyzing, describing and predicting the properties of solids based on the fundamental laws of quantum mechanics. The success of the theory is a consequence of powerful approximations to the unknown exchange and correlation energy of the interacting electrons and of sophisticated electronic structure methods that enable the computation of the density functional equations on a computer. A widely used electronic structure method is the full-potential linearized augmented plane-wave (FLAPW) method, that is considered to be one of the most precise methods of its kind and often referred to as a standard. Challenged by the demand of treating chemically and structurally increasingly more complex solids, in this thesis this method is revisited and extended along two different directions: (i) precision and (ii) efficiency.

In the full-potential linearized augmented plane-wave method the space of a solid is partitioned into nearly touching spheres, centered at each atom, and the remaining interstitial region between the spheres. The Kohn-Sham orbitals, which are used to construct the electron density, the essential quantity in DFT, are expanded into a linearized augmented plane-wave basis, which consists of plane waves in the interstitial region and angular momentum dependent radial functions in the spheres.

In this thesis it is shown that for certain types of materials, e.g., materials with very broad electron bands or large band gaps, or materials that allow the usage of large space-filling spheres, the variational freedom of the basis in the spheres has to be extended in order to represent the Kohn-Sham orbitals with high precision over a large energy spread. Two kinds of additional radial functions confined to the spheres, so-called local orbitals, are evaluated and found to successfully eliminate this error.

A new efficient basis set is developed, named linearized augmented lattice-adapted plane-wave ($(LA)^2PW$) basis, that enables substantially faster calculations at controlled precision. The basic idea of this basis is to increase the efficiency of the representation in the interstitial region by using linear combinations of plane waves, instead of single plane waves, adapted to the crystal lattice and potential of the solid. The starting point for this development is an investigation of the basis-set requirements and the changes of the basis set throughout the iterative self-consistency loop inherent to density functional theory. The results suggest the construction of a basis that is given by eigenfunctions of the first iteration. The precision and efficiency of this basis from early eigenfunctions is evaluated on a test set of materials with different properties and for a wide spectrum of physical quantities.

Zusammenfassung

Dichtefunktionaltheorie (DFT) ist die am häufigsten genutzte *first-principles* Theorie, um Eigenschaften von Festkörpern auf Basis der fundamentalen Gesetze der Quantenmechanik zu analysieren, zu beschreiben und vorherzusagen. Der Erfolg dieser Theorie ist eine Konsequenz leistungsfähiger Näherungen für die unbekannte Austauch- und Korrelationsenergie der interagierenden Elektronen und fortgeschrittener Elektronenstrukturmethoden, die die Berechnung der Dichtefunktionalgleichungen auf Computern ermöglichen. Eine weit verbreitete Elektronenstrukturmethode ist die *full-potential linearized augmented plane-wave* (FLAPW) Methode, die als eine der präzisesten Methoden ihrer Art gilt und oft als Maßstab genutzt wird. Herausgefordert durch die Bedürfnisse, chemisch und strukturell immer komplexere Festkörper zu beschreiben, wird diese Methode in dieser Arbeit in zwei Richtungen überdacht und erweitert: (i) Genauigkeit und (ii) Effizienz.

In der *full-potential linearized augmented plane-wave* Methode wird der Raum in einem Festkörper in sich fast berührende, an den Atomen zentrierte Kugeln und dem übrigbleibenden Interstitialbereich zwischen den Kugeln aufgeteilt. Die Kohn-Sham Orbitale, die genutzt werden um die essentielle Größe von DFT, die Elektronendichte, zu erzeugen, werden in eine *linearized augmented plane-wave* Basis ent-wickelt, die aus ebenen Wellen im Interstitialbereich und drehimpulsabhängigen Radialfunktionen in den Kugeln besteht.

In dieser Arbeit wird gezeigt, dass die variationelle Freiheit der Basis in den Kugeln für bestimmte Materialien, z.B. Materialien mit sehr breiten Bändern oder großen Bandlücken oder Materialien, die die Nutzung sehr großer Kugeln ermöglichen, erweitert werden muss, um die Kohn-Sham Orbitale über einen weiten Energiebereich hinweg mit hoher Präzision zu beschreiben. Zur Eliminierung des Fehlers werden zwei Arten von auf die Kugeln beschränkten zusätzlichen Radialfunktionen, sogenannten lokalen Orbitalen, evaluiert und als erfolgreich erkannt.

Es wird eine neue effiziente Basis, benannt als *linearized augmented lattice-adapted plane-wave* ($(LA)^2PW$) Basis, die substantiell schnellere Berechnungen mit kontrollierter Präzision ermöglicht, entwickelt. Die zugrundeliegende Idee dieser Basis ist die Steigerung der Effizienz der Darstellung im Interstitialbereich durch Nutzung kristallgitter- und potentialangepasster Linearkombinationen ebener Wellen anstatt einzelner ebener Wellen. Der Startpunkt dieser Entwicklung ist eine Untersuchung der Basissatzanforderungen und der Änderungen der Basis über die iterative Selbstkonsistenzschleife der Dichtefunktionaltheorie hinweg. Die Resultate regen eine Kon-

struktion der Basis anhand der Eigenfunktionen der ersten Iteration an. Die Genauigkeit und Effizienz dieser *basis from early eigenfunctions* wird anhand einer Testmenge von Materialien mit unterschiedlichen Eigenschaften für ein breites Spektrum physikalischer Größen evaluiert.

Contents

1 Introduction

Today's technological innovations often rely to a significant extent on the development of new materials with unique properties adapted to the respective application. For example, the properties and usefulness of fuel cells, batteries, integrated circuits, sensors, actuators, computer memories, solar cells, lasers, and many other modern devices and applications are strongly influenced by the capabilities of the underlying materials. Research responds to these demands with the design and investigation of materials involving metals, semiconductors, insulators, alloys, composite materials, heterostructures, quantum dots, multiferroics, metamaterials, porous materials, transparent conducting oxides, quasicrystals, topological insulators, modern steel, and various other structures. In many cases, the geometries, chemical compositions, or magnetic characteristics of these materials are very complex. Thus, one can deduce that understanding and predicting properties of complex materials is an important key to the future technological development. The required prediction power of the involved sciences is achieved by sophisticated numerical approaches that have been established in the last decades as a consequence of the ongoing revolution in computer technology, which follows a miniaturization trend called Moore's law [1] that states that the transistor density in integrated circuits grows exponentially with time. Indeed, the increase of available computational resources together with the development of advanced algorithms and scientific models made simulations an invaluable tool to investigate materials in new ways besides experiments and classical theoretical modeling.

An important example for this development is the rise and ever refining development of *density functional theory* [2, 3] (DFT) in the domains of condensed matter physics, chemistry, and biochemistry. DFT allows us to numerically calculate the quantum mechanical ground states of condensed matter systems, i.e., crystals, molecules, thin films, clusters of atoms, and so on. This is a task that is infeasible without the use of computers as it requires tremendous computing resources. The growth of the available computing capacity allows us to perform such calculations for more and more complex materials and to realize DFT with an ever increasing accuracy.

In detail, DFT is based on the fact that a quantum mechanical system of many interacting electrons is completely defined by its ground state density. This finding by Hohenberg and Kohn means that every observable can be obtained as a functional of this density. On the basis of this theorem Kohn and Sham then developed a practical

iterative calculation scheme to obtain the ground state density by mapping the problem onto a system of noninteracting electrons that features the same ground state density as the interacting particle system by construction. Solving the quantum mechanical problem for this Kohn-Sham system is considerably less demanding than approaching the interacting particle system directly.

Calculations performed on the basis of density functional theory can have many uses. For example, they provide information on quantities that are not accessible through experiments. As a consequence, DFT simulations are often used as a supplement to experiments in order to better understand the experimental results. On the other hand, DFT calculations can also be a guide for experiments. Since they are typically less expensive than experiments, it is feasible to investigate more materials with this numerical approach than with experimental methods. Performing DFT simulations on a wide set of systems then allows to pick out the most interesting candidates for materials with certain properties and investigate them in more detail by experiments. Besides the fruitful interplay between DFT simulations and experiments, DFT calculations can also be used in combination with more abstract theoretical approaches by providing high-quality input data.

Indeed, the multifarious applications of DFT together with their ever increasing number have the consequence that the yearly number of scientific publications related to this method is steadily growing. For the last decades, figure 1.1 shows the development of the number of publications mentioning DFT in their title or abstract. Meanwhile, one has produced so many DFT results and DFT calculations have become inexpensive enough such that one starts to collect these results in large databases to lift materials design to a new level where it is assisted by data mining techniques. An excellent example for such an approach is the *materials project* [4].

Nevertheless, practical realizations of DFT are still computationally demanding such that the complexity of the investigated materials is limited. At the complexity frontier of materials for which DFT simulations are still feasible, calculations have to be performed on supercomputers with hundreds of thousands of computing cores. Of course, these high computational demands entail the development of approaches to reduce them. As a consequence, many different practical approaches to DFT have been established of which each one is adapted to a certain class of materials, e.g., molecules or crystals, and represents a unique tradeoff between computational demands and accuracy by employing different approximations. The choice of the method used for a given investigation then depends on the material and the requirements on accuracy and computational efficiency. The diversity of modern materials and properties of interest then yields a research environment in which different investigations require the strengths of different DFT realizations. Thus, a large variety of DFT implementations is in use and each approach has a wide range of applications in which it is superior to other DFT realizations.

One of the most accurate and popular practical approaches to DFT for all types of crystals, thin films, and one-dimensional structures is the *all-electron full-potential linearized augmented plane-wave* (FLAPW) method [6, 7]. Irrespective of the chemical composition of the investigated systems this method is often considered to be

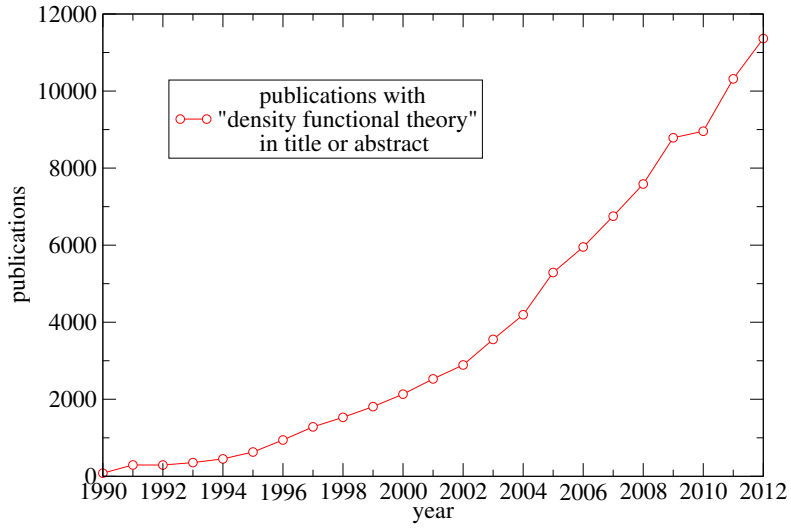

Figure 1.1.: Number of scientific publications mentioning density functional theory. The figure shows for each year of the last decades the number of publications that include the term 'density functional theory' in their title or abstract. It is based on a search with the *Web of Knowledge* [5] in scientific journals.

an accuracy standard. The name of the method sketches the main aspects by which different DFT realizations deviate. *All-electron* means that where a couple of other approaches only treat the valence electrons of the quantum mechanical systems within the DFT scheme, the FLAPW method describes all electrons, also energetically deep lying *core electrons* on this footing. The next term in the name states that the method does not make any approximations to the potential in the given material. Lastly, *linearized augmented plane-waves* (LAPWs) denote a set of basis functions used to represent the wave functions of the electrons in the given Kohn-Sham problem. The basis set is a central part within a DFT program that has huge impacts on the precision of the approach and the computational demands. In the ideal case one has a basis set that features a very high *description efficiency*, i.e., the wave functions are precisely representable with very few basis functions.

Having its origins in J. C. Slater's augmented plane-wave (APW) method [8] developed in 1937, the FLAPW method, which was first formulated in 1975 by O. K. Andersen without treating the full potential, is a major step forward as it considerably reduces the computational demands of the approach by redesigning the basis functions. In detail, the method eliminates a dependency of the basis functions on the eigenvalues of the Kohn-Sham wave functions. It is based on a partitioning of space into nearly touching so-called muffin-tin (MT) spheres centered at the atomic nuclei and the interstitial region between the spheres. In each of these regions it comprises problem-adapted descriptions of the given system. For example, the LAPW basis

consists of plane waves in the interstitial region that are augmented with numerically determined radial functions times spherical harmonics in the MT spheres, i.e., the radial functions are linearly combined to match the given plane wave in value and slope at the MT sphere boundaries. In detail, one uses two types of radial functions. The first type of functions solve for a predetermined angular momentum dependent energy parameter the scalar-relativistic approximation to the radial Dirac equation employing the spherical potential in the given MT sphere. The second type of functions are the energy derivatives of the first functions. This allows a linearized representation of wave functions in the vicinity of the predetermined energy parameter.

Though the FLAPW method is considered to be highly accurate and efficient, the growing demands and popularity of DFT calculations provide a constant pressure to steadily improve these properties. As a consequence, there have been many developments based on an FLAPW fundament. Of course, one of the most important developments in this regard is the progress in the formulation of the basis functions. Here, most work in the last decades was performed on the description in the MT spheres. First, the description capabilities were improved by adding local orbitals (LOs) to the basis set [9, 10, 11, 12]. These are additional basis functions that are completely confined within a given MT sphere. Next, the quality of the description has also been evaluated in detail [13]. Furthermore, to improve the efficiency of the method, a slightly different augmentation scheme, APW+lo, has been proposed that reduces the required number of basis functions [14, 15]. In the interstitial region there has been less progress. One notable idea in this context is the augmented distorted plane-wave method that uses structure-adapted coordinates [16].

In this thesis we will investigate the LAPW basis in detail. This means that we will analyze the precision of the basis set and its properties in comparison to the wave functions. In order to considerably reduce the computational demands of the method to make calculations on more complex materials feasible, we will then use the analysis of the basis as a starting point to develop a new basis set that is even more problem-adapted. As the shape of a basis function in the LAPW scheme is mainly given by its interstitial region part and the matching conditions to the MT spheres, the adaption to the actual crystal especially addresses these properties of the basis functions. We replace the single plane wave in the interstitial region by a smart linear combination of plane waves to obtain a highly efficient representation of the wave functions. Finally, we evaluate this new basis on a test set of materials with different properties to relate its description efficiency to that of the LAPW basis and measure the speedup associated with the use of the new basis.

The thesis is organized as follows. In chapter 2 we provide a general introduction to DFT. This covers the theoretical foundations which are mainly given by the Hohenberg-Kohn theorem and the reduction of the quantum mechanical interacting particle problem onto the auxiliary Kohn-Sham system of noninteracting particles. Furthermore, on the side of practical realizations the DFT introduction provides an overview on the approximations by which different DFT programs differ. This field is called *electronic structure methods*.

In chapter 3 we introduce the FLAPW method in detail. We start this introduction

with a discussion on the LAPW basis and modifications of it. Next, we describe the setup of the problem dependent Hamilton and overlap matrices for this basis. Note that this is a crucial part of the chapter since the setup of these matrices is one of the most time-consuming steps within FLAPW calculations. It considerably affects the computational demands. We will also discuss the construction of the electron density, which is less time consuming, but still important for the overall runtime of a calculation. Next, we describe how to obtain the total energy of a quantum mechanical system from an FLAPW calculation. This is the central quantity which we will use to evaluate the basis sets. Finally, we sketch a couple of developments in the environment of the FLAPW method.

The analysis of the LAPW basis will be performed in chapter 4. In detail, we will discuss the so-called linearization error, which is a representation error in the MT spheres that is due to an incompleteness in the basis set. In clear words, the linearized description by the two radial functions in the MT spheres is only adequate for a small energy region around the predetermined energy parameters. In materials that imply large discrepancies between the energy parameters and the Kohn-Sham wave functions this description is not enough. The linearization error cannot be eliminated by converging the basis set in terms of the cutoff parameters used to control the basis set size and their accuracy. It can, however, be eliminated by adding LOs to the basis. We evaluate for different types of LOs their capabilities to eliminate the linearization error. Besides the analysis of the linearization error we will also discuss the matching conditions of the LAPW basis functions at the MT sphere boundaries in comparison to those of the wave functions. Furthermore, we investigate the changes of the Kohn Sham problem, the wave functions, and the basis functions in the different iterations of the DFT calculation.

Based on the results obtained in chapter 4, in chapter 5 we then propose a different analytical form of basis functions that allows the construction of more problem-adapted basis sets. In detail, we replace the plane waves in the interstitial region by linear combinations of plane waves and call this new form of basis functions a *linearized augmented lattice-adapted plane-wave* (abbreviated as (LA)^{2}PW or *LA*^{2}PW) basis. The idea is that one can construct the linear combinations of plane waves such that they are adapted to the crystal lattice of the given material. We then discuss the implementation of such a basis into a given FLAPW program[1].

The construction of the linear combinations of plane waves in (LA)^{2}PWs is decoupled from the general form of the functions. On the basis of the observations made in chapter 4 we propose a first idea of a construction principle in chapter 6. This construction principle, which we call the *basis from early eigenfunctions* (BEE), uses the FLAPW eigenfunctions of a single FLAPW iteration to construct the (LA)^{2}PWs which are then used in every other iteration. We then evaluate the description efficiency of this basis for a test set of materials with different properties to obtain a

[1] The underlying FLAPW program used for the investigations and developments in this work is the FLEUR code [17]. However, the results and new approaches are transferable to other FLAPW implementations as well.

representative picture. Finally we measure the speedup obtained with these new basis functions and propose an approximation to make this already very efficient basis even more efficient.

A conclusion of the thesis and a short outlook is presented in chapter 7. Furthermore, as a small add-on we test the capabilities of atomic orbitals in combination with conventional LAPWs to be an efficient $(LA)^2PW$ basis in appendix A. The results of these tests provide hints on the required ingredients for a basis set construction beyond the BEE-$(LA)^2PW$ approach.

2 Density functional theory

Contents

Determining the quantum mechanical ground state of a system of interacting electrons in an external potential, e.g., due to atomic nuclei, is an important task in a wide range of sciences. All physical properties of the respective system can be derived from this state. Unfortunately, systems with many interacting electrons also possess many degrees of freedom. This makes solving the problem very difficult. The advent of density functional theory [2, 3] (DFT) a few decades ago drastically changed this situation. DFT opened a path to obtain the ground states of systems with many interacting particles through calculations on auxiliary systems with noninteracting particles. This drastically reduced the complexity of the task to be solved. As a consequence, performing highly predictive calculations on the electronic ground state of many-electron systems has become a daily routine.

Density functional theory provides a general concept of how to obtain the electronic ground state. Based on a couple of introductions to density functional theory [18, 19, 20, 21], we provide a general overview on this concept in section 2.1. Beyond the theoretical scheme of DFT, realizations of this method in computer programs are exposed to further challenges to make DFT calculations feasible. The approximations and design decisions associated with these challenges form the wide field of electronic structure methods, which we discuss in section 2.2.

2.1 Theoretical foundations

In this section we provide an overview on the theoretical foundations of density functional theory. We start by defining the underlying quantum mechanical many-particle problem in section 2.1.1. Next, we discuss the central statement of DFT, the Hohenberg-Kohn theorem, in section 2.1.2 and describe the Kohn-Sham procedure to practically solve the given quantum mechanical problem with the help of an auxiliary noninteracting particle system in section 2.1.3. The chapter closes with the generalization of the theory for spin-polarized materials in section 2.1.4 and an overview on commonly used approximations to the exchange-correlation potential that simulates the missing exchange and correlation interactions in the Kohn-Sham system in section 2.1.5.

2.1.1 The Born-Oppenheimer approximation

To obtain an exact description of the electronic ground state of a condensed matter system, the associated time-independent many-body problem described by

$$\hat{H}\left|\psi\right\rangle = E\left|\psi\right\rangle \tag{2.1}$$

with the many-body wave function ψ and the Hamiltonian

$$\hat{H} = \underbrace{-\sum_{i}^{N_{\text{elec}}} \frac{1}{2}\nabla_i^2}_{\hat{T}_\text{e}} \underbrace{-\sum_{\alpha}^{N_{\text{atom}}} \frac{1}{2m_\alpha}\nabla_\alpha^2}_{\hat{T}_\text{i}} + \underbrace{\frac{1}{2}\sum_{\substack{i,j \\ i\neq j}}^{N_{\text{elec}}} \frac{1}{|\boldsymbol{r}_i - \boldsymbol{r}_j|}}_{\hat{V}_\text{ee}} + \underbrace{\frac{1}{2}\sum_{\substack{\alpha,\beta \\ \alpha\neq\beta}}^{N_{\text{atom}}} \frac{Z_\alpha Z_\beta}{|\boldsymbol{\tau}_\alpha - \boldsymbol{\tau}_\beta|}}_{\hat{V}_\text{ii}} \underbrace{-\sum_{i}^{N_{\text{elec}}}\sum_{\alpha}^{N_{\text{atom}}} \frac{Z_\alpha}{|\boldsymbol{r}_i - \boldsymbol{\tau}_\alpha|}}_{\hat{V}_\text{ei}} \tag{2.2}$$

has to be solved[1], where i and j label the N_{elec} electrons, α and β are indices for the N_{atom} atoms, $\boldsymbol{r}_i$ and $\boldsymbol{\tau}_\alpha$ are the positions of the i-th electron and the α-th atomic nucleus, and m_α and Z_α are the mass and charge the nucleus of atom α.

We denote the different terms of the Hamiltonian. The kinetic energy operators for the atomic nuclei and the electrons are $\hat{T}_\text{i}$ and $\hat{T}_\text{e}$, respectively. Furthermore we name the operator for the Coulomb interactions between the electrons $\hat{V}_\text{ee}$, between the atomic nuclei $\hat{V}_\text{ii}$, and between the electrons and the nuclei $\hat{V}_\text{ei}$.

Unfortunately it is not feasible to solve the given many-body problem for any but the simplest systems. Thus, one has to approximate the problem to deal with it. The first approximation to be performed in this context is the Born-Oppenheimer approximation [22] that abstracts the problem from the movements of the atomic nuclei. As the mass of an atomic nucleus is at least three orders of magnitude larger than the electron mass[2], this is a very reasonable approximation: The movements of

[1] We use atomic units $\hbar = m_\text{e} = e = 1$.

[2] proton mass $m_\text{p} = 938.272\ \text{MeV/c}^2$ vs. electron mass $m_\text{e} = 0.511\ \text{MeV/c}^2$

the electrons and the atomic nuclei take place on completely different time scales, such that on the time scale for the atomic nuclei, the electrons are always in the electronic ground state with respect to the positions of the atomic nuclei.

In practice, the Born-Oppenheimer approximation is the neglect of the kinetic energy operator for the atomic nuclei $\hat{T}_\mathrm{i}$ in equation (2.2). With this neglect one ends up with the Born-Oppenheimer Hamiltonian

$$\hat{H}_\mathrm{BO} = \hat{T}_\mathrm{e} + \hat{V}_\mathrm{ee} + \hat{V}_\mathrm{ii} + \hat{V}_\mathrm{ei} = \hat{T}_\mathrm{e} + \hat{V}_\mathrm{ee} + \hat{V}_\mathrm{ii} + \sum_i^{N_\mathrm{elec}} V_\mathrm{ext}(\boldsymbol{r}_i), \tag{2.3}$$

where $V_\mathrm{ext}(\boldsymbol{r})$ denotes the external potential.

The Born Oppenheimer approximation is a large step forward towards solving the given many-body problem (2.1). However, a ground-state solution to the problem is a many-body wave function

$$\psi(\boldsymbol{r}_1, \boldsymbol{r}_2, \ldots, \boldsymbol{r}_{N_\mathrm{elec}}) \tag{2.4}$$

that is defined in a $3N_\mathrm{elec}$ dimensional space. Considering a numerical sampling of a many-body wave function in each of these dimensions, the storage requirements for such a function scale exponentially with the number of electrons in the system under investigation [23]. As the unit cells of modern crystalline materials often contain hundreds or even thousands of electrons it is clear that the given problem is still infeasible to solve, even with numerical approaches: No problem with exponentially scaling storage requirements can be solved for any but the most trivial problem sizes.

Nevertheless, the Born-Oppenheimer Hamiltonian (2.3) gives us the starting point for a crucial step that can be made to obtain an accurate quantum mechanical *ab-initio* description of complex materials. This is density functional theory.

2.1.2 The Hohenberg-Kohn theorem

The non-manageable storage requirements of many-body wave functions can be overcome by making use of the Hohenberg-Kohn theorem [2] which essentially consists of two very important statements:

The Hohenberg-Kohn theorem

1. Up to a constant potential shift, the external potential V_{ext} is a unique functional of the ground-state electron density ρ_0:

$$V_{\text{ext}}(\boldsymbol{r}) = V_{\text{ext}}[\rho_0(\boldsymbol{r})]. \tag{2.5}$$

   This implies that the Hamiltonian can be obtained with the ground-state density ρ_0 and hence also the wave functions ψ_ν and all observables, in particular the total energy, are functionals of ρ_0.

2. For a given external potential V_{ext} and a given number of electrons N_{elec}, the ground-state electron density ρ_0 minimizes the total energy E:

$$E[\rho] \geq E[\rho_0] = E_0 \qquad \text{for all } \rho \text{ with } \int \rho(\boldsymbol{r}) d^3r = \int \rho_0(\boldsymbol{r}) d^3r = N_{\text{elec}}. \tag{2.6}$$

We summarize the original proof of this theorem by Hohenberg and Kohn [2] for systems with a non-degenerate ground state. The first observation one has to make in this context is that if a function ψ is an eigenstate of two different Hamiltonians $\hat{H}_1 = \hat{T}_{\text{e}} + \hat{V}_{\text{ee}} + \hat{V}_{\text{ii}} + \sum_i^{N_{\text{elec}}} V^1_{\text{ext}}(\boldsymbol{r}_i)$ and $\hat{H}_2 = \hat{T}_{\text{e}} + \hat{V}_{\text{ee}} + \hat{V}_{\text{ii}} + \sum_i^{N_{\text{elec}}} V^2_{\text{ext}}(\boldsymbol{r}_i)$ then $V^1_{\text{ext}}(\boldsymbol{r})$ and $V^2_{\text{ext}}(\boldsymbol{r})$ may differ only by a constant:

By subtracting $\hat{H}_1|\psi\rangle = E_1|\psi\rangle$ from $\hat{H}_2|\psi\rangle = E_2|\psi\rangle$ it follows that

$$\left[\sum_i^{N_{\text{elec}}} V^2_{\text{ext}}(\boldsymbol{r}_i) - V^1_{\text{ext}}(\boldsymbol{r}_i)\right]|\psi\rangle = (E_2 - E_1)|\psi\rangle \tag{2.7}$$

for every point in the underlying $3N_{\text{elec}}$-dimensional space.

Now assume that ψ_1 and ψ_2 are two differing ground-state wave functions for $\hat{H}_1$ and $\hat{H}_2$, respectively, that both produce the same ground-state electron density $\rho_0(\boldsymbol{r})$. From the minimal-energy property of the ground state it now follows that

$$E_1 = \langle\psi_1|\hat{H}_1|\psi_1\rangle < \langle\psi_2|\hat{H}_1|\psi_2\rangle = \langle\psi_2|\hat{H}_2 + \hat{V}^1_{\text{ei}} - \hat{V}^2_{\text{ei}}|\psi_2\rangle, \tag{2.8}$$

$$E_2 = \langle\psi_2|\hat{H}_2|\psi_2\rangle < \langle\psi_1|\hat{H}_2|\psi_1\rangle = \langle\psi_1|\hat{H}_1 + \hat{V}^2_{\text{ei}} - \hat{V}^1_{\text{ei}}|\psi_1\rangle \tag{2.9}$$

if the ground state is non-degenerate. With the density operator

$$\hat{\rho}(\boldsymbol{r}) = \sum_{i=1}^{N_{\text{elec}}} \delta(\boldsymbol{r} - \boldsymbol{r}_i) \tag{2.10}$$

we then write $\hat{V}_{\text{ei}}$ as

$$\hat{V}_{\text{ei}} = \int V_{\text{ext}}(\boldsymbol{r})\hat{\rho}(\boldsymbol{r}) d^3r. \tag{2.11}$$

Evaluating the expressions on the right-hand sides of equations (2.8) and (2.9) then yields

$$E_1 < E_2 + \int \left[V^1_{\text{ext}}(\boldsymbol{r}) - V^2_{\text{ext}}(\boldsymbol{r})\right]\rho_0(\boldsymbol{r})d^3r, \tag{2.12}$$

$$E_2 < E_1 + \int \left[V^2_{\text{ext}}(\boldsymbol{r}) - V^1_{\text{ext}}(\boldsymbol{r})\right]\rho_0(\boldsymbol{r})d^3r. \tag{2.13}$$

Adding (2.13) to (2.12) finally leads to the contradiction

$$E_2 + E_1 < E_1 + E_2 \tag{2.14}$$

that completes the proof of the first statement of the Hohenberg-Kohn theorem.

A functional for the total energy is given by

$$E[\rho] = T[\rho] + V_{\text{ee}}[\rho] + E_{\text{ii}} + \int V_{\text{ext}}(\boldsymbol{r})\rho(\boldsymbol{r})d^3r = F_{\text{HK}}[\rho] + E_{\text{ii}} + \int V_{\text{ext}}(\boldsymbol{r})\rho(\boldsymbol{r})d^3r, \tag{2.15}$$

where $T[\rho]$ is the kinetic energy, $V_{\text{ee}}[\rho]$ is the Coulomb interaction energy between the electrons, and E_{ii} is the Coulomb interaction energy between the nuclei. The first two of these ingredients are typically combined to obtain the universal functional $F_{\text{HK}}[\rho]$. The form of this functional does not depend on the investigated system.

The second statement of the Hohenberg-Kohn theorem is that the variational principle for the ground-state wave functions also applies to the ground-state electron density. This can easily be seen by considering that the first statement implies that the ground-state wave function is a functional of the ground-state density. It follows

$$E_0 = \langle\psi_0[\rho_0]|\hat{H}|\psi_0[\rho_0]\rangle < \langle\psi'_0[\rho]|\hat{H}|\psi'_0[\rho]\rangle \tag{2.16}$$

for any $\rho(\boldsymbol{r}) \neq \rho_0(\boldsymbol{r})$.

Note that various other proofs for the Hohenberg-Kohn theorem have been found. Here, we explicitly mention the very nice proof by Levy [24]. The statement of the Hohenberg-Kohn theorem that all properties of a system are functionals of the ground state density is also true for systems with degenerate ground states [25]. Levy provides a procedure of how to obtain the wave functions for such a system [26].

The essence of the Hohenberg-Kohn theorem is that the high-dimensional many-particle wave functions (2.4) can be replaced by the only three-dimensional ground-state density $\rho_0(\boldsymbol{r})$ as central information carrier of the respective system. However, the question how to calculate the ground-state density $\rho_0(\boldsymbol{r})$ is still open. It is answered by Kohn and Sham who introduce an auxiliary independent-particle system that features the same ground-state density as the associated many-body system of interacting particles.

2.1.3 The Kohn-Sham system

The approach of Kohn and Sham to develop a practical scheme to obtain the ground state density of a given system [3] starts by expressing the energy functional $E[\rho]$ as

$$E[\rho] = T_{\text{s}}[\rho] + E_{\text{H}}[\rho] + E_{\text{ext}}[\rho] + E_{\text{xc}}[\rho] + E_{\text{ii}}. \tag{2.17}$$

In this expression

$$E_{\mathrm{H}}[\rho] = \frac{1}{2}\int \frac{\rho(\boldsymbol{r})\rho(\boldsymbol{r}')}{|\boldsymbol{r}-\boldsymbol{r}'|} d^3r d^3r' \tag{2.18}$$

denotes the Hartree energy,

$$E_{\mathrm{ext}}[\rho] = \int V_{\mathrm{ext}}(\boldsymbol{r})\rho(\boldsymbol{r}) d^3r, \tag{2.19}$$

the energy due to the external potential, and E_{ii} the already denoted Coulomb interaction energy for the nuclei.

The crucial aspect in the expression of the total energy by Kohn and Sham are the remaining two terms that split the kinetic energy together with the difference between the Hartree energy and the Coulomb interaction energy for the electrons into the kinetic energy of a system of N_{elec} non-interacting electrons

$$T_{\mathrm{s}}[\rho] = -\frac{1}{2}\sum_{\nu=1}^{N_{\mathrm{elec}}} \langle \psi_\nu[\rho] | \nabla^2 | \psi_\nu[\rho] \rangle \tag{2.20}$$

and a term that covers the exchange and correlation interactions $E_{\mathrm{xc}}[\rho]$. The expression of the total energy (2.17) is exact. However, an analytical expression for $E_{\mathrm{xc}}[\rho]$ is not known and therefore this term has to be approximated.

The replacement of the many-body system of interacting electrons by an auxiliary system of non-interacting electrons opens the path to efficiently calculate the ground state density. For this, one first defines the auxiliary system of N_{elec} non-interacting electrons by the external potential to end up with an overall effective potential

$$V_{\mathrm{eff}}(\boldsymbol{r}) = V_{\mathrm{H}}(\boldsymbol{r}) + V_{\mathrm{ext}}(\boldsymbol{r}) + V_{\mathrm{xc}}(\boldsymbol{r}) \tag{2.21}$$

with

$$V_{\mathrm{H}}(\boldsymbol{r}) = \frac{\delta E_{\mathrm{H}}[\rho]}{\delta\rho(\boldsymbol{r})} = \int \frac{\rho(\boldsymbol{r}')}{|\boldsymbol{r}-\boldsymbol{r}'|} d^3r', \tag{2.22}$$

$$V_{\mathrm{xc}}(\boldsymbol{r}) = \frac{\delta E_{\mathrm{xc}}[\rho]}{\delta\rho(\boldsymbol{r})}. \tag{2.23}$$

On the basis of an initial guess for the ground-state density $\rho_{\mathrm{old}}(\boldsymbol{r})$ Kohn and Sham [3] propose to calculate $V_{\mathrm{eff}}(\boldsymbol{r})$, solve the Kohn-Sham equations, which are the single-particle Schrödinger equations for the auxiliary system

$$\left[-\frac{1}{2}\nabla^2 + V_{\mathrm{eff}}(\boldsymbol{r})\right]\psi_\nu(\boldsymbol{r}) = E_\nu \psi_\nu(\boldsymbol{r}), \tag{2.24}$$

and obtain a new density

$$\rho_0(\boldsymbol{r}) = \sum_\nu \omega_\nu |\psi_\nu(\boldsymbol{r})|^2 \tag{2.25}$$

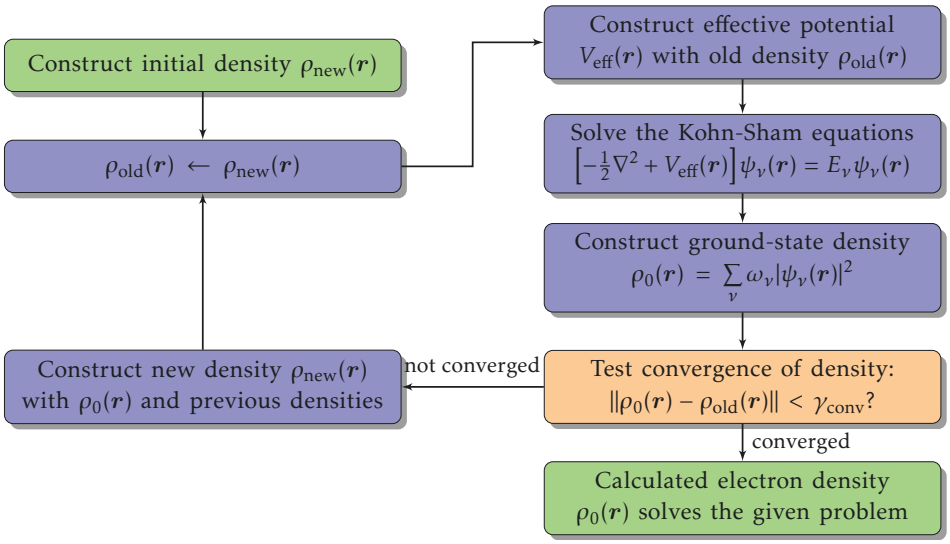

Figure 2.1.: The self-consistency cycle in the Kohn and Sham formalism. An initial guess for the ground state density is iteratively improved by solving the Kohn-Sham equations for the associated effective potential and mixing the resulting new density into the old one until convergence is reached. Here, we check the convergence by comparing the norm of the difference between the input and output densities of a given iteration with an arbitrarily chosen small number γ_{conv}.

with the occupation numbers ω_ν that sum up to the number of electrons N_{elec}. With a mixture of the old density and the new density this procedure is iteratively repeated until one ends up with a self-consistent solution.

In conclusion, Hohenberg and Kohn showed that the ground-state electron density contains all information about a given electron system, such that even the external potential can be obtained from it. This is the starting point to determine the ground-state density in a self consistent manner, which Kohn and Sham transform into a practical calculation scheme that is sketched in figure 2.1.

Note that only the ground state density ρ_0 of the Kohn-Sham auxiliary system has a strict connection to the original many-body system of interacting electrons. On the other hand, most eigenvalues ϵ_ν and eigenfunctions ψ_ν of the Kohn-Sham system have no strict physical meaning. However, in practice they are often used to obtain semiquantitative information about the actual physics in a material [27].

2.1.4 Spin-polarized DFT

Density functional theory, as we have presented it so far, does not consider the electron spin. To allow descriptions of magnetic materials it is typically extended by discriminating between the spin-up density $\rho^\uparrow(r)$ and the spin-down density $\rho^\downarrow(r)$.

The total charge density then becomes

$$\rho(\boldsymbol{r}) = \rho^{\uparrow}(\boldsymbol{r}) + \rho^{\downarrow}(\boldsymbol{r}) \tag{2.26}$$

and one additionally defines the magnetization density

$$m(\boldsymbol{r}) = \mu_{\mathrm{B}}(\rho^{\uparrow}(\boldsymbol{r}) - \rho^{\downarrow}(\boldsymbol{r})), \tag{2.27}$$

where μ_{B} is the Bohr magneton.

The consequence of this extended description in the Hohenberg-Kohn theorem is that functionals that depend on the ground-state density in the original formulation now depend on both, the ground-state charge density $\rho_0(\boldsymbol{r})$, as well as the ground-state magnetization density $m_0(\boldsymbol{r})$.

The spin dependence also translates into modified Kohn-Sham equations

$$\left[-\frac{1}{2}\nabla^2 + V_{\mathrm{eff},\sigma}(\boldsymbol{r})\right]\psi_{\nu,\sigma}(\boldsymbol{r}) = E_{\nu,\sigma}\psi_{\nu,\sigma}(\boldsymbol{r}), \tag{2.28}$$

where σ distinguishes between spin up $\uparrow$ ($\sigma = 1/2$) and spin down $\downarrow$ ($\sigma = -1/2$). The changes in the now spin-dependent effective potential $V_{\mathrm{eff},\sigma}(\boldsymbol{r})$, however, do not affect all of its terms. Besides the introduction of a Zeeman term to incorporate an external $\boldsymbol{B}$ field, the only other source for the spin-dependence of the effective potential is the now spin-dependent exchange-correlation functional. Neither the Hartree potential nor the external potential are modified. In detail, the effective potential becomes

$$V_{\mathrm{eff},\sigma}(\boldsymbol{r}) = V_{\mathrm{H}}(\boldsymbol{r}) + V_{\mathrm{ext}}(\boldsymbol{r}) + \mu_{\mathrm{B}} g_{\mathrm{e}} \sigma B + V_{\mathrm{xc},\sigma}(\boldsymbol{r}), \tag{2.29}$$

where g_{e} is the g-factor for the electron.

A derivation of spin-polarized density functional theory in terms of density matrices is given in [28].

2.1.5 The exchange-correlation functional

An exact analytical form of the exchange-correlation (XC) functional is not known. However, there is a large activity in developing more and more accurate functionals. In allusion to the Jacob's ladder from earth to heaven described in the Book of Genesis this process is called *Climbing the Jacob's ladder* since an exact XC functional is recognized as heaven of accuracy. We sketch some milestones of this activity.

2.1.5.1 The local density approximation

The local density approximation (LDA), often formulated in its spin-dependent form as local spin density approximation (LSDA), is based on the observation that the exact XC functional for a homogeneous electron gas is local. Although this is not the case in realistic systems, the approximation assumes such a local relation between the

charge and XC energy densities in every point in space. In detail, the XC energy is approximated by

$$\begin{aligned} E_{\mathrm{xc}}^{\mathrm{LSDA}}\left[\rho^{\uparrow}(\boldsymbol{r}),\rho^{\downarrow}(\boldsymbol{r})\right] &= \int \rho(\boldsymbol{r})\epsilon_{\mathrm{xc}}^{\mathrm{hom}}\left(\rho^{\uparrow}(\boldsymbol{r}),\rho^{\downarrow}(\boldsymbol{r})\right)d^3r \\ &= \int \rho(\boldsymbol{r})\left[\epsilon_{\mathrm{x}}^{\mathrm{hom}}\left(\rho^{\uparrow}(\boldsymbol{r}),\rho^{\downarrow}(\boldsymbol{r})\right)+\epsilon_{\mathrm{c}}^{\mathrm{hom}}\left(\rho^{\uparrow}(\boldsymbol{r}),\rho^{\downarrow}(\boldsymbol{r})\right)\right]d^3r, \end{aligned} \tag{2.30}$$

where $\epsilon_{\mathrm{x}}^{\mathrm{hom}}$ and $\epsilon_{\mathrm{c}}^{\mathrm{hom}}$ are functions of the spin-polarized density that provide the exchange and correlation energy densities for the homogeneous electron gas. For $\epsilon_{\mathrm{x}}^{\mathrm{hom}}$ the exact expression

$$\epsilon_{\mathrm{x}}^{\mathrm{hom}}\left(\rho^{\uparrow},\rho^{\downarrow}\right) = -6\left(\frac{3}{4\pi}\right)^{1/3}\frac{1}{\rho}\left(\rho^{\uparrow\,4/3}+\rho^{\downarrow\,4/3}\right) \tag{2.31}$$

is the ordinary Hartree-Fock exchange for such a system [28]. The correlation energy density $\epsilon_{\mathrm{c}}^{\mathrm{hom}}$ on the other hand is not given by a simple analytical formula but can, for example, be obtained from Monte Carlo simulations [29].

In practice, a couple of LSDA functionals are in use that differ only in details [28, 30, 31].

2.1.5.2 The generalized gradient approximation

In realistic systems exchange and correlation are not local. As a consequence, in order to obtain a more accurate approach one has to go beyond local approximations to the XC functional. A very popular approach is the use of semilocal functionals in terms of generalized gradient approximations (GGAs). GGAs do not only depend on the density but also on the magnitude of the density's gradient and higher derivatives. In detail, the energy density in a GGA is given by

$$E_{\mathrm{xc}}^{\mathrm{GGA}}\left[\rho^{\uparrow}(\boldsymbol{r}),\rho^{\downarrow}(\boldsymbol{r})\right] = \int \rho(\boldsymbol{r})\epsilon_{\mathrm{xc}}\left(\rho^{\uparrow}(\boldsymbol{r}),\rho^{\downarrow}(\boldsymbol{r}),|\nabla\rho^{\uparrow}(\boldsymbol{r})|,|\nabla\rho^{\downarrow}(\boldsymbol{r})|,\dots\right)d^3r. \tag{2.32}$$

A first approach in constructing a GGA may be to expand ϵ_{xc} in terms of the density and the magnitudes of the density's derivatives [32, 33, 34]. However, it turns out that such a low-order gradient expansion approximation (GEA) is no improvement over the LSDA since it breaks important properties of the XC functional [32].

A much more successful development is the construction of GGAs by considering different behaviors for limits of density gradients and other conditions [35, 36, 37]. Especially the functional by Perdew, Burke, and Ernzerhof (PBE) [37, 38] is very common in today's density functional calculations. It provides accurate results for ground-state properties of many materials.

2.1.5.3 LDA+U

Deficiencies of LDA and GGA often show up in materials with electronic structures that differ strongly from the homogeneous electron gas. For example, such situations

appear in materials with strongly localized electrons, i.e., transition metal oxides, materials including elements with f electrons, and so on. Here, it comes into play that each electron is exposed to an effective potential that involves contributions from the respective electron itself. In clear words, the Hartree energy implies an unphysical self-interaction of each electron with itself that cannot be corrected by local or semilocal functionals. As a consequence, the localized electrons in such materials are not localized enough. A typical effect of the self-interaction error in such cases is the prediction of a metal, while the material under investigation actually is an insulator.

Since the inaccuracies in such calculations originate to a large amount from the mentioned self-interaction error in very few localized electron orbitals they may be improved with an additional correction term only for these orbitals. This is the approach of the LDA+U method [39, 40]. In detail, the method adds a Hubbard U [41] to such orbitals with the effect that the orbitals shift in energy. This can correct for wrong occupations of the highly localized orbitals and thus may yield an improvement over predictions from LDA or GGA calculations for such materials on a qualitative level.

An often criticized drawback of the LDA+U approach is that material dependent energy parameters U are introduced and the question arises how the U parameters are determined. Three approaches are to either obtain them by fitting to experiments, to determine them with constrained DFT calculations, or to extract them from constrained random phase approximation (cRPA) calculations [42, 43, 44, 45, 46]. Note that although the name suggests that LDA+U is only used to extend the LDA functional, in practice the term also covers GGA+U calculations that are very common, too.

2.1.5.4 Hybrid functionals

Another option to correct the self-interaction error is the use of so-called hybrid functionals. Just like LDA+U this class of functionals uses the Kohn-Sham orbitals as a starting point, such that it is a density functional only in an indirect sense. It replaces a part of the exchange energy of the LDA or GGA functional by the same fraction of the exact exchange (EXX) energy

$$E_{\mathrm{x}}^{\mathrm{EXX}} = -\frac{1}{2}\sum_{i,j,\sigma}\omega_i^\sigma\omega_j^\sigma\int\int\frac{\psi_i^{\sigma*}(\boldsymbol{r}_1)\psi_j^{\sigma*}(\boldsymbol{r}_2)\psi_j^\sigma(\boldsymbol{r}_1)\psi_i^\sigma(\boldsymbol{r}_2)}{|\boldsymbol{r}_1-\boldsymbol{r}_2|}d^3r_1d^3r_2, \tag{2.33}$$

which is structurally identical to the Hartree-Fock exchange, though in this case one does not plug in Hartee-Fock but Kohn-Sham orbitals.

A couple of hybrid functionals have been established as commonly used tools. An early and important development in this sense is the B3LYP functional [47, 48] that found widespread adoption in the realm of quantum chemistry. In the B3LYP functional, the exchange-correlation energy is given by

$$E_{\mathrm{xc}}^{\mathrm{B3LYP}} = E_{\mathrm{x}}^{\mathrm{LSDA}} + a_{\mathrm{EXX}}(E_{\mathrm{x}}^{\mathrm{EXX}} - E_{\mathrm{x}}^{\mathrm{LSDA}}) + a_{\mathrm{x}}\Delta E_{\mathrm{x}}^{\mathrm{B88}} + E_{\mathrm{c}}^{\mathrm{VWN}} + a_{\mathrm{c}}(E_{\mathrm{c}}^{\mathrm{LYP}} - E_{\mathrm{c}}^{\mathrm{VWN}}), \tag{2.34}$$

where E_x^{LSDA} is the exchange energy from the LSDA, E_x^{B88} is a gradient correction for the exchange energy [35], and E_c^{VWN} and E_c^{LYP} are the correlation energies according to the VWN [30] and LYP [49] functionals. The coefficients $a_{EXX} = 0.2$, $a_x = 0.72$, and $a_c = 0.81$ are empirically determined by fitting to experimental data for a test set of materials [47].

Due to the nonlocality of the EXX term in space and the long range of the Coulomb interaction, the B3LYP functional gives rise to considerably increased computational demands. A solution to this problem is given by the PBE based HSE hybrid functional [50, 51] that screens the Coulomb interaction for the exact exchange such that this term only contains short range contributions and the long range contributions are neglected.

In comparison to the LDA+U approach, hybrid functionals do not contain material dependent parameters. They do, however, contain at least one material independent parameter that defines the fraction of exact exchange that contributes to the energy functional.

2.1.5.5 EXX+RPA and beyond

In some materials one observes correlation interactions between the electrons that are not covered by any of the so far mentioned XC functionals. For example, van der Waals interactions between molecules are beyond the description capabilities of these functionals. Thus, one has the desire to take the next step on the Jacob's ladder and approximate the XC functional in a more systematic manner that also covers these correlation interactions.

By adiabatically connecting [52, 53, 54] the Kohn-Sham system of noninteracting electrons to a fully interacting system one recognizes that a very accurate approximation for the XC energy is obtained by combining the exact exchange (EXX) energy with a systematic approximation to the correlation energy, which is known as the random phase approximation (RPA) [55, 56, 57, 58, 59]. Though this technique is computationally expensive, several research groups follow this route and realize EXX+RPA in their DFT codes. Due to this popularity several elaborate reviews on this topic have been published [60, 61].

We limit the discussion on EXX+RPA to the presentation of the RPA correlation energy that is given by

$$E_c^{RPA} = \frac{1}{2\pi} \int_0^\infty \int\int\int \ln\left(1 - \frac{\chi(\boldsymbol{r}, \boldsymbol{r}', i\omega)}{|\boldsymbol{r} - \boldsymbol{r}'|}\right) + \frac{\chi(\boldsymbol{r}, \boldsymbol{r}', i\omega)}{|\boldsymbol{r} - \boldsymbol{r}'|} d^3r d^3r' d\omega, \tag{2.35}$$

where $\chi(\boldsymbol{r}, \boldsymbol{r}', i\omega)$ is the Kohn-Sham response function for the system of noninteracting electrons. Equations (2.33) and (2.35) are then combined to obtain the xc energy in the EXX+RPA approach

$$E_{xc}^{EXX+RPA} = E_x^{EXX} + E_c^{RPA}. \tag{2.36}$$

One finds that the RPA provides a very accurate description of long-range correlations, while it has deficiencies in the short range [62]. To overcome this weakness, people already consider the next steps beyond EXX+RPA. A pragmatic way of addressing this issue is to mix the RPA with functionals that are more adequate for short-range correlations. For example, in the RPA+ approach [63, 64] the RPA is combined with a conventional semilocal GGA functional.

In a more systematic correction of the RPA one can also consider the missing contributions to the XC functional on a more fundamental level. One possible approach in this direction is to identify the second-order screened exchange [65, 66, 67] (SOSEX) corrections to be complementary to the RPA, such that it is reasonable to combine them. Ren *et al.* also consider renormalized single excitation (rSE) corrections [68] as another important ingredient for a next generation XC functional and combine RPA, SOSEX, and rSE in a unifying method that they call renormalized second-order perturbation theory [69] (r2PT).

In a concluding remark we note that the ever increasing computer power enables the adoption of more and more accurate XC functionals. While the XC functional represents only a small contribution to the total energy of a Kohn-Sham system, the approximation to this term is a critical ingredient when it comes to the accuracy of predictions from DFT calculations. With the advent of more and more ambitious and systematic approximations to this functional, the prediction power of DFT reaches an ever higher level and becomes more and more independent of the respective material.

2.2 Aspects of electronic structure methods

When DFT is realized in practice, many design decisions have to be made that lead to a trade-off between accuracy and required computing resources. The large field of different approaches in this regard is called electronic structure methods. In this chapter we provide a short overview on the different options in this context. Figure 2.2 gives a sketch of these options for the different elements of the Kohn-Sham equations.

From a theoretical point of view the most fundamental aspect of the Kohn-Sham equation is the choice of the approximation to the exchange-correlation (XC) functional, that is typically interchangeable in DFT programs. We have already discussed this issue in section 2.1.5. In this chapter we discuss the realization of the other terms within the Kohn-Sham equation in computer programs. We start with a discussion on the different possible degrees of relativity in 2.2.1. One also has to decide if all electrons are included in the calculations or only the valence electrons since energetically deep lying core electrons only have a limited influence on the valence structure. This aspect is covered in section 2.2.2.

The last two sections in this chapter cover representation aspects. First we discuss the option of abstracting from some features of the potential in section 2.2.3 before we finally provide an overview on different ways to represent the wave functions in section 2.2.4. This last aspect is very important with regards to the question which of

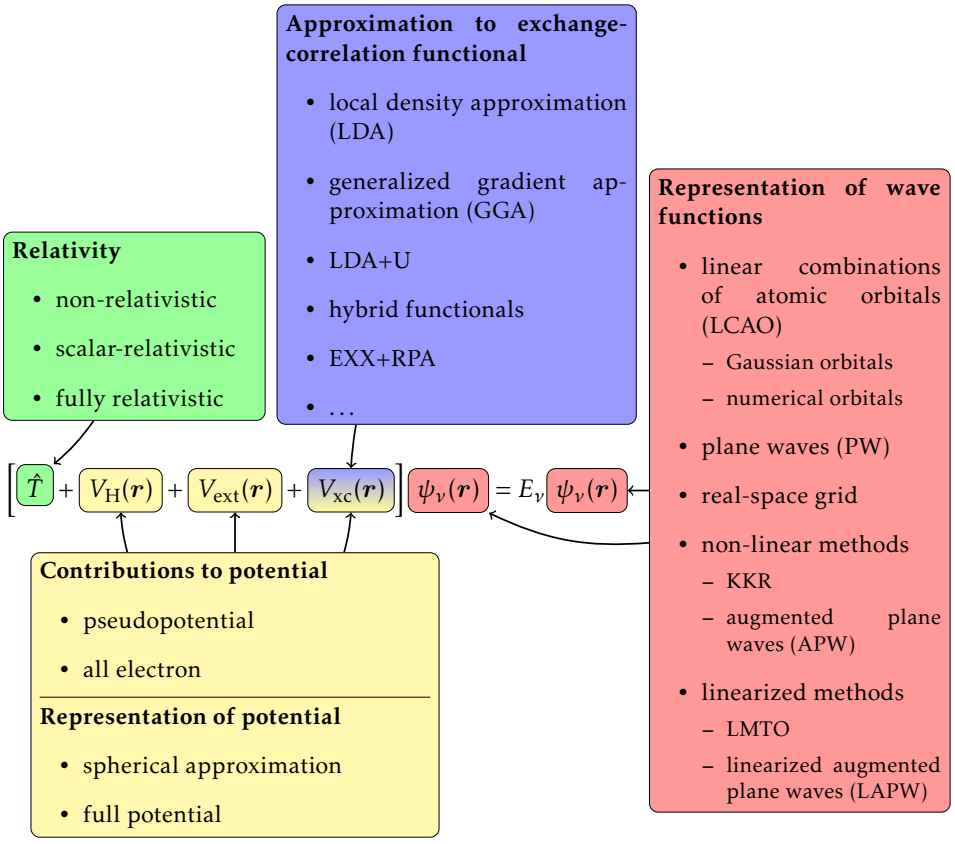

Figure 2.2.: Design choices for electronic structure methods[3]. The figure illustrates the main options on the implementations of the different terms of the Kohn-Sham equations in a DFT program.

the aforementioned approximations have to be performed. Furthermore, the representation of the wave functions is also a key component when it comes to the aspect of the efficiency of a DFT program.

2.2.1 From non-relativistic to fully relativistic calculations

We presented the basic introduction to DFT in chapter 2.1 in a non-relativistic fashion. However, in many materials relativistic effects are very important. Especially electrons in the vicinity of heavy atomic nuclei are affected by relativity. Hence, in

[3]The figure is motivated by similar illustrations in [20, 70].

order to deal with such effects a more adequate description replaces the Kohn-Sham equations (2.24) by the fully relativistic Kohn-Sham-Dirac equations[4] [72, 73]

$$\left[c\boldsymbol{\alpha}\cdot\boldsymbol{p}+(\beta-1)m_{\mathrm{e}}c^2+V_{\mathrm{eff}}(\boldsymbol{r})\right]\psi_i=E_i\psi_i. \tag{2.37}$$

Here, ψ_i is a 4 component wave function, c is the speed of light, $\boldsymbol{p}$ is the momentum operator, and α is a 3 element vector of 4×4 matrices with

$$\alpha_i=\begin{pmatrix}0 & \sigma_i\\ \sigma_i & 0\end{pmatrix}, \tag{2.38}$$

where σ_i are the Pauli spin matrices

$$\sigma_1=\begin{pmatrix}0 & 1\\ 1 & 0\end{pmatrix},\qquad \sigma_2=\begin{pmatrix}0 & -i\\ i & 0\end{pmatrix},\qquad \sigma_3=\begin{pmatrix}1 & 0\\ 0 & -1\end{pmatrix}. \tag{2.39}$$

Finally, β is also a 4×4 matrix with

$$\beta=\begin{pmatrix}1 & 0 & 0 & 0\\ 0 & 1 & 0 & 0\\ 0 & 0 & -1 & 0\\ 0 & 0 & 0 & -1\end{pmatrix}. \tag{2.40}$$

Unfortunately it is computationally very expensive to deal with 4 component wave functions and thus one wants to avoid solving the fully relativistic problem, at least for those electrons that are not strongly affected by relativistic effects.

One reasonable approach is thus to handle electrons in the inner electron shells, so called core electrons, in terms of a fully relativistic description, while the valence electron model abstracts from relativistic effects and describes the electrons by a non-relativistic Kohn-Sham equation. An intermediate approach is the scalar-relativistic approximation to the Dirac equation [74, 75] in which the spin-orbit coupling is taken out of the relativistic description but all other relativistic effects remain. By introducing this approximation the wave function is reduced to two components.

2.2.2 Pseudopotential or all-electron

The effective potential has singularities at the atomic nuclei. As a consequence, in the vicinity of the nuclei wave functions are often strongly oscillating. The description of wave functions with such features is expensive. Assuming a Fourier expansion of the wave functions into plane waves, one can observe a very slow convergence. On

[4] Note that the here presented Kohn-Sham-Dirac Hamiltonian features a term $-1m_{\mathrm{e}}c^2$ that subtracts the mass energy of the electron [71]. This is only required to obtain a consistent formulation with the non-relativistic equations in which the mass energy of the electron is neglected. Often, the Kohn-Sham-Dirac equations are formulated without this extra term.

the other hand, sampling the wave functions spatially requires a very fine mesh, especially in the near of the nuclei. The requirement of such expensive representations imposes very high computational demands and one has to ask if this can be avoided.

The introduction of pseudopotentials is a very common option to reduce the costs associated with the representation of the wave functions. Pseudopotentials are based on the observation that the chemistry is nearly completely determined by the valence electrons. Since the core electrons are strongly localized around the atomic nuclei, in a crystal or molecule one does not observe a significant overlap of core electrons from one atom with those from adjacent atoms. This leads to the fact that the orbitals of core electrons in crystals are nearly identical to those in isolated atoms. They neither significantly affect the crystal nor are affected by the crystal. The basic question now is if a good model can be found that abstracts from the core electrons and yields the electronic structure of a given material not by an all-electron calculation but by a calculation that incorporates only the valence electrons. The introduction of a pseudopotential is the answer to this question.

In pseudopotential calculations the description of the core electrons is replaced by an altered potential around each atom that incorporates the influence of the core electrons on the valence electrons and additionally leads to smooth valence electron wave functions that possess similar properties in comparison to the valence wave functions from all-electron calculations. In detail pseudopotentials are often constructed such that for prototype atom configurations four properties are fulfilled [76]:

Properties of pseudopotentials

1. The valence wave functions obtained from pseudopotentials are radially nodeless.
2. Beyond a cutoff radius r_{cut} the pseudopotential wave functions $\psi_v^{\text{PP}}(r)$ are identical to the corresponding all-electron wave functions above the c core states $\psi_{v+c}^{\text{AE}}(r)$[a]:
$$\psi_v^{\text{PP}}(r) = \psi_{v+c}^{\text{AE}}(r) \qquad \forall r : r > r_{\text{cut}}. \tag{2.41}$$
3. Norm conservation: Pseudopotential and all-electron wave functions give rise to the same amount of charge:
$$\int_0^{r_{\text{cut}}} r^2 |\psi_v^{\text{PP}}(r)|^2 dr = \int_0^{r_{\text{cut}}} r^2 |\psi_{v+c}^{\text{AE}}(r)|^2 dr. \tag{2.42}$$
4. Pseudopotential and all-electron wave functions have the same eigenvalues:
$$\epsilon_v^{\text{PP}} = \epsilon_{v+c}^{\text{AE}}. \tag{2.43}$$

[a] Some authors mention this property also for the logarithmic derivatives of the first energy derivatives of the wave functions [77].

The construction of pseudopotentials[5] is often angular momentum l dependent and follows a scheme that starts with the generation of the all-electron valence wave function $\psi_l^{\text{AE}}(r)$ for the prototype atom configuration. Next, the wave function is replaced by the pseudized wave function $\psi_l^{\text{PP}}(r)$ which is identical to $\psi_l^{\text{AE}}(r)$ outside of the chosen r_{cut} and offers the mentioned properties for $r < r_{\text{cut}}$, e.g., it is radially nodeless and smooth. The actual construction of the pseudopotential is now performed by inverting the Schrödinger equation. For the given l-channel a screened pseudopotential that includes the contributions from the valence electrons to the Hartree and exchange-correlation potentials is then obtained as

$$V_{\text{scr},l}^{\text{PP}}(r) = \epsilon_l - \frac{l(l+1)}{2r^2} + \frac{1}{2r\psi_l^{\text{PP}}(r)} \frac{d^2}{dr^2} \left[r\psi_l^{\text{PP}}(r) \right]. \tag{2.44}$$

To use the pseudopotential in DFT calculations the screening from the valence electrons has to be removed. This is easily achieved by subtracting the corresponding Hartree and exchange-correlation terms. By doing this one obtains the unscreened ionic pseudopotential

$$V_{\text{ion},l}^{\text{PP}}(r) = V_{\text{scr},l}^{\text{PP}}(r) - V_{\text{H}}^{\text{PP}}(r) - V_{\text{xc}}^{\text{PP}}(r). \tag{2.45}$$

[5] We follow the construction as it is presented in [76].

Summing up all l-channels, one finally ends up with the overall ionic pseudopotential

$$V_{\text{ion}}^{\text{PP}}(\boldsymbol{r}) = \sum_{lm} |\text{Y}_{lm}\rangle V_{\text{ion},l}^{\text{PP}}(r)\langle \text{Y}_{lm}|. \tag{2.46}$$

The so-constructed pseudopotentials are local in the radial coordinates and nonlocal in the angular coordinates. Unfortunately this semilocal form leads to high computational demands. To circumvent these demands, Kleinman and Bylander [78] transform them into a fully nonlocal and separable form that does not suffer from such limitations. Another important limitation of these norm-conserving pseudopotentials is that they are only efficient in lowering the frequencies of wave functions that possess radial nodes in all-electron calculations. Wave functions without radial nodes can only be slightly smoothed by going to a pseudopotential model. This aspect is addressed by Vanderbilt [79], who removes the norm-conservation requirement from the list of properties of the pseudopotentials to obtain so-called ultra-soft pseudopotentials.

As a final note we point out that pseudopotentials have successfully been used in the description of many materials. However, one has to keep in mind that the pseudopotential approximation strongly relies on an assumed negligible influence coming from the core electrons and that pseudopotentials are created for a prototype atom configuration that typically does not feature a strong connection to the actual material under investigation. Therefore, the transferability of the pseudopotentials always has to be questioned.

2.2.3 Spherical approximation or full-potential

For atoms with nuclear charge Z the effective potential exhibits a $-Z/r$ behavior in the vicinity of the atomic nucleus. These singularities at the atom positions give rise to representations of the electronic structure in which the atom positions are special points. Often they are centers of spheres in which the wave functions, potential and density are represented by linear combinations of products of radial functions and spherical harmonics.

Whenever such a representation of the potential is used, a reduction of the computational demands for constructing the Hamilton and overlap matrices can be achieved by applying an approximation to the shape of the potential. In detail, Slater [8] proposes an approximation in which the potential is assumed to be spherical, meaning it only possesses coefficients for the spherical harmonic with angular momentum $l = 0$.

Note that such a spherical approximation is justified since the spherical part of the potential strongly dominates the other parts in the vicinity of the nucleus. Especially for close-packed materials (fcc, hcp lattices) this approach works very well. However, it is limited when materials are investigated that involve strongly directed covalent bonds. Here, the consideration of the full potential is mandatory.

2.2.4 Representing the wave functions

When it comes to the computational demands of DFT calculations the representation of the wave functions is one of the most important aspects. Often the Kohn-Sham eigenvalue problem is transformed into an algebraic problem by expanding the wave functions into some set of basis functions $\{\phi_i(\boldsymbol{r})\}$. By doing this, the Kohn-Sham Hamiltonian becomes a matrix

$$H_{ij} = \langle \phi_i | \hat{H} | \phi_j \rangle \tag{2.47}$$

and the eigenvalue problem becomes a generalized algebraic eigenvalue problem

$$\sum_j z_{\nu j} H_{ij} = \epsilon_\nu \sum_j z_{\nu j} S_{ij}, \tag{2.48}$$

where $S_{ij} = \langle \phi_i | \phi_j \rangle$ is the overlap matrix whose elements are the overlaps between two basis functions, ϵ_ν is the ν-th eigenvalue, and $z_{\nu j}$ is the expansion coefficient of the ν-th eigenfunction into the j-th basis function. Note that both, H_{ij} and S_{ij}, are hermitian matrices.

The computational demands for diagonalizing such a problem scale cubically with the size of the matrices, i.e., the number of basis functions. In typical DFT programs this step either dominates the overall runtime required for an iteration of the self-consistency loop or is at least one of the main time consumers. Another demanding step may be the setup of the Hamilton and overlap matrices, that may also scale cubically with the system size, although only quadratically with the number of basis functions.

As the basis set size drastically affects the computational demands, it is a good idea to put some effort into problem descriptions that require only small basis sets. For example, the usage of the aforementioned pseudopotentials is a method to reduce the demands on the basis sets such that it is easier to describe the wave functions with basis sets incorporating only very few functions. Another option is the construction of a sophisticated problem-adapted basis that offers a high description efficiency, i.e., the results converge very fast with growing basis set size, even without the usage of pseudopotentials. More fundamentally, one also wants to have a basis, that can systematically be extended, such that calculation results can be converged with respect to the basis set size without missing important features of the wave functions. On the other hand, it is also a desirable characteristic of basis functions that the matrix elements are easy to formulate and to compute. These different properties are partially contradictory to each other and a certain basis is always a tradeoff between them and may give rise to the demand to introduce further approximations. In the following we give a short overview on basis sets that are commonly used in the context of electronic structure calculations.

2.2.4.1 Linear combination of atomic orbitals (LCAO)

Electron orbitals in a molecule or in a bulk material are often strongly related to a specific atom and localized around this atom. Considering this fact, a natural approach for a basis is a set of atomically centered functions. Such basis sets of atomic orbitals are successfully used in various DFT programs. For the atomically centered functions one may use Gaussian-type [80] or Slater-type [81] orbitals. Beyond these analytically determined basis function sets, the use of numerically calculated atomic orbitals [82, 83, 84] has also become a very successfully and widely used approach.

The numerically determined atomic basis sets have the potential to possess a high description efficiency. Furthermore, they can also be constructed to be strictly localized, i.e., each basis function is zero outside of some sphere around the associated atom. This can strongly reduce computational demands and is typically done in programs using such bases. Nevertheless, LCAO basis sets also have an important disadvantage: They are typically constructed to perform especially well for a test set of prototype materials and it is not clear how they can systematically be extended. One therefore has to hope that the description efficiency of the basis is transfered to the material under investigation and no important feature of the wave function is missing in the description. This has to be considered especially when materials are taken under scrutiny that exhibit physical properties that strongly deviate from the prototype materials for which the basis sets are optimized. To cover a broad range of materials, the basis sets are typically constructed with covalent bonds in mind, which represent a challenge for LCAO basis sets.

2.2.4.2 Plane waves

While LCAO basis sets approach the description from an atom point of view, one may also start from a crystal point of view in which the basis functions are constructed by considering the Bloch theorem stating that a wave function in a crystal has the form

$$\psi_{\nu\boldsymbol{k}}(\boldsymbol{r}) = e^{i\boldsymbol{k}\boldsymbol{r}} u_{\nu\boldsymbol{k}}(\boldsymbol{r}), \tag{2.49}$$

where $\boldsymbol{k}$ is the Bloch vector and $u_{\nu\boldsymbol{k}}(\boldsymbol{r})$ is a periodic function with the periodicity given by the unit cell of the crystal. Due to the periodicity of $u_{\nu\boldsymbol{k}}(\boldsymbol{r})$ it is natural to expand this function in terms of plane waves. One thus ends up with a description

$$\psi_{\nu\boldsymbol{k}}(\boldsymbol{r}) = e^{i\boldsymbol{k}\boldsymbol{r}} \sum_{\boldsymbol{G}} z_{\nu\boldsymbol{k}}^{\boldsymbol{G}} e^{i\boldsymbol{G}\boldsymbol{r}} = \sum_{\boldsymbol{G}} z_{\nu\boldsymbol{k}}^{\boldsymbol{G}} e^{i(\boldsymbol{k}+\boldsymbol{G})\boldsymbol{r}}, \tag{2.50}$$

where the reciprocal lattice vectors $\boldsymbol{G}$ are the wave vectors for the plane waves and the $z_{\nu\boldsymbol{k}}^{\boldsymbol{G}}$ are the plane wave expansion coefficients of $u_{\nu\boldsymbol{k}}(\boldsymbol{r})$. The restriction to let all $\boldsymbol{G}$ be reciprocal lattice vectors of course automatically yields the required periodicity of $u_{\nu\boldsymbol{k}}(\boldsymbol{r})$.

Plane waves are a complete set of functions with respect to the lattice periodic functions $u_{\nu\boldsymbol{k}}(\boldsymbol{r})$ and finite sets of plane waves are systematically extendable by incorporating plane waves with ever shorter wavelength. As the kinetic energy associated

with a given plane wave scales with $|\boldsymbol{k}+\boldsymbol{G}|^2$ this is in fact a way of extending the basis that systematically covers all relevant physics.

However, the oscillations of the wave functions in the near of the atomic nuclei possess rather high spatial frequencies, such that very large plane wave basis sets are required to describe them accurately. As a consequence, the size of the required basis sets makes calculations on most materials infeasible. To overcome this drawback, one either has to make use of the pseudopotential approximation (see chapter 2.2.2), use the projector augmented wave (PAW) approach [85], or apply an alternative description of the wave functions in the near of the atomic nuclei. Each of these approaches is successfully and commonly used.

2.2.4.3 Real-space grid

Dual to a plane wave representation of the wave functions in reciprocal space, one can also solve the Kohn-Sham equations on a real-space mesh. Considering a perfect representation of the wave functions on such a mesh, according to the Whittaker-Shannon interpolation formula this is actually a basis of sinc functions. But as sinc functions are not very localized one considers simpler interpolation schemes to evaluate the kinetic energy of wave functions represented on a real-space grid in terms of finite differences. With this approach, in a real-space mesh representation the Kohn-Sham Hamiltonian is local.

A real-space representation has the same drawbacks as a plane wave representation: The oscillations of the wave functions in the near of the atomic nuclei call for a very fine mesh. Of course, this problem can be approached again by introducing pseudopotentials or alternative representations in the near of the atomic nuclei.

2.2.4.4 Non-linear methods

The alternative to the usage of approximations to overcome the challenges associated with the singularities of the effective potential is the introduction of basis sets whose analytic form is adapted to the differing demands in different regions within a unit cell. The first step in such a region-specific description is the definition of the regions. For this, the augmented plane wave (APW) method [8] uses nonoverlapping so-called muffin-tin spheres centered at the atom positions and an interstitial region between the spheres. With the so-defined regions, the singularities of the potential are in the centers of the spheres, while the interstitial region features a rather flat and slowly varying potential.

Assuming the spherical approximation (see chapter 2.2.3) one can construct energy-dependent basis functions $u_l(r, E_{\boldsymbol{k}\nu l})Y_{lm}(\theta, \phi)$ within the muffin-tin spheres by solving the corresponding radial Schrödinger equation for an energy parameter $E_{\boldsymbol{k}\nu l}$ as a differential equation from the centers of the spheres outwards to obtain functions

with regular behavior in the sphere centers. In detail, one solves

$$\left[-\frac{1}{2r^2}\frac{d}{dr}\left(r^2\frac{d}{dr}\right)+\frac{l(l+1)}{2r^2}+V_{\text{eff}}^{\text{sphr}}(r)-E_{\boldsymbol{k}\nu l}\right]u_l(r,E_{\boldsymbol{k}\nu l})=0, \tag{2.51}$$

where r is the radial coordinate relative to the position of the nucleus. The radial functions $u_{\nu l}(r,E_{\boldsymbol{k}nl})$ can be represented on an exponential mesh that has a very fine sampling near the atomic nucleus and a coarser sampling in the outer regions of the sphere. In the interstitial region, the wave functions can be represented by a rapidly converging plane wave expansion.

The drawback of this method is that the basis itself is specific for each Kohn-Sham orbital and the energy parameters $E_{\boldsymbol{k}\nu l}$ are given as the eigenenergies of the Kohn-Sham orbitals for the complete system. Since these eigenenergies are not known in the run-up to the calculation, they have to be determined self-consistently with the eigenenergies. This makes APW calculations computationally expensive.

In the Korringa-Kohn-Rostocker (KKR) method [86, 87, 88, 89] another partitioning of space is used. Here, the space is subdivided into atomic polyhedra. Of course, this subdivision of space translates into adapted representations of the respective physical functions. The characteristic function indicating a certain atomic polyhedron can be expanded into products of spherical harmonics and radial functions around some given atom α. In detail, this shape function is

$$\begin{aligned}\theta_\alpha(\boldsymbol{r}) &= \begin{cases} 1 & \text{for } \boldsymbol{r}\in \text{Poly}_\alpha \\ 0 & \text{else}\end{cases} \\ &= \sum_L \theta_{\alpha L}(r_\alpha)Y_L(\hat{r}_\alpha).\end{aligned} \tag{2.52}$$

Functions like the potential around an atom are then also expressed in terms of products of radial functions and spherical harmonics. To restrict these functions to the associated polyhedron, they are multiplied with $\theta_\alpha(\boldsymbol{r})$.

Besides this unique partitioning of space, the specialty of the KKR method is its development into a multi-scattering Green function method [90, 91]. This means that in contrast to the so far discussed wave function methods, the central information carrier in KKR is the Green function $G(\boldsymbol{r},\boldsymbol{r}',E)$ describing the propagation of an electron between $\boldsymbol{r}$ and $\boldsymbol{r}'$. It is defined by

$$\left[E+\frac{1}{2}\nabla^2-V(\boldsymbol{r})\right]G(\boldsymbol{r},\boldsymbol{r}',E)=\delta(\boldsymbol{r}-\boldsymbol{r}'). \tag{2.53}$$

Starting with the Green function $G_0(\boldsymbol{r},\boldsymbol{r}',E)$ for the free space, in the KKR method the crystal Green function is calculated with the Dyson equation

$$G(\boldsymbol{r},\boldsymbol{r}',E)=G_0(\boldsymbol{r},\boldsymbol{r}',E)+\int G_0(\boldsymbol{r},\boldsymbol{r}'',E)V(\boldsymbol{r}'')G(\boldsymbol{r}'',\boldsymbol{r}',E)d^3r''. \tag{2.54}$$

To connect this approach to DFT one has to express the density in terms of the Green function. Here, one makes use of the fact that the spatially resolved density

of states $\rho(\boldsymbol{r}, E)$ is given by the imaginary part of the Green function. The density is then obtained by integrating this quantity over all energies below the Fermi level. In detail, the density is given by

$$\rho(\boldsymbol{r}) = \int_{-\infty}^{E_\mathrm{F}} \rho(\boldsymbol{r}, E) dE = -\frac{1}{\pi} \int_{-\infty}^{E_\mathrm{F}} \mathrm{Im}\left[G(\boldsymbol{r}, \boldsymbol{r}, E)\right] dE. \tag{2.55}$$

2.2.4.5 Linearized methods

In the APW method the energy parameter $E_{\boldsymbol{k}\nu l}$ and thus also the associated radial functions $u_l(r, E_{\boldsymbol{k}\nu l})$ are specific to each wave function. Unfortunately, the determination of these adapted energy parameters yields a very time consuming method such that one wants to have a method which does not require this direct link between the energy parameters and the wave functions.

To overcome this problem several approaches have been proposed to change the augmentation of the plane waves in the muffin-tin spheres. One important step in this regard is the modified APW (MAPW) [92, 93, 94] method. In this method the plane waves are also extended into the muffin-tin spheres, though for low angular momentum channels they are replaced by linear combinations of radial functions $u_{nl}(r, E_{nl})$ solving equation 2.51 for different energy parameters E_{nl}. In this case the radial functions neither depend on the $\boldsymbol{k}$ point nor on the wave functions anymore. Continuity is not enforced for the basis functions but for the wave functions continuity of value and slope is achieved by introducing additional constraints when solving the eigenvalue problem. Another important variation of the APW approach is the spline APW (SAPW) [95] method. Here, spline functions are used to augment the plane waves in the muffin-tin spheres.

A very popular approach that decouples the energy parameters from the wave functions is the linearized APW (LAPW) method [6]. Here, the idea is that a $u_l(r, E_{\boldsymbol{k}\nu l})$ at the energy $E_{\boldsymbol{k}\nu l}$ of the wave function can approximately be represented by a radial function $u_l(r, E_l)$ and the energy derivative of this function $\partial u_l(r, E)/\partial E|_{E=E_l} = \dot{u}_l(r, E_l)$, where E_l is in the near of $E_{\boldsymbol{k}\nu l}$.

In contrast to APW, the LAPW method replaces the $u_l(r, E_{\boldsymbol{k}\nu l})$ in the MT spheres by the two radial functions $u_l(r, E_l)$ and $\dot{u}_l(r, E_l)$. In detail, one constructs basis functions in which the plane wave in the interstitial region is matched to a linear combination of $u_l(r, E_l)$ and $\dot{u}_l(r, E_l)$, where the matching is determined by enforcing continuity of the basis function's value and slope at the MT sphere boundary. We will discuss this approach in detail in chapter 3.

The linearized muffin-tin orbitals (LMTO) method [6, 96] also uses the functions $u_l(r, E_l)$ and $\dot{u}_l(r, E_l)$ in MT spheres. However, in contrast to the LAPW method, beyond the MT sphere boundary the basis functions are not plane waves but Hankel functions times spherical harmonics that decay with growing distance to the respective atom.

As the LAPW method has its origins in plane wave methods, it is motivated by the shape of Bloch waves in crystals. The LMTO method, on the other hand has its origin in methods that use atomic orbitals as basis functions. This more direct connection to atomic orbitals yields a highly efficient basis set. However, it is not clear how to extend an LMTO basis in a systematic way. LAPW calculations are more systematically convergable.

3 The all-electron full-potential linearized augmented plane-wave method

Contents

Within the multifarious zoo of electronic structure methods, the all-electron full-potential linearized augmented plane-wave (FLAPW) method [6, 7] is one of the most accurate approaches of DFT in practice. As the name already suggests, it features a full potential treatment and explicitly handles core and valence electrons on an equal footing. To enable such an accurate treatment it is based on a partitioning of space

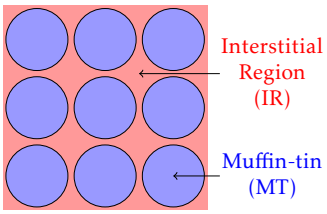

Figure 3.1.: Partitioning of space in the FLAPW method. A unit cell comprises nonoverlapping MT spheres centered at the atomic nuclei and the interstitial region between the spheres.

into so-called muffin-tin (MT) spheres centered at the atom positions and the remaining interstitial region between the spheres. An illustration for such a subdivision of space is shown in figure 3.1 in terms of a 2D projection of an example unit cell.

The representations of the wave functions, the electron density, and the potential are adapted to this subdivision of the unit cell. Within the MT spheres these quantities are represented by products of radial functions and spherical harmonics Y_L[1] and in the interstitial region they are represented by plane waves.

Based on several excellent introductions to FLAPW [18, 97, 70, 98], in this chapter we discuss the FLAPW method in detail. We start in section 3.1 by introducing the linearized augmented plane wave basis to represent the valence wave functions. In that section we will also discuss the treatment of the core electrons, as well as several extensions to the valence electron description. We continue in section 3.2 with a discussion on the setup of the Hamilton and overlap matrices. In section 3.3 we describe the construction of the charge density, before we sketch the calculation of the total energy in section 3.4. Finally, we list a couple of developments for the FLAPW method in section 3.5.

3.1 The linearized augmented plane-wave basis

The FLAPW method describes the valence electrons in terms of linearized augmented plane wave (LAPW) basis functions. These are plane waves in the IR and numerically determined radial functions times spherical harmonics Y_L in the MT spheres. The MT functions are matched in value and slope to the plane wave in the IR. In detail, an LAPW of Bloch vector $\boldsymbol{k}$ and reciprocal lattice vector $\boldsymbol{G}$ is defined as

$$\phi_{\boldsymbol{kG}}(\boldsymbol{r}) = \begin{cases} \frac{1}{\sqrt{\Omega}} e^{i(\boldsymbol{k}+\boldsymbol{G})\boldsymbol{r}} & \text{for } \boldsymbol{r} \in \mathrm{IR} \\ \sum_L \left[a^{L\alpha}_{\boldsymbol{kG}} u^{\alpha}_l(r_\alpha, E^{\alpha}_l) + b^{L\alpha}_{\boldsymbol{kG}} \dot{u}^{\alpha}_l(r_\alpha, E^{\alpha}_l) \right] Y_L(\hat{\boldsymbol{r}}_{\boldsymbol{\alpha}}) & \text{for } \boldsymbol{r} \in \mathrm{MT}^{\alpha} \end{cases}, \tag{3.1}$$

[1] $L = (l, m)$ is a compound index comprising the angular momentum and magnetic quantum numbers.

where $\boldsymbol{r}$ is the position vector and Ω is the volume of the unit cell. Within the MT sphere of atom α the basis functions depend on $\boldsymbol{r}_\alpha = \boldsymbol{r} - \boldsymbol{\tau}_\alpha$, which is the position vector relative to the atom position $\boldsymbol{\tau}_\alpha$, and on angular momentum dependent energy parameters E_l^α. The radial functions themselves are a linear combination of the functions $u_l^\alpha(r_\alpha, E_l^\alpha)$ and $\dot{u}_l^\alpha(r_\alpha, E_l^\alpha)$, where the coefficients $a_{\boldsymbol{kG}}^{L\alpha}$ and $b_{\boldsymbol{kG}}^{L\alpha}$ are obtained through the matching condition that LAPW basis functions are continuous in value and slope at the MT sphere boundaries. The functions $u_l^\alpha(r_\alpha, E_l^\alpha)$ and $\dot{u}_l^\alpha(r_\alpha, E_l^\alpha)$ are solutions to the scalar-relativistic approximation [74, 18] (SRA) to the radial Dirac equation for the spherical part of the potential within the MT sphere and their energy derivatives. In the SRA wave functions possess two components, a large component $g_l^\alpha(r_\alpha, E_l^\alpha)$ and a small component $f_l^\alpha(r_\alpha, E_l^\alpha)$. They are obtained by solving the differential equations

$$\begin{aligned}
\frac{\partial g_l^\alpha(r_\alpha, E_l^\alpha)}{\partial r_\alpha} &= 2M_l(r_\alpha, E_l^\alpha) c f_l^\alpha(r_\alpha, E_l^\alpha), \\
\frac{\partial f_l^\alpha(r_\alpha, E_l^\alpha)}{\partial r_\alpha} &= \left[\frac{l(l+1)}{2M_l(r_\alpha, E_l^\alpha) c r_\alpha^2} + \frac{1}{c}\left(V_{l=0}^\alpha(r_\alpha) - E_l^\alpha \right) \right] g_l^\alpha(r_\alpha, E_l^\alpha) \\
&\quad - \frac{2}{r_\alpha} f_l^\alpha(r_\alpha, E_l^\alpha),
\end{aligned} \tag{3.2}$$

for the energy parameter E_l^α from $r_\alpha = 0$ outwards to obtain solutions with regular behavior at the nuclei. In this equation system $V_{l=0}^\alpha(r_\alpha)$ is the $l = 0$ component of the effective potential and the quantity $M_l(r_\alpha, E_l^\alpha)$ is an abbreviation for

$$M_l(r_\alpha, E_l^\alpha) = m_e + \frac{1}{2c^2}\left(E_l^\alpha - V_{l=0}^\alpha(r_\alpha) \right). \tag{3.3}$$

For the matching at the MT boundaries one only considers the large component and neglects the small component.

The large and small components of the energy derivative $\dot{u}_l^\alpha(r_\alpha, E_l^\alpha)$ are obtained similarly after differentiating the equations with respect to the energy parameter to obtain

$$\begin{aligned}
\frac{\partial \dot{g}_l^\alpha(r_\alpha, E_l^\alpha)}{\partial r_\alpha} &= 2M_l(r_\alpha, E_l^\alpha) c \dot{f}_l^\alpha(r_\alpha, E_l^\alpha) + 2\dot{M}_l(r_\alpha, E_l^\alpha) c f_l^\alpha(r_\alpha, E_l^\alpha), \\
\frac{\partial \dot{f}_l^\alpha(r_\alpha, E_l^\alpha)}{\partial r_\alpha} &= \left[\frac{l(l+1)}{2M_l(r_\alpha, E_l^\alpha) c r_\alpha^2} + \frac{1}{c}\left(V_{l=0}^\alpha(r_\alpha) - E_l^\alpha \right) \right] \dot{g}_l^\alpha(r_\alpha, E_l^\alpha) \\
&\quad - \left[\frac{\dot{M}_l(r_\alpha, E_l^\alpha) l(l+1)}{2M_l^2(r_\alpha, E_l^\alpha) c r_\alpha^2} + \frac{1}{c} \right] g_l^\alpha(r_\alpha, E_l^\alpha) - \frac{2}{r_\alpha} \dot{f}_l^\alpha(r_\alpha, E_l^\alpha).
\end{aligned} \tag{3.4}$$

The idea of LAPW basis functions and their principle form is illustrated in figure 3.2.

In practice only a limited amount of basis functions can be used. To define these functions one introduces a reciprocal cutoff radius $K_{\max}$, i.e., all LAPWs fulfilling

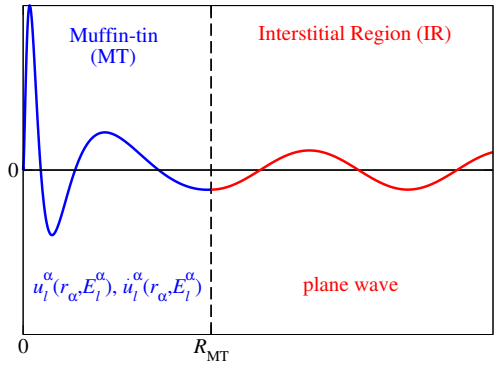

Figure 3.2.: Illustration of an LAPW basis function. The strongly oscillating part of the wave functions inside the MT spheres is described by the functions $u_l^\alpha(r_\alpha,E_l^\alpha)$ and $\dot{u}_l^\alpha(r_\alpha,E_l^\alpha)$, while plane waves are used in the interstitial region. Within a given LAPW basis function one forms a linear combination of the MT functions to obtain an overall continuous value and slope of the basis function at the MT sphere boundary.

the condition $|\boldsymbol{k}+\boldsymbol{G}| = |\boldsymbol{K}| \leq K_{\mathrm{max}}$ are part of the basis set. The definition of the cutoff in this way enforces a symmetric basis set such that no artificial asymmetries are injected into the DFT calculations. Additionally one introduces a cutoff for the maximal angular momentum in each MT sphere. These l_{max}^α restrict the L summation in equation (3.1) to those L with $l \leq l_{\mathrm{max}}^\alpha$. FLAPW calculations can be converged with respect to both, K_{max} and l_{max}^α. Within the interstitial region this systematically enables representations of wave functions on an ever finer scale since basis functions with higher and higher kinetic energy $\frac{1}{2}(\boldsymbol{k}+\boldsymbol{G})^2$ are included. In the MT spheres this is slightly different. Here, l_{max}^α controls the maximum angular momentum considered in the sphere and calculations can also be converged with respect to this limitation. Another aspect, however, is the variational freedom in a given l-channel which is restricted to the two radial functions $u_l^\alpha(r_\alpha,E_l^\alpha)$ and $\dot{u}_l^\alpha(r_\alpha,E_l^\alpha)$.

In the spherical approximation, the functions $u_l^\alpha(r_\alpha,E_l^\alpha)$ provide a perfect MT representation of wave functions with the same energy. The inclusion of the energy derivative $\dot{u}_l^\alpha(r_\alpha,E_l^\alpha)$ on the other hand enables the freedom to precisely represent wave functions with energies deviating from the energy parameter E_l^α. To assess the error made in the representation of such a wave function at energy E, one may in a first approximation write down a Taylor expansion of the wave function

$$u_l^\alpha(r_\alpha,E) = u_l^\alpha(r_\alpha,E_l^\alpha) + (E-E_l^\alpha)\dot{u}_l^\alpha(r_\alpha,E_l^\alpha) + \mathcal{O}\left((E-E_l^\alpha)^2\right) \tag{3.5}$$

to find that the linearized description around the energy parameter E_l^α leaves an error that scales with the square of the energy difference. Note however that this error estimation is somewhat hand waving since the wave function is determined by a variational method such that the expansion coefficients of the radial functions have

the freedom to deviate from those in the Taylor expansion. Another aspect that is not covered by this estimation is the capability of the radial functions to represent wave functions if the spherical approximation is not applied and the electrons are exposed to the full potential. Nevertheless, in practice it turns out that the radial functions $u_l^\alpha(r_\alpha, E_l^\alpha)$ and $\dot{u}_l^\alpha(r_\alpha, E_l^\alpha)$ enable a precise description of the Kohn-Sham wave functions within an interval of a few eV around the chosen energy parameter. In many materials this is sufficient to represent the valence electrons with a single energy parameter per angular momentum quantum number.

3.1.1 Treatment of the core electrons

In the FLAPW method valence and core electrons are separated from each other, such that the core electrons are only exposed to the spherical potential around their associated atomic nucleus and their wave functions are determined for each atom separately. The valence electrons, on the other hand, are exposed to the full potential and described by the LAPW basis. This splitting of the treatment is done on the one hand to reduce the computational demands of the method by decreasing the number of electrons that have to be described by the LAPW basis and on the other hand to increase the accuracy of the method as it allows to treat the core electrons in a fully relativistic fashion. The separation of core and valence electrons is possible if the LAPW basis is orthogonal to the core states. If this cannot be guaranteed one may obtain a description of core electron states with the LAPW basis, which may appear within the window of occupied valence states. As a consequence, such an unphysical *ghost band* might become occupied which would yield a completely wrong valence structure.

The orthogonality between the core states and the LAPW basis can be shown if one assumes that the LAPW basis functions in the MT spheres were determined by the nonrelativistic equations

$$\left[-\frac{1}{2}\frac{\partial^2}{\partial r_\alpha^2} + \frac{l(l+1)}{2r_\alpha^2} + V_{\text{eff}}^{\text{sphr}}(r_\alpha)\right] r_\alpha u_l^\alpha(r_\alpha, E_l^\alpha) = E_l^\alpha r_\alpha u_l^\alpha(r_\alpha, E_l^\alpha) \tag{3.6}$$

and

$$\left[-\frac{1}{2}\frac{\partial^2}{\partial r_\alpha^2} + \frac{l(l+1)}{2r_\alpha^2} + V_{\text{eff}}^{\text{sphr}}(r_\alpha)\right] r_\alpha \dot{u}_l^\alpha(r_\alpha, E_l^\alpha) = E_l^\alpha r_\alpha \dot{u}_l^\alpha(r_\alpha, E_l^\alpha) + r_\alpha u_l^\alpha(r_\alpha, E_l^\alpha) \tag{3.7}$$

and that the similarly nonrelativistically determined core states are strictly confined within the MT sphere. For this, one considers a core wave function $u_{l,\text{c}}^\alpha(r_\alpha, E_{l,\text{c}}^\alpha)$ determined on the basis of equation (3.6).

The simple proof starts by multiplying equation (3.6) for the LAPW basis with $r_\alpha u_{l,\text{c}}^\alpha(r_\alpha, E_{l,\text{c}}^\alpha)$ and the equivalent equation for the core state with $r_\alpha u_l^\alpha(r_\alpha, E_l^\alpha)$. By

subtracting these two new equations from each other one obtains

$$\frac{1}{2}r_\alpha u_{l,\mathrm{c}}^\alpha(r_\alpha,E_{l,\mathrm{c}}^\alpha)\frac{\partial^2}{\partial r_\alpha^2}r_\alpha u_l^\alpha(r_\alpha,E_l^\alpha)-\frac{1}{2}r_\alpha u_l^\alpha(r_\alpha,E_l^\alpha)\frac{\partial^2}{\partial r_\alpha^2}r_\alpha u_{l,\mathrm{c}}^\alpha(r_\alpha,E_{l,\mathrm{c}}^\alpha)$$
$$=(E_l^\alpha-E_{l,\mathrm{c}}^\alpha)u_l^\alpha(r_\alpha,E_l^\alpha)r_\alpha^2u_{l,\mathrm{c}}^\alpha(r_\alpha,E_{l,\mathrm{c}}^\alpha). \tag{3.8}$$

Integrating both sides of the equation from 0 to R_{MT^α} and considering the function value and derivative of $u_{l,\mathrm{c}}^\alpha(r_\alpha,E_{l,\mathrm{c}}^\alpha)$ at the MT boundary then yields

$$0=\langle u_{l,\mathrm{c}}^\alpha|u_l^\alpha\rangle_{R_{\mathrm{MT}^\alpha}}. \tag{3.9}$$

For $\dot{u}_l^\alpha(r_\alpha,E_l^\alpha)$ one analogously multiplies equation (3.7) with $r_\alpha u_{l,\mathrm{c}}^\alpha(r_\alpha,E_{l,\mathrm{c}}^\alpha)$ and the differential equation for the core wave function with $r_\alpha\dot{u}_l^\alpha(r_\alpha,E_l^\alpha)$. By subtracting these two equations from each other one obtains

$$\frac{1}{2}r_\alpha u_{l,\mathrm{c}}^\alpha(r_\alpha,E_{l,\mathrm{c}}^\alpha)\frac{\partial^2}{\partial r_\alpha^2}r_\alpha\dot{u}_l^\alpha(r_\alpha,E_l^\alpha)-\frac{1}{2}r_\alpha\dot{u}_l^\alpha(r_\alpha,E_l^\alpha)\frac{\partial^2}{\partial r_\alpha^2}r_\alpha u_{l,\mathrm{c}}^\alpha(r_\alpha,E_{l,\mathrm{c}}^\alpha)$$
$$-u_{l,\mathrm{c}}^\alpha(r_\alpha,E_{l,\mathrm{c}}^\alpha)r_\alpha^2u_l^\alpha(r_\alpha,E_l^\alpha)=(E_{l,\mathrm{c}}^\alpha-E_l^\alpha)\dot{u}_l^\alpha(r_\alpha,E_l^\alpha)r_\alpha^2u_{l,\mathrm{c}}^\alpha(r_\alpha,E_{l,\mathrm{c}}^\alpha). \tag{3.10}$$

After the integration this becomes

$$0=\langle u_{l,\mathrm{c}}^\alpha|\dot{u}_l^\alpha\rangle_{R_{\mathrm{MT}^\alpha}}. \tag{3.11}$$

However, the derivation of these orthogonality relations is based on two assumptions that are only approximately fulfilled. First, the core states are not completely confined within the MT spheres so that the valence basis is not strictly orthogonal to the core states. Second, a similar derivation of the scalar products between the valence basis functions and the core states with the scalar-relativistic differential equations (3.2) and (3.4) yields

$$\int_0^{R_{\mathrm{MT}^\alpha}}r_\alpha^2\left[g_{l,\mathrm{c}}^\alpha(r_\alpha,E_{l,\mathrm{c}}^\alpha)g_l^\alpha(r_\alpha,E_l^\alpha)+f_{l,\mathrm{c}}^\alpha(r_\alpha,E_{l,\mathrm{c}}^\alpha)f_l^\alpha(r_\alpha,E_l^\alpha)\right]dr_\alpha$$
$$=-\int_0^{R_{\mathrm{MT}^\alpha}}\frac{l(l+1)}{4c^2M_{l,\mathrm{c}}(r_\alpha,E_{l,\mathrm{c}}^\alpha)M_l(r_\alpha,E_l^\alpha)r_\alpha^2}r_\alpha^2g_{l,\mathrm{c}}^\alpha(r_\alpha,E_{l,\mathrm{c}}^\alpha)g_l^\alpha(r_\alpha,E_l^\alpha)dr_\alpha \tag{3.12}$$

and

$$\int_0^{R_{\mathrm{MT}^\alpha}}r_\alpha^2\left[g_{l,\mathrm{c}}^\alpha(r_\alpha,E_{l,\mathrm{c}}^\alpha)\dot{g}_l^\alpha(r_\alpha,E_l^\alpha)+f_{l,\mathrm{c}}^\alpha(r_\alpha,E_{l,\mathrm{c}}^\alpha)\dot{f}_l^\alpha(r_\alpha,E_l^\alpha)\right]dr_\alpha$$
$$=\int_0^{R_{\mathrm{MT}^\alpha}}\frac{l(l+1)}{8c^4M_{l,\mathrm{c}}(r_\alpha,E_{l,\mathrm{c}}^\alpha)M_l^2(r_\alpha,E_l^\alpha)r_\alpha^2}r_\alpha^2g_{l,\mathrm{c}}^\alpha(r_\alpha,E_{l,\mathrm{c}}^\alpha)g_l^\alpha(r_\alpha,E_l^\alpha)dr_\alpha$$
$$-\int_0^{R_{\mathrm{MT}^\alpha}}\frac{l(l+1)}{4c^2M_{l,\mathrm{c}}(r_\alpha,E_{l,\mathrm{c}}^\alpha)M_l(r_\alpha,E_l^\alpha)r_\alpha^2}r_\alpha^2g_{l,\mathrm{c}}^\alpha(r_\alpha,E_{l,\mathrm{c}}^\alpha)\dot{g}_l^\alpha(r_\alpha,E_l^\alpha)dr_\alpha, \tag{3.13}$$

where the index c once again denotes quantities associated with the core states. Obviously the scalar products do not vanish. This means that with the scalar-relativistically determined radial functions in the LAPW basis, the valence basis is not orthogonal to equivalently determined core states, even if the core states were completely confined within the MT spheres. However, also here the deviation from perfect orthogonality is small which can quickly be seen by noticing the powers of the speed of light in the denominators of the integrands. Thus, for all practical reasons these terms can be neglected and one keeps the approach to treat the core electrons apart from the valence electrons. Note that the here presented considerations do not cover the question how large the projection of the fully relativistically determined core states onto the LAPW basis is.

3.1.2 Extending the LAPW basis with local orbitals

As already mentioned, the assumption that core electron wave functions are completely confined within a MT sphere is only an approximation. Especially for energetically high-lying core states this approximation breaks down. The orthogonality approximation between the LAPW basis and such *semicore states* is inadequate and depending on the portion of the semicore wave function that is extended beyond the MT sphere boundary this may cause significant problems. In the worst case one obtains a mediocre description of the state by the LAPW basis. If this is the case the state may appear as a so-called *ghost state* within the valence states and may even get occupied. As a consequence, in such situations the state is doubly occupied, once as a core state and once as a valence state. One cannot obtain meaningful DFT results in such cases.

To handle such situations, Singh [9] proposed the extension of the LAPW basis by so-called *local orbitals* (LOs). These are additional basis functions that are completely confined within a MT sphere. For this, Singh introduces a new radial function $u_l^\alpha(r_\alpha, E_l^{\alpha,\mathrm{SC}})$ that is a solution to equations (3.2) for an energy $E_l^{\alpha,\mathrm{SC}}$ in the near of the semicore state. The $2l+1$ local orbitals are then constructed as

$$\phi_L^{\alpha,\mathrm{LO}}(\boldsymbol{r}) = \left[a_l^{\alpha,\mathrm{LO}} u_l^\alpha(r_\alpha, E_l^\alpha) + b_l^{\alpha,\mathrm{LO}} \dot{u}_l^\alpha(r_\alpha, E_l^\alpha) + c_l^{\alpha,\mathrm{LO}} u_l^\alpha(r_\alpha, E_l^{\alpha,\mathrm{SC}})\right] Y_L(\hat{\boldsymbol{r_\alpha}}), \qquad (3.14)$$

where LO is used as an index to address a certain local orbital within atom α. The coefficients $a_l^{\alpha,\mathrm{LO}}$, $b_l^{\alpha,\mathrm{LO}}$, and $c_l^{\alpha,\mathrm{LO}}$ are obtained by enforcing vanishing value and slope of the LO at the MT sphere boundary, as well as the normalization condition $\langle \phi_L^{\alpha(\boldsymbol{r}),\mathrm{LO}} | \phi_L^{\alpha(\boldsymbol{r}),\mathrm{LO}} \rangle = 1$. Figure 3.3 sketches the idea of a local orbital.

Semicore states form nearly dispersionless bands since their overlap with orbitals from other atoms is small. Thus, the radial function $u_l^\alpha(r_\alpha, E_l^{\alpha,\mathrm{SC}})$ already provides a highly precise representation of the associated states. An additional energy derivative at $E_l^{\alpha,\mathrm{SC}}$ is typically not required. With this excellent description, the semicore state can be treated by the valence framework and is removed from the core electrons. Note however that the treatment of these states with the valence basis also implies a transition from a fully relativistic to a scalar-relativistic description.

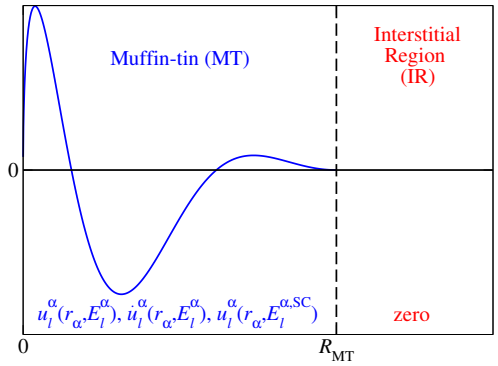

Figure 3.3.: Illustration of a local orbital. Local orbitals are additional localized basis functions, mostly used to describe semicore states. They consist of the functions $u_l^\alpha(r_\alpha, E_l^\alpha)$, $\dot{u}_l^\alpha(r_\alpha, E_l^\alpha)$, and a third function which is typically a $u_l^\alpha(r_\alpha, E_l^{\alpha,\mathrm{SC}})$, evaluated at an energy parameter in the near of the semicore state. These functions are linearly combined such that the resulting LO is normalized and features vanishing value and slope at the MT sphere boundaries.

3.1.3 Determination of the energy parameters

The energy parameters E_l^α of the LAPW basis functions have to be set in the run-up of an iteration of the DFT self consistency loop and the question arises how to choose them in the best way. Here we discuss two automatic and commonly used methods of determining these parameters.

The first approach, which we denote as *energy center of mass* (ECM) method, considers in a MT sphere the l projected density of states for the occupied states of the preceding iteration and sets the parameter to the energy center of mass of these states. In detail, one defines the $\boldsymbol{k}$ point resolved l-like charge originating from the eigenstate $\psi_{\boldsymbol{k}}^\nu$ as

$$\rho_{\boldsymbol{k},l}^{\nu,\alpha} = \omega_{\boldsymbol{k}}^\nu \int\limits_{\mathrm{MT}^\alpha} |\psi_{\boldsymbol{k},l}^{\nu,\alpha}(\boldsymbol{r})|^2 d^3r, \tag{3.15}$$

where $\psi_{\boldsymbol{k}l}^{\nu,\alpha}$ is the l-projection of $\psi_{\boldsymbol{k}}^\nu$ in the MT sphere around atom α and $\omega_{\boldsymbol{k}}^\nu$ is the occupation of this state, which also includes a weight for the respective $\boldsymbol{k}$ point.

The determination of the energy parameter is now based on the minimization of the quadratic error of the mismatch between the eigenstate energies and the energy parameter, weighted by the occupation of the states. Formally, one demands

$$\frac{\partial}{\partial E_l^\alpha} \sum_{\boldsymbol{k}} \sum_{\nu} \left(\epsilon_{\boldsymbol{k}}^\nu - E_l^\alpha\right)^2 \rho_{\boldsymbol{k},l}^{\nu,\alpha} = 0 \tag{3.16}$$

to obtain

$$E_l^\alpha = \frac{\sum_{\boldsymbol{k}} \sum_\nu \epsilon_{\boldsymbol{k}}^\nu \rho_{\boldsymbol{k},l}^{\nu,\alpha}}{\sum_{\boldsymbol{k}} \sum_\nu \rho_{\boldsymbol{k},l}^{\nu,\alpha}}. \tag{3.17}$$

The determination of the energy parameters in this way minimizes the leading rest term of the Taylor expansion (3.5) under consideration of the occupation of the states. Thus, it is a highly systematic approach to obtain nearly optimal energy parameters. Remaining deviations from the optimal energy parameters are associated with higher order terms in the Taylor expansion. Furthermore, the variational determination of the wave functions provides the freedom to obtain representations with expansion coefficients deviating from the Taylor expansion. As these additional degrees of freedom are not considered, this is another source for variations from the optimal energy parameters.

Semicore states, that are described by LOs within the valence framework, are typically excluded from the states contributing to the determination of the energy parameters. This is reasonable as one uses a separate radial function $u_l^\alpha(r_\alpha, E_l^{\alpha,\mathrm{SC}})$ with an adapted energy parameter to represent the semicore states. Thus, an inclusion of the semicore state in the determination of the energy parameters for the valence states would unnecessarily shift the energy parameters to lower energies and away from the valence states far above the semicore states.

The second approach, which we denote as *atomic energy parameters* (AEP) method, is based on the consideration that the bands in a crystal form out of atomic states when well separated isolated atoms are moved nearer to each other until they are in their final positions in the solid. With this premise, the AEP method determines the eigenenergies of the states of an artificial atomic problem, which consists of the spherical part of the effective potential in the MT sphere of the associated atom in the solid and a confining extension of this potential beyond the MT sphere boundary. For each l the energy parameter is then set to the energy of the atomic eigenstate with the same l and the same main quantum number which corresponds to the valence electrons of the atom in the solid. If the atom does not possess any valence electrons in a given l channel, the energy parameter is set to the energy of the lowest atomic eigenstate with same l above the core states. However, since this energy can be far above the valence states for high l quantum numbers, this algorithm is only performed for low l quantum numbers, e.g., for $l \leq 3$. For higher l one chooses an energy parameter in the near of the valence states, e.g., by setting $E_{l>3}^\alpha$ to $E_{l=3}^\alpha$.

Note that the ECM method depends on the occupations of the Kohn-Sham orbitals. Due to changes of the eigenenergies between consecutive iterations of the DFT self-consistency loop, these occupations can change drastically. Especially in materials with very flat bands near the Fermi level this can yield a problematic oscillatory behavior of the energy parameters, which, in the worst case, can impede a convergence of the charge density. The AEP method is not affected by this problem as it does not rely on the occupation numbers. Thus, this approach of determining the energy parameters yields a much more stable convergence behavior. On the other hand the

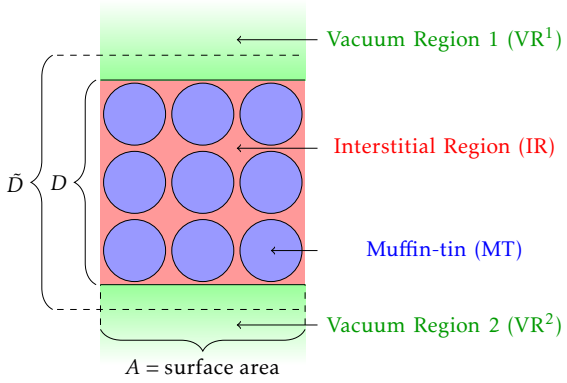

Figure 3.4.: Partitioning of space in the FLAPW method for film calculations. Additionally to the setup in Figure 3.1 there are vacuum regions attached to the unit cell at the boundaries in z direction. The unit cell is periodically continued only in x and y direction. In the illustration D is the extent of the interstitial region with respect to the matching at the z boundaries, while $\tilde{D}$ defines the interstitial region for the definition of the wave vectors. The surface area of the unit cell is denoted by A.

AEP method does not consider states from adjacent atoms that are extended into the respective MT sphere for which the energy parameter is determined. Such states give rise to an l-like charge that can be energetically far away from the associated energy parameter. Hence, atomic energy parameters are less problem adapted than ECM parameters.

3.1.4 The LAPW basis for thin films

The 3D geometry of bulk materials is not adequate for all materials of interest. Often, one is interested in the physics of surfaces. Such a configuration may be modeled by a thin film that is thick enough to possess bulk-like behavior in its central atom layers. An often followed approach to realize such a system in DFT codes is the usage of large unit cells that incorporate the thin film and a large region of space without any atoms in it to simulate a vacuum. In this case the atom-free region has to be large enough to decouple the thin films from neighboring unit cells. With a non-localized basis set such setups are inefficient since many basis functions have to be used to describe the atom-free region. For the FLAPW method another approach has been established [99].

Thin film calculations with the LAPW basis are performed in a 2D setup in which the unit cell is periodically continued only in the x and y direction, while additional vacuum regions (VRs) are attached to the unit cell boundaries in z direction. This setup is sketched in figure 3.4.

Similarly to the augmentation in the MT spheres the plane waves in the interstitial

region are augmented by special functions in the VRs. In detail one uses the projections of the plane waves in the IR onto the plane of the film $e^{i(\boldsymbol{k}_\parallel+\boldsymbol{G}_\parallel)\boldsymbol{r}_\parallel}$ times the functions $u^{\mathrm{vac}}_{\boldsymbol{k}_\parallel\boldsymbol{G}_\parallel}(z,E^{\mathrm{vac}})$ and $\dot{u}^{\mathrm{vac}}_{\boldsymbol{k}_\parallel\boldsymbol{G}_\parallel}(z,E^{\mathrm{vac}})$ which are solutions and energy derivatives to the Schrödinger equation to the planarly averaged effective potential $V^{\mathrm{avg,vac}}_{\mathrm{eff}}(z)$ in the region $\mathrm{VR}^{\mathrm{vac}}$ at the energy parameter E^{vac}. Numerically one solves

$$\left[-\frac{1}{2}\frac{\partial^2}{\partial z^2}+\frac{1}{2}\left(\boldsymbol{k}_\parallel+\boldsymbol{G}_\parallel\right)^2+V^{\mathrm{avg,vac}}_{\mathrm{eff}}(z)-E^{\mathrm{vac}}\right]u^{\mathrm{vac}}_{\boldsymbol{k}_\parallel\boldsymbol{G}_\parallel}(z,E^{\mathrm{vac}})=0 \tag{3.18}$$

and

$$\left[-\frac{1}{2}\frac{\partial^2}{\partial z^2}+\frac{1}{2}\left(\boldsymbol{k}_\parallel+\boldsymbol{G}_\parallel\right)^2+V^{\mathrm{avg,vac}}_{\mathrm{eff}}(z)-E^{\mathrm{vac}}\right]\dot{u}^{\mathrm{vac}}_{\boldsymbol{k}_\parallel\boldsymbol{G}_\parallel}(z,E^{\mathrm{vac}})=u^{\mathrm{vac}}_{\boldsymbol{k}_\parallel\boldsymbol{G}_\parallel}(z,E^{\mathrm{vac}}), \tag{3.19}$$

where $\boldsymbol{k}_\parallel$ is the two-dimensional Bloch vector in the plane of the film and $\boldsymbol{G}_\parallel$ is the projection of the wave vector onto the plane of the film.

Putting the ingredients together one ends up with the LAPW basis for film calculations in which a given basis function is defined as

$$\phi_{\boldsymbol{k}_\parallel\boldsymbol{G}}(\boldsymbol{r})=\begin{cases}\frac{1}{\sqrt{\Omega}}e^{i(\boldsymbol{k}_\parallel+\boldsymbol{G})\boldsymbol{r}} & \text{for } \boldsymbol{r}\in\mathrm{IR}\\ \sum\limits_L\left[a^{L\alpha}_{\boldsymbol{k}_\parallel\boldsymbol{G}}u^\alpha_l(r_\alpha,E^\alpha_l)+b^{L\alpha}_{\boldsymbol{k}_\parallel\boldsymbol{G}}\dot{u}^\alpha_l(r_\alpha,E^\alpha_l)\right]Y_L(\hat{\boldsymbol{r}}_{\boldsymbol{\alpha}}) & \text{for } \boldsymbol{r}\in\mathrm{MT}^\alpha\\ \left[a^{\mathrm{vac}}_{\boldsymbol{k}_\parallel\boldsymbol{G}}u^{\mathrm{vac}}_{\boldsymbol{k}_\parallel\boldsymbol{G}_\parallel}(z,E^{\mathrm{vac}})+b^{\mathrm{vac}}_{\boldsymbol{k}_\parallel\boldsymbol{G}}\dot{u}^{\mathrm{vac}}_{\boldsymbol{k}_\parallel\boldsymbol{G}_\parallel}(z,E^{\mathrm{vac}})\right]\frac{1}{\sqrt{A}}e^{i(\boldsymbol{k}_\parallel+\boldsymbol{G}_\parallel)\boldsymbol{r}_\parallel} & \text{for } \boldsymbol{r}\in\mathrm{VR}^{\mathrm{vac}}\end{cases}, \tag{3.20}$$

where A is the surface area of the film and the factor $1/\sqrt{A}$ is included for normalization purposes. In analogy to the matching at the MT sphere boundaries, the matching coefficients $a^{\mathrm{vac}}_{\boldsymbol{k}_\parallel\boldsymbol{G}}$ and $b^{\mathrm{vac}}_{\boldsymbol{k}_\parallel\boldsymbol{G}}$ are determined by enforcing continuity of the basis functions in value and slope at the vacuum boundaries. As shown in figure 3.4 the interstitial region of the unit cell has a width D. However, for the construction of the plane waves, this region is extended to cover a width of $\tilde{D}$ to avoid implicit periodic boundary conditions at the vacuum boundaries and to increase the variational freedom of the basis.

Similarly to the treatment of two-dimensional geometries, the FLAPW method is also defined and successfully used for one-dimensional structures [100] by introducing an adequate vacuum region for such cases. However, this aspect is beyond the scope of this work.

3.1.5 Other extensions and modifications of the LAPW basis

The LAPW basis is very sophisticated as it offers a high description efficiency, meaning that a very limited number of basis functions is enough to precisely represent

valence electron wave functions in a full potential and all electron model. However, over the years a couple of approaches have been proposed to measure and further strengthen these advantages. Beyond the already discussed extensions, we provide an overview over these developments which mostly address the MT part of the LAPW basis.

To enable precise descriptions of wave functions over a wider energy window, L. Smrčka [101, 102] proposed the quadratically augmented plane-wave (QAPW) method in which a third radial function $\ddot{u}_l^\alpha(r_\alpha, E_l^\alpha)$, which is the second energy derivative of $u_l^\alpha(r_\alpha, E_l^\alpha)$, is introduced in the MT regions. To incorporate this function Smrčka does not employ additional matching conditions at the MT sphere boundaries but enforces an algebraic relationship between the different radial functions.

Next, E. Krasovskii analyzed the precision of representation of the wave functions inside the MT spheres [13]. To improve the description he addressed the limited variational freedom of the basis in the MT spheres by adding pairs of LOs with $u_l^\alpha(r_\alpha, E_l^{\alpha,\mathrm{LO}})$ and $\dot{u}_l^\alpha(r_\alpha, E_l^{\alpha,\mathrm{LO}})$ as third radial functions to the basis to create the extended LAPW (ELAPW) basis [10, 11, 12]. In this approach the additional energy parameters $E_l^{\alpha,\mathrm{LO}}$ are typically chosen within the range of the unoccupied bands and hence also mainly improve the description for these states. However, in his publications on the ELAPW method Krasovskii was not explicit about the concept how to choose the energy parameters.

Precise descriptions of unoccupied bands are also required for a couple of techniques going beyond conventional DFT. In the context of EXX-OEP calculations Betzinger *et al.* [103] proposed to include local orbitals with $u_l^\alpha(r_\alpha, E_l^{\alpha,\mathrm{LO}})$ as a third radial function, where the energy parameters are chosen such that the logarithmic derivative

$$D_l^\alpha(E) = \left.\frac{u'^\alpha_l(r_\alpha, E)}{u_l^\alpha(r_\alpha, E)}\right|_{r_\alpha = R_{\mathrm{MT}^\alpha}} \tag{3.21}$$

at the MT boundary at R_{MT^α} becomes $-(l+1)$ which corresponds to evanescent solutions of the scalar-relativistic Dirac equation for a constant effective potential $V_{\mathrm{eff}}^\alpha = E = 0$. It is known [6] that radial functions chosen in this way are orthogonal to each other and to the completely confined core states.

Unoccupied bands also contribute to the GW [104] approximation of many-body perturbation theory (MBPT), which can be performed on top of LAPW and FLAPW calculation results [105, 106, 107, 108, 109]. For such calculations, C. Friedrich *et al.* [110] showed that it is also possible to precisely describe the unoccupied bands with LOs created with higher order energy derivatives of $u_l^\alpha(r_\alpha, E_l^\alpha)$ at the valence energy parameter E_l^α. Note that the energy derivatives of $u_l^\alpha(r_\alpha, E_l^\alpha)$ form a set of linearly independent functions.

To reduce the required basis set size, Sjöstedt *et al.* [14] relaxed the matching conditions at the MT sphere boundaries such that the requirement for a continuous derivative is dropped. The radial function $\ddot{u}_l^\alpha(r_\alpha, E_l^\alpha)$ is then included in terms of local orbitals that feature vanishing value but finite slope at the MT boundaries. Sjöstedt *et al.* named this alternative linearization of the APW method APW+lo, where the

lower case abbreviation 'lo' indicates that the local orbitals in this case differ from the LOs defined by Singh [9] as the derivative of Sjöstedt's local orbitals does not vanish at the MT boundaries and only two radial functions are involved in their construction. To compensate for the kinks in the basis functions at the MT sphere boundaries, Sjöstedt introduces an additional term in the Hamiltonian that accounts for the associated drawback in the kinetic energy. While the matching of value and slope at the MT sphere boundaries makes the conventional LAPW basis a little stiff, the relaxed matching conditions in APW+lo to some extent decouple the representation in the MT spheres from the interstitial representation. As a consequence one obtains converged calculation results for smaller $K_{\max}$ and even though one introduces additional lo basis functions, the overall required basis set size is often considerably reduced.

In APW+lo the additional local orbitals are typically only added for low angular momentum quantum numbers up to about $l = 3$. Madsen *et al.* [15] therefore proposed to deal with the matching for the higher l components equivalently to LAPW. With this approach one obtains the advantages of the APW+lo method while also guaranteeing continuity of value and slope of the wave functions for the higher l components. For large basis set cutoffs LAPW and APW+lo calculations in terms of Madsen's formulation converge to the same total energy.

The LAPW basis can also be modified in the interstitial region. Since the precision of the description is systematically convergable in this region, modifications to the LAPW basis in this context mainly address the required basis set size. For this, Bultmark *et al.* [16] introduce the augmented distorted plane wave basis in which the interstitial part of the basis is defined on structure-adapted coordinates. Another approach to reduce the basis set size by a more efficient description in the IR was proposed by Kotani *et al.* [111] who introduced additional LMTO basis functions such that the $K_{\max}$ cutoff can be reduced to yield an overall smaller basis set that already offers a very good description.

An alternative but also common formulation of the LAPW basis, which eliminates discontinuities due to finite $l^{\alpha}_{\max}$ cutoffs, was proposed by Soler and Williams [112]. In this formulation, the l components of the plane waves in the interstitial region beyond $l^{\alpha}_{\max}$ reach into the MT spheres. This is realized by assuming that the plane waves cover the whole unit cell. In the MT spheres the contributions to the overlap and Hamilton matrices due to the low l channels of the plane waves are then replaced by the contributions due to the radial functions $u^{\alpha}_{l}(r_{\alpha}, E^{\alpha}_{l})$ and $\dot{u}^{\alpha}_{l}(r_{\alpha}, E^{\alpha}_{l})$. This formulation of the LAPW basis has less stringent requirements with respect to the angular momentum cutoffs. In practice, $l^{\alpha}_{\max} = 3$ is often enough to obtain accurate results. However, the replacement of the MT contributions is computationally expensive.

3.2 Hamilton and Overlap matrices

Due to the region-dependent definitions of the potential and the basis functions and the locality of the Hamiltonian in real space, the construction of the Hamilton $H^{\boldsymbol{k}}_{\boldsymbol{G}\boldsymbol{G}'}$

and overlap $S^{\boldsymbol{k}}_{\boldsymbol{GG'}}$ matrices can also be subdivided into contributions from the different regions. In detail one constructs these matrices as

$$H^{\boldsymbol{k}}_{\boldsymbol{GG'}} = H^{\boldsymbol{k},\mathrm{IR}}_{\boldsymbol{GG'}} + \sum_{\alpha} H^{\boldsymbol{k},\alpha}_{\boldsymbol{GG'}} + \sum_{\mathrm{vac}} H^{\boldsymbol{k},\mathrm{vac}}_{\boldsymbol{GG'}} \tag{3.22}$$

and

$$S^{\boldsymbol{k}}_{\boldsymbol{GG'}} = S^{\boldsymbol{k},\mathrm{IR}}_{\boldsymbol{GG'}} + \sum_{\alpha} S^{\boldsymbol{k},\alpha}_{\boldsymbol{GG'}} + \sum_{\mathrm{vac}} S^{\boldsymbol{k},\mathrm{vac}}_{\boldsymbol{GG'}}, \tag{3.23}$$

where the superscript IR is associated to the interstitial contributions, the superscript α indicates contributions from the MT sphere around atom α, and the superscript vac gives the contributions from $\mathrm{VR}^{\mathrm{vac}}$. We will discuss the calculation of these matrices in each region of the unit cell in the following.

However, before we go into detail, we first discuss how to obtain a Hermitian Hamilton matrix. This is a consideration that enters the construction of this matrix in each region.

3.2.1 Hermiticity of the Hamilton matrix

To obtain real energy eigenvalues of the wave functions, the Hamilton and overlap matrices have to be Hermitian. However, one can easily show that Hamilton matrices for the LAPW basis do not obtain this property in a trivial way.

Hermitian Hamilton matrices have the property

$$\begin{aligned} H^{\boldsymbol{k}}_{\boldsymbol{GG'}} - \left(H^{\boldsymbol{k}}_{\boldsymbol{G'G}}\right)^* &= \left\langle \phi_{\boldsymbol{kG}} \middle| \hat{H} \middle| \phi_{\boldsymbol{kG'}} \right\rangle - \left(\left\langle \phi_{\boldsymbol{kG'}} \middle| \hat{H} \middle| \phi_{\boldsymbol{kG}} \right\rangle \right)^* \\ &= \int \phi^*_{\boldsymbol{kG}}(\boldsymbol{r}) \hat{H} \phi_{\boldsymbol{kG'}}(\boldsymbol{r}) - \phi_{\boldsymbol{kG'}}(\boldsymbol{r}) \hat{H} \phi^*_{\boldsymbol{kG}}(\boldsymbol{r}) d^3r \\ &= 0. \end{aligned} \tag{3.24}$$

We test if this property is fulfilled with the LAPW basis functions. Considering a setup of a bulk system the Hamilton matrix becomes a sum of contributions from the different regions. Thus, the difference between $H^{\boldsymbol{k}}_{\boldsymbol{GG'}}$ and $\left(H^{\boldsymbol{k}}_{\boldsymbol{G'G}}\right)^*$ is

$$\begin{aligned} H^{\boldsymbol{k}}_{\boldsymbol{GG'}} - \left(H^{\boldsymbol{k}}_{\boldsymbol{G'G}}\right)^* &= \left\langle \phi^{\mathrm{IR}}_{\boldsymbol{kG}} \middle| \hat{H} \middle| \phi^{\mathrm{IR}}_{\boldsymbol{kG'}} \right\rangle_{\mathrm{IR}} - \left(\left\langle \phi^{\mathrm{IR}}_{\boldsymbol{kG'}} \middle| \hat{H} \middle| \phi^{\mathrm{IR}}_{\boldsymbol{kG}} \right\rangle_{\mathrm{IR}} \right)^* \\ &\quad + \sum_{\alpha} \left\langle \phi^{\alpha}_{\boldsymbol{kG}} \middle| \hat{H} \middle| \phi^{\alpha}_{\boldsymbol{kG'}} \right\rangle_{\mathrm{MT}^{\alpha}} - \left(\left\langle \phi^{\alpha}_{\boldsymbol{kG'}} \middle| \hat{H} \middle| \phi^{\alpha}_{\boldsymbol{kG}} \right\rangle_{\mathrm{MT}^{\alpha}} \right)^* \\ &= -\frac{1}{2} \left\{ \int_{\mathrm{IR}} \left(\phi^{\mathrm{IR}}_{\boldsymbol{kG}}(\boldsymbol{r})\right)^* \nabla^2 \phi^{\mathrm{IR}}_{\boldsymbol{kG'}}(\boldsymbol{r}) - \phi^{\mathrm{IR}}_{\boldsymbol{kG'}}(\boldsymbol{r}) \nabla^2 \left(\phi^{\mathrm{IR}}_{\boldsymbol{kG}}(\boldsymbol{r})\right)^* d^3r \right. \\ &\quad \left. + \sum_{\alpha} \int_{\mathrm{MT}^{\alpha}} \left(\phi^{\alpha}_{\boldsymbol{kG}}(\boldsymbol{r})\right)^* \nabla^2 \phi^{\alpha}_{\boldsymbol{kG'}}(\boldsymbol{r}) - \phi^{\alpha}_{\boldsymbol{kG'}}(\boldsymbol{r}) \nabla^2 \left(\phi^{\alpha}_{\boldsymbol{kG}}(\boldsymbol{r})\right)^* d^3r \right\}, \end{aligned} \tag{3.25}$$

where $\phi^{\mathrm{IR}}_{\boldsymbol{kG}}$ and $\phi^{\alpha}_{\boldsymbol{kG}}$ denote the IR and MT$^{\alpha}$ representations of basis function $\phi_{\boldsymbol{kG}}$ and it has been used that the contributions due to the potential cancel each other. With Green's theorem these volume integrals can be expressed through surface integrals over the MT sphere boundaries. One obtains

$$H^{\boldsymbol{k}}_{\boldsymbol{GG'}} - \left(H^{\boldsymbol{k}}_{\boldsymbol{G'G}}\right)^* = -\frac{1}{2}\left\{\sum_{\alpha}\int\limits_{\partial \mathrm{MT}^{\alpha}} -\left[\left(\phi^{\mathrm{IR}}_{\boldsymbol{kG}}(\boldsymbol{r})\right)^* \nabla \phi^{\mathrm{IR}}_{\boldsymbol{kG'}}(\boldsymbol{r})\right]\boldsymbol{n} + \left[\phi^{\mathrm{IR}}_{\boldsymbol{kG'}}(\boldsymbol{r})\nabla\left(\phi^{\mathrm{IR}}_{\boldsymbol{kG}}(\boldsymbol{r})\right)^*\right]\boldsymbol{n}\right.$$
$$\left. + \left[\left(\phi^{\alpha}_{\boldsymbol{kG}}(\boldsymbol{r})\right)^* \nabla \phi^{\alpha}_{\boldsymbol{kG'}}(\boldsymbol{r})\right]\boldsymbol{n} - \left[\phi^{\alpha}_{\boldsymbol{kG'}}(\boldsymbol{r})\nabla\left(\phi^{\alpha}_{\boldsymbol{kG}}(\boldsymbol{r})\right)^*\right]\boldsymbol{n} dS\right\}, \tag{3.26}$$

where $\boldsymbol{n}$ is a normal vector on the respective MT boundary pointing out of the MT and dS a surface element. The derived expression vanishes if the IR and MT$^{\alpha}$ representations $\phi^{\mathrm{IR}}_{\boldsymbol{kG}}$ and $\phi^{\alpha}_{\boldsymbol{kG}}$ posses identical values and gradients on the MT sphere boundaries.

However, this is not the case for LAPW basis functions since the angular momentum cutoff implies deviations for higher l quantum numbers. Furthermore, the determination of the basis functions in the MT spheres with the SRA to the radial Dirac equation implies a two-component basis function in this region, while the IR part of the basis function consists of a single component. The matching at the MT sphere boundaries only considers the large component of the MT function, which implies further deviations between the two representations.

In conclusion, constructing the Hamilton matrix in a naive way yields a matrix that is not Hermitian. To overcome this problem one considers in each region the application of the kinetic energy operator to the left as well as to the right basis function and averages over the two resulting matrix contributions. One can show that in this way not only the Hamilton matrix over the whole unit cell, but also the Hamilton matrices for each region become Hermitian.

3.2.2 The setup for the interstitial region

In the interstitial region the FLAPW method is based on a nonrelativistic description of the electrons. This is justified as the kinetic energy is small in comparison to the regions around the atomic nuclei where the singularities of the potential and the angular momentum barrier lead to high kinetic energy contributions.

The contributions to the Hamilton and overlap matrices in the IR are given by the matrix elements

$$H^{\boldsymbol{k},\mathrm{IR}}_{\boldsymbol{GG'}} = \left\langle \phi_{\boldsymbol{kG}} \middle| \hat{H} \middle| \phi_{\boldsymbol{kG'}} \right\rangle_{\mathrm{IR}}$$
$$= \frac{1}{\Omega}\int\limits_{\mathrm{IR}} e^{-i(\boldsymbol{k}+\boldsymbol{G})\boldsymbol{r}}\left(-\frac{1}{2}\boldsymbol{\nabla}^2 + V(\boldsymbol{r})\right)e^{i(\boldsymbol{k}+\boldsymbol{G'})\boldsymbol{r}} d^3r \tag{3.27}$$

for the Hamiltonian and

$$S^{\boldsymbol{k},\mathrm{IR}}_{\boldsymbol{G}\boldsymbol{G}'} = \langle \phi_{\boldsymbol{k}\boldsymbol{G}} | \phi_{\boldsymbol{k}\boldsymbol{G}'} \rangle_{\mathrm{IR}} = \frac{1}{\Omega} \int_{\mathrm{IR}} e^{-i(\boldsymbol{k}+\boldsymbol{G})\boldsymbol{r}} e^{i(\boldsymbol{k}+\boldsymbol{G}')\boldsymbol{r}} d^3r \tag{3.28}$$

for the overlap.

Unfortunately it is cumbersome to calculate integrals over the IR directly. To evaluate the integrals in an elegant way one first applies the kinetic energy operator and then introduces a step function

$$\Theta(\boldsymbol{r}) = \begin{cases} 1 & \text{for } \boldsymbol{r} \in \mathrm{IR} \\ 0 & \text{for } \boldsymbol{r} \in \mathrm{MT}^{\alpha} \end{cases} \tag{3.29}$$

to cut out the MT spheres from the unit cell and transform the integrals over the IR into integrals over the whole unit cell. With this step function and a replacement of the LAPW basis functions $\phi_{\boldsymbol{k}\boldsymbol{G}}$ with their interstitial representation extended over the whole unit cell $\tilde{\phi}_{\boldsymbol{k}\boldsymbol{G}}$ equations (3.27) and (3.28) become

$$\begin{aligned} H^{\boldsymbol{k},\mathrm{IR}}_{\boldsymbol{G}\boldsymbol{G}'} &= \left\langle \tilde{\phi}_{\boldsymbol{k}\boldsymbol{G}} \middle| V(\boldsymbol{r})\Theta(\boldsymbol{r}) - \frac{1}{2}\Theta(\boldsymbol{r})\nabla^2 \middle| \tilde{\phi}_{\boldsymbol{k}\boldsymbol{G}'} \right\rangle_{\Omega} \\ &= \frac{1}{\Omega} \int_{\Omega} e^{-i(\boldsymbol{G}-\boldsymbol{G}')\boldsymbol{r}} V(\boldsymbol{r})\Theta(\boldsymbol{r}) d^3r + \frac{(\boldsymbol{k}+\boldsymbol{G}')^2}{2\Omega} \int_{\Omega} e^{-i(\boldsymbol{G}-\boldsymbol{G}')\boldsymbol{r}} \Theta(\boldsymbol{r}) d^3r \end{aligned} \tag{3.30}$$

and

$$\begin{aligned} S^{\boldsymbol{k},\mathrm{IR}}_{\boldsymbol{G}\boldsymbol{G}'} &= \left\langle \tilde{\phi}_{\boldsymbol{k}\boldsymbol{G}} \middle| \Theta(\boldsymbol{r}) \middle| \tilde{\phi}_{\boldsymbol{k}\boldsymbol{G}'} \right\rangle_{\Omega} \\ &= \frac{1}{\Omega} \int_{\Omega} e^{-i(\boldsymbol{G}-\boldsymbol{G}')\boldsymbol{r}} \Theta(\boldsymbol{r}) d^3r. \end{aligned} \tag{3.31}$$

In real space it is still problematic to solve these integrals. However, the reciprocal cutoff for the wave vectors $\boldsymbol{G}$ and $\boldsymbol{G}'$ makes a computation of the integrals in reciprocal space reasonable. For this, the step function is analytically expressed in terms of the Fourier expansion

$$\Theta(\boldsymbol{G}) = \delta_{\boldsymbol{G},\boldsymbol{0}} - \sum_{\alpha} e^{-i\boldsymbol{G}\boldsymbol{\tau}_{\alpha}} \frac{4\pi (R_{\mathrm{MT}^{\alpha}})^3}{\Omega} \frac{j_1(GR_{\mathrm{MT}^{\alpha}})}{GR_{\mathrm{MT}^{\alpha}}}, \tag{3.32}$$

where j_1 is the spherical Bessel function for $l = 1$.

To calculate the contributions to the Hamilton matrix, also the Fourier coefficients of the product of the potential $V(\boldsymbol{r})$ and the step function $\Theta(\boldsymbol{r})$ have to be obtained. For this, the analytically determined reciprocal representation of the step function is numerically transformed onto the real space grid again, employing a Fast Fourier

Transform (FFT). Here, it is pointwise multiplied with $V(\boldsymbol{r})$. The product $(V\Theta)(\boldsymbol{r})$ is then backtransformed to reciprocal space to obtain its Fourier expansion $(V\Theta)(\boldsymbol{G})$.

In the next step of the calculation of the matrix elements it is now exploited that different plane waves are orthogonal to each other. Thus, all but a single Fourier coefficient of $\Theta(\boldsymbol{G})$ and $(V\Theta)(\boldsymbol{G})$ lead to vanishing contributions to the matrices. In the end one obtains

$$H^{\boldsymbol{k},\mathrm{IR}}_{\boldsymbol{G}\boldsymbol{G}'} = (V\Theta)(\boldsymbol{G}-\boldsymbol{G}') + \frac{(\boldsymbol{k}+\boldsymbol{G}')^2}{2}\Theta(\boldsymbol{G}-\boldsymbol{G}') \tag{3.33}$$

and

$$S^{\boldsymbol{k},\mathrm{IR}}_{\boldsymbol{G}\boldsymbol{G}'} = \Theta(\boldsymbol{G}-\boldsymbol{G}'). \tag{3.34}$$

Note that due to the reciprocal cutoff $K_{\max}$ for the basis functions and the single required Fourier coefficient $\boldsymbol{G}-\boldsymbol{G}'$ of $\Theta(\boldsymbol{G})$ and $(V\Theta)(\boldsymbol{G})$, the Fourier expansions of these functions are also only needed up to a limited cutoff that is twice as large as the maximal wave vector found in the basis. The calculation of $(V\Theta)(\boldsymbol{G})$ however may require a higher cutoff, depending on the convergence behavior of the reciprocal representation of the potential $V(\boldsymbol{G})$.

Finally, the hermiticity of the Hamilton matrix is established by averaging over the application of the kinetic energy operator to the left and to the right basis function. With this the IR contributions become

$$H^{\boldsymbol{k},\mathrm{IR}}_{\boldsymbol{G}\boldsymbol{G}'} = (V\Theta)(\boldsymbol{G}-\boldsymbol{G}') + \frac{(\boldsymbol{k}+\boldsymbol{G})^2 + (\boldsymbol{k}+\boldsymbol{G}')^2}{4}\Theta(\boldsymbol{G}-\boldsymbol{G}'). \tag{3.35}$$

3.2.3 The setup for the muffin-tin spheres

Within the MT spheres the contributions to the matrices are subdivided into spherical contributions and contributions to the Hamilton matrix due to the nonspherical part of the potential. In detail for the MT sphere around an atom α one calculates

$$\begin{aligned}
H^{\boldsymbol{k},\alpha}_{\boldsymbol{G}\boldsymbol{G}'} &= H^{\boldsymbol{k},\alpha,\mathrm{sphr}}_{\boldsymbol{G}\boldsymbol{G}'} + H^{\boldsymbol{k},\alpha,\mathrm{nsphr}}_{\boldsymbol{G}\boldsymbol{G}'} \\
&= \left\langle \phi_{\boldsymbol{k}\boldsymbol{G}} \middle| \hat{H}^{\alpha,\mathrm{sphr}} \middle| \phi_{\boldsymbol{k}\boldsymbol{G}'} \right\rangle_{\mathrm{MT}^\alpha} + \left\langle \phi_{\boldsymbol{k}\boldsymbol{G}} \middle| \hat{H}^{\alpha,\mathrm{nsphr}} \middle| \phi_{\boldsymbol{k}\boldsymbol{G}'} \right\rangle_{\mathrm{MT}^\alpha} \\
&= \underbrace{\int\limits_{\mathrm{MT}^\alpha} \phi^*_{\boldsymbol{k}\boldsymbol{G}}(\boldsymbol{r}) \left[\hat{T} + V^\alpha_{l=0}(r_\alpha) Y_{0,0}(\hat{\boldsymbol{r}}_\alpha)\right] \phi_{\boldsymbol{k}\boldsymbol{G}'}(\boldsymbol{r}) d^3r}_{\text{spherical part}} \\
&\quad + \underbrace{\int\limits_{\mathrm{MT}^\alpha} \phi^*_{\boldsymbol{k}\boldsymbol{G}}(\boldsymbol{r}) \left[\sum_{l''=1}^{l^\alpha_{\max}} \sum_{m''=-l''}^{l''} V^\alpha_{L''}(r_\alpha) Y_{L''}(\hat{\boldsymbol{r}}_\alpha)\right] \phi_{\boldsymbol{k}\boldsymbol{G}'}(\boldsymbol{r}) d^3r}_{\text{nonspherical contributions}}
\end{aligned} \tag{3.36}$$

for the Hamilton matrix and

$$S^{\boldsymbol{k},\alpha}_{\boldsymbol{G}\boldsymbol{G}'} = \langle \phi_{\boldsymbol{k}\boldsymbol{G}} | \phi_{\boldsymbol{k}\boldsymbol{G}'} \rangle_{\mathrm{MT}^\alpha} = \int_{\mathrm{MT}^\alpha} \phi^*_{\boldsymbol{k}\boldsymbol{G}}(\boldsymbol{r}) \phi_{\boldsymbol{k}\boldsymbol{G}'}(\boldsymbol{r}) d^3r \tag{3.37}$$

for the overlap matrix. We discuss the computation of these integrals in detail in the following sections.

3.2.3.1 Determination of the matching coefficients

In the MT spheres the LAPW basis consists of the radial functions $u^\alpha_l(r_\alpha, E^\alpha_l)$ and $\dot{u}^\alpha_l(r_\alpha, E^\alpha_l)$ and the matching coefficients $a^{L\alpha}_{\boldsymbol{k}\boldsymbol{G}}$ and $b^{L\alpha}_{\boldsymbol{k}\boldsymbol{G}}$. To obtain the matching coefficients for the MT sphere around atom α one performs the Rayleigh expansion

$$\frac{1}{\sqrt{\Omega}} e^{i\boldsymbol{K}\boldsymbol{r}} = \frac{4\pi}{\sqrt{\Omega}} e^{i\boldsymbol{K}\boldsymbol{\tau}_\alpha} \sum_L i^l Y^*_L(\hat{\boldsymbol{K}}) j_l(Kr_\alpha) Y_L(\hat{\boldsymbol{r}}_\alpha) \Big|_{r_\alpha = R_{\mathrm{MT}^\alpha}} \tag{3.38}$$

of the plane wave with $\boldsymbol{K} = \boldsymbol{k} + \boldsymbol{G}$ in the IR into spherical harmonics $Y_L(\hat{\boldsymbol{r}}_\alpha)$ and spherical Bessel functions $j_l(Kr_\alpha)$ at the MT sphere boundaries[2].

The matching conditions now state that the basis functions and their slopes are continuous at the MT boundaries. One obtains these conditions for each (l,m) channel separately by calculating the $a^{L\alpha}_{\boldsymbol{k}\boldsymbol{G}}$ and $b^{L\alpha}_{\boldsymbol{k}\boldsymbol{G}}$ with the equations

$$a^{L\alpha}_{\boldsymbol{k}\boldsymbol{G}} u^\alpha_l(r_\alpha, E^\alpha_l) + b^{L\alpha}_{\boldsymbol{k}\boldsymbol{G}} \dot{u}^\alpha_l(r_\alpha, E^\alpha_l)\big|_{r_\alpha = R_{\mathrm{MT}^\alpha}} = \frac{4\pi}{\sqrt{\Omega}} e^{i\boldsymbol{K}\boldsymbol{\tau}_\alpha} i^l Y^*_L(\hat{\boldsymbol{K}}) j_l(Kr_\alpha) Y_L(\hat{\boldsymbol{r}}_\alpha) \Big|_{r_\alpha = R_{\mathrm{MT}^\alpha}} \tag{3.39}$$

and

$$a^{L\alpha}_{\boldsymbol{k}\boldsymbol{G}} u'^\alpha_l(r_\alpha, E^\alpha_l) + b^{L\alpha}_{\boldsymbol{k}\boldsymbol{G}} \dot{u}'^\alpha_l(r_\alpha, E^\alpha_l)\big|_{r_\alpha = R_{\mathrm{MT}^\alpha}} = \frac{4\pi}{\sqrt{\Omega}} e^{i\boldsymbol{K}\boldsymbol{\tau}_\alpha} i^l Y^*_L(\hat{\boldsymbol{K}}) j'_l(Kr_\alpha) Y_L(\hat{\boldsymbol{r}}_\alpha) \Big|_{r_\alpha = R_{\mathrm{MT}^\alpha}} \tag{3.40}$$

in which $'$ denotes the derivative with respect to r_α. Solving this system of linear equations analytically then leads to

$$\begin{aligned} a^{L\alpha}_{\boldsymbol{k}\boldsymbol{G}} &= \frac{4\pi}{\sqrt{\Omega}} e^{i\boldsymbol{K}\boldsymbol{\tau}_\alpha} \frac{1}{W} Y^*_L(\hat{\boldsymbol{K}}) \left[\dot{u}^\alpha_l(R_{\mathrm{MT}^\alpha}, E^\alpha_l) j'_l(KR_{\mathrm{MT}^\alpha}) - \dot{u}'^\alpha_l(R_{\mathrm{MT}^\alpha}, E^\alpha_l) j_l(KR_{\mathrm{MT}^\alpha}) \right] \\ &= c^{L\alpha}_{\boldsymbol{k}\boldsymbol{G}} a^{l\alpha}_{\boldsymbol{k}\boldsymbol{G}} \end{aligned} \tag{3.41}$$

[2] Note that in order to reduce computational demands FLAPW codes typically exploit symmetry relations to group symmetry equivalent atoms. In this case the local coordinate system in a MT sphere also has to comply with the associated symmetry operation $\bar{S}^\alpha$, which maps an atom of the equivalence class to the representative of the class. As a consequence the argument of the spherical harmonic $Y^*_L(\hat{\boldsymbol{K}})$ in the Rayleigh expansion has to be modified and one obtains $Y^*_L(\widehat{\bar{S}^\alpha \boldsymbol{K}})$.

and

$$b_{\boldsymbol{kG}}^{L\alpha} = \frac{4\pi}{\sqrt{\Omega}} e^{i\boldsymbol{K}\boldsymbol{\tau}_\alpha} \frac{1}{W} Y_L^*(\hat{\boldsymbol{K}}) \left[u_l'^{\alpha}(R_{\mathrm{MT}^\alpha}, E_l^\alpha) j_l(KR_{\mathrm{MT}^\alpha}) - u_l^\alpha(R_{\mathrm{MT}^\alpha}, E_l^\alpha) j_l'(KR_{\mathrm{MT}^\alpha}) \right]$$
$$= c_{\boldsymbol{kG}}^{L\alpha} b_{\boldsymbol{kG}}^{l\alpha} \tag{3.42}$$

where the Wronskian W is given by

$$W = \dot{u}_l^\alpha(R_{\mathrm{MT}^\alpha}, E_l^\alpha) u_l'^{\alpha}(R_{\mathrm{MT}^\alpha}, E_l^\alpha) - u_l^\alpha(R_{\mathrm{MT}^\alpha}, E_l^\alpha) \dot{u}_l'^{\alpha}(R_{\mathrm{MT}^\alpha}, E_l^\alpha) \tag{3.43}$$
$$= \frac{2}{R_{\mathrm{MT}^\alpha}^2}. \tag{3.44}$$

Note that the matching coefficients (3.41) and (3.42) are given as a product of an l and m dependent quantity

$$c_{\boldsymbol{kG}}^{L\alpha} = \frac{4\pi}{\sqrt{\Omega}} e^{i\boldsymbol{K}\boldsymbol{\tau}_\alpha} \frac{1}{W} Y_L^*(\hat{\boldsymbol{K}}) = \frac{2\pi R_{\mathrm{MT}^\alpha}^2}{\sqrt{\Omega}} e^{i\boldsymbol{K}\boldsymbol{\tau}_\alpha} Y_L^*(\hat{\boldsymbol{K}}) \tag{3.45}$$

identical for both, the $a_{\boldsymbol{kG}}^{L\alpha}$ and the $b_{\boldsymbol{kG}}^{L\alpha}$ coefficient, and solely l dependent parts $a_{\boldsymbol{kG}}^{l\alpha}$ and $b_{\boldsymbol{kG}}^{l\alpha}$.

3.2.3.2 Spherical contributions to the Hamilton and Overlap matrices

In the MT spheres the LAPW basis functions are a linear combination of the functions $u_l^\alpha(r_\alpha, E_l^\alpha)$ and $\dot{u}_l^\alpha(r_\alpha, E_l^\alpha)$, and partially additional radial functions in local orbitals. These functions are explicitly constructed to fulfill certain relations with the spherical part of the Hamiltonian $\hat{H}^{\alpha,\mathrm{sphr}}$. First of all, the radial function $u_l^\alpha(r_\alpha, E_l^\alpha)$ is the normalized solution to this part of the Hamiltonian with regular behavior at the nucleus. Thus, it fulfills

$$\hat{H}^{\alpha,\mathrm{sphr}} |u_l^\alpha\rangle = E_l |u_l^\alpha\rangle \tag{3.46}$$

together with the normalization $\langle u_l^\alpha | u_l^\alpha \rangle_{\mathrm{MT}^\alpha} = 1$. The radial function $\dot{u}_l^\alpha(r_\alpha, E_l^\alpha)$, on the other hand, is the energy derivative of $u_l^\alpha(r_\alpha, E_l^\alpha)$ and therefore fulfills

$$\hat{H}^{\alpha,\mathrm{sphr}} |\dot{u}_l^\alpha\rangle + \dot{\hat{H}}^{\alpha,\mathrm{sphr}} |u_l^\alpha\rangle = E_l |\dot{u}_l^\alpha\rangle + |u_l^\alpha\rangle. \tag{3.47}$$

Furthermore, one adds multiples of $u_l^\alpha(r_\alpha, E_l^\alpha)$ to $\dot{u}_l^\alpha(r_\alpha, E_l^\alpha)$ to ensure that the orthogonality $\langle u_l^\alpha | \dot{u}_l^\alpha \rangle_{\mathrm{MT}^\alpha} = 0$ holds. The term $\dot{\hat{H}}^{\alpha,\mathrm{sphr}} |u_l^\alpha\rangle$ only appears in the SRA to the radial Dirac equation and vanishes in a nonrelativistic consideration. It is typically neglected since it is small in comparison to the other terms in equation (3.47). With this, one approximates

$$\hat{H}^{\alpha,\mathrm{sphr}} |\dot{u}_l^\alpha\rangle \approx E_l |\dot{u}_l^\alpha\rangle + |u_l^\alpha\rangle. \tag{3.48}$$

With these simple expressions the spherical contributions to the matrices can be calculated in an elegant and efficient way, which starts by expressing the matrix elements in terms of the matching coefficients $a_{\boldsymbol{kG}}^{L\alpha}$ and $b_{\boldsymbol{kG}}^{L\alpha}$. For the contributions to the Hamilton matrix this leads to

$$H_{\boldsymbol{GG'}}^{\boldsymbol{k},\alpha,\mathrm{sphr}} = \sum_{l=0}^{l_{\max}^{\alpha}} \sum_{m=-l}^{l} E_l \left[\left(a_{\boldsymbol{kG}}^{L\alpha} \right)^* a_{\boldsymbol{kG'}}^{L\alpha} + \langle \dot{u}_l^{\alpha} | u_l^{\alpha} \rangle_{\mathrm{MT}^{\alpha}} \left(b_{\boldsymbol{kG}}^{L\alpha} \right)^* b_{\boldsymbol{kG'}}^{L\alpha} \right] + \left(a_{\boldsymbol{kG}}^{L\alpha} \right)^* b_{\boldsymbol{kG''}}^{L\alpha}. \tag{3.49}$$

By plugging in the expressions for the matching coefficients (3.41) and (3.42) one obtains for the first term

$$\sum_{l=0}^{l_{\max}^{\alpha}} \sum_{m=-l}^{l} E_l \left(a_{\boldsymbol{kG}}^{L\alpha} \right)^* a_{\boldsymbol{kG'}}^{L\alpha} = \sum_{l=0}^{l_{\max}^{\alpha}} E_l \left(a_{\boldsymbol{kG}}^{l\alpha} \right)^* a_{\boldsymbol{kG'}}^{l\alpha} \sum_{m=-l}^{l} \left(c_{\boldsymbol{kG}}^{L\alpha} \right)^* c_{\boldsymbol{kG'}}^{L\alpha}, \tag{3.50}$$

where the summation over the m quantum number can be performed analytically by applying the addition theorem for spherical harmonics

$$\sum_{m=-l}^{l} \frac{4\pi}{2l+1} Y_L^*(\hat{\boldsymbol{K}}) Y_L(\hat{\boldsymbol{K}}') = P_l \left(\frac{\boldsymbol{KK'}}{|\boldsymbol{KK'}|} \right) \tag{3.51}$$

to obtain

$$\begin{aligned} \sum_{m=-l}^{l} \left(c_{\boldsymbol{kG}}^{L\alpha} \right)^* c_{\boldsymbol{kG'}}^{L\alpha} &= \frac{4\pi^2 R_{\mathrm{MT}^{\alpha}}^4}{\Omega} e^{i(\boldsymbol{K'}-\boldsymbol{K})\boldsymbol{\tau}_{\alpha}} \sum_{m=-l}^{l} Y_L^*(\hat{\boldsymbol{K}}) Y_L(\hat{\boldsymbol{K}}') \\ &= \frac{(2l+1)\pi R_{\mathrm{MT}^{\alpha}}^4}{\Omega} e^{i(\boldsymbol{K'}-\boldsymbol{K})\boldsymbol{\tau}_{\alpha}} P_l \left(\frac{\boldsymbol{KK'}}{|\boldsymbol{KK'}|} \right). \end{aligned} \tag{3.52}$$

By combining equations (3.50) and (3.52) one obtains

$$\sum_{l=0}^{l_{\max}^{\alpha}} \sum_{m=-l}^{l} E_l \left(a_{\boldsymbol{kG}}^{L\alpha} \right)^* a_{\boldsymbol{kG'}}^{L\alpha} = \sum_{l=0}^{l_{\max}^{\alpha}} E_l \left(a_{\boldsymbol{kG}}^{l\alpha} \right)^* a_{\boldsymbol{kG'}}^{l\alpha} \frac{(2l+1)\pi R_{\mathrm{MT}^{\alpha}}^4}{\Omega} e^{i(\boldsymbol{K'}-\boldsymbol{K})\boldsymbol{\tau}_{\alpha}} P_l \left(\frac{\boldsymbol{KK'}}{|\boldsymbol{KK'}|} \right). \tag{3.53}$$

Similarly, the summation over the magnetic quantum number can also be performed analytically for the second and third term of the spherical contributions to the Hamiltonian (3.49). By doing this one ends up with

$$\begin{aligned} H_{\boldsymbol{GG'}}^{\boldsymbol{k},\alpha,\mathrm{sphr}} = & \sum_{l=0}^{l_{\max}^{\alpha}} \frac{(2l+1)\pi R_{\mathrm{MT}^{\alpha}}^4}{\Omega} e^{i(\boldsymbol{K'}-\boldsymbol{K})\boldsymbol{\tau}_{\alpha}} P_l \left(\frac{\boldsymbol{KK'}}{|\boldsymbol{KK'}|} \right) \\ & \times \left\{ E_l \left[\left(a_{\boldsymbol{kG}}^{l\alpha} \right)^* a_{\boldsymbol{kG'}}^{l\alpha} + \langle \dot{u}_l^{\alpha} | u_l^{\alpha} \rangle_{\mathrm{MT}^{\alpha}} \left(b_{\boldsymbol{kG}}^{l\alpha} \right)^* b_{\boldsymbol{kG'}}^{l\alpha} \right] + \left(a_{\boldsymbol{kG}}^{l\alpha} \right)^* b_{\boldsymbol{kG'}}^{l\alpha} \right\}. \end{aligned} \tag{3.54}$$

Finally, one also has to ensure the hermiticity of the matrix by averaging over the results of applying the Hamiltonian to the right and to the left basis functions. By

doing this one obtains the final expression

$$H_{\boldsymbol{GG'}}^{\boldsymbol{k},\alpha,\mathrm{sphr}} = \sum_{l=0}^{l_{\max}^{\alpha}} \frac{(2l+1)\pi R_{\mathrm{MT}^{\alpha}}^{4}}{\Omega} e^{i(\boldsymbol{K'}-\boldsymbol{K})\boldsymbol{\tau}_{\alpha}} P_l\left(\frac{\boldsymbol{KK'}}{|\boldsymbol{KK'}|}\right) \times \left\{E_l\left[\left(a_{\boldsymbol{kG}}^{l\alpha}\right)^{*} a_{\boldsymbol{kG'}}^{l\alpha} + \langle \dot{u}_l^{\alpha}|\dot{u}_l^{\alpha}\rangle_{\mathrm{MT}^{\alpha}} \left(b_{\boldsymbol{kG}}^{l\alpha}\right)^{*} b_{\boldsymbol{kG'}}^{l\alpha}\right] + \frac{1}{2}\left(\left(a_{\boldsymbol{kG}}^{l\alpha}\right)^{*} b_{\boldsymbol{kG'}}^{l\alpha} + \left(b_{\boldsymbol{kG}}^{l\alpha}\right)^{*} a_{\boldsymbol{kG'}}^{l\alpha}\right)\right\}. \tag{3.55}$$

Note that calculating the spherical contributions to the Hamilton matrix in terms of a Hermitian version of equation (3.49) gives a scaling of $\mathcal{O}\left((l_{\max}+1)^2 N_{\mathrm{atom}} N_{\mathrm{LAPW}}^2\right)$, where N_{atom} is the number of atoms, N_{LAPW} is the number of LAPW basis functions, and $l_{\max}$ is a representative for the actually atom dependent $l_{\max}^{\alpha}$ cutoffs, e.g., $l_{\max} = \sup\{l_{\max}^{\alpha}\}$. If the summation over m is performed analytically as it is done in equation (3.55) this scaling is reduced to $\mathcal{O}\left((l_{\max}+1) N_{\mathrm{atom}} N_{\mathrm{LAPW}}^2\right)$, which effectively yields a material dependent speedup of a factor of about 10.

In analogy to equation (3.49) one can also write down the MT contributions to the overlap matrix as

$$S_{\boldsymbol{GG'}}^{\boldsymbol{k},\alpha} = \sum_{l=0}^{l_{\max}^{\alpha}} \sum_{m=-l}^{l} \left(a_{\boldsymbol{kG}}^{L\alpha}\right)^{*} a_{\boldsymbol{kG'}}^{L\alpha} + \langle \dot{u}_l^{\alpha}|\dot{u}_l^{\alpha}\rangle \left(b_{\boldsymbol{kG}}^{L\alpha}\right)^{*} b_{\boldsymbol{kG'}}^{L\alpha}. \tag{3.56}$$

By performing the same steps as for the Hamilton matrix one ends up with

$$S_{\boldsymbol{GG'}}^{\boldsymbol{k},\alpha} = \sum_{l=0}^{l_{\max}^{\alpha}} \frac{(2l+1)\pi R_{\mathrm{MT}^{\alpha}}^{4}}{\Omega} e^{i(\boldsymbol{K'}-\boldsymbol{K})\boldsymbol{\tau}_{\alpha}} P_l\left(\frac{\boldsymbol{KK'}}{|\boldsymbol{KK'}|}\right) \times \left\{\left(a_{\boldsymbol{kG}}^{l\alpha}\right)^{*} a_{\boldsymbol{kG'}}^{l\alpha} + \langle \dot{u}_l^{\alpha}|\dot{u}_l^{\alpha}\rangle_{\mathrm{MT}^{\alpha}} \left(b_{\boldsymbol{kG}}^{l\alpha}\right)^{*} b_{\boldsymbol{kG'}}^{l\alpha}\right\}. \tag{3.57}$$

Note that this expression is indeed very similar to the corresponding contributions to the Hamilton matrix (3.54). In practice these similarities between the equations for the Hamilton matrix and the corresponding expressions for the overlap matrix lead to a computation of the Hamilton matrix that provides the overlap matrix as a byproduct. We mention in passing that this statement not only applies to the MT spheres but also to the other regions within the unit cell (IR, $\mathrm{VR}^{\mathrm{vac}}$).

3.2.3.3 Contributions due to the nonspherical potential

The contributions to the Hamilton matrix due to the nonspherical potential within the MT sphere around atom α,

$$H_{\boldsymbol{GG'}}^{\boldsymbol{k},\alpha,\mathrm{nsphr}} = \int_{\mathrm{MT}^{\alpha}} \phi_{\boldsymbol{kG}}^{*}(\boldsymbol{r}) \left[\sum_{l''=1}^{l_{\max}^{\alpha}} \sum_{m''=-l''}^{l''} V_{L''}^{\alpha}(r_{\alpha}) Y_{L''}(\hat{\boldsymbol{r}}_{\alpha})\right] \phi_{\boldsymbol{kG'}}(\boldsymbol{r}) d^3 r, \tag{3.58}$$

are also expressed in terms of the MT part of the LAPW basis as

$$\begin{aligned} H_{\boldsymbol{GG'}}^{\boldsymbol{k},\alpha,\mathrm{nsphr}} = \int\limits_{\mathrm{MT}^\alpha} \sum_L \sum_{L''} \sum_{L'} \Big[a_{\boldsymbol{kG}}^{L\alpha} u_l^\alpha(r_\alpha, E_l^\alpha) + b_{\boldsymbol{kG}}^{L\alpha} \dot{u}_l^\alpha(r_\alpha, E_l^\alpha) \Big]^* \\ \times V_{L''}^\alpha(r_\alpha) \Big[a_{\boldsymbol{kG}}^{L'\alpha} u_{l'}^\alpha(r_\alpha, E_{l'}^\alpha) + b_{\boldsymbol{kG}}^{L'\alpha} \dot{u}_{l'}^\alpha(r_\alpha, E_{l'}^\alpha) \Big] \\ \times Y_L^*(\hat{\boldsymbol{r}}_{\boldsymbol{\alpha}}) Y_{L''}(\hat{\boldsymbol{r}}_{\boldsymbol{\alpha}}) Y_{L'}(\hat{\boldsymbol{r}}_{\boldsymbol{\alpha}}) d^3 r. \end{aligned} \tag{3.59}$$

To calculate this expression one first makes use of the fact that the integral over the product of three spherical harmonics gives a gaunt coefficient

$$G_{ll''l'}^{mm''m'} = \int_0^{2\pi} \int_0^{\pi} Y_L^*(\theta,\phi) Y_{L''}(\theta,\phi) Y_{L'}(\theta,\phi) \sin(\theta) d\theta d\varphi. \tag{3.60}$$

With this, one precalculates the four integrals

$$\begin{aligned} t_{LL'}^{\alpha[\circ][\diamond]} &= \int\limits_{\mathrm{MT}^\alpha} \sum_{L''} {}^{[\circ]}u_l^\alpha(r_\alpha, E_l^\alpha) V_{L''}^\alpha(r_\alpha) {}^{[\diamond]}u_{l'}^\alpha(r_\alpha, E_{l'}^\alpha) Y_L^*(\hat{\boldsymbol{r}}_{\boldsymbol{\alpha}}) Y_{L''}(\hat{\boldsymbol{r}}_{\boldsymbol{\alpha}}) Y_{L'}(\hat{\boldsymbol{r}}_{\boldsymbol{\alpha}}) d^3 r \\ &= \int_0^{R_{\mathrm{MT}^\alpha}} r_\alpha^2 {}^{[\circ]}u_l^\alpha(r_\alpha, E_l^\alpha) V_{L''}^\alpha(r_\alpha) {}^{[\diamond]}u_{l'}^\alpha(r_\alpha, E_{l'}^\alpha) \sum_{L''} G_{ll''l'}^{mm''m'} dr_\alpha, \end{aligned} \tag{3.61}$$

where $[\circ]$ and $[\diamond]$ either denote u or $\dot{u}$, respectively. Note that the $t_{LL'}^{\alpha[\circ][\diamond]}$ integrals are independent of the LAPW basis functions as they do not depend on the matching coefficients $a_{\boldsymbol{kG}}^{L\alpha}$ and $b_{\boldsymbol{kG}}^{L\alpha}$, which make the difference in the MT part of different LAPW basis functions. As a consequence the basis function independent precalculation of these expensive integrals saves a lot of time.

The final expression for the calculation of the nonspherical contributions is derived by combining equations (3.59) and (3.61) to obtain

$$\begin{aligned} H_{\boldsymbol{GG'}}^{\boldsymbol{k},\alpha,\mathrm{nsphr}} &= \sum_L \sum_{L'} \Big(a_{\boldsymbol{kG}}^{L\alpha} \Big)^* t_{LL'}^{\alpha[\,][\,]} a_{\boldsymbol{kG'}}^{L'\alpha} + \Big(a_{\boldsymbol{kG}}^{L\alpha} \Big)^* t_{LL'}^{\alpha[\,][\cdot]} b_{\boldsymbol{kG'}}^{L'\alpha} \\ &\quad + \Big(b_{\boldsymbol{kG}}^{L\alpha} \Big)^* t_{LL'}^{\alpha[\cdot][\,]} a_{\boldsymbol{kG'}}^{L'\alpha} + \Big(b_{\boldsymbol{kG}}^{L\alpha} \Big)^* t_{LL'}^{\alpha[\cdot][\cdot]} b_{\boldsymbol{kG'}}^{L'\alpha} \end{aligned} \tag{3.62}$$

$$\begin{aligned} &= \sum_L \Big(a_{\boldsymbol{kG}}^{L\alpha} \Big)^* \left(\sum_{L'} t_{LL'}^{\alpha[\,][\,]} a_{\boldsymbol{kG'}}^{L'\alpha} \right) + \Big(a_{\boldsymbol{kG}}^{L\alpha} \Big)^* \left(\sum_{L'} t_{LL'}^{\alpha[\,][\cdot]} b_{\boldsymbol{kG'}}^{L'\alpha} \right) \\ &\quad + \Big(b_{\boldsymbol{kG}}^{L\alpha} \Big)^* \left(\sum_{L'} t_{LL'}^{\alpha[\cdot][\,]} a_{\boldsymbol{kG'}}^{L'\alpha} \right) + \Big(b_{\boldsymbol{kG}}^{L\alpha} \Big)^* \left(\sum_{L'} t_{LL'}^{\alpha[\cdot][\cdot]} b_{\boldsymbol{kG'}}^{L'\alpha} \right), \end{aligned} \tag{3.63}$$

where the last expression also shows that the sums over L' are independent of the basis functions on the left side, which allows to calculate them independently of the left hand basis functions to save some more time.

To further speed up the calculation of these contributions to the Hamilton matrix one typically reduces the $l^{\alpha}_{\max}$ cutoffs applied to the sums over L and L'. This $l^{\alpha,\mathrm{nsphr}}_{\max}$ is typically on the order of $l^{\alpha}_{\max} - 2$ or $l^{\alpha}_{\max} - 4$. In conclusion, this part of the matrix setup features a scaling behavior of $\mathcal{O}\left((l^{\mathrm{nsphr}}_{\max}+1)^2 N_{\mathrm{atom}} N^2_{\mathrm{LAPW}}\right)$, where $l^{\mathrm{nsphr}}_{\max}$ is a representative for the atom dependent $l^{\alpha,\mathrm{nsphr}}_{\max}$. For typical LAPW calculations this is a major part of a DFT iteration. Dependent on the investigated material it takes about 40% of the overall iteration runtime. This is about the same fraction of time which is required for solving the generalized eigenvalue problem.

3.2.4 The setup for the vacuum regions

Similar to the MT spheres, the LAPW basis in the vacuum regions also consists of functions that solve the actual problem for an averaged potential at a predetermined energy parameter and energy derivatives to these functions. In consequence, the matrix setup in the vacuum regions is performed in analogy to the setup in the MT spheres.

We start the introduction to this setup by expressing the potential in a vacuum region as

$$V^{\mathrm{vac}}(\boldsymbol{r}) = \sum_{\boldsymbol{G}''_{\parallel}} V^{\mathrm{vac}}_{\boldsymbol{G}''_{\parallel}}(z) e^{i\boldsymbol{G}''_{\parallel}\boldsymbol{r}_{\parallel}}, \tag{3.64}$$

where $V^{\mathrm{vac,avg}}_{\mathrm{eff}}(z) = V^{\mathrm{vac}}_{\boldsymbol{G}''_{\parallel}=\boldsymbol{0}}(z)$ is the two-dimensional average of the effective potential. The other components are the deviations from this average in the plane of the film.

Next, one subdivides the contributions to the Hamilton matrix into contributions due to the average potential $H^{\boldsymbol{k},\mathrm{vac,avg}}_{\boldsymbol{G}\boldsymbol{G}'}$ and contributions due to deviations from this averaged potential $H^{\boldsymbol{k},\mathrm{vac,dev}}_{\boldsymbol{G}\boldsymbol{G}'}$. So, in a formal notation one constructs the contributions due to the vacuum vac as

$$H^{\boldsymbol{k},\mathrm{vac}}_{\boldsymbol{G}\boldsymbol{G}'} = H^{\boldsymbol{k},\mathrm{vac,avg}}_{\boldsymbol{G}\boldsymbol{G}'} + H^{\boldsymbol{k},\mathrm{vac,dev}}_{\boldsymbol{G}\boldsymbol{G}'}. \tag{3.65}$$

Analogously to the construction of the $u^{\alpha}_{l}(r_{\alpha}, E^{\alpha}_{l})$ and $\dot{u}^{\alpha}_{l}(r_{\alpha}, E^{\alpha}_{l})$ in the MT spheres, the $u^{\mathrm{vac}}_{\boldsymbol{k}_{\parallel}\boldsymbol{G}_{\parallel}}(z, E^{\mathrm{vac}})$ and $\dot{u}^{\mathrm{vac}}_{\boldsymbol{k}_{\parallel}\boldsymbol{G}_{\parallel}}(z, E^{\mathrm{vac}})$ are constructed to fulfill

$$\hat{H}^{\mathrm{vac,avg}} |u^{\mathrm{vac}}_{\boldsymbol{k}_{\parallel}\boldsymbol{G}_{\parallel}}\rangle = E^{\mathrm{vac}} |u^{\mathrm{vac}}_{\boldsymbol{k}_{\parallel}\boldsymbol{G}_{\parallel}}\rangle \tag{3.66}$$

with $\langle u^{\mathrm{vac}}_{\boldsymbol{k}_{\parallel}\boldsymbol{G}_{\parallel}} | u^{\mathrm{vac}}_{\boldsymbol{k}_{\parallel}\boldsymbol{G}_{\parallel}}\rangle_{\mathrm{vac}} = 1$ and

$$\hat{H}^{\mathrm{vac,avg}} |\dot{u}^{\mathrm{vac}}_{\boldsymbol{k}_{\parallel}\boldsymbol{G}_{\parallel}}\rangle = E^{\mathrm{vac}} |\dot{u}^{\mathrm{vac}}_{\boldsymbol{k}_{\parallel}\boldsymbol{G}_{\parallel}}\rangle + |u^{\mathrm{vac}}_{\boldsymbol{k}_{\parallel}\boldsymbol{G}_{\parallel}}\rangle \tag{3.67}$$

with $\langle \dot{u}^{\mathrm{vac}}_{\boldsymbol{k}_{\parallel}\boldsymbol{G}_{\parallel}} | u^{\mathrm{vac}}_{\boldsymbol{k}_{\parallel}\boldsymbol{G}_{\parallel}}\rangle_{\mathrm{vac}} = 0$.

As a consequence the contributions due to the averaged potential are

$$H^{\boldsymbol{k},\mathrm{vac,avg}}_{\boldsymbol{G}\boldsymbol{G}'} = \delta_{\boldsymbol{G}_\parallel \boldsymbol{G}'_\parallel} \Big\{ E^{\mathrm{vac}} \Big[\left(a^{\mathrm{vac}}_{\boldsymbol{k}_\parallel \boldsymbol{G}}\right)^* a^{\mathrm{vac}}_{\boldsymbol{k}_\parallel \boldsymbol{G}'} + \langle \dot{u}^{\mathrm{vac}}_{\boldsymbol{k}_\parallel \boldsymbol{G}_\parallel} | \dot{u}^{\mathrm{vac}}_{\boldsymbol{k}_\parallel \boldsymbol{G}'_\parallel} \rangle_{\mathrm{vac}} \left(b^{\mathrm{vac}}_{\boldsymbol{k}_\parallel \boldsymbol{G}}\right)^* b^{\mathrm{vac}}_{\boldsymbol{k}_\parallel \boldsymbol{G}'} \Big] + \frac{1}{2} \Big[\left(a^{\mathrm{vac}}_{\boldsymbol{k}_\parallel \boldsymbol{G}}\right)^* b^{\mathrm{vac}}_{\boldsymbol{k}_\parallel \boldsymbol{G}'} + \left(b^{\mathrm{vac}}_{\boldsymbol{k}_\parallel \boldsymbol{G}}\right)^* a^{\mathrm{vac}}_{\boldsymbol{k}_\parallel \boldsymbol{G}'} \Big] \Big\}, \tag{3.68}$$

where we already averaged over the application of the Hamiltonian to the left and to the right basis functions to make the matrix explicitly hermitian.

The contributions to the overlap matrix can also be constructed in analogy to the MT part of the overlap matrix. One obtains

$$S^{\boldsymbol{k},\mathrm{vac}}_{\boldsymbol{G}\boldsymbol{G}'} = \delta_{\boldsymbol{G}_\parallel \boldsymbol{G}'_\parallel} \Big[\left(a^{\mathrm{vac}}_{\boldsymbol{k}_\parallel \boldsymbol{G}}\right)^* a^{\mathrm{vac}}_{\boldsymbol{k}_\parallel \boldsymbol{G}'} + \langle \dot{u}^{\mathrm{vac}}_{\boldsymbol{k}_\parallel \boldsymbol{G}_\parallel} | \dot{u}^{\mathrm{vac}}_{\boldsymbol{k}_\parallel \boldsymbol{G}'_\parallel} \rangle_{\mathrm{vac}} \left(b^{\mathrm{vac}}_{\boldsymbol{k}_\parallel \boldsymbol{G}}\right)^* b^{\mathrm{vac}}_{\boldsymbol{k}_\parallel \boldsymbol{G}'} \Big]. \tag{3.69}$$

Finally, the contributions due to the deviations from the averaged effective potential,

$$V^{\mathrm{vac,dev}}_{\mathrm{eff}}(\boldsymbol{r}) = \sum_{\boldsymbol{G}''_\parallel \neq \boldsymbol{0}} V^{\mathrm{vac}}_{\boldsymbol{G}''_\parallel}(z) e^{i \boldsymbol{G}''_\parallel \boldsymbol{r}_\parallel}, \tag{3.70}$$

are computed by precalculating the four integrals

$$\begin{aligned} t^{\mathrm{vac}[\circ][\diamond]}_{\boldsymbol{k}_\parallel \boldsymbol{G}_\parallel \boldsymbol{G}'_\parallel} &= \frac{1}{A} \int_{\mathrm{vac}} \sum_{\boldsymbol{G}_\parallel} \sum_{\boldsymbol{G}'_\parallel} \sum_{\boldsymbol{G}''_\parallel \neq \boldsymbol{0}} e^{-i(\boldsymbol{k}_\parallel + \boldsymbol{G}_\parallel)\boldsymbol{r}_\parallel} {}^{[\circ]}u^{\mathrm{vac}}_{\boldsymbol{k}_\parallel \boldsymbol{G}_\parallel}(z, E^{\mathrm{vac}}) \\ &\qquad \times e^{i(\boldsymbol{G}''_\parallel)\boldsymbol{r}_\parallel} V^{\mathrm{vac}}_{\boldsymbol{G}''_\parallel}(z) \\ &\qquad \times e^{i(\boldsymbol{k}_\parallel + \boldsymbol{G}'_\parallel)\boldsymbol{r}_\parallel} {}^{[\diamond]}u^{\mathrm{vac}}_{\boldsymbol{k}_\parallel \boldsymbol{G}'_\parallel}(z, E^{\mathrm{vac}}) d^2\boldsymbol{r}_\parallel dz \\ &= \left(1 - \delta_{\boldsymbol{G}_\parallel \boldsymbol{G}'_\parallel}\right) \delta_{\boldsymbol{G}_\parallel (\boldsymbol{G}'_\parallel + \boldsymbol{G}''_\parallel)} \\ &\quad \times \int_{\mathrm{vac}} {}^{[\circ]}u^{\mathrm{vac}}_{\boldsymbol{k}_\parallel \boldsymbol{G}_\parallel}(z, E^{\mathrm{vac}}) V^{\mathrm{vac}}_{\boldsymbol{G}''_\parallel}(z) {}^{[\diamond]}u^{\mathrm{vac}}_{\boldsymbol{k}_\parallel \boldsymbol{G}'_\parallel}(z, E^{\mathrm{vac}}) dz \end{aligned} \tag{3.71}$$

to finally obtain

$$\begin{aligned} H^{\boldsymbol{k},\mathrm{vac,dev}}_{\boldsymbol{G}\boldsymbol{G}'} &= \left(a^{\mathrm{vac}}_{\boldsymbol{k}_\parallel \boldsymbol{G}}\right)^* t^{\mathrm{vac}[\,][\,]}_{\boldsymbol{k}_\parallel \boldsymbol{G}_\parallel \boldsymbol{G}'_\parallel} a^{\mathrm{vac}}_{\boldsymbol{k}_\parallel \boldsymbol{G}'} + \left(a^{\mathrm{vac}}_{\boldsymbol{k}_\parallel \boldsymbol{G}}\right)^* t^{\mathrm{vac}[\,][\cdot]}_{\boldsymbol{k}_\parallel \boldsymbol{G}_\parallel \boldsymbol{G}'_\parallel} b^{\mathrm{vac}}_{\boldsymbol{k}_\parallel \boldsymbol{G}'} \\ &\quad + \left(b^{\mathrm{vac}}_{\boldsymbol{k}_\parallel \boldsymbol{G}}\right)^* t^{\mathrm{vac}[\cdot][\,]}_{\boldsymbol{k}_\parallel \boldsymbol{G}_\parallel \boldsymbol{G}'_\parallel} a^{\mathrm{vac}}_{\boldsymbol{k}_\parallel \boldsymbol{G}'} + \left(b^{\mathrm{vac}}_{\boldsymbol{k}_\parallel \boldsymbol{G}}\right)^* t^{\mathrm{vac}[\cdot][\cdot]}_{\boldsymbol{k}_\parallel \boldsymbol{G}_\parallel \boldsymbol{G}'_\parallel} b^{\mathrm{vac}}_{\boldsymbol{k}_\parallel \boldsymbol{G}'}. \end{aligned} \tag{3.72}$$

3.3 Constructing the electron density

In analogy to the LAPW basis functions, the electron density $\rho(\boldsymbol{r})$ is represented piecewise: In the interstitial region it is represented in terms of plane waves, whereas

in the MT spheres it consists of radial functions $\rho_L^\alpha(r_\alpha)$ times spherical harmonics and in the vacuum regions it is given by decaying functions perpendicular to the plane of the film times two-dimensional plane waves. In detail its analytical form is[3]

$$\rho(\boldsymbol{r}) = \begin{cases} \sum_{\boldsymbol{G}} \rho_{\boldsymbol{G}} e^{i\boldsymbol{G}\boldsymbol{r}} & \text{for } \boldsymbol{r} \in \mathrm{IR} \\ \sum_{\alpha} \sum_{L} \rho_L^\alpha(r_\alpha) Y_L(\hat{\boldsymbol{r}}_{\boldsymbol{\alpha}}) & \text{for } \boldsymbol{r} \in \mathrm{MT}^\alpha \\ \sum_{\mathrm{vac}} \sum_{\boldsymbol{G}_\parallel} \rho_{\boldsymbol{G}_\parallel}^{\mathrm{vac}}(z) e^{i\boldsymbol{G}_\parallel r_\parallel} & \text{for } \boldsymbol{r} \in \mathrm{VR}^{\mathrm{vac}} \end{cases} . \tag{3.73}$$

Note that the density is obtained from a linear combination of squares of absolute values of eigenfunctions,

$$\begin{aligned} \rho(\boldsymbol{r}) &= 2 \int_{\mathrm{BZ}} \sum_{\nu} \omega_{\boldsymbol{k}}^{\nu} \left| \psi_{\boldsymbol{k}}^{\nu}(\boldsymbol{r}) \right|^2 d^3k \\ &= 2 \sum_{\boldsymbol{k}} \sum_{\nu} \omega_{\boldsymbol{k}}^{\nu} \left| \psi_{\boldsymbol{k}}^{\nu}(\boldsymbol{r}) \right|^2 , \end{aligned} \tag{3.74}$$

where BZ denotes the Brillouin zone and $\omega_{\boldsymbol{k}}^{\nu}$ is the occupation of the ν-th eigenfunction $\psi_{\boldsymbol{k}}^{\nu\sigma}(\boldsymbol{r})$. The factor of 2 is due to spin-degeneracy in the case of calculations that do not consider magnetism. In the case of magnetism aware calculations, this factor is replaced by a sum over the two spins and the occupation numbers and wave functions become spin-dependent.

Due to the squares in equation (3.74) the plane wave cutoff for the density has to be at least twice as large as the corresponding cutoff for the basis functions. Analogous conclusions can also be drawn for the angular momentum cutoffs in the MT spheres. However, here we keep the $l_{\max}^\alpha$ from the basis functions also for the density representation.

The partitioning of the unit cell implies that the density can be calculated as a sum of different terms originating from the different regions. Here, we discuss the construction of the density as

$$\rho(\boldsymbol{r}) = \rho^{\mathrm{IR}}(\boldsymbol{r}) + \sum_{\alpha} \rho^{\alpha}(\boldsymbol{r}) + \sum_{\mathrm{vac}} \rho^{\mathrm{vac}}(\boldsymbol{r}), \tag{3.75}$$

where $\rho^{\mathrm{IR}}(\boldsymbol{r})$ is the interstitial density, $\rho^{\alpha}(\boldsymbol{r})$ is the density in the MT sphere around atom α, and $\rho^{\mathrm{vac}}(\boldsymbol{r})$ is the density in vacuum region vac. However, the first step in the construction of the density is the representation of the eigenfunctions and the determination of the occupation of these eigenfunctions.

[3] To reduce the computational demands and the storage demands for the density, in FLAPW programs one actually uses a more compact representation in which expansion coefficients of crystal symmetry related plane waves and spherical harmonics are grouped in so-called stars and lattice harmonics, respectively [98, 18]. For the sake of simplicity we abstract from this detail.

3.3.1 Representation of the eigenfunctions

After solving the generalized eigenvalue problem, the valence wave functions $\psi^{\nu}_{\boldsymbol{k}}(\boldsymbol{r})$ for a given spin channel are given by an expansion in terms of LAPW basis functions

$$\psi^{\nu}_{\boldsymbol{k}}(\boldsymbol{r}) = \sum_{\boldsymbol{G}} z^{\nu}_{\boldsymbol{k}\boldsymbol{G}} \phi_{\boldsymbol{k}\boldsymbol{G}}(\boldsymbol{r}), \tag{3.76}$$

where the $z^{\nu}_{\boldsymbol{k}\boldsymbol{G}}$ are the expansion coefficients for the ν-th wave function. With this, the interstitial representation of the wave functions is given by an expansion in plane waves, while the matching coefficients at the boundaries to the other regions are obtained in terms of the matching to this linear combination of plane waves. In detail, the eigenfunctions are represented as

$$\psi^{\nu}_{\boldsymbol{k}}(\boldsymbol{r}) = \begin{cases} \sum\limits_{\boldsymbol{G}} z^{\nu}_{\boldsymbol{k}\boldsymbol{G}} \frac{1}{\sqrt{\Omega}} e^{i(\boldsymbol{k}+\boldsymbol{G})\boldsymbol{r}} & \text{for } \boldsymbol{r} \in \mathrm{IR} \\ \sum\limits_{L} \left[A^{L\alpha}_{\boldsymbol{k}\nu} u^{\alpha}_{l}(r_{\alpha}, E^{\alpha}_{l}) + B^{L\alpha}_{\boldsymbol{k}\nu} \dot{u}^{\alpha}_{l}(r_{\alpha}, E^{\alpha}_{l}) \right] Y_{L}(\hat{\boldsymbol{r}}_{\boldsymbol{\alpha}}) & \text{for } \boldsymbol{r} \in \mathrm{MT}^{\alpha} \\ \sum\limits_{\boldsymbol{G}_{\parallel}} \left[A^{\mathrm{vac},\nu}_{\boldsymbol{k}_{\parallel}\boldsymbol{G}_{\parallel}} u^{\mathrm{vac}}_{\boldsymbol{k}_{\parallel}\boldsymbol{G}_{\parallel}}(z, E^{\mathrm{vac}}) + B^{\mathrm{vac},\nu}_{\boldsymbol{k}_{\parallel}\boldsymbol{G}_{\parallel}} \dot{u}^{\mathrm{vac}}_{\boldsymbol{k}_{\parallel}\boldsymbol{G}_{\parallel}}(z, E^{\mathrm{vac}}) \right] \frac{1}{\sqrt{A}} e^{i(\boldsymbol{k}_{\parallel}+\boldsymbol{G}_{\parallel})\boldsymbol{r}_{\parallel}} & \text{for } \boldsymbol{r} \in \mathrm{VR}^{\mathrm{vac}} \end{cases} \tag{3.77}$$

with

$$A^{L\alpha}_{\boldsymbol{k}\nu} = \sum_{\boldsymbol{G}} z^{\nu}_{\boldsymbol{k}\boldsymbol{G}} a^{L\alpha}_{\boldsymbol{k}\boldsymbol{G}}, \tag{3.78}$$

$$B^{L\alpha}_{\boldsymbol{k}\nu} = \sum_{\boldsymbol{G}} z^{\nu}_{\boldsymbol{k}\boldsymbol{G}} b^{L\alpha}_{\boldsymbol{k}\boldsymbol{G}}, \tag{3.79}$$

$$A^{\mathrm{vac},\nu}_{\boldsymbol{k}_{\parallel}\boldsymbol{G}_{\parallel}} = \sum_{\substack{\boldsymbol{G}' \\ \boldsymbol{G}'_{\parallel}=\boldsymbol{G}_{\parallel}}} z^{\nu}_{\boldsymbol{k}\boldsymbol{G}'} a^{\mathrm{vac}}_{\boldsymbol{k}_{\parallel}\boldsymbol{G}'}, \tag{3.80}$$

$$B^{\mathrm{vac},\nu}_{\boldsymbol{k}_{\parallel}\boldsymbol{G}_{\parallel}} = \sum_{\substack{\boldsymbol{G}' \\ \boldsymbol{G}'_{\parallel}=\boldsymbol{G}_{\parallel}}} z^{\nu}_{\boldsymbol{k}\boldsymbol{G}'} b^{\mathrm{vac}}_{\boldsymbol{k}_{\parallel}\boldsymbol{G}'}. \tag{3.81}$$

3.3.2 Occupying the eigenstates

To construct the electron density, one has to consider the occupation of the eigenstates. This is done by filling the states from the energetically lowest state upwards until all electrons in the material are assigned to a state. Furthermore one considers a temperature smearing with a Fermi-Dirac distribution

$$f(E) = \frac{1}{e^{(E-E_{\mathrm{F}})/k_{\mathrm{B}}T} + 1}, \tag{3.82}$$

where E_{F} is the Fermi energy and T is an artificial energy parameter. Although one is interested in the electronic ground state, which implies no occupation of excited

states, this temperature smearing is important in practice to enable a stable convergence behavior for metals. Within the DFT self-consistency cycle one can observe that the energies of the eigenstates slightly shift throughout the iterations. It also happens that bands reorder. If something like this happens near the Fermi energy it can lead to strongly changing occupations from one iteration to the next, resulting in a very problematic convergence behavior or no convergence at all. The finite temperature smearing considerably suppresses this effect since it involves fractional occupations, even for states that are located slightly above the Fermi level. One obtains a continuous occupation behavior in dependence of the energy of an eigenstate.

Beyond the temperature parameter the Fermi energy E_F is another parameter in the Fermi-Dirac distribution. Of course, this parameter cannot be manually set but is from the condition

$$N_\mathrm{elec} = 2 \sum_{\boldsymbol{k}} \sum_{\nu} \omega(\boldsymbol{k}) \frac{1}{e^{(\epsilon^\nu_{\boldsymbol{k}} - E_\mathrm{F})/k_\mathrm{B}T} + 1}, \tag{3.83}$$

where N_elec is the number of electrons in the unit cell, $\omega(\boldsymbol{k})$ is the weight for a given $\boldsymbol{k}$ point in the irreducible wedge of the Brillouin zone (IBZ), and $\epsilon^\nu_{\boldsymbol{k}}$ is the energy of the eigenstate $\psi^\nu_{\boldsymbol{k}}(\boldsymbol{r})$. The factor of 2 in equation (3.83) once again is due to spin-degeneracy and is replaced by a sum over spins in the case of calculations on magnetic materials. In the latter case the eigenvalues also become spin-dependent.

Finally, the occupation $\omega^\nu_{\boldsymbol{k}}$ of a state $\psi^\nu_{\boldsymbol{k}}(\boldsymbol{r})$ is given by

$$\omega^\nu_{\boldsymbol{k}} = \omega(\boldsymbol{k}) \frac{1}{e^{(\epsilon^\nu_{\boldsymbol{k}} - E_\mathrm{F})/k_\mathrm{B}T} + 1}. \tag{3.84}$$

3.3.3 The interstitial density

The plane wave expansion of the interstitial valence density is given by reciprocal space convolutions of eigenfunctions with themselves. For a given plane wave coefficient $\rho_{\boldsymbol{G}}$ one obtains

$$\rho_{\boldsymbol{G}} = 2 \sum_{\boldsymbol{k}} \sum_{\nu} \omega^\nu_{\boldsymbol{k}} \sum_{\boldsymbol{G'}} \sum_{\substack{\boldsymbol{G''} \\ \boldsymbol{G''} - \boldsymbol{G'} = \boldsymbol{G}}} \left(z^\nu_{\boldsymbol{k}\boldsymbol{G'}}\right)^* \left(z^\nu_{\boldsymbol{k}\boldsymbol{G''}}\right). \tag{3.85}$$

However, the calculation of the interstitial density by explicitly performing the convolution is very time-consuming as it scales with $\mathcal{O}(N_\mathrm{occ} N^2_\mathrm{LAPW})$, where N_occ is the number of occupied bands. Since N_occ and N_LAPW both scale linearly with the size of the unit cell, this is a cubic scaling behavior with respect to the system size, the same scaling as for the setup of the matrices and the diagonalization. Fortunately, the well-known convolution theorem tells us that a convolution in reciprocal space can be replaced by a pointwise product in real space. Together with the fact that the transformation between real and reciprocal space can be performed in $\mathcal{O}(N_\mathrm{mesh} \cdot \log(N_\mathrm{mesh}))$[4]

[4] N_mesh is the number of points on the real space mesh, as well as on the reciprocal space mesh.

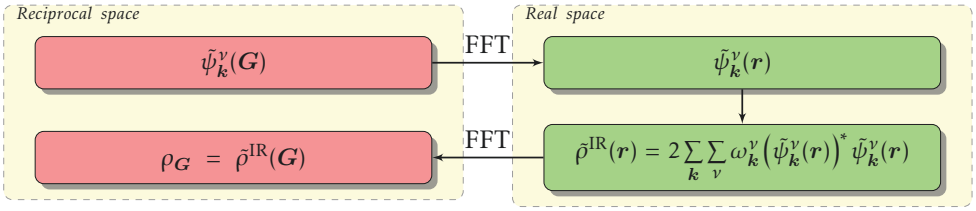

Figure 3.5.: Sketch of the calculation of the interstitial contributions to the density. A real space representation of the functions $\tilde{\psi}^{\nu}_{\boldsymbol{k}}$ is obtained by Fourier transforming their original reciprocal representations. The interstitial density $\tilde{\rho}^{\mathrm{IR}}$ is then calculated in real space and finally transformed back to reciprocal space to obtain the plane wave expansion coefficients.

by the Fast Fourier Transform (FFT) algorithm, this gives us a recipe to obtain the interstitial density in a more efficient way.

In detail, one removes the augmentation from the eigenfunctions by defining the functions

$$\tilde{\psi}^{\nu}_{\boldsymbol{k}}(\boldsymbol{r}) = \sum_{\boldsymbol{G}} z^{\nu}_{\boldsymbol{k}\boldsymbol{G}} \frac{1}{\sqrt{\Omega}} e^{i(\boldsymbol{k}+\boldsymbol{G})\boldsymbol{r}} \tag{3.86}$$

in which the plane wave expansion of the eigenfunctions covers the whole space. Next, one transforms the reciprocal space representation of these functions with a FFT onto a real space grid[5]. At each point of this grid one computes the square of the absolute value of these functions and performs a $\omega^{\nu}_{\boldsymbol{k}}$ weighted sum over these squares to obtain a real space representation of the interstitial density $\tilde{\rho}^{\mathrm{IR}}(\boldsymbol{r})$, which covers the whole unit cell. Finally, one performs the backtransformation to reciprocal space to get access to the plane wave coefficients $\rho_{\boldsymbol{G}} = \tilde{\rho}^{\mathrm{IR}}(\boldsymbol{G})$. Figure 3.5 sketches this procedure. Note that one has to perform these operations on a mesh that is fine enough to represent the interstitial density. With this requirement N_{mesh} is eight times larger than N_{LAPW}.

Computing the interstitial contributions to the density in this way yields a scaling behavior of $\mathcal{O}(N_{\mathrm{occ}}N_{\mathrm{mesh}} \cdot \log(N_{\mathrm{mesh}}) + N_{\mathrm{occ}}N_{\mathrm{mesh}})$, which is considerably better than the cubic scaling of the naive approach.

3.3.4 The density in the MT spheres

The valence electron density in the MT sphere around atom α is

$$\rho^{\alpha}(\boldsymbol{r}) = 2\sum_{L} \rho^{\alpha}_{L}(r_{\alpha}) Y_{L}(\hat{\boldsymbol{r}}_{\boldsymbol{\alpha}}) \tag{3.87}$$

[5] Actually one abstracts from the Bloch factor $e^{i\boldsymbol{k}\boldsymbol{r}}$ by performing this step. However, this is not problematic since the Bloch factor cancels with its conjugate complex when the square of the absolute value is computed in real space.

with

$$\rho_L^\alpha(r_\alpha) = \sum_{\boldsymbol{k}} \sum_\nu \omega_{\boldsymbol{k}}^\nu \sum_{L'} \sum_{L''} \left[A_{\boldsymbol{k}\nu}^{L'\alpha} u_{l'}^\alpha(r_\alpha, E_{l'}^\alpha) + B_{\boldsymbol{k}\nu}^{L'\alpha} \dot{u}_{l'}^\alpha(r_\alpha, E_{l'}^\alpha) \right]^* \times \left[A_{\boldsymbol{k}\nu}^{L''\alpha} u_{l''}^\alpha(r_\alpha, E_{l''}^\alpha) + B_{\boldsymbol{k}\nu}^{L''\alpha} \dot{u}_{l''}^\alpha(r_\alpha, E_{l''}^\alpha) \right] \times G_{l''l'l}^{m''m'm} \tag{3.88}$$

To save time in the computation of this sum, one exploits that the radial functions $u_l^\alpha(r_\alpha, E_l^\alpha)$ and $\dot{u}_l^\alpha(r_\alpha, E_l^\alpha)$ do not depend on the magnetic quantum number. In detail one calculates

$$\begin{aligned}
\rho_L^\alpha(r_\alpha) = &\sum_{l',l''} \left[\sum_{\boldsymbol{k},\nu} \omega_{\boldsymbol{k}}^\nu \sum_{m',m''} \left(A_{\boldsymbol{k}\nu}^{L'\alpha} \right)^* A_{\boldsymbol{k}\nu}^{L''\alpha} G_{l''l'l}^{m''m'm} \right] u_{l'}^\alpha(r_\alpha, E_{l'}^\alpha) u_{l''}^\alpha(r_\alpha, E_{l''}^\alpha) \\
&+ \sum_{l',l''} \left[\sum_{\boldsymbol{k},\nu} \omega_{\boldsymbol{k}}^\nu \sum_{m',m''} \left(A_{\boldsymbol{k}\nu}^{L'\alpha} \right)^* B_{\boldsymbol{k}\nu}^{L''\alpha} G_{l''l'l}^{m''m'm} \right] u_{l'}^\alpha(r_\alpha, E_{l'}^\alpha) \dot{u}_{l''}^\alpha(r_\alpha, E_{l''}^\alpha) \\
&+ \sum_{l',l''} \left[\sum_{\boldsymbol{k},\nu} \omega_{\boldsymbol{k}}^\nu \sum_{m',m''} \left(B_{\boldsymbol{k}\nu}^{L'\alpha} \right)^* A_{\boldsymbol{k}\nu}^{L''\alpha} G_{l''l'l}^{m''m'm} \right] \dot{u}_{l'}^\alpha(r_\alpha, E_{l'}^\alpha) u_{l''}^\alpha(r_\alpha, E_{l''}^\alpha) \\
&+ \sum_{l',l''} \left[\sum_{\boldsymbol{k},\nu} \omega_{\boldsymbol{k}}^\nu \sum_{m',m''} \left(B_{\boldsymbol{k}\nu}^{L'\alpha} \right)^* B_{\boldsymbol{k}\nu}^{L''\alpha} G_{l''l'l}^{m''m'm} \right] \dot{u}_{l'}^\alpha(r_\alpha, E_{l'}^\alpha) \dot{u}_{l''}^\alpha(r_\alpha, E_{l''}^\alpha).
\end{aligned} \tag{3.89}$$

With a time complexity of $\mathcal{O}(N_{\text{atom}} N_{\text{occ}})$ the calculation of the MT parts of the valence density is not a dominant part in the time requirements of an FLAPW iteration. Note however that the radial dependence of the MT density implies a large prefactor to this system size dependent scaling: There are typically several hundred radial mesh points on which r_α is sampled.

3.3.5 The density in the vacuum regions

The valence electron density in one of the vacuum regions is

$$\rho^{\text{vac}}(\boldsymbol{r}) = 2 \sum_{\boldsymbol{G}_\parallel} \rho_{\boldsymbol{G}_\parallel}^{\text{vac}}(z) e^{i \boldsymbol{G}_\parallel \boldsymbol{r}_\parallel} \tag{3.90}$$

with

$$\begin{aligned}
\rho_{\boldsymbol{G}_\parallel}^{\text{vac}}(z) = \sum_{\boldsymbol{k}_\parallel} \sum_\nu \omega_{\boldsymbol{k}}^\nu \sum_{\boldsymbol{G}'_\parallel} \sum_{\substack{\boldsymbol{G}''_\parallel \\ \boldsymbol{G}''_\parallel - \boldsymbol{G}'_\parallel = \boldsymbol{G}_\parallel}} &\left[A_{\boldsymbol{k}_\parallel \boldsymbol{G}'_\parallel}^{\text{vac},\nu} u_{\boldsymbol{k}_\parallel \boldsymbol{G}'_\parallel}^{\text{vac}}(z, E^{\text{vac}}) + B_{\boldsymbol{k}_\parallel \boldsymbol{G}'_\parallel}^{\text{vac},\nu} \dot{u}_{\boldsymbol{k}_\parallel \boldsymbol{G}'_\parallel}^{\text{vac}}(z, E^{\text{vac}}) \right]^* \\
&\times \left[A_{\boldsymbol{k}_\parallel \boldsymbol{G}''_\parallel}^{\text{vac},\nu} u_{\boldsymbol{k}_\parallel \boldsymbol{G}''_\parallel}^{\text{vac}}(z, E^{\text{vac}}) + B_{\boldsymbol{k}_\parallel \boldsymbol{G}''_\parallel}^{\text{vac},\nu} \dot{u}_{\boldsymbol{k}_\parallel \boldsymbol{G}''_\parallel}^{\text{vac}}(z, E^{\text{vac}}) \right].
\end{aligned} \tag{3.91}$$

In the actual calculation of this quantity one eliminates the sum over $\boldsymbol{G}''_\parallel$ by exploiting the condition $\boldsymbol{G}''_\parallel - \boldsymbol{G}'_\parallel = \boldsymbol{G}_\parallel$ to directly calculate the single $\boldsymbol{G}''_\parallel$ for which this requirement is met, $\boldsymbol{G}''_\parallel = \boldsymbol{G}'_\parallel + \boldsymbol{G}_\parallel$. Finally, one calculates

$$\begin{aligned}
\rho^{\mathrm{vac}}_{\boldsymbol{G}_\parallel}(z) = &\sum_{\boldsymbol{k}_\parallel,\nu} \omega^\nu_{\boldsymbol{k}} \sum_{\boldsymbol{G}'_\parallel} \left(A^{\mathrm{vac},\nu}_{\boldsymbol{k}_\parallel \boldsymbol{G}'_\parallel}\right)^* A^{\mathrm{vac},\nu}_{\boldsymbol{k}_\parallel (\boldsymbol{G}'_\parallel + \boldsymbol{G}_\parallel)} u^{\mathrm{vac}}_{\boldsymbol{k}_\parallel \boldsymbol{G}'_\parallel}(z, E^{\mathrm{vac}}) u^{\mathrm{vac}}_{\boldsymbol{k}_\parallel (\boldsymbol{G}'_\parallel + \boldsymbol{G}_\parallel)}(z, E^{\mathrm{vac}}) \\
&+ \sum_{\boldsymbol{k}_\parallel,\nu} \omega^\nu_{\boldsymbol{k}} \sum_{\boldsymbol{G}'_\parallel} \left(A^{\mathrm{vac},\nu}_{\boldsymbol{k}_\parallel \boldsymbol{G}'_\parallel}\right)^* B^{\mathrm{vac},\nu}_{\boldsymbol{k}_\parallel (\boldsymbol{G}'_\parallel + \boldsymbol{G}_\parallel)} u^{\mathrm{vac}}_{\boldsymbol{k}_\parallel \boldsymbol{G}'_\parallel}(z, E^{\mathrm{vac}}) \dot{u}^{\mathrm{vac}}_{\boldsymbol{k}_\parallel (\boldsymbol{G}'_\parallel + \boldsymbol{G}_\parallel)}(z, E^{\mathrm{vac}}) \\
&+ \sum_{\boldsymbol{k}_\parallel,\nu} \omega^\nu_{\boldsymbol{k}} \sum_{\boldsymbol{G}'_\parallel} \left(B^{\mathrm{vac},\nu}_{\boldsymbol{k}_\parallel \boldsymbol{G}'_\parallel}\right)^* A^{\mathrm{vac},\nu}_{\boldsymbol{k}_\parallel (\boldsymbol{G}'_\parallel + \boldsymbol{G}_\parallel)} \dot{u}^{\mathrm{vac}}_{\boldsymbol{k}_\parallel \boldsymbol{G}'_\parallel}(z, E^{\mathrm{vac}}) u^{\mathrm{vac}}_{\boldsymbol{k}_\parallel (\boldsymbol{G}'_\parallel + \boldsymbol{G}_\parallel)}(z, E^{\mathrm{vac}}) \\
&+ \sum_{\boldsymbol{k}_\parallel,\nu} \omega^\nu_{\boldsymbol{k}} \sum_{\boldsymbol{G}'_\parallel} \left(B^{\mathrm{vac},\nu}_{\boldsymbol{k}_\parallel \boldsymbol{G}'_\parallel}\right)^* B^{\mathrm{vac},\nu}_{\boldsymbol{k}_\parallel (\boldsymbol{G}'_\parallel + \boldsymbol{G}_\parallel)} \dot{u}^{\mathrm{vac}}_{\boldsymbol{k}_\parallel \boldsymbol{G}'_\parallel}(z, E^{\mathrm{vac}}) \dot{u}^{\mathrm{vac}}_{\boldsymbol{k}_\parallel (\boldsymbol{G}'_\parallel + \boldsymbol{G}_\parallel)}(z, E^{\mathrm{vac}}).
\end{aligned} \tag{3.92}$$

Since the number of LAPW basis functions scales cubically with the volume of the unit cell and the number of projections of plane waves onto the plane of the film scales quadratically, the calculation of the vacuum contributions to the vacuum density from all $\boldsymbol{G}_\parallel$ scales with $\mathcal{O}(N_{\mathrm{occ}} N^{4/3}_{\mathrm{LAPW}})$. Note that this is more efficient than the cubic scaling behavior that dominates the time requirements of an FLAPW iteration.

3.3.6 Contributions to the density from the core electrons

Within a MT sphere the core electron states of the associated atom form a completely spherical charge density that is, to a large extent, confined within the sphere. However, for a precise representation of the density one goes beyond this approximation and also considers the tail of the core electron density that leaps out of the MT sphere. In fact, one assumes that the density due to the core states from the different atoms covers the whole unit cell. It is therefore given as

$$\rho_{\mathrm{c}}(\boldsymbol{r}) = \begin{cases} \sum\limits_{\boldsymbol{G}} \rho_{\mathrm{c}\boldsymbol{G}} e^{i\boldsymbol{G}\boldsymbol{r}} & \text{for } \boldsymbol{r} \in \mathrm{IR} \\ \sum\limits_{\alpha} \sum\limits_{L} \rho^\alpha_{\mathrm{c}L}(r_\alpha) Y_L(\hat{\boldsymbol{r}}_{\boldsymbol{\alpha}}) & \text{for } \boldsymbol{r} \in \mathrm{MT}^\alpha \\ \sum\limits_{\mathrm{vac}} \sum\limits_{\boldsymbol{G}_\parallel} \rho^{\mathrm{vac}}_{\mathrm{c}\boldsymbol{G}_\parallel}(z) e^{i\boldsymbol{G}_\parallel \boldsymbol{r}_\parallel} & \text{for } \boldsymbol{r} \in \mathrm{VR}^{\mathrm{vac}} \end{cases}. \tag{3.93}$$

To obtain the IR part of the core density one has to expand the core tails into plane waves. In practice this is done by Fourier transforming the whole core electron density originating from a given atom, including the MT part. Unfortunately the MT part of the core density features a very slow convergence in this expansion. Therefore, one replaces this part by a smooth function that ensures a fast convergence of the plane wave expansion.

In detail, one uses a spherical pseudo density $\tilde{\rho}_{\mathrm{c}}^{\alpha}(r_\alpha)Y_{l=0,m=0}(\hat{\boldsymbol{r}}_\alpha)$ with

$$\tilde{\rho}_{\mathrm{c}}^{\alpha}(r_\alpha) = \begin{cases} a_\alpha e^{-b_\alpha r_\alpha^2} & \text{for } r_\alpha < R_{\mathrm{MT}^\alpha} \\ \rho_{\mathrm{c}}^{\alpha}(r_\alpha) & \text{for } r_\alpha \geq R_{\mathrm{MT}^\alpha} \end{cases}, \tag{3.94}$$

where $\rho_{\mathrm{c}}^{\alpha}(r_\alpha)$ is the spherical core electron density originating from the atom. The coefficients a_α and b_α are obtained by enforcing continuity of value and slope of the density at the MT sphere boundary.

The plane wave expansion coefficients $\rho_{\mathrm{c}\boldsymbol{G}}^{\alpha}$ for the IR density originating from the given atom are then calculated by a Fourier transformation as

$$\rho_{\mathrm{c}\boldsymbol{G}}^{\alpha} = \sqrt{\frac{4\pi}{\Omega}} e^{i\boldsymbol{G}\boldsymbol{\tau}_\alpha} \int_0^\infty \tilde{\rho}_{\mathrm{c}}^{\alpha}(r_\alpha) j_0(Gr_\alpha) r_\alpha^2 dr_\alpha. \tag{3.95}$$

Finally, summing over the coefficients for each atom results in

$$\rho_{\mathrm{c}\boldsymbol{G}} = \sum_\alpha \rho_{\mathrm{c}\boldsymbol{G}}^{\alpha}. \tag{3.96}$$

All in all, the calculation of the core electron density contribution to the IR density scales quadratically with the system size as $\mathcal{O}(N_{\mathrm{atom}} N_{\rho\text{-PW}})$, where $N_{\rho\text{-PW}}$ is the number of plane waves used to represent the density in the IR.

To obtain the expansion of the core tails in the different MT spheres, one has to expand $\rho_{\mathrm{c}\boldsymbol{G}} e^{i\boldsymbol{G}\boldsymbol{r}}$ in terms of a Rayleigh expansion into products of spherical harmonics and Bessel functions, centered at the respective atom. This external tail charge density is

$$\rho_{\mathrm{c}L}^{\alpha,\,\mathrm{ext}}(r_\alpha) = \frac{4\pi}{\sqrt{\Omega}} \sum_{\boldsymbol{G}} \rho_{\mathrm{c}\boldsymbol{G}} i^l e^{i\boldsymbol{G}\boldsymbol{\tau}_\alpha} j_l(Gr_\alpha) Y_L^*(\hat{\boldsymbol{G}}). \tag{3.97}$$

The calculation of this part of the density inside the MT spheres of all atoms again scales quadratically with the system size as $\mathcal{O}(N_{\mathrm{atom}} N_{\rho\text{-PW}})$. Note, however, that it also includes the onsite contribution which we have to subtract again to obtain the core electron density in the MT spheres as

$$\rho_{\mathrm{c}L}^{\alpha}(r_\alpha) = \left[\rho_{\mathrm{c}}^{\alpha}(r_\alpha) - a_\alpha e^{-b_\alpha r_\alpha^2}\right] Y_{l=0,m=0}(\hat{\boldsymbol{r}}_\alpha) + \sum_L \rho_{\mathrm{c}L}^{\alpha,\,\mathrm{ext}}(r_\alpha) Y_L(\hat{\boldsymbol{r}}_\alpha). \tag{3.98}$$

Finally, one also has to determine the vacuum region part of the core electron density. For this, one approximates the potential in the vacuum region to have a constant value. The consequence is that each wave function decays exponentially into the vacuum region, where the decay constant depends on the energy difference between the potential in the vacuum and the eigenvalue of the function. This also translates into an exponential decay of the associated contribution to the density.

For the different wave functions contributing to the core tails one now assumes an effective energy such that the whole core tail density can be approximated to possess

an exponential decay in the vacuum region. This is a reasonable approximation as the core tails reaching into the vacuum originate from wave functions in a small energy window far below the vacuum potential, i.e., they are about 1 Htr below the potential. Wave functions with higher energies would be treated within the valence framework, while core states with far lower energies are well confined within the MT spheres such that they do not contribute to the core density in the vacuum regions.

In conclusion, one makes the approximate approach

$$\rho^{\mathrm{vac}}_{\mathrm{c}\boldsymbol{G}_\parallel}(z) = \rho^{\mathrm{vac}}_{\mathrm{c}\boldsymbol{G}_\parallel}(z^{\mathrm{vac}}) e^{-\frac{z^{\mathrm{vac}}}{|z^{\mathrm{vac}}|}\alpha^{\mathrm{vac}}_{\boldsymbol{G}_\parallel}(z-z^{\mathrm{vac}})}, \tag{3.99}$$

where z^{vac} is the z coordinate of the vacuum boundary and $\alpha^{\mathrm{vac}}_{\boldsymbol{G}_\parallel}$ is the $\boldsymbol{G}_\parallel$ dependent decay constant for vacuum region vac. The parameters $\rho^{\mathrm{vac}}_{\mathrm{c}\boldsymbol{G}_\parallel}(z^{\mathrm{vac}})$ and $\alpha^{\mathrm{vac}}_{\boldsymbol{G}_\parallel}$ are determined by demanding continuity of value and slope of the core density at the vacuum boundary.

3.4 Calculating the total energy

The total energy of the electronic ground state of a given structural and magnetic configuration of a material is a basic quantity calculatable with DFT. This quantity can be used to compare different structural and magnetic configurations of a material to determine the energetically most favorable one. For example, the equilibrium lattice constant of a material can be calculated by determining the lattice constant exhibiting the lowest total energy with respect to a set of configurations with different test lattice constants. Weinert *et al.* [113] demonstrate a numerically well-behaved method of calculating the total energy within the FLAPW method. We abstract from the details of such a method and just provide a short sketch on the total energy calculation.

In principle the total energy of a Kohn-Sham system is given by

$$E_{\mathrm{total}}[\rho^{\uparrow},\rho^{\downarrow}] = T_{\mathrm{s}}[\rho^{\uparrow},\rho^{\downarrow}] + E_{\mathrm{H}}[\rho] + E_{\mathrm{ext}}[\rho] + E_{\mathrm{xc}}[\rho^{\uparrow},\rho^{\downarrow}] + E_{ii}, \tag{3.100}$$

where E_{ii} is the Madelung term

$$E_{ii} = \frac{1}{2}\sum_{\alpha}^{N_{\mathrm{atom}}} \sum_{\substack{\beta \\ \alpha\neq\beta}} \frac{Z_\alpha Z_\beta}{|\boldsymbol{\tau}_\alpha - \boldsymbol{\tau}_\beta|} \tag{3.101}$$

that covers the Coulomb interaction energy between the N_{atom} atomic nuclei α in the unit cell Ω and all nuclei β in the whole space.

The kinetic energy $T_{\mathrm{s}}[\rho^{\uparrow},\rho^{\downarrow}]$ can be obtained from the Kohn Sham orbitals. However, one wants to avoid applying the kinetic energy operator explicitly as the application of this operator is numerically problematic and, on the other hand, the kinetic energy can also be expressed in terms of quantities that are a byproduct of the DFT

calculation. In detail, one expresses the total energy by rearranging the Kohn-Sham equations with respect to the kinetic energy operator applied to the Kohn Sham orbital. This gives us

$$-\frac{1}{2}\nabla^2|\psi_{\nu,\sigma}\rangle = [E_{\nu,\sigma} - V_{\mathrm{eff},\sigma}(\boldsymbol{r})]\,|\psi_{\nu,\sigma}\rangle. \tag{3.102}$$

By projecting this equation onto $\langle\psi_{\nu,\sigma}|$ and summing up the resulting kinetic energy contributions over all occupied states, one obtains

$$T_\mathrm{s}[\rho^\uparrow,\rho^\downarrow] = \sum_\sigma \left(\sum_{\nu=1}^{N_\mathrm{occ}^\sigma} E_{\nu,\sigma}\right) - \int_\Omega \rho^\sigma(\boldsymbol{r}) V_{\mathrm{eff},\sigma}(\boldsymbol{r}) d^3r. \tag{3.103}$$

Plugging this expression into equation (3.100) and inserting also the expressions for the other energy terms finally yields

$$\begin{aligned} E_\mathrm{total}[\rho^\uparrow,\rho^\downarrow] = &\left[\sum_\sigma \left(\sum_{\nu=1}^{N_\mathrm{occ}^\sigma} E_{\nu,\sigma}\right) - \int_\Omega \rho^\sigma(\boldsymbol{r}) V_{\mathrm{eff},\sigma}(\boldsymbol{r}) d^3r\right] \\ &+ \frac{1}{2}\int_{\mathbb{R}^3}\int_\Omega \frac{\rho(\boldsymbol{r})\rho(\boldsymbol{r}')}{|\boldsymbol{r}-\boldsymbol{r}'|} d^3r d^3r' + \int_\Omega V_\mathrm{ext}(\boldsymbol{r})\rho(\boldsymbol{r}) d^3r \\ &+ E_\mathrm{xc}[\rho^\uparrow,\rho^\downarrow] + \frac{1}{2}\sum_\alpha^{N_\mathrm{atom}} \sum_{\substack{\beta \\ \alpha\neq\beta}} \frac{Z_\alpha Z_\beta}{|\boldsymbol{\tau}_\alpha - \boldsymbol{\tau}_\beta|}, \end{aligned} \tag{3.104}$$

where $E_\mathrm{xc}[\rho^\uparrow,\rho^\downarrow]$ is evaluated according to the used XC functional.

3.5 Developments for the FLAPW method

Beyond the basic calculation scheme of the FLAPW method presented in this chapter, there have been many developments within this approach to extend the area of application with respect to the types of materials and quantities that can be described. We list a few of these developments.

First of all, to make FLAPW ever more accurate, a couple of advanced XC functional have been implemented in the method. This includes LDA+U [114], the hybrid functionals PBE0 [115] and HSE [116], and the realization of exact exchange [103].

Next, one can realize that on the basis of DFT calculation results, a couple of quantities can be expressed as derivatives of a directly accessible quantity with respect to another quantity. For example, the force on an atom α is the negative of the energy derivative with respect to the atom position,

$$\boldsymbol{F}_\alpha = -\frac{\delta E}{\delta \boldsymbol{\tau}_\alpha}. \tag{3.105}$$

The calculation of forces has been realized within the FLAPW method by identifying and implementing the method specific force terms [117, 118, 119] in addition to the well-known Hellman-Feynman forces. This allows efficient structural relaxations of atom positions in complex unit cells.

Another derived quantity is the response function, which is the functional derivative of the charge density with respect to the effective potential,

$$\chi(\boldsymbol{r}, \boldsymbol{r}') = \frac{\delta\rho(\boldsymbol{r})}{\delta V_{\text{eff}}(\boldsymbol{r}')}. \tag{3.106}$$

In the context of the EXX-OEP approach, the efficient calculation of this quantity in FLAPW has been realized by Betzinger et al. [120, 121]. This involves the consideration of the incompleteness of the used LAPW basis sets and a resulting correction that makes such calculations feasible with small basis sets. Besides the realization of several advanced XC functionals, the response function can also be used to calculate a couple of other quantities. As examples we name phonon dispersion relations, magnons, and susceptibilities.

The description of materials by the FLAPW method has especially been refined in the context of magnetic materials. Here, we first note that in a classical FLAPW calculation the description of the valence electrons in the MT spheres follows the scalar-relativistic approximation, while the description in the IR is nonrelativistic. Of course, there are many materials that require a higher level of relativity in the description. For this, the missing spin orbit interaction has also been implemented within the FLAPW method [122, 123]. Spin orbit coupling (SoC) is the main driving interaction leading to magnetocrystalline anisotropy and especially important in materials with heavy elements. Also, the description of Dzyaloshinskii-Moriya interactions relies on the inclusion of SoC. Besides the inclusion of SoC and in order to describe complex spin structures, one has also realized the description of noncollinear magnetism within the FLAPW method [124] on the basis of the generalized Bloch theorem.

Beyond the extension of the FLAPW method there have also been a couple of developments on top of FLAPW calculation results. For example, the *GW* approximation to MBPT [104] is an approach beyond DFT, but has been realized on an FLAPW basis, such that FLAPW calculation results are used as an input [105, 106, 107, 108, 109]. Furthermore, there has been a development to project wave functions obtained by the FLAPW method onto maximally localized Wannier functions [125]. Such a representation of the wave functions can, for example, be used as an input for further calculations based on model Hamiltonians. For example, calculations on the ballistic transport through one-dimensional junctions have been realized on this basis [126].

4 Analysis of the linearized augmented plane-wave basis

Contents

As the analytical form of the LAPW basis is adapted to each region of space to provide precise representations of the wave functions with very few basis functions per atom, it can be considered to be highly sophisticated and efficient. In this chapter we take a closer look at the properties of the LAPW basis and evaluate its limitations.

In detail, we analyze the limitations of the linearized description of the wave functions in the MT spheres in section 4.1. Whenever this description is not sufficient, it can be improved by adding local orbitals to the LAPW basis. Therefore, in section 4.1 we also evaluate what type of local orbitals is best suited to eliminate the remaining linearization error and investigate the impact of these additional local orbitals on the required basis set size[1]. The chapter continues with an investigation and a comparison of some general properties of the basis functions and the wave functions in section 4.2. In detail, we investigate the matching conditions to the MT spheres, the

[1] Note that we have already published the contents of section 4.1 in the journal *Computer Physics Communications* [127].

changes of the potential in the MT spheres over the self-consistency iterations and its consequences on the basis functions, and the changes of the wave functions in the IR, also over the iterations of the self-consistency cycle.

4.1 The linearization error

The MT part of the LAPW basis consists of the angular momentum dependent radial functions $u_l^\alpha(r_\alpha, E_l^\alpha)$ and $\dot{u}_l^\alpha(r_\alpha, E_l^\alpha)$, evaluated at predetermined energy parameters E_l^α. We already mentioned that the usage of these two types of radial functions enables precise representations of wave functions with energy eigenvalues in the vicinity of the energy parameters. However, as Singh pointed out [9], the description of semicore states within the valence band requires additional local orbitals (LOs) constructed with a $u_l^\alpha(r_\alpha, E_l^{\alpha,\mathrm{SC}})$ for an energy parameter $E_l^{\alpha,\mathrm{SC}}$ near the energy of the semicore state. It was also shown that additional LOs are required to describe high-lying unoccupied states [110, 103], whenever they are needed for advanced methods on top of self-consistent FLAPW calculations.

Of course, the energy eigenvalues of semicore states on the one hand and high-lying unoccupied states on the other hand strongly deviate from the energy parameters typically chosen to describe the valence states. Since even the number of nodes of the required radial functions deviates between these energies, it is clear that the valence band radial functions cannot provide a precise representation in such a large energy interval. However, these observations bring us to the question to what extent the linearized description around E_l^α yields precise descriptions of wave functions within the valence band. We already mentioned (cf. Eq. (3.5)) that in a first approximation in terms of a Taylor expansion,

$$u_l^\alpha(r_\alpha, E) = u_l^\alpha(r_\alpha, E_l^\alpha) + (E - E_l^\alpha)\dot{u}_l^\alpha(r_\alpha, E_l^\alpha) + \mathcal{O}\left((E - E_l^\alpha)^2\right), \tag{4.1}$$

the error due to the linearization should depend quadratically on the energy difference $E - E_l^\alpha$ between the energy E of a state and the energy parameter E_l^α. Here, we analyze this error in detail and evaluate different types of LOs to eliminate it.

We start this analysis with the definition of additional LOs and a first discussion on the energy dependence of solutions to the scalar-relativistic approximation (SRA) to the radial Dirac equation in section 4.1.1. Next, we provide a broad overview on the investigated materials and the parametrization of the calculations in section 4.1.2. In the succeeding step we discuss the linearization error in terms of an abstract representation error in section 4.1.3. Of course, this discussion involves the evaluation of the different LO extended basis sets on this level of abstraction. A discussion of the error and the different basis sets in terms of ground state properties, e.g. total energies and equilibrium lattice constants, of the materials is then provided in section 4.1.4. Finally, we also discuss the influence of the error on the Kohn-Sham band gap in section 4.1.5 and evaluate the impact of the basis set extensions on the required basis set size in section 4.1.6 before we conclude the discussion on the linearization error in section 4.1.7.

4.1.1 LO extensions and energy dependence of radial solutions

To eliminate the linearization error we consider extensions of the conventional LAPW basis with two different types of sets of LOs for the s, p, d, and f channels[2]. In the first variant [110], which we denote higher derivative local orbitals (HDLOs), the third radial function in the LOs is a higher order energy derivative of $u_l^\alpha(r_\alpha, E_l^\alpha)$. However, in the context of the elimination of the linearization error we restrict ourselves to a single additional set of LOs, constructed with the second energy derivative $\ddot{u}_l^\alpha(r_\alpha, E_l^\alpha)$. We denote this extension as HDLO×1. Note that the addition of $\ddot{u}_l^\alpha(r_\alpha, E_l^\alpha)$ to the radial functions within a MT sphere effectively enables a representation of the second order term in the Taylor expansion (4.1), such that the error in the representation of a wave function is reduced to the order $\mathcal{O}\left((E - E_l^\alpha)^3\right)$.

The second variant of LOs [103], already described in chapter 3.1.5, is constructed with solutions to the SRA to the radial Dirac equation $u_l^\alpha(r_\alpha, E_l^{\alpha,\mathrm{LO}})$, evaluated for energy parameters within the unoccupied bands, $E_l^{\alpha,\mathrm{LO}} > E_l^\alpha$. To choose these energy parameters, we consider the logarithmic derivative

$$D_l^\alpha(E) = \left.\frac{u'^\alpha_l(r_\alpha, E)}{u_l^\alpha(r_\alpha, E)}\right|_{r_\alpha = R_{\mathrm{MT}^\alpha}} \tag{4.2}$$

and enforce the condition $D_l^\alpha(E) = -(l+1)$. We denote these local orbitals as higher energy local orbitals (HELOs). Starting with the branch of the logarithmic derivative directly above the valence branch, for each additional set of HELOs we increase the number of nodes of $u_l^\alpha(r_\alpha, E_l^{\alpha,\mathrm{LO}})$ by one. The radial functions chosen in this way are orthogonal to each other and we consider adding one (HELO×1) or two (HELO×2) sets of local orbitals constructed in this way. The orthogonality ensures that the addition of more and more sets of HELOs do not yield a linearly dependent basis, but efficiently enables precise descriptions in broader and broader energy intervals. However, this aspect only gets important if many sets of LOs are used to describe very high lying unoccupied states. To describe the valence states the choice of other criteria for the energies of the HELOs may also be reasonable. In the limit $E_l^{\alpha,\mathrm{LO}} \to E_l^\alpha$ the extension of the basis by HELOs becomes equivalent to the extension by HDLOs, although numerical problems may preclude this way of realizing HDLOs.

Figure 4.1 sketches the behavior of the logarithmic derivative and the choice of the HELO energy parameters for the d-channel of fcc Ce. These curves can easily be understood since the radial solutions get more and more nodes when going from lower to higher energies. At some energy, a node enters the MT sphere at its boundary. Here, the value of the radial solution is zero, while it also has a finite slope. Thus, the logarithmic derivative at this energy is infinite. By going upwards in energy, one

[2] The extension by one set of LOs for s, p, d, and f yields 16 additional basis functions for the associated atom.

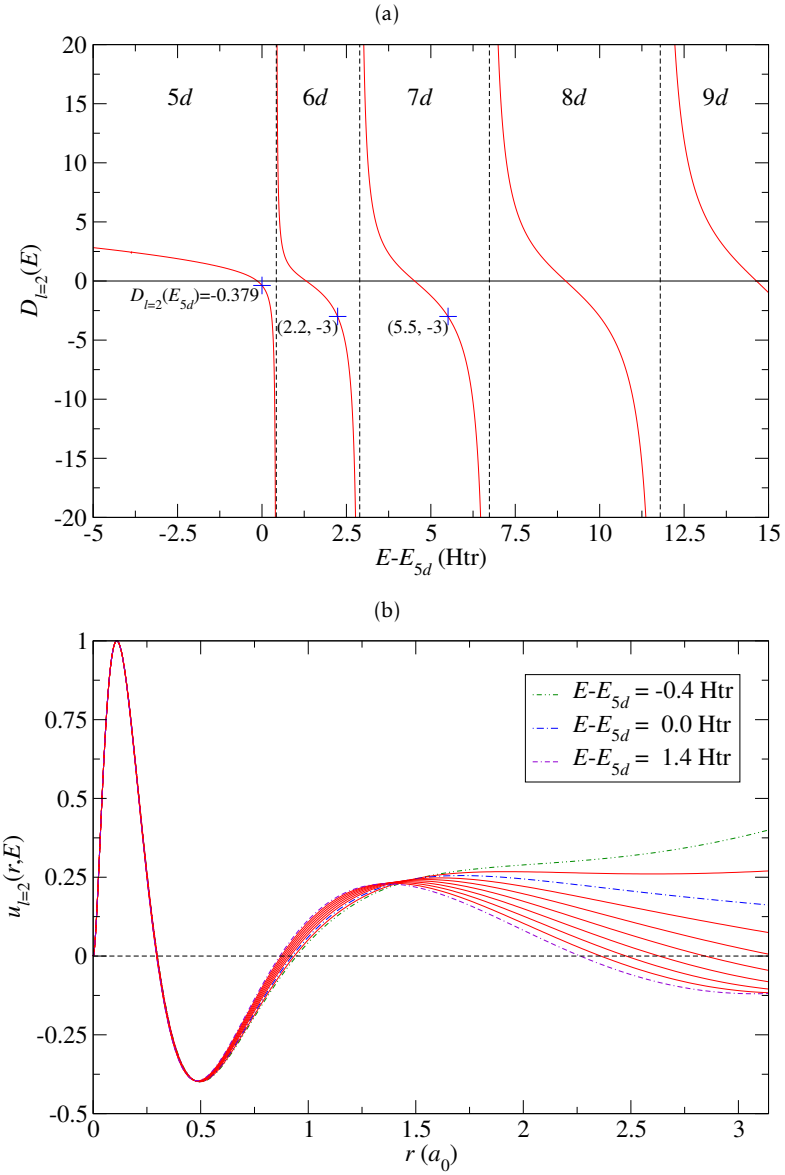

Figure 4.1.: Energy dependence of the logarithmic derivative and of the solutions $u_l^\alpha(r_\alpha, E)$ of the SRA to the radial Dirac equation for the d channel in fcc Ce. (a) Logarithmic derivative. The highlighted points mark the logarithmic derivative of the $5d$ valence band energy parameter E_{5d}, as well as the energies fulfilling the $D_l^\alpha(E) = -(l+1) = -3$ criterion for the construction of the HELO×1 and HELO×2 extensions to the LAPW basis. (b) Solutions $u_l^\alpha(r_\alpha, E)$ for different energies, sampled every 0.2 Htr between $E - E_{5d} = -0.4$ Htr and $E - E_{5d} = 1.4$ Htr. The solutions are scaled such that the first maximum of the curves coincides.

passes through a region where value and slope at the MT boundary have an identical sign, such that the logarithmic derivative is positive. Then, one reaches a point where the slope is zero, while the value of the radial solution at the MT boundary is finite. At this energy the logarithmic derivative becomes zero. Beyond this energy, value and slope of $u_l^\alpha(r_\alpha, E)$ at the MT boundary have opposite signs, such that one obtains a negative logarithmic derivative until another node enters the MT sphere.

We also observe another remarkable behavior in the energy dependence of $u_l^\alpha(r_\alpha, E)$. Near the atomic nucleus the qualitative behavior of the radial solutions does not depend on the energy. In figure 4.1(b) it is shown that the radial solutions can be scaled such that up to a distance of 0.5 a_0 nearly no difference can be seen between the solutions, although they cover a broad energy interval of 1.8 Htr. The main difference in this region comes through the norm of the solutions, which is strongly affected by the behavior in the outer parts of the MT sphere. The qualitative energy independence in the inner part of the sphere can be understood by recognizing that the behavior of the radial solutions in this region is strongly determined by the singularities of the effective potential and the angular momentum barrier at the atomic nucleus. A strong energy dependence, on the other hand, can be expected in regions where changes in the potential occur at an energy that is comparable to the energy of the radial solution. This is the case in the outer parts of the MT sphere.

4.1.2 Investigated materials and calculation parametrization

We investigate the linearization error and evaluate the different basis sets for a test set of materials for which we expect to see a significant impact of the error on calculated physical quantities. Under consideration of the observations on the energy dependence of radial solutions $u_l^\alpha(r_\alpha, E)$ in the previous section, we select materials with large MT radii to obtain a large region in the MT spheres in which the function's behavior is not dominated by the singularities at the atomic nucleus. In numbers, this means that we are interested in materials with MT radii of about 3 a_0. Furthermore, we consider materials that give rise to large deviations between the energy parameters and the eigenenergies of states affecting the investigated quantities. For example, the calculation of large Kohn-Sham band gaps implies a large difference between the valence band energy parameters and the lowest unoccupied state, which is also relevant for the calculation. Materials with very broad valence bands are another example for large discrepancies between the energy parameters and the eigenenergies of relevant states.

Furthermore, the materials are chosen such that their properties yield an increased sensitivity of the investigated quantities on imprecisions in the representation of the wave functions. For example, we investigate the impact of the linearization error on the equilibrium lattice constant for materials with a small bulk modulus.

Unless otherwise stated, the calculational parameters for the different materials are chosen such that the calculations with the conventional LAPW basis are converged

Table 4.1.: Calculational parameters for the materials considered for the analysis of the linearization error. The table first lists the applied exchange-correlation functional and the basic structural parameters, i.e., the crystal structures and the experimental lattice constants used for the calculations. In the middle section it lists the manually determined MT radii (R_{MT}), plane wave cutoffs as $K_{\max}R_{\mathrm{MT}}$ and resulting $\boldsymbol{k}$ point averaged number of LAPW basis functions per atom, angular momentum cutoffs $l^{\alpha}_{\max}$ for each atom, number of $\boldsymbol{k}$ points in the IBZ, and the included semicore LOs. The last section of the table covers the self-consistently determined atomic energy parameters relative to the Fermi level $E_l - E_{\mathrm{F}}$ for the conventional LAPW basis. For $l > 3$ the energy parameters are set to $E_{l=3}$.

parameter	Ce	KCl (K, Cl)	Ar	V
xc functional	PZ-LDA[3]	PZ-LDA	PZ-LDA	PZ-LDA
crystal structure	fcc	rock-salt	fcc	bcc
lattice constant (a_0)[4]	9.05	11.89	9.93	5.73
R_{MT} (a_0)	3.14	2.8, 2.8	3.15	2.41
$K_{\max}R_{\mathrm{MT}}$	13	13	13	10.845
LAPWs / atom	222	355	295	145
$l^{\alpha}_{\max}$	12	12, 12	10	10
$\boldsymbol{k}$ points in IBZ	182	60	60	190
semicore LOs	5s,5p	3s,3p (K)		
atomic energy parameters (eV)				
$E_{l=0} - E_{\mathrm{F}}$	−1.18	6.14, 11.95	−14.43	−3.34
$E_{l=1} - E_{\mathrm{F}}$	1.81	8.97, −0.39	−0.49	−0.22
$E_{l=2} - E_{\mathrm{F}}$	0.88	9.27, 10.88	14.78	0.05
$E_{l\geq 3} - E_{\mathrm{F}}$	0.73	15.63, 16.08	20.56	2.05

with respect to these parameters. Furthermore the MT radii are chosen such that the MT spheres nearly touch and the energy parameters are obtained with the atomic energy parameter (AEP) method. In detail, table 4.1 lists the parameters for the different materials.

The first investigated material is fcc cerium, which we primarily chose to compare to existing APW+lo calculations on this material [14]. However, Ce allows the usage of very large MT spheres and features a small bulk modulus. Thus, we expect to observe a significant linearization error with an impact on the calculated equilibrium lattice constant. For a first evaluation of the automatically determined energy parameters, figure 4.2 shows these parameters together with the Ce band structure along the high-symmetry lines K–Γ–L and the density of states (DOS) for this material.

The lower valence band edge for this material is of s character and about 3 eV

[3] PZ-LDA denotes the Perdew-Zunger parametrization of the local density approximation [31].

[4] The experimental lattice constants for Ce, KCl, Ar, and V were taken from [14], [128], [129], and [130], respectively.

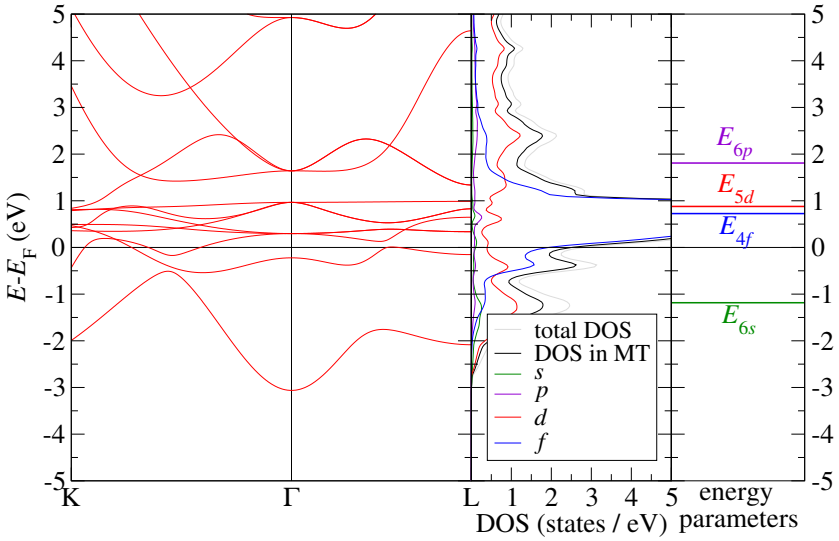

Figure 4.2.: Energy parameters for fcc Ce, obtained from a conventional LAPW calculation. The figure shows the energy parameters (right panel) together with the corresponding band structure along the high-symmetry lines K–Γ–L (left panel) and the density of states, projected onto the different l-channels up to $l = 3$ (center panel).

below the Fermi energy E_F. The values of the atomic energy parameters are well-chosen as these parameters all lie near the center of the associated bands with the same l character and within a range of a few eV of the occupied valence states.

KCl is the second material to be taken under scrutiny. It also allows the usage of large MT radii, which, for the sake of simplicity, we choose to be equal for K and Cl. KCl also has a small bulk modulus such that we expect to see an impact of the linearization error on the equilibrium lattice constant. Another quantity which we will investigate for this material is its large band gap of about 5 eV. Figure 4.3 shows the atomic energy parameters obtained for this material, together with its density of states. The band structure is discussed in detail in chapter 4.1.5. For the valence states, which are of Cl 3p character we again observe that the corresponding energy parameter is well-chosen. However, these states extend beyond the Cl MT sphere boundary into the MT sphere of K, where they give rise to DOS contributions of different d and f character. Such a situation is not covered by the construction of the AEPs and as a consequence, the K energy parameters required to describe the extension of these states into K are energetically far away.

The third material is Ar. Beyond the possibility to use large MT spheres, this material is of interest since it possesses a very large band gap and we expect to observe a significant impact of the large energy discrepancy between the energy parameters for the valence band and the lowest unoccupied state in this material. Figure 4.4

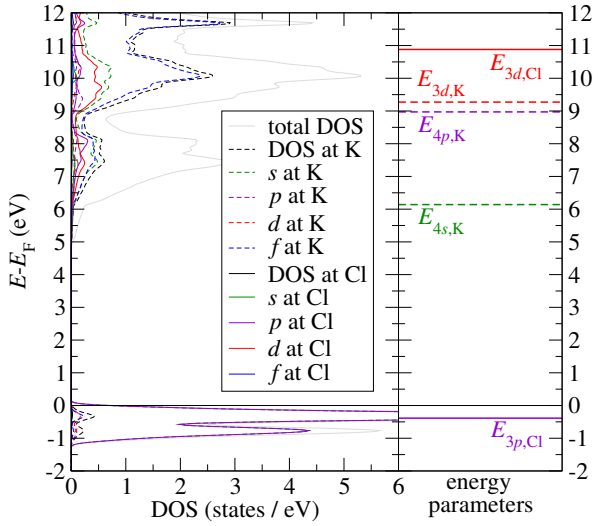

Figure 4.3.: Energy parameters for KCl in rock salt structure, obtained from a conventional LAPW calculation. The figure shows the energy parameters (right panel) together with the density of states, projected onto the different l-channels up to $l = 3$ (left panel).

shows the AEPs for this material together with its density of states. The band structure is discussed in detail in chapter 4.1.5. Similar to KCl, we observe that E_{3p} is very well-chosen to describe the $3p$ valence states. However, the lower band edge of the conduction band in this material is of $4s$ character, which is far away from the energy parameter for the s states at $E - E_F = -14.43$ eV, used to describe the $3s$ valence states.

For the last material, bcc V, we do not provide a detailed discussion on the choice of the energy parameters, since we will primarily use this material to demonstrate the projection of semicore states onto the different basis sets.

4.1.3 The linearization error as a representation error

Before we evaluate the consequences of the linearization error on calculated physical quantities, we discuss the error as an abstract representation error together with the capabilities of the different basis set extensions to eliminate the error on this abstraction level. We define the representation error for a normalized solution $u_l^\alpha(r_\alpha, E)$ of the SRA to the radial Dirac equation as

$$\Delta_l(E) = \|u_l - \tilde{u}_l\| = \left(\int r^2 \left[u_l^\alpha(r_\alpha, E) - \tilde{u}_l(r_\alpha, E) \right]^2 dr \right)^{\frac{1}{2}}, \tag{4.3}$$

where $\tilde{u}_l(r_\alpha, E)$ is the best representation of $u_l^\alpha(r_\alpha, E)$ by the radial functions of the considered basis set. It is obtained by projecting $u_l^\alpha(r_\alpha, E)$ onto the radial functions

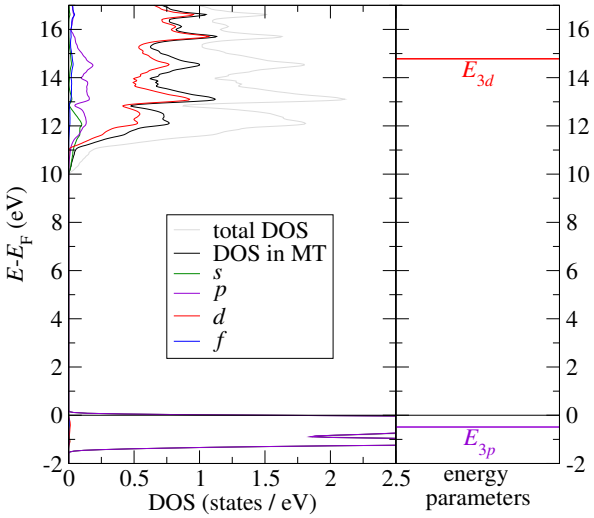

Figure 4.4.: Energy parameters for fcc Ar, obtained from a conventional LAPW calculation. The figure shows the energy parameters (right panel) together with the density of states, projected onto the different l-channels up to $l = 3$ (left panel).

of the basis. If $u_l^\alpha(r_\alpha, E)$ can be represented pointwise by the basis, the error $\Delta_l(E)$ becomes 0. On the other hand, if $u_l^\alpha(r_\alpha, E)$ is orthogonal to the function space spanned by the radial functions within the basis set, the error becomes 1.

Note that the error (4.3) is only defined for the MT part of the basis. This is reasonable since the IR part of the basis can systematically be extended by plane waves with ever higher kinetic energy, such that the representation in this region can be converged within the concept of the conventional LAPW basis. Depending on the investigated material and the considered Kohn-Sham orbital, the fraction of the wave function that is affected by the representation error varies. For example, valence d and f states are typically localized around the associated atom. As a consequence, a very large part of the wave function of such a state is within the MT sphere and only a small fraction is extended beyond the MT sphere boundary. On the other hand, in the limit of very high lying unoccupied states the form of the wave function is largely determined by the kinetic energy, while the potential only has a small effect. In an approximation the potential can be considered as constant for such states. The result is that in this limit the fraction of the wave functions within the MT spheres approaches the volume fraction of the MT spheres with respect to the whole unit cell. This fraction is typically between 30 percent in open structures like the zinc blende structure and 70 percent in closed structures like fcc oder hcp lattices with a single atom in the unit cell.

The representation error (4.3) also abstracts from the matching conditions at the MT sphere boundaries, which reduce the flexibility of the basis by limiting the pos-

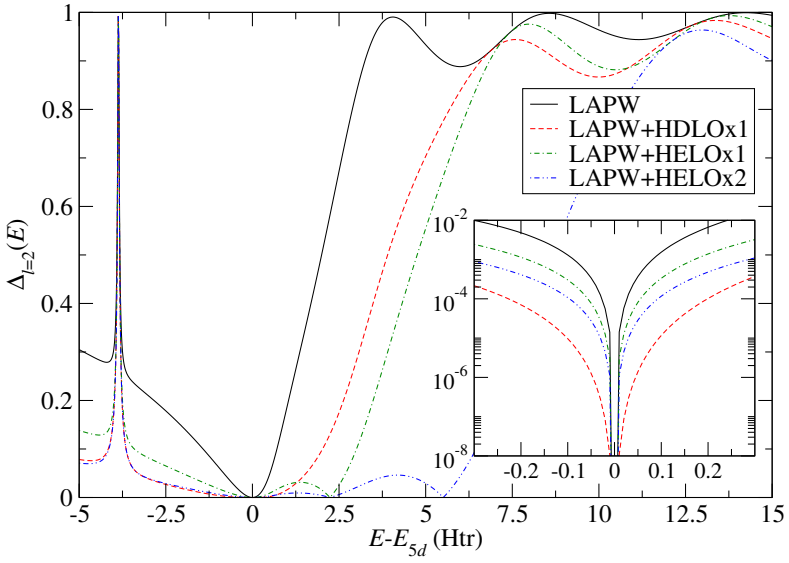

Figure 4.5.: Representation error $\Delta_{l=2}(E)$ for the d channel in fcc Ce. The peak of the representation error at $E - E_{5d} = -3.87$ Htr corresponds to the $4d$ core state, which is orthogonal to the evaluated basis sets since it is completely confined inside the MT sphere. The inset provides a detailed view on the behavior of the representation error for energies within a range of 0.3 Htr to the energy parameter E_{5d}. Note that the inset uses a logarithmic scale for the ordinate.

sible combinations of the radial functions used to represent $u_l^\alpha(r_\alpha, E)$. Due to the neglection of these conditions, the here defined representation error can be considered as a lower bound for the representations within the MT spheres by the complete LAPW basis and the here discussed extended basis sets. Note however that the Kohn-Sham wave functions are variationally determined. As a consequence, in practice the restrictions due to the matching are relaxed by allowing a part of the imprecision within the MT spheres to couple into the IR.

We discuss the energy dependence of the representation error $\Delta_l(E)$ for the d channel of fcc Ce. On the basis of a self-consistent solution for this material obtained with the conventional LAPW basis, we take the effective potential from this system and evaluate $\Delta_{l=2}(E)$ for the different basis sets in the vicinity of the atomic energy parameter for this channel E_{5d}. Figure 4.5 shows the representation errors with this setup for the different basis sets.

The valence states are typically within a range of a few eV around the energy parameters. With an energy interval of ± 0.3 Htr $\approx \pm 8$ eV around the energy parameter this range is covered by the inset of figure 4.5. We observe that the maximal error for the conventional LAPW basis in this interval is $1.5 \cdot 10^{-2}$. Extending the basis with LOs considerably reduces this error. Adding a single set of HELOs to the basis

yields a maximal error of $3.3 \cdot 10^{-3}$. Using two sets of these LOs gives us an even smaller maximal error of $1.1 \cdot 10^{-3}$. The best result, however, is obtained with the LAPW+HDLO×1 basis which features a maximal error of $3.8 \cdot 10^{-4}$. Compared to the conventional LAPW basis this is a reduction of the maximal error in this energy range by a factor of 40. Furthermore, the representation error for the HDLO extended basis exhibits a better scaling behavior in the vicinity of E_{5d}. Here, the error scales with $\mathcal{O}(|E - E_{5d}|^2)$ for the conventional LAPW basis, while it scales with $\mathcal{O}(|E - E_{5d}|^3)$ for the LAPW+HDLO×1 basis.

On the larger energy scale we observe that for high-lying unoccupied states, the representation error for the conventional LAPW basis quickly raises to values near 1. The HDLO extension slows this raise of the error. However, we can best control the error on this scale with the HELO extensions. Each set of HELOs makes additional radial functions $u_l^\alpha(r_\alpha, E_l^{\alpha,\mathrm{LO}})$ with ever higher energy parameters $E_l^{\alpha,\mathrm{LO}}$ available in the MT sphere. As a consequence, the representation error for the LAPW+HELO×1 and LAPW+HELO×2 basis sets vanishes at the energies of these parameters. For the d channel in the here discussed example these energy parameters are located at $E - E_{5d} = 2.23$ Htr for the first set of HELOs, and at $E - E_{5d} = 5.50$ Htr for the second set of HELOs. The representation error between the energy parameters of a HELO extended basis is typically rather small, such that we obtain a precise description of the valence states and the unoccupied states up to the highest energy parameter. Note that the quality of the description in this interval can further be controlled by adding more HELOs at energies that don't fulfill the here used logarithmic derivative criterion for the determination of the energy parameters. However, we remark that such HELOs are not orthogonal to each other.

In figure 4.5 we also observe a sharp peak of the representation error at $E - E_{5d} = -3.87$ Htr. This peak is due to the $4d$ core state which is completely confined within the MT sphere and therefore orthogonal to the function space spanned by the radial functions of the evaluated basis sets. We recall that the orthogonality of the core states to the valence basis is an important condition for the separate treatment of the core states in a fully relativistic framework. The sharp peak of the representation error for such states is therefore a desirable property.

Figure 4.6 shows the representation error for the p channel in bcc V. Here, the $3p$ semicore state at $E - E_{4p} = -1.7$ Htr is extended beyond the MT sphere boundary and therefore not orthogonal to the valence basis sets. The direct consequence is that this state does not yield a sharp, but only a shallow peak in the energy dependence of the representation error. In fact, the feature can be considered to be merely a shoulder. The representation of the semicore state by the different basis sets can be described as mediocre. For each of the considered basis sets the representation error is well below 1. On the other hand, in each case it is still significant and too large to obtain a precise description of the state by the tested basis sets within the valence electron framework.

Mediocre descriptions of semicore states are problematic since they may result in an appearance of the state as a ghost band somewhere in the energy range of the occupied valance states. For the tested basis sets, this problem only arises for the

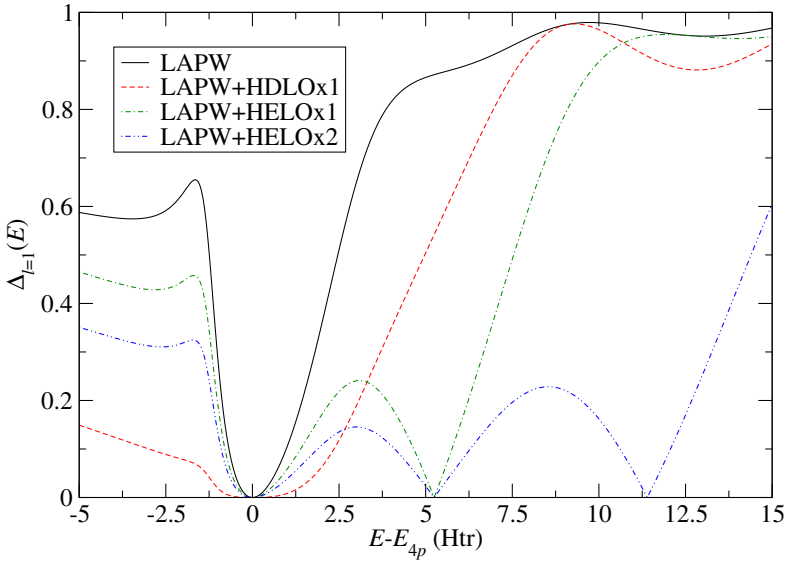

Figure 4.6.: Representation error $\Delta_{l=1}(E)$ for the p channel in bcc V. The $3p$ semicore state located at $E - E_{4p} = -1.7$ Htr is extended beyond the MT sphere boundary. As a consequence it is not orthogonal to the evaluated valence basis sets and the representation errors for this state by the different basis sets are considerably smaller than 1.

LAPW+HDLO×1 basis, where it precludes a successful self-consistent DFT calculation. For the other basis sets a self-consistent solution can be obtained. However, we note that the missing orthogonality of the valence states to the $3p$ state may affect the form and energy eigenvalues of the Kohn-Sham orbitals, such that one has to be cautious in the interpretation of the quantities obtained from such calculation. The solution to the problems arising from mediocre descriptions of semicore states is the extension of the basis by classical semicore LOs as proposed by Singh [9]. This provides a precise description of the semicore state by the valence basis. Nevertheless, we also mention that such a precise description can also be obtained by adding more and more HDLOs with ever increasing order of the energy derivative to the basis. Since more and more HDLOs systematically broaden the interval around the valence energy parameter in which precise descriptions of wave functions are obtained, at some point a precise description of the semicore state is also covered by this approach. However, this is a less efficient way of dealing with semicore states than the usage of classical LOs.

Beyond the appearance of a semicore state, the energy dependence of the representation error in figure 4.6 is qualitatively similar to the corresponding curves in figure 4.5. This demonstrates that the qualitative statements made for these curves are in fact independent of the respective material.

So far we have discussed the energy dependence of the representation error. This addresses the issue of the choice of the energy parameters, since different energy parameters yield different deviations from the Kohn-Sham valence eigenstates. Of course, energy parameters are determined self-consistently together with the ground state density. The MT radius is another parameter that also affects the representation error. However, this parameter cannot be automatically adapted between different FLAPW iterations, but has to be set in the run-up to the calculation.

Typically, one chooses the radii of the non-overlapping MT spheres to be as large as possible to reduce the volume of the IR such that only a small plane wave cutoff $K_{\max}$ is required. By doing this, one also reduces problems caused by semicore states reaching out of the MT sphere. However, in heterogeneous materials with more than one chemical element the choice of the MT radii is less straightforward. Here, the possible sizes of MT spheres from different atoms compete with each other and there is a tradeoff between the optimal MT spheres for the different atoms. For example, enlarging a MT sphere for one atom to ensure a high level of confinement of the core states may conflict with the confinement of core states in the MT sphere of another atom. The reduction of the IR volume is another objective that may be considered in such situations. One often used method to choose the MT spheres automatically is to determine their relative sizes according to tabulated atomic radii and expand them with this constraint until they are as large as possible. Nevertheless, such a choice of the MT radii is typically not optimal and one often has to modify the MT radii manually afterwards to ensure a well-behaved convergence of the FLAPW calculation.

Due to the different objectives in the choice of the MT radii it is desirable that calculation results are independent of these parameters. However, the linearization error in the MT spheres may preclude this behavior as it surely depends on the MT radii. We evaluate the MT radius dependence of the representation error for the different basis sets in figure 4.7 for the example of $5d$ states in fcc Ce at a fixed energy 0.1 Htr below the E_{5d} energy parameter. The effective potential used for these calculations was obtained through self-consistent calculations with the conventional LAPW basis for each MT radius. The plane wave cutoff $K_{\max}$ was adapted to each calculation to keep the product $K_{\max} R_{\mathrm{MT}}$ fixed to 13. In each calculation the energy parameters were chosen with the AEP method. All other numerical parameters are identical to those from the previous calculations on Ce.

Independent of the chosen basis, we observe that a reduction of the MT radius goes hand in hand with a reduction of the representation error. This is comprehensible as we have seen in figure 4.1(b) that the energy dependence of solutions of the SRA to the radial Dirac equation $u_l^\alpha(r_\alpha, E)$ is mainly localized in the outer parts of the MT sphere. In going from the largest to the smallest tested MT radius, the representation error for the conventional LAPW basis is reduced from $1.3 \cdot 10^{-3}$ to $2.5 \cdot 10^{-4}$. Of course, the HELO and HDLO extended basis sets generally suppress the representation error. As a consequence the dependence of the error on the MT radii takes place on a considerably lower level. The best result is once again obtained with the LAPW+HDLO×1 basis, for which the dependence of the error on the MT radii is reduced by two orders of magnitude in comparison to the conventional LAPW basis.

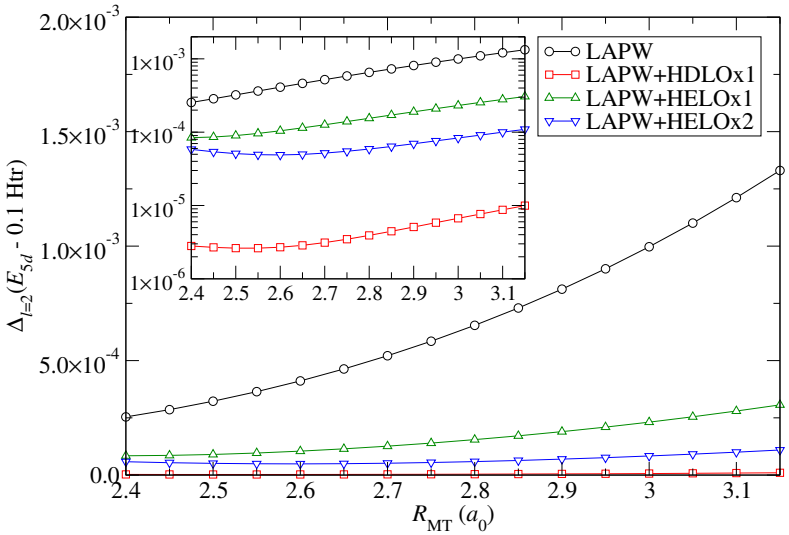

Figure 4.7.: Dependence of the representation error $\Delta_{l=2}(E_{5d} - 0.1\ \text{Htr})$ at a fixed energy $E_{5d} - 0.1$ Htr on the MT radius in fcc Ce. The inset shows the same dependence on a logarithmic plot.

4.1.4 The linearization error and physical properties

After discussing the linearization error as an abstract representation error in the previous section, we now turn to the evaluation of physical properties obtained from self-consistent FLAPW calculations with the different basis sets. In detail, we discuss the total energy E_{total}, as well as the equilibrium lattice constant a, which is obtained by fitting the Murnaghan equation of states [131] to a set of total energies calculated for different test lattice constants $\tilde{a}$. To assess the impact of the representation error on these calculated quantities, we explicitly investigate their dependence on the applied MT radii. If the linearization error is negligible for the calculation of these quantities, the results for the different basis sets and for the different MT radii should be almost identical. We also discuss the dependence of the total energy on the choice of the energy parameters, which also have a large influence on the linearization error.

In going from an isolated investigation on the linearization error for the spherical part of the effective potential in a MT sphere to the investigation of quantities obtained from self-consistent calculations, the demands on the basis set rise. As the self-consistent calculations are sensitive to the full LAPW basis and not only to the MT part, they are influenced by the reduction of the basis set flexibility imposed by the matching conditions at the MT sphere boundaries. Furthermore, the MT part of the basis has to represent the wave functions obtained for the full potential, although it is adapted solely to the spherical potential.

We start the discussion on the impact of the linearization error on physical quanti-

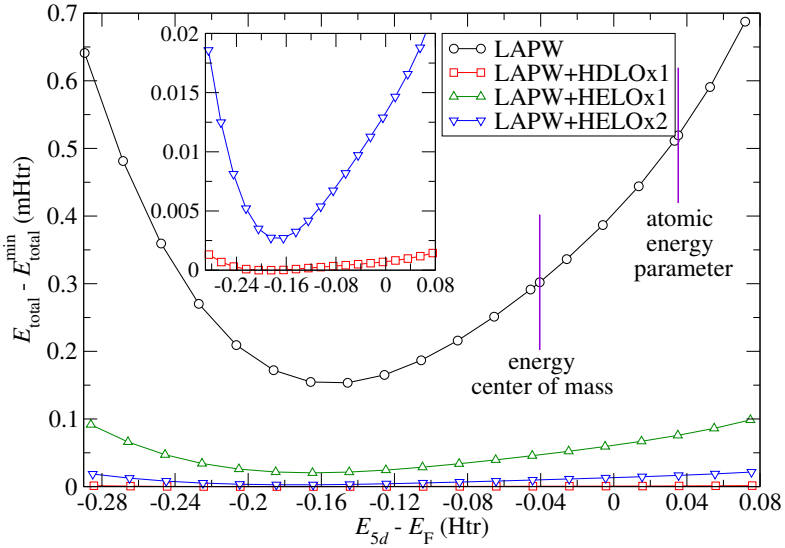

Figure 4.8.: Total energy of fcc Ce as a function of the $E_{l=2}$ energy parameter. The total energy is given relative to the minimal total energy $E_{\text{total}}^{\text{min}}$ obtained for this set of calculations, while the energy parameter is given relative to the Fermi level E_{F}. The energy parameters for the conventional LAPW basis as obtained automatically from the ECM and AEP methods are marked in the plot. The inset gives a detailed view for the two best performing basis sets, LAPW+HELO×2 and LAPW+HDLO×1. Note that the extended basis sets only include additional LOs for the d channel, such that the linearization error in the other l channels is not taken into account.

ties by investigating the dependence of the total energy on the choice of the d energy parameter in fcc Ce in figure 4.8. Beyond the energy parameter for the d channel all other numerical parameters in the underlying self-consistent calculations comply with the parameters in table 4.1. Furthermore, and as an exception for these calculations, the extended basis sets do not contribute full sets of LOs for $l = 0,\ldots,3$, but only LOs for the d channel. Thus, the shown results abstract from the linearization error in the other l channels.

In the calculations the energy parameter is varied between −0.29 and 0.08 Htr (≈ between −7.9 and 2.2 eV) relative to the Fermi energy. Within this interval we observe that the conventional LAPW basis yields a strong dependence of the total energy on the choice of the energy parameter of about 0.5 mHtr. This dependence can be reduced by several orders of magnitude by using an extended basis set. Here, the LAPW+HDLO×1 basis again offers the most favorable behavior with a variation of the total energy that is more than 2 orders of magnitude smaller than with the conventional LAPW basis.

Within the tested range of energy parameters we also observe an optimal energy parameter, which yields the minimal total energy for the respective basis. The posi-

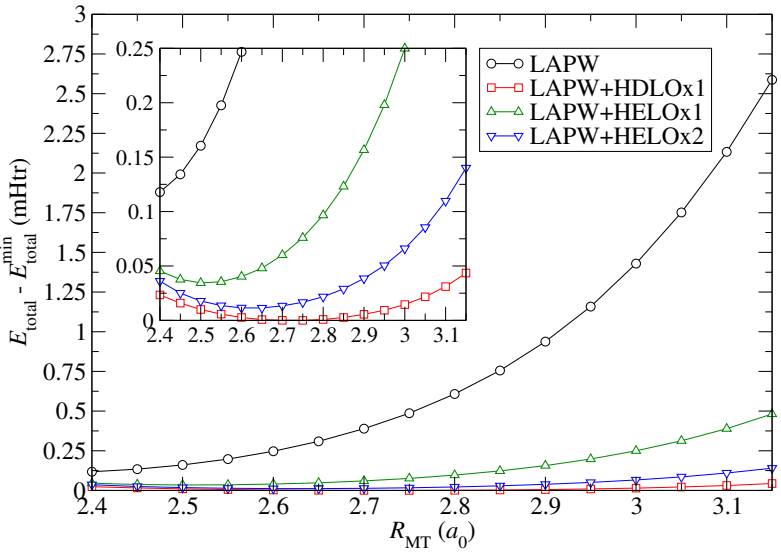

Figure 4.9.: Dependence of the ground state total energy of fcc Ce on the MT radius for different basis sets. All energies are given relative to the minimal total energy $E_{\text{total}}^{\text{min}}$ in this set of calculations. The inset provides a detailed view on the behavior of the LO extended basis sets. The best result is obtained for the LAPW+HDLO×1 basis, which nearly completely eliminates the here shown dependence.

tion of this optimal energy parameter only slightly depends on the basis set and is located at $E_{5d} - E_{\text{F}} = -0.16$ Htr. This is about 1.3 eV below the lower valence band edge. Note that for the conventional LAPW basis, this optimal energy parameter still yields energies which are more than 0.15 mHtr higher than the energies obtained with the LAPW+HDLO×1 basis. Thus, an optimization of the energy parameters for the conventional LAPW basis does not eliminate the consequences of the linearization error completely. Furthermore, neither the determination of the energy parameter with the ECM method ($E_{5d}^{\text{ECM}} - E_{\text{F}} = -0.04$ Htr) nor the determination with the AEP method ($E_{5d}^{\text{AEP}} - E_{\text{F}} = 0.04$ Htr) yields this optimal parameter. Both methods give rise to a significant increase of the linearization error, where the ECM method provides a slightly better parameter than the AEP method. In the case of the ECM method one may argue that the suboptimal choice of the energy parameter is due to the neglection of the semicore states which also contribute to the DOS of the considered l channel in MT spheres of atoms adjacent to the atom associated with the semicore state. However, this is not true. Comparative calculations show that the ECM energy parameter is shifted by only 0.01 Htr if the semicore states are included.

Beyond the dependence on the energy parameter, we already observed in chapter 4.1.3 that the linearization error strongly depends on the MT radii. Of course, the reduction of the MT radii is an option to reduce the linearization error. However, as

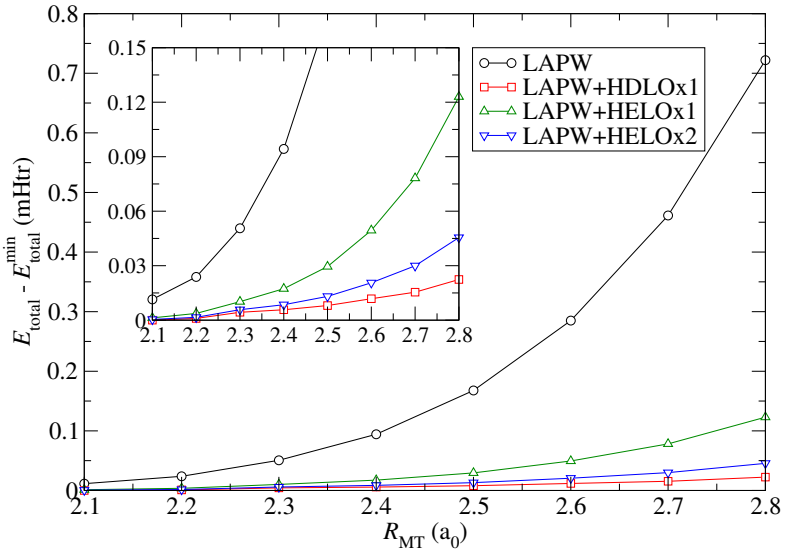

Figure 4.10.: Dependence of the ground state total energy of rock salt KCl on the MT radii for different basis sets. For simplicity the MT radii of K and Cl are chosen to be equal. All energies are given relative to the minimal total energy $E_{\text{total}}^{\text{min}}$ in this set of calculations. The inset provides a detailed view on the behavior of the LO extended basis sets. The best result is obtained for the LAPW+HDLO×1 basis, which nearly completely eliminates the here shown dependence.

already discussed, this approach involves an increase of the plane wave cutoff and thus the usage of considerably more LAPW basis functions. Here, we show that the dependence of the abstract representation error on the MT radii translates to a dependence of calculated physical quantities on this parameter. We perform calculations for fcc Ce and for KCl in rock salt structure. For both systems we vary the used MT radii while keeping the product $K_{\text{max}}R_{\text{MT}}$ constant. The energy parameters are automatically chosen with the AEP method. All other parameters are in accordance to table 4.1. Note that the representation of the 3*s* and 3*p* semicore states in K with classic semicore LOs together with a sophisticated elimination of the linearization error for the valence states by HELOs or HDLOs may cause problems when the MT radii are reduced. Especially in the case of HDLOs the basis becomes nearly linearly dependent for small MT radii. To avoid these problems we abstain from adding HELOs or HDLOs in the *s* and *p* channels of K.

Figures 4.9 and 4.10 show the dependence of the total energy on the MT radii for Ce and KCl, respectively. We observe that the conventional LAPW basis exhibits a strong dependence of this basic ground state property on the MT radii, while the LO extended basis sets suppress the dependence. The best result is once again obtained for the LAPW+HDLO×1 basis. For the largest MT sphere the conventional LAPW basis shows a deviation from the minimal total energy of more than 2.5 mHtr (0.7 mHtr)

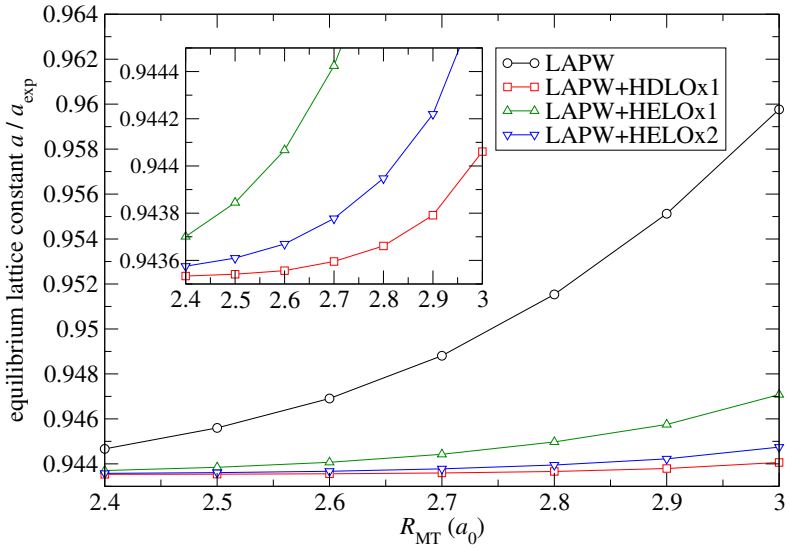

Figure 4.11.: Equilibrium lattice constant of Ce calculated with the different basis sets and plotted as a function of the MT radius. Each data point is obtained from a Murnaghan fit to the total energies of 15 test lattice constants $\tilde{a}$ between 0.938 a_{exp} and 0.966 a_{exp}. The inset shows a detailed view on the best results.

for Ce (KCl). This is reduced to about 0.12 mHtr (0.01 mHtr) by going to the smallest MT radii. For the LAPW+HDLO×1 basis the maximal deviation from the minimal value is less than 0.05 mHtr (0.03 mHtr), even for the largest MT radii. In the case of Ce we also observe that for very small MT radii the total energies obtained from the LO extended basis sets begin to rise again. This is due to the 4*d* core states that begin to reach out of the MT sphere.

Calculations on the equilibrium lattice constant do not rely on the total energy but on differences between total energies obtained for different test lattice constants $\tilde{a}$. Thus, one may argue that the consequences of the linearization error on the ground state total energy do not necessarily translate to imprecisions in the determination of the equilibrium lattice constant. In the optimal case the errors in the total energies will cancel each other. On the other hand one may also argue that a reduction of the test lattice constant $\tilde{a}$ goes hand in hand with an increase of the overlap of atomic states. As a consequence the band width increases and the description of the valence electrons has to cover a broader energy interval, such that the linearization error becomes larger. It is difficult to estimate the scale of these two effects and relate it to the precision required for calculations on the equilibrium lattice constant.

To obtain a more direct answer to the question to what extent the linearization error affects this derived quantity, we show the dependence of the equilibrium lattice constant on the MT radii in figures 4.11 and 4.12 for Ce and KCl, respectively. With a strong dependence for the conventional LAPW basis and nearly a complete

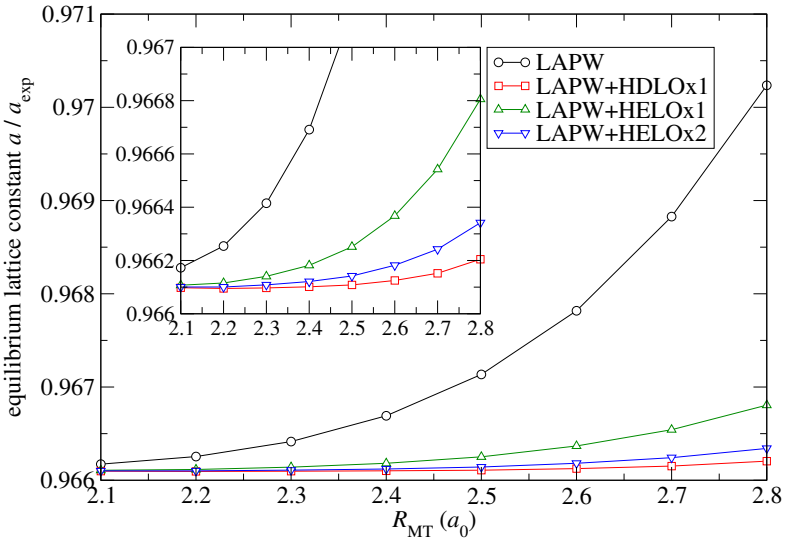

Figure 4.12.: Equilibrium lattice constant of KCl calculated with the different basis sets and plotted as a function of the MT radii. Each data point is obtained from a Murnaghan fit to the total energies of 9 test lattice constants $\tilde{a}$ between 0.958 a_{exp} and 0.974 a_{exp}. The inset shows a detailed view on the best results.

elimination of this dependence with the HDLO×1 extended basis, these plots paint a similar picture as the previous observations. In detail, for the conventional LAPW basis the result for the largest MT radii deviates by more than 1.6 % (0.4 %) for Ce (KCl) from the best result obtained with the LAPW+HDLO×1 basis. When going to the smallest MT radii this deviation is reduced to about 0.1 % (0.01 %). With the LAPW+HDLO×1 basis the change of the calculated equilibrium lattice constant when moving from large to small MT radii are about 0.06 % (0.01 %). Note that the imprecisions of about 1% obtained with the conventional LAPW basis are in the same ballpark as the inaccuracies due to the limitations of commonly used exchange correlation functionals. Thus, with the rise of more sophisticated functionals in the future, the elimination of the linearization error will become more and more important.

We learn from the observations on the equilibrium lattice constant that a possible error cancellation of the linearization error between different structural configurations does not eliminate the need to carefully converge the MT sphere representation of the basis functions. Beyond the lattice relaxation performed here, this result for calculated total energies is also applicable for the optimization of atom positions in a given unit cell with fixed volume.

To put the elimination of the linearization error by using LO extended basis sets in context to a possible elimination by a reduction of the MT radii, we note that each set of LOs for $l = 0,\ldots,3$ contains 16 additional basis functions. On the other hand, for the conventional LAPW basis, a reduction of the MT radii from 3.15 a_0 (2.8 a_0) to

2.4 a_0 (2.1 a_0) in the here performed total energy calculations increases the number of LAPW basis functions per atom averaged over all $\boldsymbol{k}$ points from 220 (354) to 499 (841) for Ce (KCl). Note however that these generally high numbers are due to the choice of very high $K_{\max}R_{\mathrm{MT}}$ of 13 (13) to ensure well converged representations in the IR. On the other hand the proportion between the number of basis functions for the different MT radii depends on $K_{\max}^3$. Thus, a reduction of the MT radii implies a cubic growth of the number of basis functions. In the here used examples this more than doubles the number of basis functions when going from the largest to the smallest MT radii, irrespective of the concrete $K_{\max}R_{\mathrm{MT}}$. Assuming a typical basis set size of about 80 LAPWs per atom for large MT radii, it is clear that an elimination of the linearization error with LO extended basis sets is much more efficient than a reduction of the MT radii.

4.1.5 The linearization error and the Kohn-Sham band gap

For semiconductors and insulators an often investigated quantity is the Kohn-Sham band gap. Since this quantity is calculated as the difference between the energies of the lowest unoccupied and the highest occupied band, the basis functions have to represent not only the bands required to obtain a precise ground state density, but also the lowest unoccupied bands. With respect to the construction of the LAPWs this is a fundamental difference. The energy parameters are typically chosen such that a precise representation of the occupied states is enabled. This does not guarantee a precise representation of the lowest unoccupied states. In fact, the states in these different energy intervals may differ in fundamental properties like, for example, the main quantum number.

To evaluate the conventional and extended basis sets for the lowest unoccupied states we calculate the band structures of rock salt KCl and crystalline Ar along the high symmetry lines K–Γ–L. The parametrization of these calculations is given in table 4.1. For the conventional LAPW basis, as well as for LAPW+HDLO×1, figures 4.13 and 4.14 show the band structures of KCl and Ar, respectively. Note that the LAPW+HELO×1 and LAPW+HELO×2 basis sets yield band structures that lie on top of the LAPW+HDLO×1 result, at least in the energy interval and on the energy scale of the figures. When going to very high unoccupied states, extending the basis with HELOs is a more efficient means of obtaining precise eigenenergies than the extension with HDLOs.

However, we are especially interested in the energy interval shown in the figures. On the shown energy scale we note that the eigenenergies of the occupied states calculated with the conventional LAPW basis lie on top of the energies obtained with the HDLO×1 extended basis. Contrary to this nice agreement, the eigenenergies of the unoccupied states partially strongly differ between the two basis sets. Depending on the l character of the respective unoccupied band and the value of the energy parameter for this l, the two basis sets either agree or disagree on the eigenenergies.

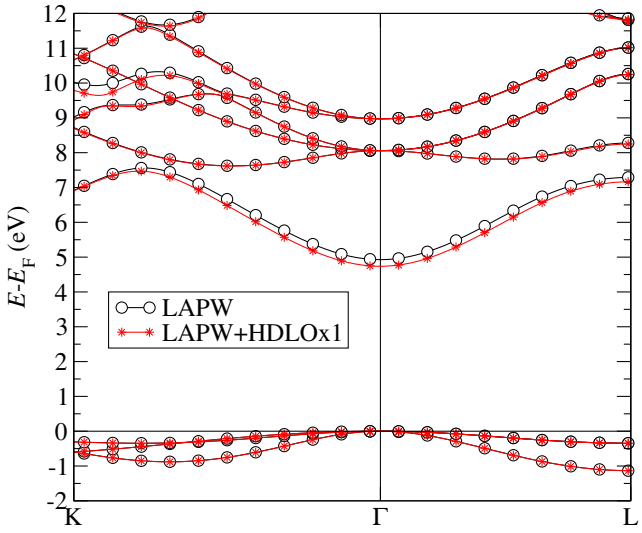

Figure 4.13.: Band structure of KCl for the conventional LAPW basis, as well as for the LAPW+HDLO×1 basis as a representative of an LO extended basis. In the shown energy interval and with the energy resolution of this graph, the band structures obtained with the LAPW+HELO×1 and LAPW+HELO×2 basis sets are indistinguishable from the LAPW+HDLO×1 result.

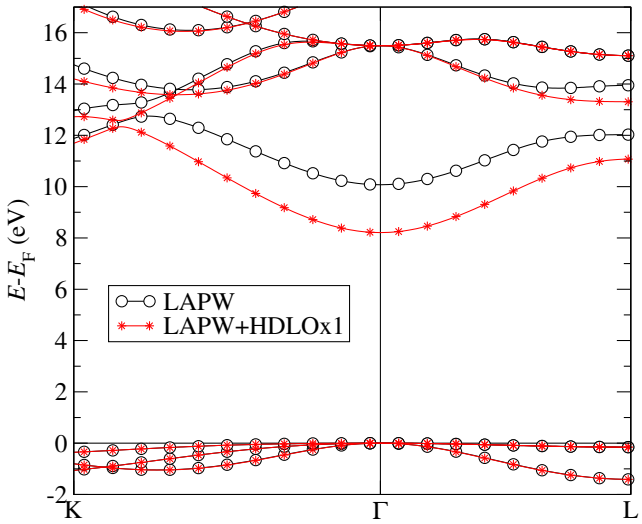

Figure 4.14.: Band structure of Ar for the conventional LAPW basis, as well as for the LAPW+HDLO×1 basis as a representative of an LO extended basis. In the shown energy interval and with the energy resolution of this graph, the band structures obtained with the LAPW+HELO×1 and LAPW+HELO×2 basis sets are indistinguishable from the LAPW+HDLO×1 result.

Both materials, KCl and Ar, possess a direct band gap at the Γ point. We evaluate the precision of the calculations on this band gap. For the conventional LAPW basis these band gaps are 4.93 eV (10.07 eV) for KCl (Ar). By extending the basis with HDLOs the better representation of the lowest unoccupied bands causes a lowering of their eigenenergies. As a consequence the band gaps shrink by 0.19 eV (1.87 eV) to 4.74 eV (8.20 eV). This is a reduction of the band gaps of 4% (19%). Thus, the effects of the linearization error on this quantity are even larger than the effects on the equilibrium lattice constant. Note also that in going to even higher energies, the representation of the unoccupied states by the conventional LAPW basis gets worse and worse. Hence, the very common extension of the LAPW basis by LOs in the context of methods that rely on the unoccupied bands, e.g., in the optimized-effective potential method [103] or in the GW approximation [132], is very reasonable.

4.1.6 Basis set size convergence for the different basis sets

The matching of values and slopes of the LAPW basis functions at the MT sphere boundaries couple the shapes of the basis functions in the different regions of the unit cell strongly to each other. The result is a reduced flexibility of the basis. As a consequence, to fully cover the function space spanned by the radial functions in the MT spheres, large plane wave cutoffs $K_{\max}$ have to be applied. The introduction of the APW+lo method by Sjöstedt *et al.* [14] relaxed the matching at the MT sphere boundaries by dropping the condition for the basis function's slope and using only the radial functions $u_l^\alpha(r_\alpha, E_l^\alpha)$ for the matching. For low l the $\dot{u}_l^\alpha(r_\alpha, E_l^\alpha)$ were included in terms of a new type of local orbitals constructed with $u_l^\alpha(r_\alpha, E_l^\alpha)$ and $\dot{u}_l^\alpha(r_\alpha, E_l^\alpha)$ and featuring zero value but also a finite slope at the MT boundaries. The resulting kinks in the basis functions were compensated by introducing an additional term in the construction of the Hamilton matrix, which quantifies the disadvantage of these kinks in the kinetic energy.

The decoupling of the different regions by a relaxation of the matching conditions is highly efficient. Nevertheless, one may ask if the extension of the conventional LAPW basis with LOs yields a similar effect. After all, the additionally used radial functions for the HELOs and HDLOs not only widen the energy interval of precisely representable wave functions. They are also not orthogonal to $u_l^\alpha(r_\alpha, E_l^\alpha)$ and $\dot{u}_l^\alpha(r_\alpha, E_l^\alpha)$, so that they provide an alternative way of representing wave function features that are also representable with $u_l^\alpha(r_\alpha, E_l^\alpha)$ and $\dot{u}_l^\alpha(r_\alpha, E_l^\alpha)$. In this section we test the hypothesis that the LO extended basis sets provide a similar decoupling of the different unit cell regions as APW+lo for the example of fcc Ce.

To compare the different basis sets with respect to this aspect, figure 4.15 shows the respective convergence of the total energy of fcc Ce with respect to the plane wave cutoff $K_{\max}$ given by the product $K_{\max} R_{\mathrm{MT}}$, where $R_{\mathrm{MT}} = 3.14\ a_0$. Beyond the already well-known conventional LAPW basis set and the LO extended basis sets, we also provide results for APW+lo and a HELO×1 extended version of this basis.

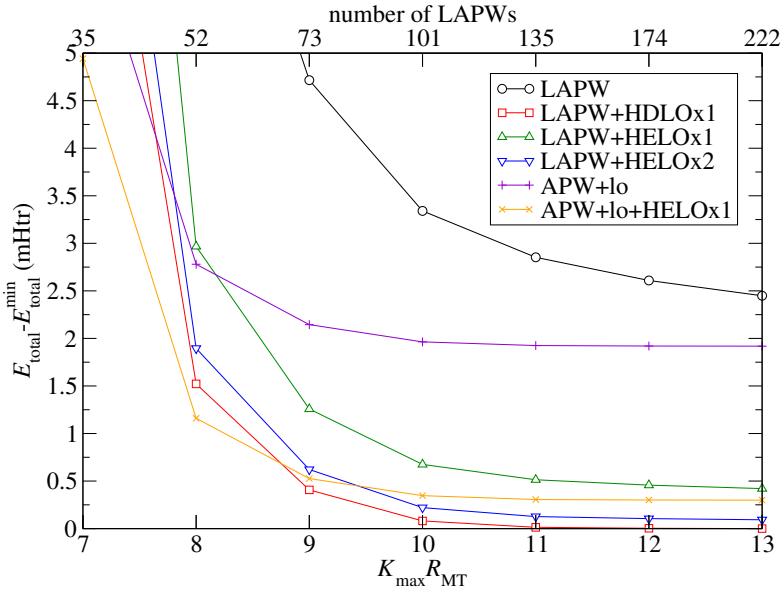

Figure 4.15.: Convergence of the total energy of fcc Ce with respect to $K_{\max}R_{\mathrm{MT}}$ for different basis sets. All total energy results are given relative to the minimal total energy $E_{\mathrm{total}}^{\min}$ in this set of calculations. The upper abscissa provides the $\boldsymbol{k}$ point averaged number of LAPW basis functions beyond any type of local orbitals. To obtain the complete number of basis functions the number of semicore LOs (4) has to be added. Furthermore the local orbital extended basis sets increase the number of basis functions by 16 (LAPW+HELO×1, LAPW+HDLO×1, APW+lo) or 32 (LAPW+HELO×2, APW+lo+HELO×1).

Note however that the here used realization of APW+lo deviates from the original idea as we follow the approach of Madsen *et al.* [15] to perform a conventional LAPW matching for l quantum numbers beyond the maximal $l = 3$ of the applied APW+lo style local orbitals.

In interpreting the results from the figure we first note that for very high $K_{\max}R_{\mathrm{MT}}$ the LAPW and APW+lo basis sets converge to the same total energy since they span the same function space in this limit. An equivalent statement can also be made for the LAPW+HELO×1 and the associated APW+lo+HELO×1 basis sets. However, at the cost of an additional set of local orbitals, the APW+lo type basis sets offer a much more efficient convergence behavior in comparison to their LAPW counterparts.

Nevertheless, both, the conventional LAPW and APW+lo basis sets, exhibit a significant linearization error, such that the elimination of this error with additional LOs is mandatory. As already seen in different tests, the LAPW+HDLO×1 basis exhibits the lowest and most precise total energies. We also observe that the addition of LOs to the conventional LAPW basis yields a more friendly convergence behavior

in the sense that the respective converged total energy is approached faster when rising $K_{\max}R_{\mathrm{MT}}$. This is very similar to the more efficient convergence behavior of the APW+lo basis, although the reduction of the required $K_{\max}R_{\mathrm{MT}}$ is larger for APW+lo. Within the set of LO extended LAPW basis sets, the best convergence behavior is obtained with the LAPW+HDLO×1 basis. When comparing the APW+lo+HELO×1 basis to the APW+lo basis we also observe that APW+lo does not profit from the additional LOs in the same way as LAPW. While the linearization error is also reduced for APW+lo, the already very good decoupling of the different regions in the unit cell is not increased in a comparable way. In fact, for the shown example, the curves for APW+lo and APW+lo+HELO×1 are only shifted by a constant energy with respect to each other.

To complete the discussion on the convergence behaviors, we mention in passing that the permission of a kink in APW+lo basis functions also transfers to a kink in the wave functions, although to a far lesser extent. A kinkless wave function possesses exactly the same matching between the radial functions and the linear combination of plane waves at the MT boundaries that is also obtained in terms of LAPWs. Thus, every kinkless wave function that is given by plane waves in the interstitial and the given radial functions in the MT spheres, is pointwise representable by LAPWs. As a consequence, whenever an APW+lo calculation yields a lower total energy than an LAPW calculation with the same plane wave cutoff parameter, a kink is retained in the wave functions. From a physical point of view this is unsatisfying as it implies a singular kinetic energy density at the MT sphere boundaries.

4.1.7 Concluding remarks on the linearization error

The here presented discussion shows that there are materials for which conventional FLAPW calculations suffer from the linearization error, which is due to the restriction to the radial functions $u_l^\alpha(r_\alpha, E_l^\alpha)$ and $\dot{u}_l^\alpha(r_\alpha, E_l^\alpha)$ in the MT spheres. We demonstrated that the consequences of this error can be in the same ballpark as inaccuracies due to the approximation to the exchange correlation functional. To eliminate the linearization error we evaluated two ways of extending the conventional LAPW basis with LOs. The first type of local orbitals, HELOs, are constructed with $u_l^\alpha(r_\alpha, E_l^{\alpha,\mathrm{LO}})$, evaluated at energies within the unoccupied bands. Of course, this type of LOs is very efficient in eliminating the linearization error for the unoccupied states. As a consequence, it is often used in the context of methods that rely on a precise representation of these states. Beyond this, we saw that HELOs also effectively reduce the linearization error for the valence states. The second type of evaluated LOs, HDLOs, are constructed with the second energy derivative $\ddot{u}_l^\alpha(r_\alpha, E_l^\alpha)$. These LOs performed even more efficient in eliminating the linearization error. In comparison to the conventional LAPW basis the addition of these LOs reduced the representation error by several orders of magnitude. The very desirable outcome of this improvement is that calculations become much more precise and also stable with respect to numerical parameters like MT radii or energy parameters.

The inclusion of additional LOs might not always be necessary. Nevertheless, the present results show that LOs can be an important ingredient when converging FLAPW calculations with respect to the basis set. Thus, the elimination of the linearization error through the extension of the LAPW basis with LOs should by part of this calculation parametrization routine. Especially in foresight of new challenges arising due to calculations with more sophisticated exchange correlation functionals on ever more complex materials this is an important statement. Furthermore, the gain in calculation stability with respect to the parametrization ensures comparability between different calculations.

Beyond the elimination of the linearization error, additional LOs also contribute to the decoupling of the wave function representation in the different regions of the unit cell. Thus, they imply a reduction of the required plane wave cutoff $K_{\max}$, which yields a lower number of conventional LAPWs. So, as a side aspect the elimination of the linearization error with LOs may also reduce the required basis set size. Nevertheless, we remark that an even better decoupling of the different regions is obtained with the APW+lo method, although without addressing the linearization error.

4.2 General properties of the basis functions and the wave functions

After analyzing the linearization error that originates in the MT spheres, we proceed by taking a closer look at the properties of the LAPW basis functions in the whole unit cell and compare them to the properties of wave functions. In section 4.2.1 we are especially interested in the matching conditions at the MT sphere boundaries, which are given by the interstitial part of the functions. A comparison between the matching conditions for the two sets of functions is important since the shape of the basis functions in the MT spheres is strongly influenced by these conditions. An efficient basis set should provide exactly those interstitial features and MT matching conditions, which are also required by the wave functions. Systematic deviations between the shapes of the basis functions from the wave functions manifest in a large number of basis functions that are required to compensate for unphysical properties of single basis functions.

The chapter continues with an investigation on the changes of the effective potential and the basis functions in the MT spheres throughout the iterations of the self-consistency cycle in section 4.2.2. Of course, the changes of the MT part of the basis functions strongly depend on the changes of the potential in that region. Small changes in potential and basis functions may open the path to speed up the calculations by precalculating certain quantities. Furthermore, small changes in the potential also result in small changes of the wave functions throughout the self-consistency cycle. To analyze the changes of the wave functions in more detail, we explicitly measure and evaluate these changes in the interstitial region in section 4.2.3.

We investigate the mentioned properties of the functions for a test set of materials,

Table 4.2.: Calculational parameters for the materials considered for the analysis of the different basis function and wave function properties. The table first lists the applied exchange-correlation functional and the basic structural parameters, i.e., the crystal structures and the experimental lattice constants used for the calculations. In the middle section it lists the manually determined MT radii (R_{MT}), plane wave cutoffs $K_{\max}$ and resulting $\boldsymbol{k}$ point averaged number of LAPW basis functions per atom, angular momentum cutoffs $l^{\alpha}_{\max}$ for each atom, as well as the reduced cutoffs $l^{\alpha,\mathrm{nsphr}}_{\max}$, number of $\boldsymbol{k}$ points in the IBZ, and the included semicore LOs. The last section of the table covers the self-consistently determined atomic energy parameters relative to the Fermi level $E_l - E_{\mathrm{F}}$. For $l > 3$ the energy parameters are set to $E_{l=3}$.

parameter	Cu	SiC (Si, C)	NaCl (Na, Cl)
XC functional	PBE-GGA[5]	PBE-GGA	PBE-GGA
crystal structure	fcc	zinc blende	rock-salt
lattice constant (a_0)[6]	6.831	8.238	10.620
R_{MT} (a_0)	2.35	2.22, 1.25	2.52, 2.52
$K_{\max}$ (a_0^{-1})	4.5	5.5	4.0
LAPWs / atom	123	196	162
$l^{\alpha}_{\max}$	8	10, 8	8, 8
$l^{\alpha,\mathrm{nsphr}}_{\max}$	6	6, 4	6, 6
$\boldsymbol{k}$ points in IBZ	182	220	28
semicore LOs			2*s*,2*p* (Na)
atomic energy parameters (eV)			
$E_{l=0} - E_{\mathrm{F}}$	−3.75	−9.22, −20.36	6.06, −12.41
$E_{l=1} - E_{\mathrm{F}}$	0.36	−4.28, −15.31	9.36, −0.93
$E_{l=2} - E_{\mathrm{F}}$	−2.61	0.96, −9.95	13.27, 9.86
$E_{l\geq 3} - E_{\mathrm{F}}$	9.26	5.52, −5.61	17.77, 14.94

which provide different properties of the wave functions in the IR and thus different demands on the basis set. In detail we look at the metallically bonded fcc Cu, zinc blende SiC as a material with covalent bonds, and NaCl as an ionically bonded material. Table 4.2 shows the parametrization of the underlying calculations on these materials.

[5] PBE-GGA denotes the Perdew-Burke-Ernzerhof parametrization of the generalized gradient approximation [37].

[6] The experimental lattice constants for Cu, SiC, and NaCl were taken from [133], [134], and [135], respectively.

4.2.1 MT matching conditions

We start the discussion on the matching conditions by reminding that the values of the basis functions at the MT sphere boundaries are given by Rayleigh expansions (cf. equation (3.38))

$$\frac{1}{\sqrt{\Omega}} e^{i\boldsymbol{K}\boldsymbol{r}} = \frac{4\pi}{\sqrt{\Omega}} e^{i\boldsymbol{K}\boldsymbol{\tau}_\alpha} \sum_L i^l Y_L^*(\hat{\boldsymbol{K}}) j_l(Kr_\alpha) Y_L(\hat{\boldsymbol{r}}_\alpha) \Big|_{r_\alpha = R_{\mathrm{MT}^\alpha}}, \tag{4.4}$$

where $K = |\boldsymbol{k} + \boldsymbol{G}|$. One immediately sees that the $L = (l, m)$ decomposed values of the functions are mainly determined by the behavior of the spherical Bessel functions $j_l(Kr_\alpha)$ at $r_\alpha = R_{\mathrm{MT}^\alpha}$. Of course, the same observation can be made for the radial derivatives of the basis functions at this boundary.

For a first estimation of the values of the LAPW basis functions in the different l channels at the MT boundaries, we show the spherical Bessel functions for $l \leq 8$ in figure 4.16. We see that for small Kr the spherical Bessel functions exhibit the well known behavior $j_l(Kr) \propto (Kr)^l$. In consequence, for small Kr the values for high l nearly vanish. This drastically changes for higher $Kr > 2$. With growing Kr the spherical Bessel functions of more and more l channels possess values which substantially deviate from zero. Together with the oscillatory form of the $j_l(Kr)$ this quickly breaks the dominance of the lower l channels ($l \leq 3$).

This behavior can also be seen in the matching conditions of LAPW basis functions in fcc Cu, illustrated in figure 4.17. The figures show that for both, the absolute values $|\phi_{\boldsymbol{k}\boldsymbol{G}}(r_\alpha = R_{\mathrm{MT}})|$ and the absolute values of the radial derivatives $|\phi'_{\boldsymbol{k}\boldsymbol{G}}(r_\alpha = R_{\mathrm{MT}})|$, the magnitude is mainly determined by the angular momentum l and hence by the spherical Bessel function $j_l(KR_{\mathrm{MT}})$. On the other hand, the magnetic quantum number m gives smaller deviations from this general magnitude.

Comparing the matching behavior of the different LAPW basis functions, we observe that for very small K only the l channels for small l make significant contributions to the values and radial derivatives of the functions. However, this changes quickly when K gets larger. Even for the very moderate $K = 2.57\ a_0^{-1}$ the dominance of the small l is completely broken. This is especially of importance if one considers the number of LAPW basis functions within some K interval. As the number of LAPW basis functions scales cubically with K_{max}, only very few LAPWs provide a clear dominance of the lower l channels. On the other hand, most of the basis functions feature significant contributions from all l channels considered in this discussion.

We compare this behavior of the LAPW matching conditions in the different l channels to the corresponding behavior of the lowest valence wave functions. For an arbitrary $\boldsymbol{k}$ point, figure 4.18 shows the matching conditions of the occupied valence wave functions in fcc Cu. Of these wave functions, $\psi_{\boldsymbol{k}}^1$ to $\psi_{\boldsymbol{k}}^5$ have $3d$ character, while $\psi_{\boldsymbol{k}}^6$ has $4s$ character. Of course, we consider a crystal with a single atom in the unit cell such that this character cannot be directly observed. For example, the $3d$ states are extended into neighboring unit cells and give contributions to the matching in

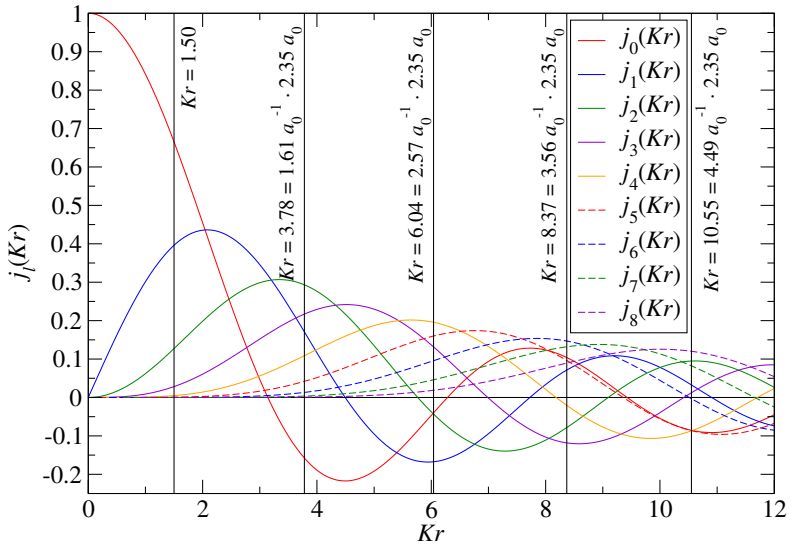

Figure 4.16.: Spherical Bessel functions $j_l(Kr)$ for $l \leq 8$ in the range $0 < Kr < 12$. The figure highlights the values of the different $j_l(Kr)$ for a radius of $r = 2.35\ a_0$ and a set of different K. The choice of the highlighted values is motivated by the matching to the MT sphere in fcc Cu (cf. figure 4.17).

different l channels at the MT boundaries in those cells. Thus, one obtains a superposition of matching conditions for equivalent atoms within a small neighborhood of unit cells. Nevertheless, we observe that the contributions to the matching conditions are clearly dominated by the low l channels. Higher l are suppressed. We note that this behavior of the matching conditions of the wave functions clearly deviates from the corresponding conditions of the majority of the LAPW basis functions.

One may wonder to what extend this observation is transferable to materials with other interstitial properties. We answer this question by providing the matching conditions of the lowest valence wave functions in SiC and NaCl. For SiC figure 4.19 shows the matching conditions of the lowest wave functions above the core states at the Si MT boundary, while figure 4.20 shows the matching at the MT boundary of C. Just like the trend observed in fcc Cu, also the MT matching of the wave functions in SiC is dominated by the lower l channels. This behavior is especially visible in C, although we have to keep in mind that this is also influenced by the very small MT sphere of C with $R_{\mathrm{MT}} = 1.25\ a_0$. Of course, a comparison with the spherical Bessel functions (cf. figure 4.16) shows that small MT radii also yield matching conditions that are dominated by low l channels for LAPW basis functions with larger K.

For NaCl figure 4.21 shows the MT matching for Na and figure 4.22 the matching for Cl. Due to the ionic bonding in this material the wave function matching at the MT spheres is much more l channel specific than in the previously investigated materials. This can easily be seen when associating the different considered wave

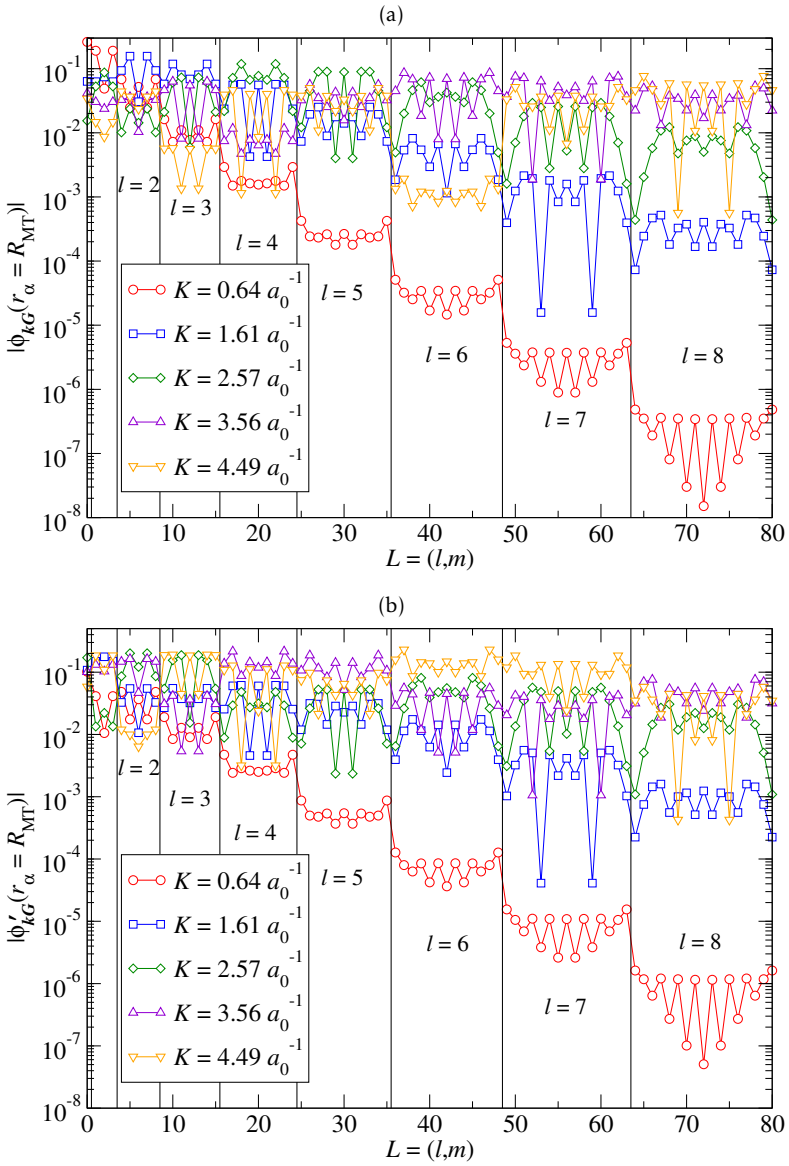

Figure 4.17.: Matching conditions at the MT boundary for a test set of LAPW basis functions in fcc Cu. Figure (a) shows the values of the functions, while (b) shows the radial derivatives. The chosen LAPW basis functions for an arbitrary $\boldsymbol{k}$ point give an impression on the whole range of $K < K_{\max}$. The index on the abscissa is given by $L = l^2 + l + m$. For each l the associated values are marked in the figures, although for $l = 0$ and $l = 1$ the denotation has not been done explicitly.

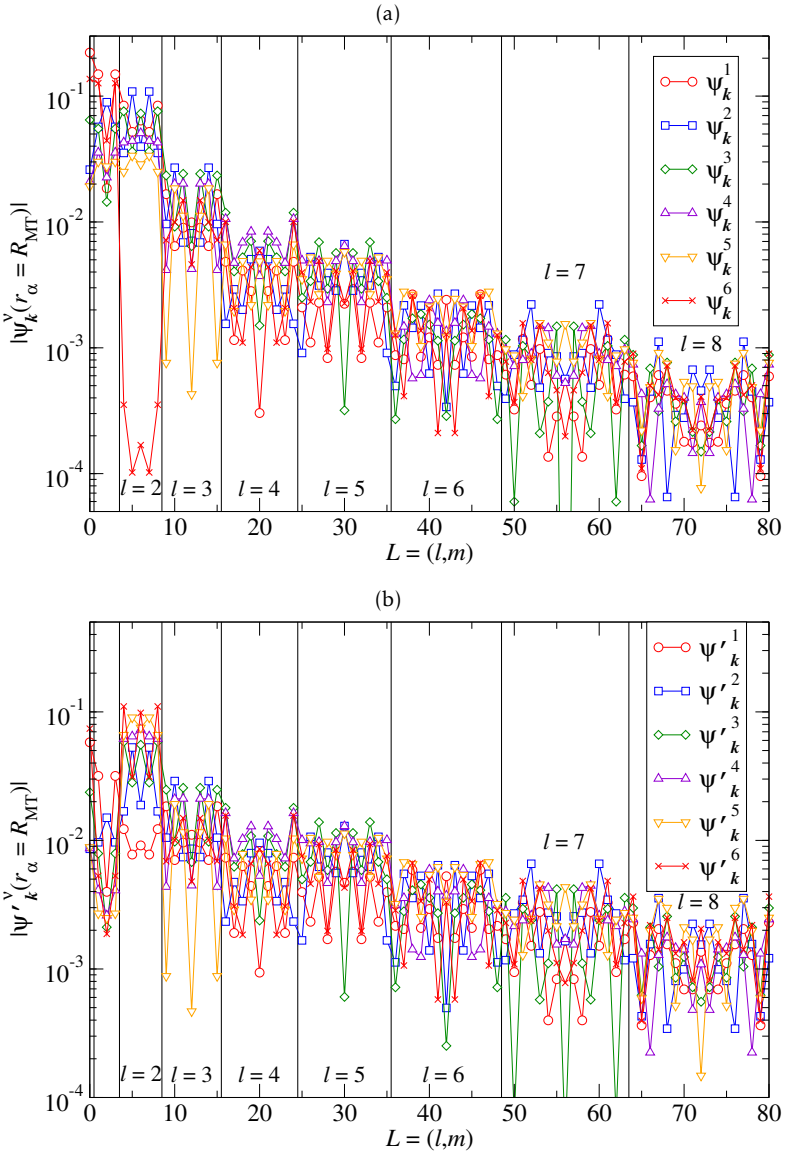

Figure 4.18.: Matching conditions at the MT boundary for the lowest wave functions above the core states in fcc Cu. Figure (a) shows the values of the functions, while (b) shows the radial derivatives. The displayed matching conditions cover the occupied valence states for an arbitrarily chosen $\boldsymbol{k}$ point. The index on the abscissa is given by $L = l^2 + l + m$. For each l the associated values are marked in the figures, although for $l = 0$ and $l = 1$ the denotation has not been done explicitly.

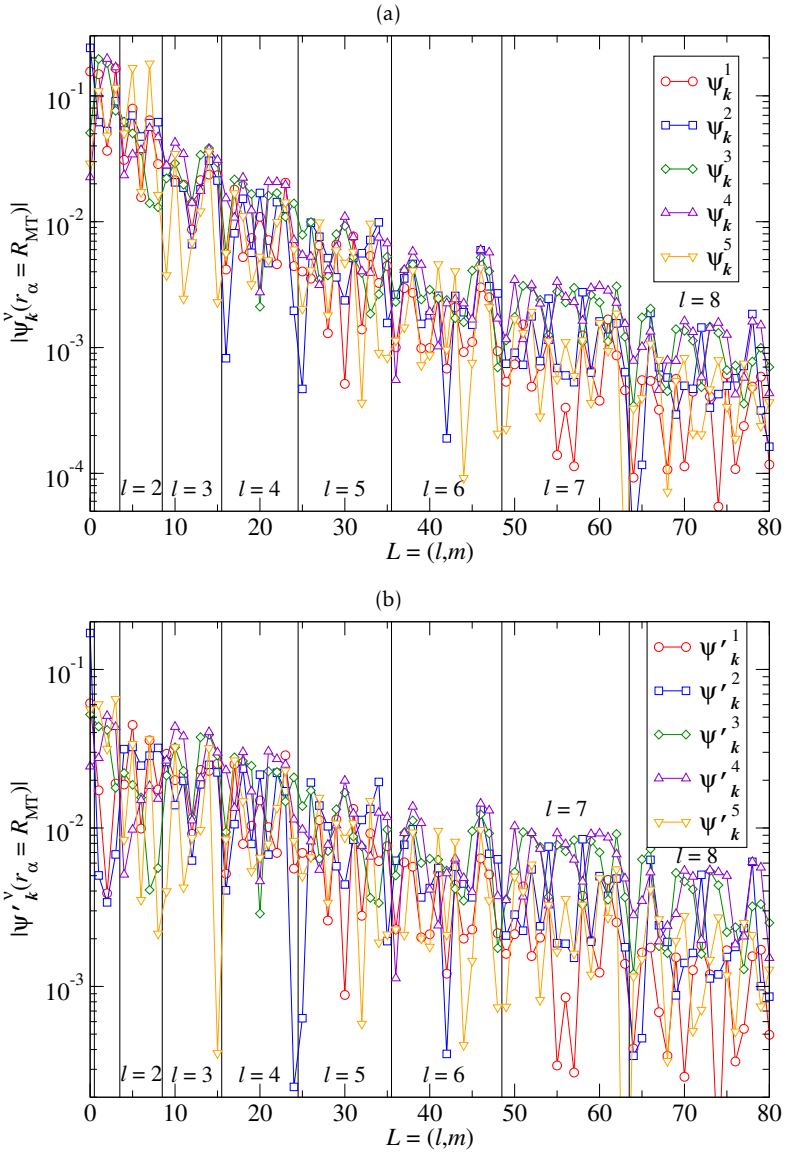

Figure 4.19.: Matching conditions at the Si MT boundary for the lowest wave functions above the core states in SiC. Figure (a) shows the values of the functions, while (b) shows the radial derivatives. The displayed matching conditions cover the occupied valence states and the lowest unoccupied state for an arbitrarily chosen $\boldsymbol{k}$ point. The index on the abscissa is given by $L = l^2 + l + m$. For each l the associated values are marked in the figures, although for $l = 0$ and $l = 1$ the denotation has not been done explicitly.

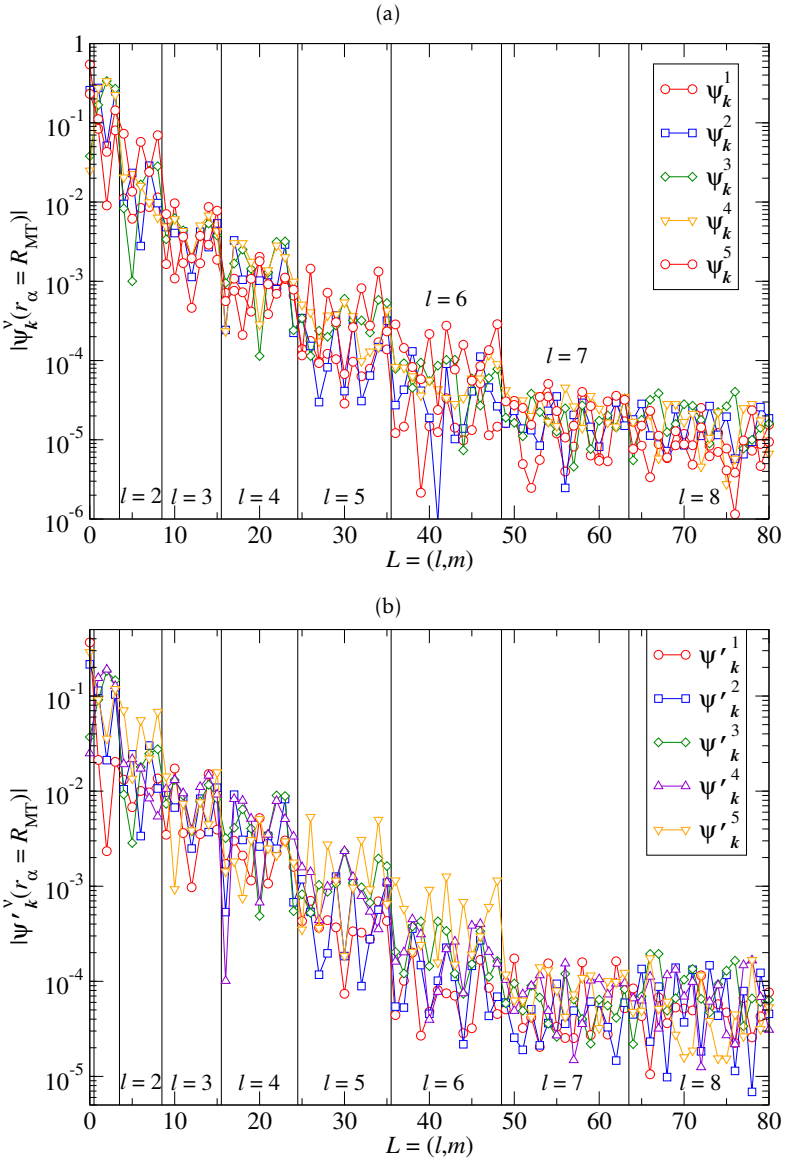

Figure 4.20.: Matching conditions at the C MT boundary for the lowest wave functions above the core states in SiC. Figure (a) shows the values of the functions, while (b) shows the radial derivatives. The displayed matching conditions cover the occupied valence states and the lowest unoccupied state for an arbitrarily chosen $\boldsymbol{k}$ point. The index on the abscissa is given by $L = l^2 + l + m$. For each l the associated values are marked in the figures, although for $l = 0$ and $l = 1$ the denotation has not been done explicitly.

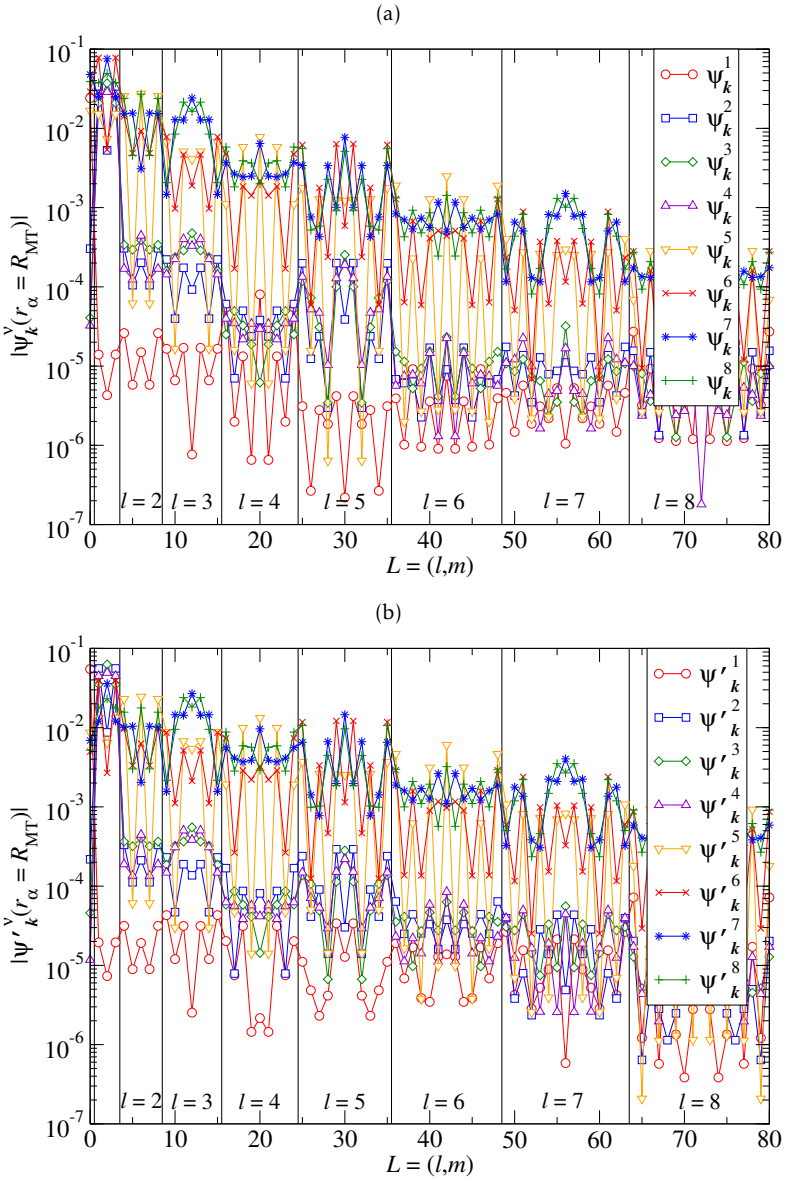

Figure 4.21.: Matching conditions at the Na MT boundary for the lowest wave functions above the core states in NaCl. Figure (a) shows the values of the functions, while (b) shows the radial derivatives. The displayed matching conditions cover the occupied valence states for an arbitrarily chosen $\boldsymbol{k}$ point. The first 4 wave functions are the $2s$ and $2p$ semicore states of Na. The index on the abscissa is given by $L = l^2 + l + m$. For each l the associated values are marked in the figures, although for $l = 0$ and $l = 1$ the denotation has not been done explicitly.

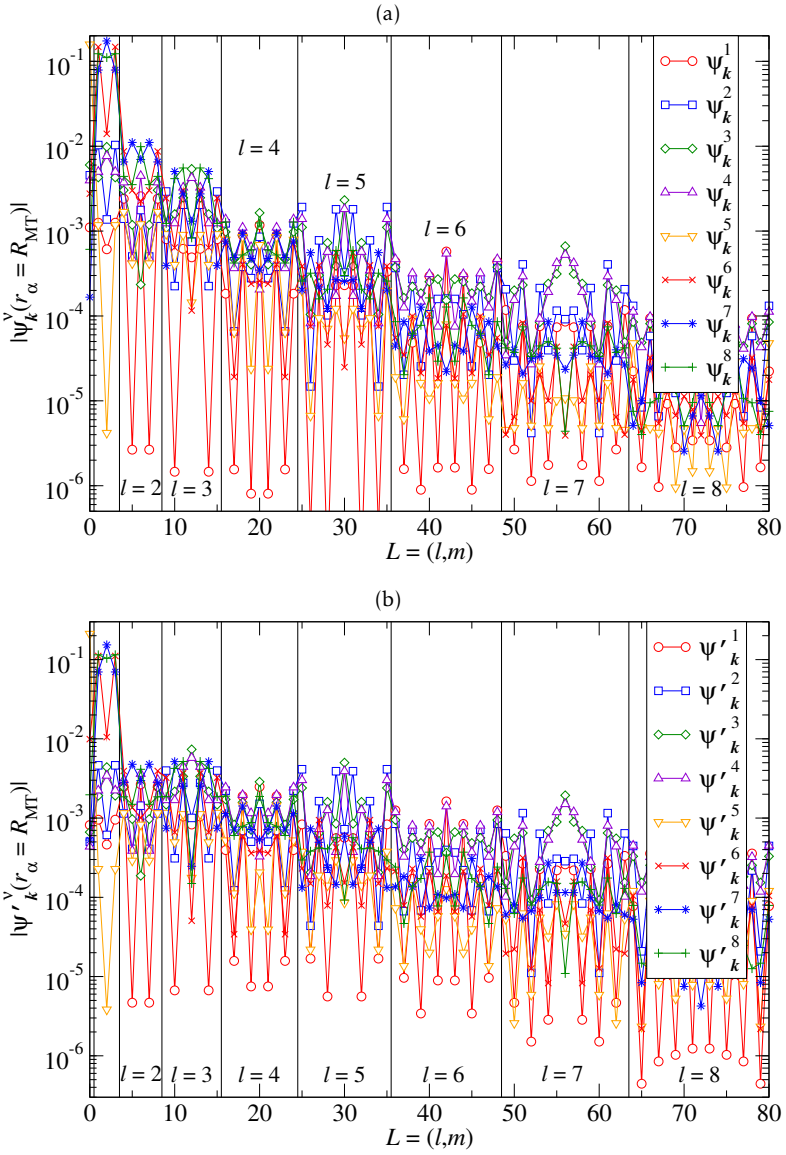

Figure 4.22.: Matching conditions at the Cl MT boundary for the lowest wave functions above the core states in NaCl. Figure (a) shows the values of the functions, while (b) shows the radial derivatives. The displayed matching conditions cover the occupied valence states for an arbitrarily chosen $\boldsymbol{k}$ point. The first 4 wave functions are the 2*s* and 2*p* semicore states of Na. The index on the abscissa is given by $L = l^2+l+m$. For each l the associated values are marked in the figures, although for $l = 0$ and $l = 1$ the denotation has not been done explicitly.

functions with the corresponding character of the state. We first identify the semi-core states in Na by noting that $\psi^1_{\boldsymbol{k}}$ is the $2s$ state and $\psi^2_{\boldsymbol{k}}$ to $\psi^4_{\boldsymbol{k}}$ are the $2p$ states. It is clearly visible in figure 4.21 that the matching is strongly dominated by the corresponding l channels $l = 0$ and $l = 1$. All other l channels provide contributions that are 2 or more orders of magnitude smaller. On the other hand the matching of these functions to the Cl MT sphere is not dominated by a single l channel. Here, a couple of channels make relevant contributions, although at a considerably lower level than the dominating matching for Na. For the higher wave functions we identify $\psi^5_{\boldsymbol{k}}$ as Cl $3s$ state and $\psi^6_{\boldsymbol{k}}$ to $\psi^8_{\boldsymbol{k}}$ as Cl $3p$ states. The contributions of the associated l channels clearly dominate the matching to the Cl MT sphere in figure 4.22. Again, all other l channels make considerably smaller contributions. Also the matching of these functions to the Na MT sphere does not show such a clear dominance of a specific l channel.

We conclude these observations by noting that the plane waves that are the IR part of LAPWs are obviously not designed to directly reflect the shapes of the electronic states in a solid. Especially localized states and directed covalent bondings possess properties at the MT sphere boundaries that deviate from the general properties of plane waves. We believe that these deviations are an opportunity to design a basis set that offers an even higher description efficiency than the LAPW basis. Nevertheless, we remark that the LAPW basis already is rather efficient. Though the plane waves in the IR are not directly adapted to the given problem, they solve the Schrödinger equation for a constant potential. As the potential in the IR is smooth, this approach is generally a good starting point.

4.2.2 Changes of the MT potential and the basis functions throughout the self-consistency loop

To better understand the aspects that have to be included in the construction of a more efficient basis, we investigate the changes of the problem throughout the different iterations of the self-consistency loop. We start by having a closer look at the changes of the potential in the MT spheres and plot the radial behavior of the different lm channels of the potential,

$$V(\boldsymbol{r}) = V_{lm}(r_\alpha) Y_{lm}(\hat{r}_\alpha), \tag{4.5}$$

in the MT spheres in the first iteration and for the self-consistent solution.

For Cu, the changes of the potential are visualized in figure 4.23. Inspecting this figure, we first note that only very few lm channels contribute to the potential. The largest contribution comes from the spherical part $V_{l=0,m=0}$. Of course, this part of the potential features a $\propto -Z_\alpha/(r_\alpha \cdot Y_{l=0,m=0})$ behavior[7] near the atomic nucleus, where the other lm channels vanish. However, even at the MT boundary R_{MT} the spherical potential is still the dominant contribution to the potential. Nevertheless, the

[7] Z_α is the core charge of atom α, $Y_{l=0,m=0} = \frac{1}{\sqrt{4\pi}}$.

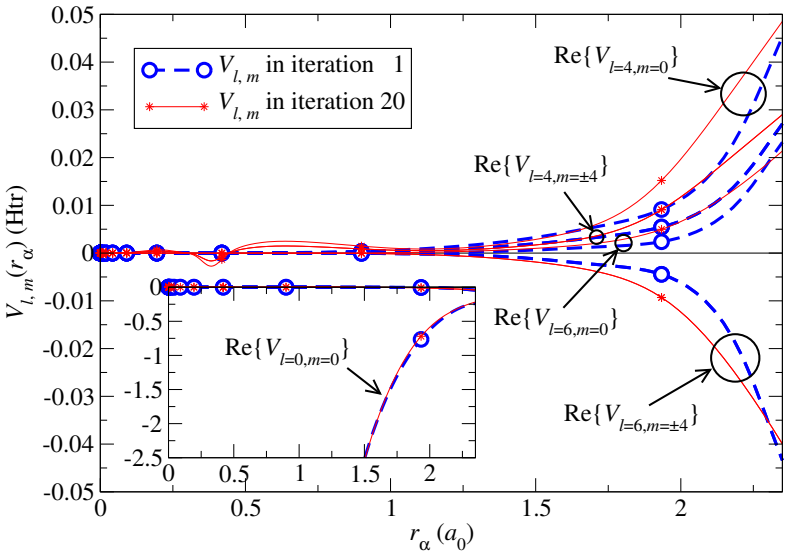

Figure 4.23.: Changes of the MT potential in fcc Cu throughout the self-consistency loop. The figure shows the potential of the first iteration in comparison to the potential for the self-consistent solution in the 20th iteration. Displayed are only those lm channels with $l \leq 6$ that feature finite contributions to the potential. The inset shows the spherical potential, which is on another energy scale. Symbols mark the different curves every 51 mesh points of the logarithmic radial mesh.

nonspherical contributions become more important in the near of the MT boundary, where, dependent on the lm channel, they nearly reach a similar order of magnitude in comparison to the spherical potential.

The differences between the potential in the first iteration and the one of the self-consistent solution are small. Especially for the spherical part the associated curves lie nearly on top of each other and no significant difference is observable on the energy scale of the figure. For the nonspherical contributions we observe that the qualitative behavior of the potential is only exposed to marginal changes. The curves stay at the same order of magnitude, although the concrete values and especially the curvatures in the outer part of the MT sphere change. We realize that the potential in the first iteration, which is obtained on the basis of a superposition of atomic densities, is already a very good approximation to the actual potential in the crystal.

To check whether this statement can also be made for materials with other bonding mechanisms we provide equivalent figures also for SiC and for NaCl. For SiC figure 4.24 shows the development of the potential in the MT sphere of Si and figure 4.25 shows it in the C sphere. Both figures support the statement that the superposition of atomic densities already is an excellent basis that provides a potential which comes very near to the potential in the solid. This is surprising since the cova-

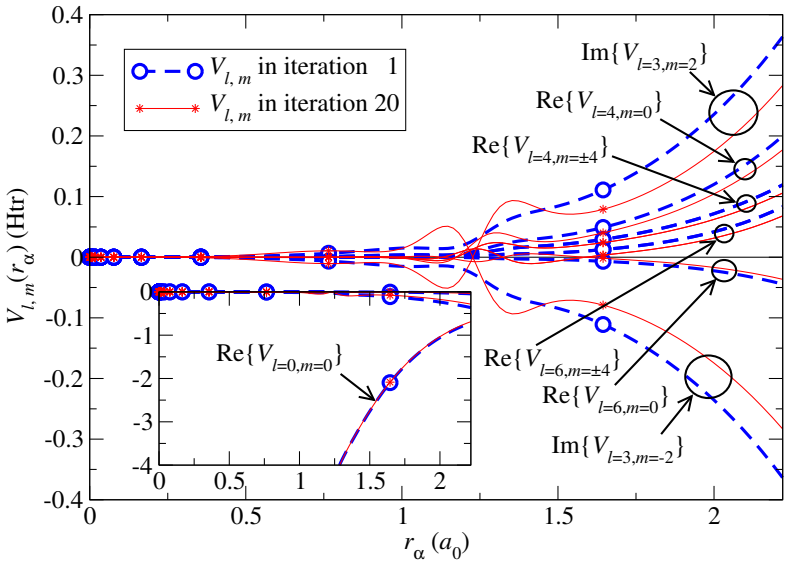

Figure 4.24.: Changes of the Si MT potential in SiC throughout the self-consistency loop, similar to figure 4.23.

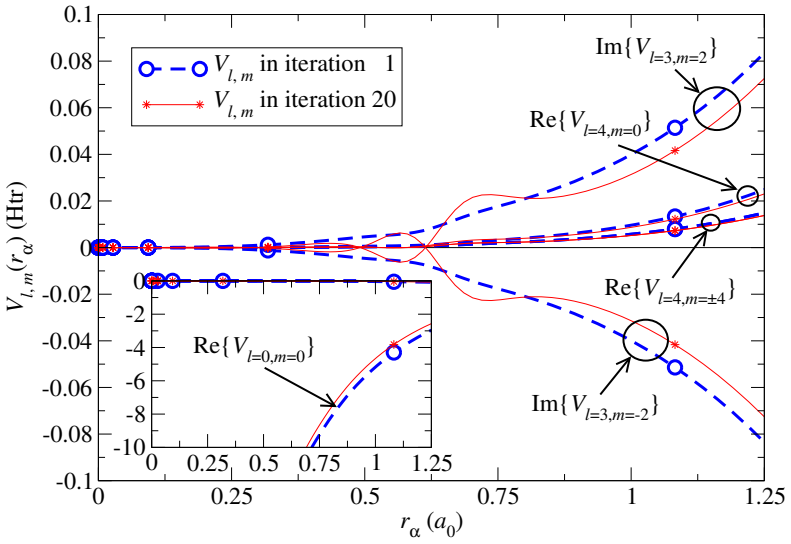

Figure 4.25.: Changes of the C MT potential in SiC throughout the self-consistency loop, similar to figure 4.23.

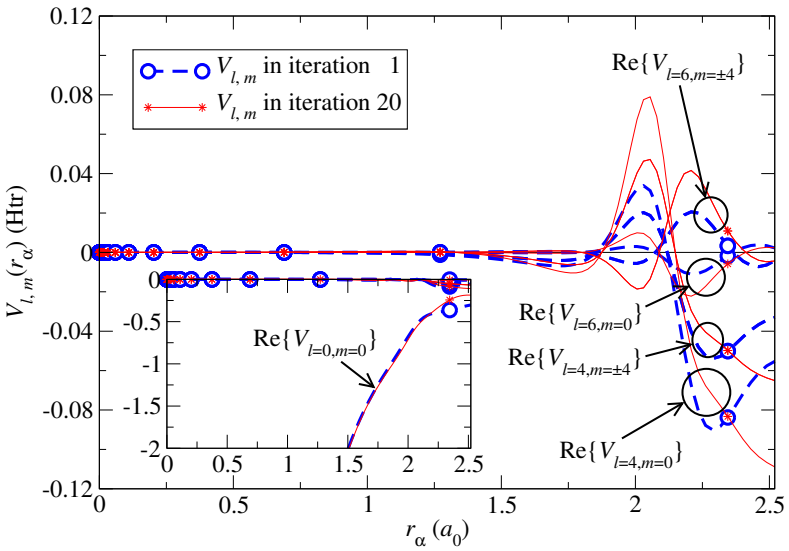

Figure 4.26.: Changes of the Na MT potential in NaCl throughout the self-consistency loop, similar to figure 4.23.

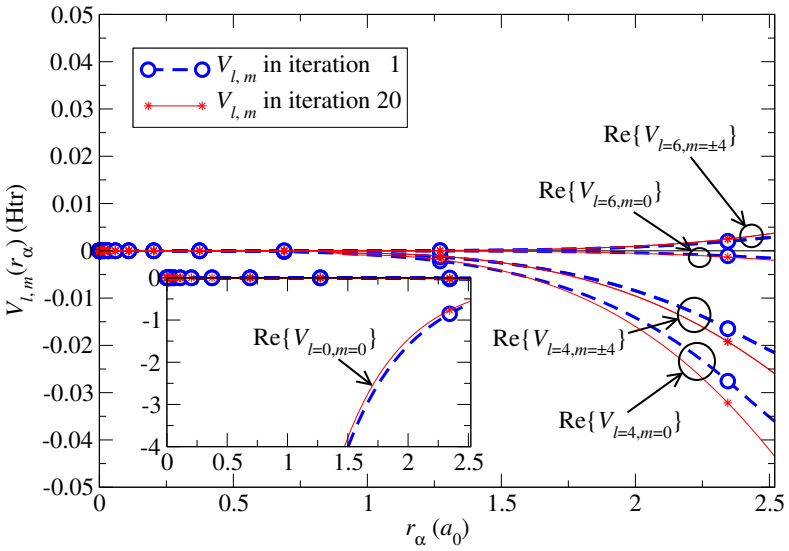

Figure 4.27.: Changes of the Cl MT potential in NaCl throughout the self-consistency loop, similar to figure 4.23.

lent bonds in this material strongly deviate from the states in isolated atoms.

For NaCl figures 4.26 and 4.27 display the changes in the MT potentials of Na and Cl, respectively. Here, the changes in the Cl MT sphere are similar to those already observed in the previous materials. However, the changes in the Na sphere are slightly larger. As a consequence of the charge transfer from Na to Cl in the first iterations of the self-consistency loop we observe that features of the nonspherical part of the potential strongly change, although on a small absolute scale.

Regardless of the material, the changes of the spherical potential over the different iterations of the self-consistency loop are small. As the MT parts of the basis functions are constructed on the basis of the spherical potential we conjecture that the associated changes of the basis functions should also be small, as long as the changes in the energy parameters are also small. This should especially apply to the $u_l^\alpha(r_\alpha, E_l^\alpha)$ and $\dot{u}_l^\alpha(r_\alpha, E_l^\alpha)$ for high l quantum numbers since with growing l the angular momentum barrier becomes more and more the dominating term in the construction of these functions and the potential becomes less important.

With the usage of the AEP method for the determination of the energy parameters, small changes in the spherical potential should translate to only small changes in the energy parameters. Thus, with this method we expect to observe only small changes in $u_l^\alpha(r_\alpha, E_l^\alpha)$ and $\dot{u}_l^\alpha(r_\alpha, E_l^\alpha)$ throughout the self-consistency loop.

For Cu, the changes in the radial functions of the LAPW basis are displayed in figure 4.28. We first compare $u_l^\alpha(r_\alpha, E_l^\alpha)$ to $\dot{u}_l^\alpha(r_\alpha, E_l^\alpha)$ and see that, as expected from figure 4.1(b), near the nucleus the $\dot{u}_l^\alpha(r_\alpha, E_l^\alpha)$ are proportional to the respective corresponding $u_l^\alpha(r_\alpha, E_l^\alpha)$. On the other hand, in the outer parts of the MT sphere $u_l^\alpha(r_\alpha, E_l^\alpha)$ and $\dot{u}_l^\alpha(r_\alpha, E_l^\alpha)$ deviate from each other to a larger extent. This is in agreement with the observation that the energy dependence of $u_l^\alpha(r_\alpha, E_l^\alpha)$ near the nucleus mainly affects the norm of the function, while there are larger dependences near the MT boundary.

As expected from the small changes in the potential, the changes in the radial functions $u_l^\alpha(r_\alpha, E_l^\alpha)$ and $\dot{u}_l^\alpha(r_\alpha, E_l^\alpha)$ are also very small. For most l channels the radial functions in the first iteration lie on top of those for the self-consistent solution. This is especially true for l channels with $l \geq 3$. The largest changes in the radial functions throughout the iterations are observable for $l = 2$. These changes can be understood by comparing the changes in the energy parameters to those in the spherical potential. For the spherical potential $V_{l=0,m=0}$, the value at the MT boundary shifts by 0.0211 Htr from −0.2378 to −0.2167 Htr. Including the spherical harmonic $Y_{l=0,m=0}$ this is a shift of 0.0060 Htr. The energy parameters also shift. $E_{l=0}$ shifts by 0.0031 Htr from 0.1653 to 0.1684 Htr relative to the zero of the potential. For the p channel $E_{l=1}$ shifts by 0.0047 Htr from 0.3149 to 0.3196 Htr, for the d channel $E_{l=2}$ shifts by −0.0528 Htr from 0.2633 to 0.2105 Htr, and for higher l the energy parameter shifts by 0.0059 Htr from 0.6408 to 0.6467 Htr. Thus, we observe the largest changes in the energy parameter of the d channel, which even feature the opposite sign of the changes of the MT boundary value of the spherical potential. Nevertheless, we remark that the changes in all energy parameters are very small. This is in agreement with the expectations.

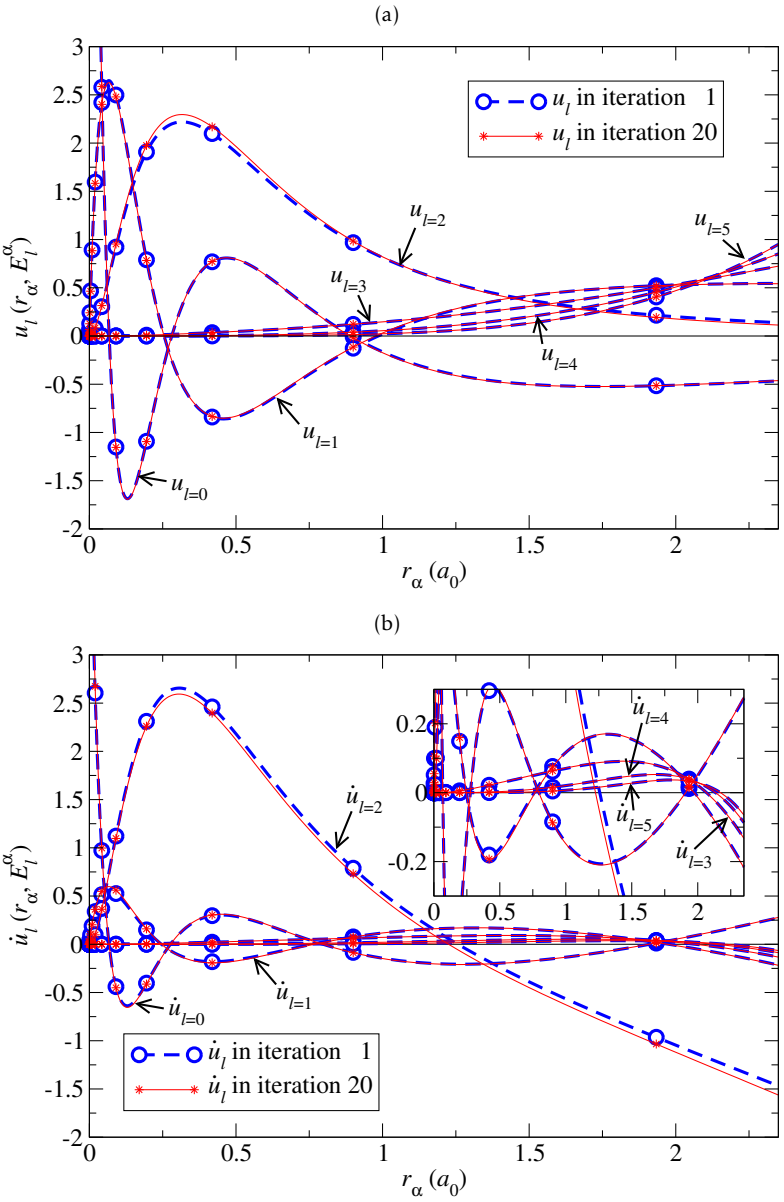

Figure 4.28.: Changes of the radial functions over the self consistency cycle for fcc Cu. The plots display the radial functions up to $l = 5$ in the 1st iteration and for the self consistent solution in iteration 20. The solutions to the SRA to the radial Dirac equation are given in (a), while their energy derivatives are shown in (b). The inset in (b) provides a detailed view on $\dot{u}_l^\alpha(r_\alpha, E_l^\alpha)$ for $l = 3, 4, 5$.

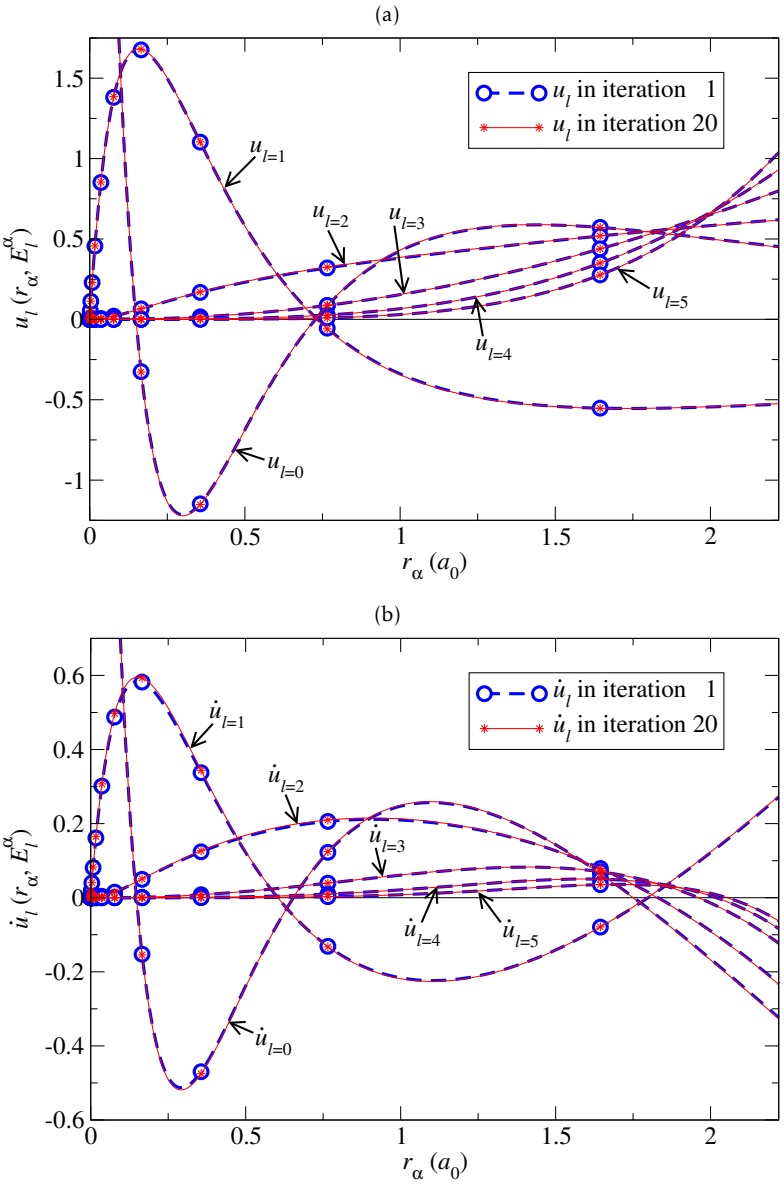

Figure 4.29.: Changes of the radial functions over the self consistency cycle in the Si MT sphere in SiC. The plots display the radial functions up to $l = 5$ in the 1st iteration and for the self consistent solution in iteration 20. The solutions to the SRA to the radial Dirac equation are given in (a), while their energy derivatives are shown in (b).

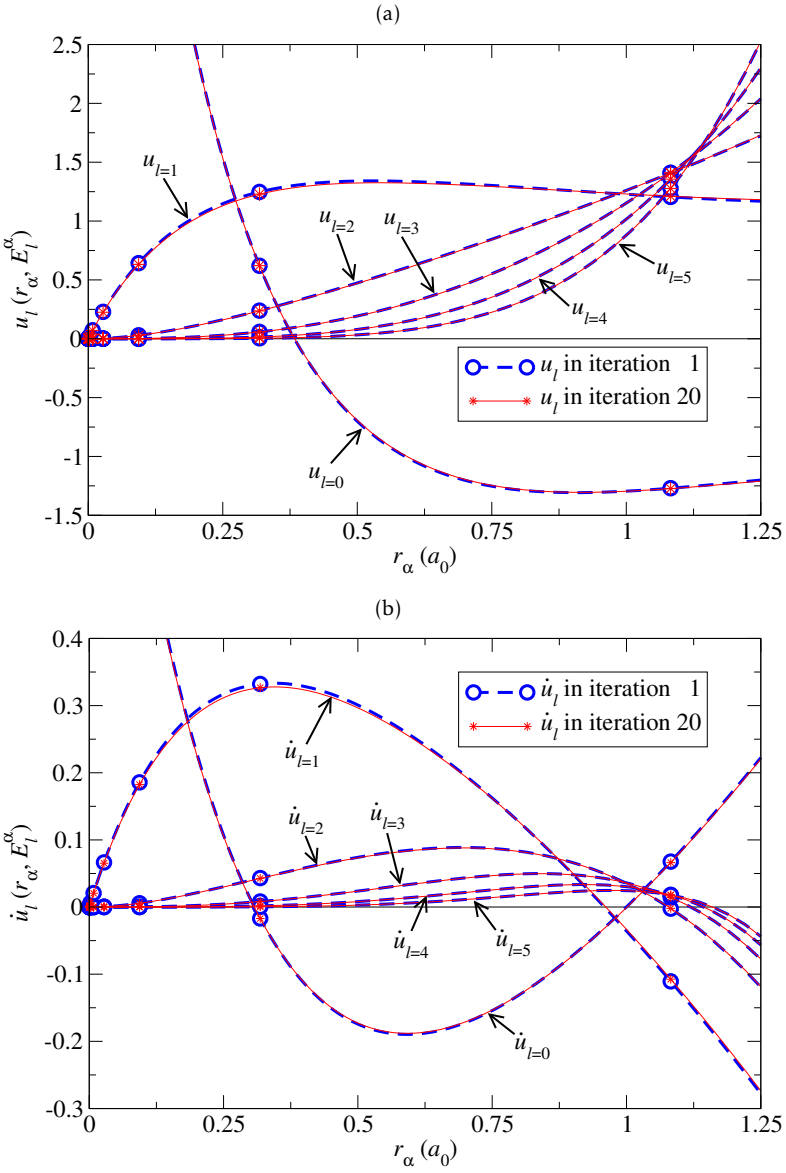

Figure 4.30.: Changes of the radial functions over the self consistency cycle in the C MT sphere in SiC. The plots display the radial functions up to $l = 5$ in the 1st iteration and for the self consistent solution in iteration 20. The solutions to the SRA to the radial Dirac equation are given in (a), while their energy derivatives are shown in (b).

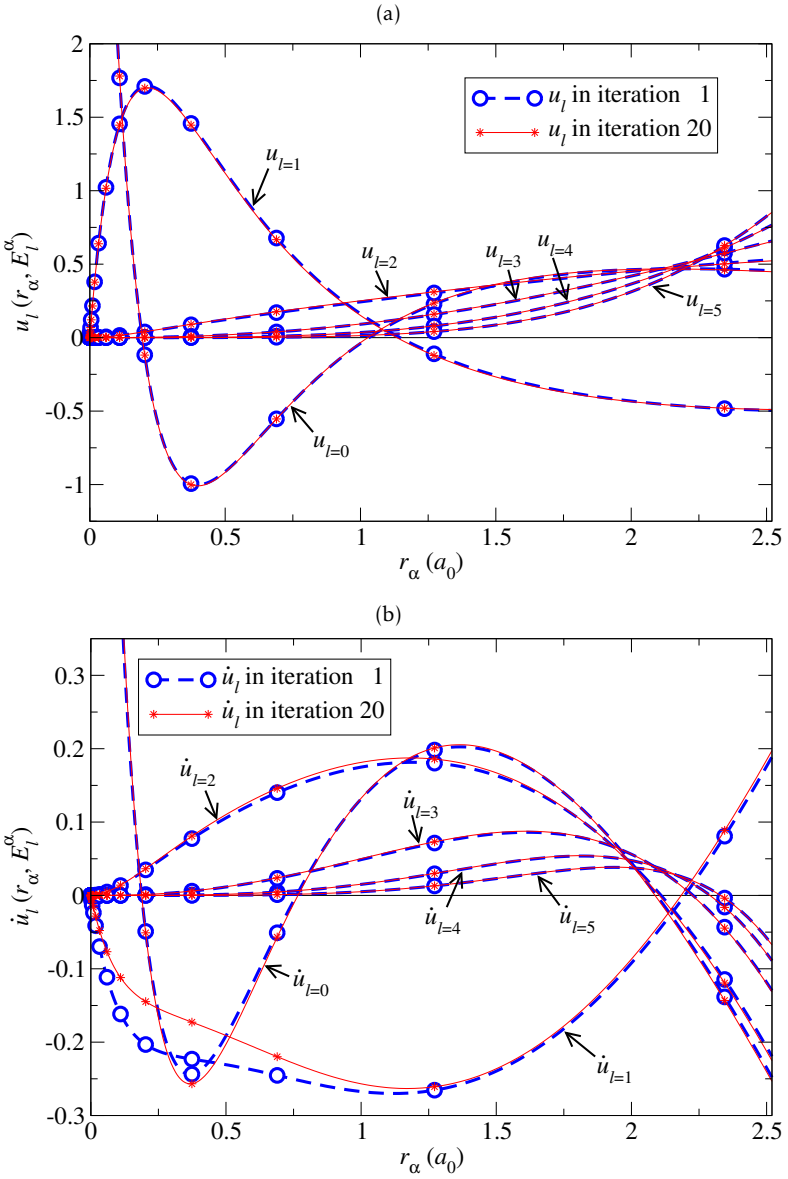

Figure 4.31.: Changes of the radial functions over the self consistency cycle in the Na MT sphere in NaCl. The plots display the radial functions up to $l = 5$ in the 1st iteration and for the self consistent solution in iteration 20. The solutions to the SRA to the radial Dirac equation are given in (a), while their energy derivatives are shown in (b).

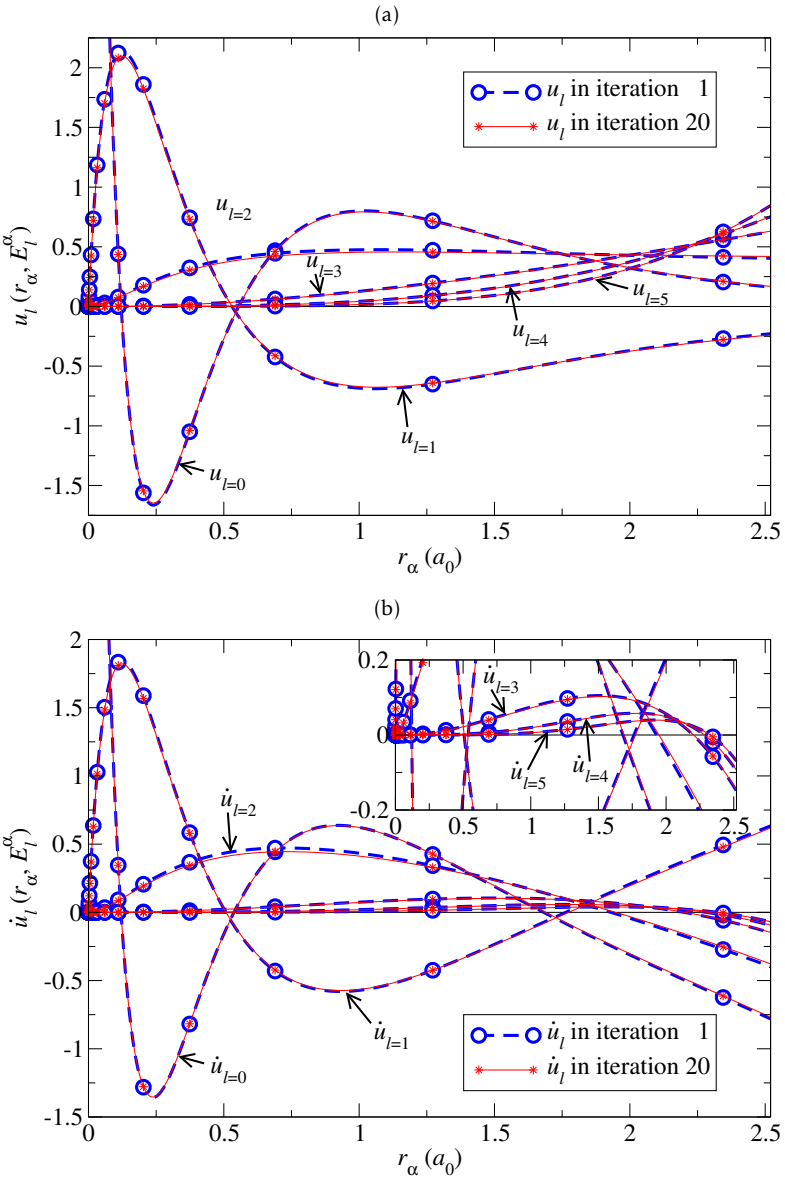

Figure 4.32.: Changes of the radial functions over the self consistency cycle in the Cl MT sphere in NaCl. The plots display the radial functions up to $l = 5$ in the 1st iteration and for the self consistent solution in iteration 20. The solutions to the SRA to the radial Dirac equation are given in (a), while their energy derivatives are shown in (b). The inset in (b) provides a detailed view on $\dot{u}_l^\alpha(r_\alpha, E_l^\alpha)$ for $l = 3, 4, 5$.

For SiC figures 4.29 and 4.30 display the changes of the radial functions for Si and C, respectively. We remember (cf. figure 4.24) that for Si the spherical potential shows nearly no changes over the iterations. Of course, this translates to nearly no changes in the energy parameters, which are exposed to shifts between the first and last iterations between 0.0052 Htr and 0.0087 Htr only, depending on the l channel. As a consequence, the respective radial functions $u_l^\alpha(r_\alpha, E_l^\alpha)$ and $\dot{u}_l^\alpha(r_\alpha, E_l^\alpha)$ are also nearly identical in these two iterations. For the C atom we observed a slight shift of the spherical potential in the outer part of the MT sphere (cf. figure 4.25). For the value of the potential on the MT boundary $V_{l=0,m=0}$ shifts by 0.3892 Htr. Including the spherical harmonic $Y_{l=0,m=0}$ this is a shift of 0.1098 Htr. However, the shifts in the energy parameters of 0.1138, 0.1114, 0.1098, and 0.1098 Htr for $l = 0, 1, 2$ and $l \geq 3$ largely compensate the shift of the spherical potential in the outer part of the MT sphere. In consequence, we again observe nearly no changes between the radial functions of the first iteration and the respective functions of the self-consistent solution.

The last material to be investigated in this context is NaCl. For this material figures 4.31 and 4.32 show the changes of the radial functions in Na and Cl, respectively. We remark that due to the charge transfer in this material the spherical potential in Na exhibits changes that especially manifest very near to the MT boundary. Including the spherical harmonic $Y_{l=0,m=0}$ the spherical potential at the MT boundary shifts by 0.0330 Htr. This shift translates into a corresponding shift in the energy parameters of 0.0262, 0.0294, 0.0314, and 0.0328 Htr for $l = 0, 1, 2$ and $l \geq 3$. Especially for higher l this nearly completely compensates the shift of the potential in the outer part of the MT sphere. We note however, that the charge transfer yields rather larger deviations of the radial function $\dot{u}_{l=1}^\alpha(r_\alpha, E_{l=1}^\alpha)$ between the first and last iterations. In the MT sphere of Cl we observed a slight shift of the spherical potential which is of the size of 0.0127 Htr (including the $Y_{l=0,m=0}$ factor) at the MT boundary. The energy parameters, on the other hand, shift by 0.0572, 0.0463, 0.0182, and 0.0130 Htr for $l = 0, 1, 2$ and $l \geq 3$. To understand these different shifts better, we remark that the changes of the spherical potential slightly inside the MT sphere are much larger. For example at $r_\alpha = 2.0\ a_0$ we observe a shift of 0.0410 Htr. Depending on the value of the energy parameter and the l channel the shifts in the energy parameters are sensitive to changes of the spherical potential in different regions. Lastly we note that the changes of the radial functions in the Cl MT sphere are small. This is in agreement to the other examples discussed here.

Beyond the very small changes of the radial functions, we observed for all materials that the energy parameters for $l = 3$ cancel the changes of the spherical potential in the outer part of the MT sphere with high precision. This is easily understandable. For this l channel the angular momentum barrier, which is independent of the energy, is already the dominant term determining the form of the radial function to a large extent. Only in the outer parts of the MT sphere the angular momentum barrier becomes small enough such that the shape of the radial function is mainly determined by the potential in this region. Beyond the MT sphere boundary the changes of the value of the spherical potential at the MT boundary directly translates into a constant

shift of the confining potential used to determine the energy parameters in the AEP method. Putting these ingredients together we conclude that for high l channels the changes of the radial functions are negligible. Iteration dependent variations of the spherical potential in the outer part of the MT sphere are compensated by an associated shift in the energy parameters. Beyond this, the radial functions for high l are mainly given by the angular momentum barrier.

4.2.3 Changes of the wave functions in the interstitial region throughout the self-consistency loop

After investigating the changes of the basis functions in the MT spheres we turn to the interstitial region. Here, the basis functions do not vary over the iterations. On the other hand, the wave functions vary as the density and hence also the potential change over the iterations. Here, we check to what extent the wave functions in the interstitial region change over the iterations.

In detail, we determine for the three test materials to what extent a wave function obtained in the first iteration $\psi^{\nu}_{\boldsymbol{k},\mathrm{iter}=1}$ already represents the corresponding wave function obtained in a later iteration. For this we calculate the best representation of the wave function $\psi^{\nu}_{\boldsymbol{k},\mathrm{iter}=n}$ in an iteration n by the associated wave function of the first iteration, $\psi^{\nu}_{\boldsymbol{k},\mathrm{iter}=1}$. This is done by projecting $\psi^{\nu}_{\boldsymbol{k},\mathrm{iter}=n}$ onto $\psi^{\nu}_{\boldsymbol{k},\mathrm{iter}=1}$ with

$$\tilde{\psi}^{\nu}_{\boldsymbol{k},\mathrm{iter}=n} = \frac{|\psi^{\nu}_{\boldsymbol{k},\mathrm{iter}=1}\rangle\langle\psi^{\nu}_{\boldsymbol{k},\mathrm{iter}=1}|\psi^{\nu}_{\boldsymbol{k},\mathrm{iter}=n}\rangle_{\mathrm{IR}}}{\langle\psi^{\nu}_{\boldsymbol{k},\mathrm{iter}=1}|\psi^{\nu}_{\boldsymbol{k},\mathrm{iter}=1}\rangle_{\mathrm{IR}}}. \tag{4.6}$$

Next, we define the iteration dependent representation error $\Delta^{\nu}_{\boldsymbol{k},\mathrm{IR}}(\mathrm{iter})$ as the norm of that part of $\psi^{\nu}_{\boldsymbol{k},\mathrm{iter}=n}$ that is orthogonal to $\tilde{\psi}^{\nu}_{\boldsymbol{k},\mathrm{iter}=n}$, in relation to the norm of $\psi^{\nu}_{\boldsymbol{k},\mathrm{iter}=n}$. This gives

$$\Delta^{\nu}_{\boldsymbol{k},\mathrm{IR}}(n) = \sqrt{\frac{\langle\tilde{\psi}^{\nu}_{\boldsymbol{k},\mathrm{iter}=n} - \psi^{\nu}_{\boldsymbol{k},\mathrm{iter}=n}|\tilde{\psi}^{\nu}_{\boldsymbol{k},\mathrm{iter}=n} - \psi^{\nu}_{\boldsymbol{k},\mathrm{iter}=n}\rangle_{\mathrm{IR}}}{\langle\psi^{\nu}_{\boldsymbol{k},\mathrm{iter}=n}|\psi^{\nu}_{\boldsymbol{k},\mathrm{iter}=n}\rangle_{\mathrm{IR}}}}. \tag{4.7}$$

For each iteration, the IR representation errors of the lowest wave functions above the core states for a representation in terms of the associated wave functions from the first iteration are plotted in figures 4.33, 4.34, and 4.35 for Cu, SiC, and NaCl, respectively.

For Cu we observe that, regardless of the concrete wave function within the set of considered functions, more than 70% of a given wave function of the self consistent solution can already be represented by the associated wave function in the first iteration. For SiC and NaCl this ratio is even higher, while it reaches 75% for SiC, NaCl exhibits only very small changes in the wave functions and we can describe at least 92% of a given wave function in the last iteration by the associated wave function in the first iteration. We remark that similar results have also been found in an investigation by E. Di Napoli [136].

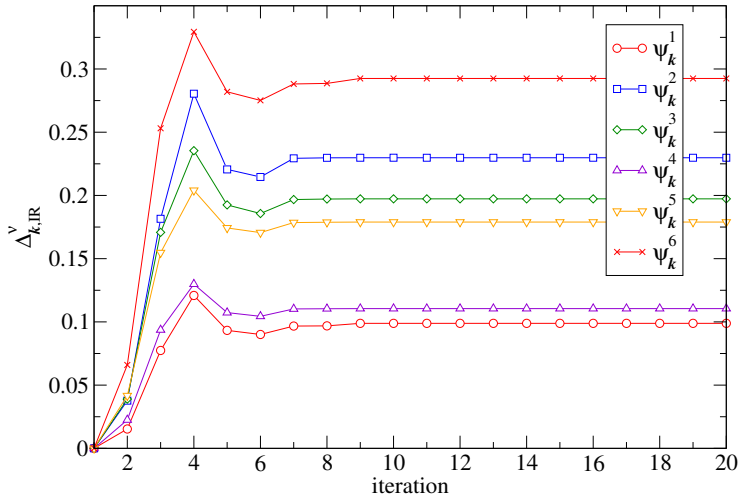

Figure 4.33.: Changes in the IR part of the wave functions throughout the iterations in fcc Cu. The figure shows for the lowest wave functions above the core states the error in the IR representation $\Delta^{\nu}_{\boldsymbol{k},\mathrm{IR}}(n)$ of a wave function $\psi^{\nu}_{\boldsymbol{k},\mathrm{iter}=n}$ in iteration n by the associated wave function in the first iteration $\psi^{\nu}_{\boldsymbol{k},\mathrm{iter}=1}$.

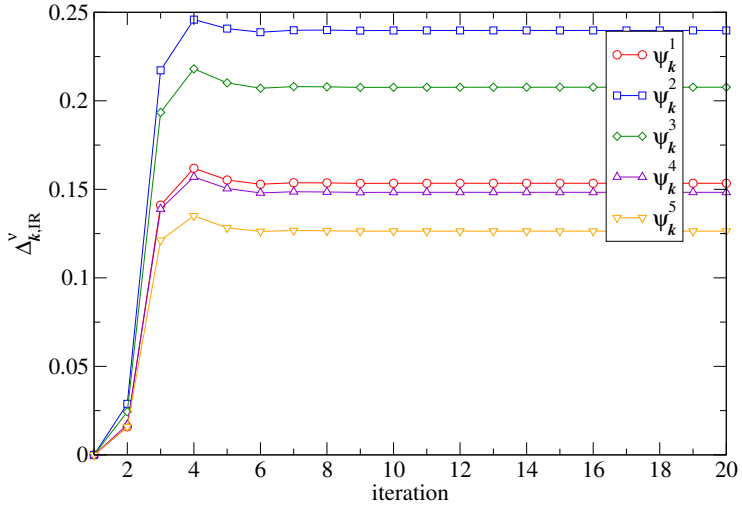

Figure 4.34.: Changes in the IR part of the wave functions throughout the iterations in zinc blende SiC. The figure shows for the lowest wave functions above the core states the error in the IR representation $\Delta^{\nu}_{\boldsymbol{k},\mathrm{IR}}(n)$ of a wave function $\psi^{\nu}_{\boldsymbol{k},\mathrm{iter}=n}$ in iteration n by the associated wave function in the first iteration $\psi^{\nu}_{\boldsymbol{k},\mathrm{iter}=1}$.

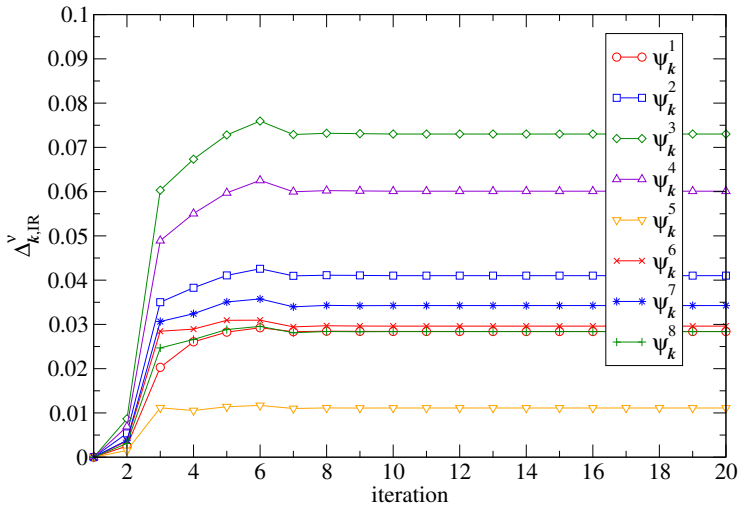

Figure 4.35.: Changes in the IR part of the wave functions throughout the iterations in rock salt NaCl. The figure shows for the lowest wave functions above the core states the error in the IR representation $\Delta^{\nu}_{\boldsymbol{k},\mathrm{IR}}(n)$ of a wave function $\psi^{\nu}_{\boldsymbol{k},\mathrm{iter}=n}$ in iteration n by the associated wave function in the first iteration $\psi^{\nu}_{\boldsymbol{k},\mathrm{iter}=1}$. Note that $\psi^1_{\boldsymbol{k},}$ to $\psi^4_{\boldsymbol{k},}$ are the interstitial parts of the $2s$ and $2p$ semicore states.

5 The linearized augmented lattice-adapted plane-wave basis

Contents

The investigations in chapter 4.2.1 showed that the MT matching conditions of the LAPW basis functions do not fit to those of the wave functions. Especially the LAPW basis functions with large reciprocal lattice vectors contribute to lm channels that are strongly suppressed in the wave functions. We assume that a more efficient convergence with respect to the basis set size may be achieved if the basis functions were better adapted to the properties of the wave functions in the periodic crystal lattice. However, though the adaption to the crystal is the central idea of such a basis, we abstract its name slightly from this term and denote it as a *lattice-adapted basis*. This notion suits better to the already elaborate naming of the LAPW basis, which is the fundament for the detailed formulation of the new concept. In this chapter we propose a *linearized augmented lattice-adapted plane-wave basis* (abbreviated as $(\mathrm{LA})^2\mathrm{PW}$ or $LA^2\mathrm{PW}$ basis) in which the plane waves in the interstitial region are replaced by smart linear combinations of plane waves that feature the desired properties.

Just like LAPWs, the new $(\mathrm{LA})^2\mathrm{PW}$s are based on the partitioning of space into MT spheres, the interstitial region, and vacuum regions. This implies a setup of the Hamilton and overlap matrices in analogy to the conventional FLAPW method. In detail, the matrices are given as

$$S_{ij}^{\boldsymbol{k}} = S_{ij}^{\boldsymbol{k},\mathrm{IR}} + \sum_{\alpha} S_{ij}^{\boldsymbol{k},\alpha} + \sum_{\mathrm{vac}} S_{ij}^{\boldsymbol{k},\mathrm{vac}} \tag{5.1}$$

for the overlap matrix and

$$H_{ij}^{\boldsymbol{k}} = H_{ij}^{\boldsymbol{k},\mathrm{IR}} + \sum_{\alpha} H_{ij}^{\boldsymbol{k},\alpha} + \sum_{\mathrm{vac}} H_{ij}^{\boldsymbol{k},\mathrm{vac}} \tag{5.2}$$

for the Hamilton matrix, where i and j denote the two (LA)^{2}PW basis functions associated with a certain matrix element. We discuss the matrix contributions coming from each region of space in detail and also present a recipe of how to deal with parts of the calculation succeeding the diagonalization.

Overall, the chapter is organized as follows. In section 5.1 we define the analytic form of the new basis and sketch first aspects of an efficient implementation. This includes the precalculation of certain quantities. Next, we discuss the setup of the Hamilton and overlap matrices in detail. In section 5.2 we discuss the contributions coming from the interstitial region, in section 5.3 we then deal with the MT contributions, and in section 5.4 we describe how to efficiently calculate the vacuum contributions. Finally, we discuss in section 5.5 how to come back to an LAPW representation of the eigenfunctions after solving the generalized eigenvalue problem and how to construct the valence density.

5.1 Analytic form of the basis functions and first implementation aspects

In an (LA)^{2}PW basis the j-th basis function has the form

$$\phi_{\boldsymbol{k}j}(\boldsymbol{r}) = \begin{cases} \frac{1}{\sqrt{\Omega}} \sum_{\boldsymbol{G}} o_{\boldsymbol{k}j}^{\boldsymbol{G}} e^{i(\boldsymbol{k}+\boldsymbol{G})\boldsymbol{r}} & \text{for } \boldsymbol{r} \in \text{IR} \\ \sum_{L} \left[a_{\boldsymbol{k}j}^{L\alpha} u_l^{\alpha}(r_\alpha, E_l^{\alpha}) + b_{\boldsymbol{k}j}^{L\alpha} \dot{u}_l^{\alpha}(r_\alpha, E_l^{\alpha}) \right] Y_L(\hat{\boldsymbol{r}}_{\boldsymbol{\alpha}}) & \text{for } \boldsymbol{r} \in \text{MT}^{\alpha} \end{cases}, \tag{5.3}$$

where the $o_{\boldsymbol{k}j}^{\boldsymbol{G}}$ are the N_{PW} plane wave expansion coefficients of the j-th basis function in the interstitial region. The radial functions in the MT spheres are not matched to single plane waves in the IR, but to the linear combination of plane waves that defines an (LA)^{2}PW basis function. The associated matching coefficients are defined by the corresponding linear combination of matching coefficients of LAPW basis functions as

$$a_{\boldsymbol{k}j}^{L\alpha} = \sum_{\boldsymbol{G}} o_{\boldsymbol{k}j}^{\boldsymbol{G}} a_{\boldsymbol{k}\boldsymbol{G}}^{L\alpha} \qquad \text{and} \qquad b_{\boldsymbol{k}j}^{L\alpha} = \sum_{\boldsymbol{G}} o_{\boldsymbol{k}j}^{\boldsymbol{G}} b_{\boldsymbol{k}\boldsymbol{G}}^{L\alpha}. \tag{5.4}$$

However, the time requirements for the calculation of the matching coefficients in this way scale with $\mathcal{O}((l_{\text{max}}+1)^2 N_{\text{atom}} N_{\text{bas}} N_{\text{PW}})$, where l_{max} is a representative for the atom dependent l_{max}^{α}, N_{atom} denotes the number of atoms, and N_{bas} is the number of (LA)^{2}PW basis functions. This is a cubic scaling with increasing system size and is thus of the same time complexity as solving the generalized eigenvalue problem. To avoid a significant impact on the calculation runtime due to the determination of the matching coefficients, this scaling behavior has to be improved.

We can achieve such an improvement if we demand the $o_{\boldsymbol{k}j}^{\boldsymbol{G}}$ coefficients to be independent of the iteration of the self-consistency loop. In this case we can precompute the L resolved MT matching conditions of the (LA)^{2}PW basis functions in the run-up

to a calculation as

$$o_{\boldsymbol{k}j}^{L\alpha} = \frac{4\pi}{\sqrt{\Omega}} \sum_{\boldsymbol{G}} o_{\boldsymbol{k}j}^{\boldsymbol{G}} i^l e^{i(\boldsymbol{k}+\boldsymbol{G})\boldsymbol{\tau}_\alpha} j_l(|\boldsymbol{k}+\boldsymbol{G}|R_{\mathrm{MT}^\alpha}) Y_L^*(\widehat{\boldsymbol{k}+\boldsymbol{G}}) \tag{5.5}$$

together with the radial derivatives $o_{\boldsymbol{k}j}^{\prime L\alpha} = \frac{d}{dr^\alpha} o_{\boldsymbol{k}j}^{L\alpha}(r^\alpha)|_{r^\alpha = R_{\mathrm{MT}^\alpha}}$ and reuse them in every iteration to calculate the matching coefficients by solving the system of linear equations

$$\begin{aligned} a_{\boldsymbol{k}j}^{L\alpha} u_l^\alpha(R_{\mathrm{MT}^\alpha}, E_l^\alpha) + b_{\boldsymbol{k}j}^{L\alpha} \dot{u}_l^\alpha(R_{\mathrm{MT}^\alpha}, E_l^\alpha) &= o_{\boldsymbol{k}j}^{L\alpha}, \\ a_{\boldsymbol{k}j}^{L\alpha} u_l'^\alpha(R_{\mathrm{MT}^\alpha}, E_l^\alpha) + b_{\boldsymbol{k}j}^{L\alpha} \dot{u}_l'^\alpha(R_{\mathrm{MT}^\alpha}, E_l^\alpha) &= o_{\boldsymbol{k}j}^{\prime L\alpha}. \end{aligned} \tag{5.6}$$

With this procedure the computational demands for calculating the matching coefficients in each iteration are reduced to a scaling behavior of $\mathcal{O}((l_{\max}+1)^2 N_{\mathrm{atom}} N_{\mathrm{bas}})$. For the precalculation step, however, the cubical scaling behavior is retained. Furthermore, we obtain the better computational complexity at the cost of higher storage requirements for the matching conditions $o_{\boldsymbol{k}j}^{L\alpha}$ and $o_{\boldsymbol{k}j}^{\prime L\alpha}$ that also scale with $\mathcal{O}((l_{\max}+1)^2 N_{\mathrm{atom}} N_{\mathrm{bas}})$. Nevertheless, this tradeoff is well justified.

Extensions of the LAPW basis with local orbitals can also be applied to an (LA)^{2}PW basis. Thus, the handling of ghost states or the elimination of the linearization error by LOs is also not a problem for an (LA)^{2}PW basis.

For two- and one-dimensional materials the step from an LAPW to an (LA)^{2}PW basis can be performed in an equivalent way. For example, for two-dimensional systems the (LA)^{2}PW generalization of the LAPW basis is

$$\phi_{\boldsymbol{k}_\parallel j}(\boldsymbol{r}) = \begin{cases} \frac{1}{\sqrt{\Omega}} \sum_{\boldsymbol{G}} o_{\boldsymbol{k}j}^{\boldsymbol{G}} e^{i(\boldsymbol{k}_\parallel+\boldsymbol{G})\boldsymbol{r}} & \text{for } \boldsymbol{r} \in \mathrm{IR} \\ \sum_L \left[a_{\boldsymbol{k}_\parallel j}^{L\alpha} u_l^\alpha(r_\alpha, E_l^\alpha) + b_{\boldsymbol{k}_\parallel j}^{L\alpha} \dot{u}_l^\alpha(r_\alpha, E_l^\alpha) \right] Y_L(\hat{\boldsymbol{r}}_{\boldsymbol{\alpha}}) & \text{for } \boldsymbol{r} \in \mathrm{MT}^\alpha \\ \sum_{\boldsymbol{G}_\parallel} D_{\boldsymbol{k}_\parallel j}^{\boldsymbol{G}_\parallel, \mathrm{vac}}(z, E^{\mathrm{vac}}) \frac{1}{\sqrt{A}} e^{i(\boldsymbol{k}_\parallel+\boldsymbol{G}_\parallel)\boldsymbol{r}_\parallel} & \text{for } \boldsymbol{r} \in \mathrm{VR}^{\mathrm{vac}} \end{cases} \tag{5.7}$$

with the decay function

$$D_{\boldsymbol{k}_\parallel j}^{\boldsymbol{G}_\parallel, \mathrm{vac}}(z, E^{\mathrm{vac}}) = a_{\boldsymbol{k}_\parallel j}^{\boldsymbol{G}_\parallel, \mathrm{vac}} u_{\boldsymbol{k}_\parallel \boldsymbol{G}_\parallel}^{\mathrm{vac}}(z, E^{\mathrm{vac}}) + b_{\boldsymbol{k}_\parallel j}^{\boldsymbol{G}_\parallel, \mathrm{vac}} \dot{u}_{\boldsymbol{k}_\parallel \boldsymbol{G}_\parallel}^{\mathrm{vac}}(z, E^{\mathrm{vac}}). \tag{5.8}$$

Similar to the calculation of the MT matching coefficients the determination of the vacuum matching coefficients $a_{\boldsymbol{k}_\parallel j}^{\boldsymbol{G}_\parallel, \mathrm{vac}}$ and $b_{\boldsymbol{k}_\parallel j}^{\boldsymbol{G}_\parallel, \mathrm{vac}}$ is also a time-consuming task. However, we can also overcome this problem in a similar way. We again only need to precompute the (LA)^{2}PW matching conditions at the vacuum boundaries. In detail, we project the basis function values and their derivatives in z direction along the interfaces to the vacuum regions onto the plane waves $\frac{1}{\sqrt{A}} e^{i(\boldsymbol{k}_\parallel+\boldsymbol{G}_\parallel)\boldsymbol{r}_\parallel}$ to obtain the matching conditions at the vacuum boundaries $o_{\boldsymbol{k}j}^{\boldsymbol{G}_\parallel, \mathrm{vac}}$ and $o_{\boldsymbol{k}j}^{\prime \boldsymbol{G}_\parallel, \mathrm{vac}}$. With these precalculated values the computation of the vacuum matching coefficients can be performed in $\mathcal{O}(N_{\mathrm{bas}} N_{\mathrm{PW2D}})$, where N_{PW2D} is the number of two-dimensional plane waves, which scales with $N_{\mathrm{PW}}^{2/3}$.

5.2 Interstitial contributions to the overlap and Hamilton matrices

The IR contributions to the overlap and Hamilton matrices are given by the integrals over the interstitial region

$$S_{ij}^{\boldsymbol{k},\mathrm{IR}} = \left\langle \phi_{\boldsymbol{k}i} \middle| \phi_{\boldsymbol{k}j} \right\rangle_{\mathrm{IR}} \tag{5.9}$$

and

$$H_{ij}^{\boldsymbol{k},\mathrm{IR}} = \left\langle \phi_{\boldsymbol{k}i} \middle| \hat{T} + V \middle| \phi_{\boldsymbol{k}j} \right\rangle_{\mathrm{IR}}, \tag{5.10}$$

where $\hat{T}$ is the kinetic energy operator and V denotes the effective potential. In analogy to the calculation of the corresponding integrals for the LAPW basis, also these integrals for the $(\mathrm{LA})^2\mathrm{PW}$ basis are calculated by transforming them into integrals over the whole unit cell. For this, we once again make use of the step function

$$\Theta(\boldsymbol{r}) = \begin{cases} 1 & \text{for } \boldsymbol{r} \in \mathrm{IR} \\ 0 & \text{for } \boldsymbol{r} \in \mathrm{MT}^{\alpha} \end{cases} \tag{5.11}$$

to suppress contributions coming from the MT spheres. Of course, the step function is analytically given in reciprocal space as

$$\Theta(\boldsymbol{G}) = \delta_{\boldsymbol{G},\boldsymbol{0}} - \sum_{\alpha} e^{-i\boldsymbol{G}\boldsymbol{\tau}_{\alpha}} \frac{4\pi (R_{\mathrm{MT}^{\alpha}})^3}{\Omega} \frac{j_1(GR_{\mathrm{MT}^{\alpha}})}{GR_{\mathrm{MT}^{\alpha}}}. \tag{5.12}$$

Beyond using the step function to transform the integral we also replace the MT augmentation of the $(\mathrm{LA})^2\mathrm{PW}$s by extending their IR parts into the spheres to obtain the functions

$$\tilde{\phi}_{\boldsymbol{k}j}(\boldsymbol{r}) = \frac{1}{\sqrt{\Omega}} \sum_{\boldsymbol{G}} o_{\boldsymbol{k}j}^{\boldsymbol{G}} e^{i(\boldsymbol{k}+\boldsymbol{G})\boldsymbol{r}}. \tag{5.13}$$

With these functions the contributions to the matrices become

$$S_{ij}^{\boldsymbol{k},\mathrm{IR}} = \left\langle \tilde{\phi}_{\boldsymbol{k}i} \middle| \Theta \middle| \tilde{\phi}_{\boldsymbol{k}j} \right\rangle_{\Omega} \tag{5.14}$$

and

$$H_{ij}^{\boldsymbol{k},\mathrm{IR}} = \left\langle \tilde{\phi}_{\boldsymbol{k}i} \middle| \Theta \hat{T} + \Theta V \middle| \tilde{\phi}_{\boldsymbol{k}j} \right\rangle_{\Omega}. \tag{5.15}$$

Analytically exact values for these contributions are obtained if the plane wave expansion of both, the step function Θ and the combined function ΘV, feature cutoffs at least twice as large as the cutoff for the plane wave expansion of the basis functions K_{max}.

In comparison to the corresponding matrix contributions for the LAPW basis, the computation of the IR contributions for the $(\mathrm{LA})^2\mathrm{PW}$ basis is computationally more expensive as the basis functions are not single plane waves but linear combinations of plane waves. Nevertheless, we find that they can be computed in a reasonable amount

of time by performing the calculations partly in real space and partly in reciprocal space. To do this, we first perform Fast Fourier Transformations on the functions $\tilde{\phi}_{\boldsymbol{k}j}(\boldsymbol{G})$, $\nabla^2\tilde{\phi}_{\boldsymbol{k}j}(\boldsymbol{G})$, $\Theta(\boldsymbol{G})$, and $\Theta V(\boldsymbol{G})$ to obtain them on a real space mesh that is fine enough to represent $\Theta(\boldsymbol{r})$ and $\Theta V(\boldsymbol{r})$ exactly according to their limited plane wave cutoffs.

In a second step we calculate the functions

$$\xi_{\boldsymbol{k}j}^{[\theta\phi]}(\boldsymbol{r}) = \Theta(\boldsymbol{r})\tilde{\phi}_{\boldsymbol{k}j}(\boldsymbol{r}), \tag{5.16}$$

$$\xi_{\boldsymbol{k}j}^{[\theta V\phi]}(\boldsymbol{r}) = \Theta V(\boldsymbol{r})\tilde{\phi}_{\boldsymbol{k}j}(\boldsymbol{r}), \tag{5.17}$$

and

$$\xi_{\boldsymbol{k}j}^{[\theta\nabla^2\phi]}(\boldsymbol{r}) = \Theta(\boldsymbol{r})\nabla^2\tilde{\phi}_{\boldsymbol{k}j}(\boldsymbol{r}) \tag{5.18}$$

on every point of the real space mesh and then transform these functions with another Fast Fourier Transformation back to reciprocal space[1].

With the reciprocal space representations of the functions $\xi_{\boldsymbol{k}j}^{[\theta\phi]}$, $\xi_{\boldsymbol{k}j}^{[\theta V\phi]}$, and $\xi_{\boldsymbol{k}j}^{[\theta\nabla^2\phi]}$, the final computation of the matrix elements reduces to a simple sum over products. In detail, one obtains the contributions to the overlap matrix as

$$\begin{aligned} S_{ij}^{\boldsymbol{k},\mathrm{IR}} &= \left\langle \tilde{\phi}_{\boldsymbol{k}i} \middle| \Theta \middle| \tilde{\phi}_{\boldsymbol{k}j} \right\rangle_\Omega \\ &= \sum_{\boldsymbol{G}} \tilde{\phi}_{\boldsymbol{k}i}(\boldsymbol{G})\xi_{\boldsymbol{k}j}^{[\theta\phi]}(\boldsymbol{G}) \end{aligned} \tag{5.19}$$

and a hermitian form of the contributions to the Hamilton matrix as

$$\begin{aligned} H_{ij}^{\boldsymbol{k},\mathrm{IR}} &= \left\langle \tilde{\phi}_{\boldsymbol{k}i} \middle| \Theta\hat{T} + \Theta V \middle| \tilde{\phi}_{\boldsymbol{k}j} \right\rangle_\Omega \\ &= -\frac{1}{4}\sum_{\boldsymbol{G}} \xi_{\boldsymbol{k}j}^{[\theta\phi]}(\boldsymbol{G})\nabla^2\tilde{\phi}_{\boldsymbol{k}i}(\boldsymbol{G}) + \tilde{\phi}_{\boldsymbol{k}i}(\boldsymbol{G})\xi_{\boldsymbol{k}j}^{[\theta\nabla^2\phi]}(\boldsymbol{G}) \\ &\quad + \sum_{\boldsymbol{G}} \tilde{\phi}_{\boldsymbol{k}i}(\boldsymbol{G})\xi_{\boldsymbol{k}j}^{[\theta V\phi]}(\boldsymbol{G}). \end{aligned} \tag{5.20}$$

The reason why this last step is performed in reciprocal space is that the sums only cover those $\boldsymbol{G}$ vectors with $|\boldsymbol{k}+\boldsymbol{G}| \leq K_{\max}$. The real space mesh, on the other hand, is constructed to represent much larger $\boldsymbol{G}$ vectors, such that it consists of 8 times more grid points. In the calculation of these contributions only the runtime of the last step scales cubically with the system size as $\mathcal{O}(N_{\mathrm{bas}}^2 N_{\mathrm{PW}})$, where N_{bas} is the number of $(\mathrm{LA})^2\mathrm{PW}$ basis functions. The time requirements of the other parts of the calculation have a more friendly scaling behavior and become less relevant when going to materials with larger unit cells.

In a concluding remark, we sketch the computation of the IR contributions for the example of the overlap matrix in figure 5.1. We also note that these contributions to

[1] Note that the factor $e^{i\boldsymbol{k}\boldsymbol{r}}$ in the functions is excluded from the operations in real space.

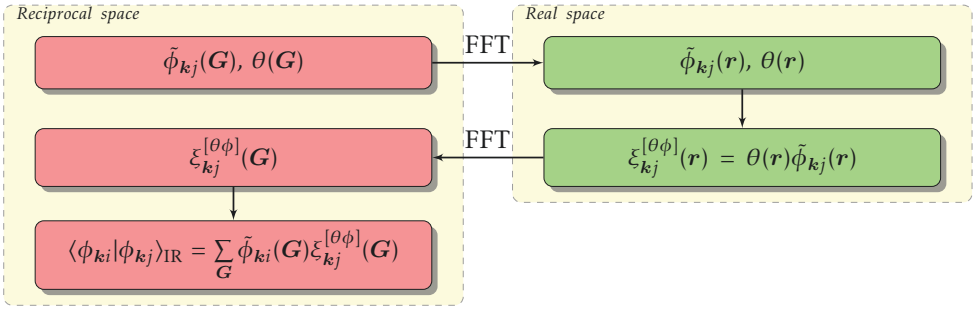

Figure 5.1.: Calculation of the IR contributions to the overlap matrix. We first perform a Fast Fourier Transformation on $\tilde{\phi}_{\boldsymbol{k}j}$ and θ to obtain these functions on a real space mesh. There, we calculate the product of the two functions, $\xi^{[\theta\phi]}_{\boldsymbol{k}j}$, and transform it back to reciprocal space. Finally, the repective matrix element is obtained by a simple sum of products in reciprocal space.

the overlap matrix and the kinetic energy contributions to the Hamilton matrix do not depend on the respective iteration of the self-consistency cycle, such that they can be precomputed, stored, and reused in every iteration. Though the time requirements for the computation of these contributions are limited, we find that such a precomputation approach is indeed an improvement when it comes to the overall runtime. For the example realization of the (LA)^{2}PW basis in this work we go this route. However, note that this comes at the prize of increased storage requirements scaling with $\mathcal{O}(N_{\mathrm{bas}}(N_{\mathrm{bas}}+1)/2)$. Depending on the respective computer architecture the alternative route of recalculating these contributions in every iteration may also be reasonable.

5.3 Muffin-tin contributions to the overlap and Hamilton matrices

Similarly to the discussion on the MT contributions in the case of the LAPW basis, we split the discussion on the corresponding contributions for (LA)^{2}PW basis functions into the contributions to the overlap matrix $S^{\boldsymbol{k},\alpha}_{ij}$, the Hamilton matrix contributions originating from the kinetic energy operator and the spherical part of the potential $H^{\boldsymbol{k},\alpha,\mathrm{sphr}}_{ij}$, and the Hamilton matrix contributions due to the nonspherical part of the potential $H^{\boldsymbol{k},\alpha,\mathrm{nsphr}}_{ij}$. Of course, the first two of these types of contributions are strongly connected.

We start by discussing the contributions to the overlap matrix. Considering the

form of the (LA)^{2}PW basis functions in the MT spheres,

$$\phi^{\alpha}_{\boldsymbol{k}j}(\boldsymbol{r}) = \sum_{L} \left[a^{L\alpha}_{\boldsymbol{k}j} u^{\alpha}_{l}(r_{\alpha}, E^{\alpha}_{l}) + b^{L\alpha}_{\boldsymbol{k}j} \dot{u}^{\alpha}_{l}(r_{\alpha}, E^{\alpha}_{l}) \right] Y_{L}(\hat{\boldsymbol{r}}_{\boldsymbol{\alpha}}), \tag{5.21}$$

and also the orthogonality relations between different spherical harmonics and between the radial functions $u^{\alpha}_{l}(r_{\alpha}, E^{\alpha}_{l})$ and $\dot{u}^{\alpha}_{l}(r_{\alpha}, E^{\alpha}_{l})$, we can write down the MT contributions to the overlap matrix as

$$\begin{aligned} S^{\boldsymbol{k},\alpha}_{ij} &= \left\langle \phi^{\alpha}_{\boldsymbol{k}i} \middle| \phi^{\alpha}_{\boldsymbol{k}j} \right\rangle \\ &= \sum_{L} a^{*L\alpha}_{\boldsymbol{k}i} a^{L\alpha}_{\boldsymbol{k}j} + b^{*L\alpha}_{\boldsymbol{k}i} b^{L\alpha}_{\boldsymbol{k}j} \left\langle \dot{u}^{\alpha}_{l} \middle| \dot{u}^{\alpha}_{l} \right\rangle \\ &= \sum_{l} S^{\boldsymbol{k},\alpha,l}_{ij}. \end{aligned} \tag{5.22}$$

After obtaining the matching coefficients with equation (5.6) we compute the contributions to the overlap matrix directly with equation (5.22).

To calculate the spherical contributions to the Hamilton matrix we make use of the fact that the radial functions $u^{\alpha}_{l}(r_{\alpha}, E^{\alpha}_{l})$ and $\dot{u}^{\alpha}_{l}(r_{\alpha}, E^{\alpha}_{l})$ are constructed to fulfill

$$\hat{H}^{\alpha,\mathrm{sphr}} |u^{\alpha}_{l}\rangle = E_{l} |u^{\alpha}_{l}\rangle \tag{5.23}$$

and

$$\hat{H}^{\alpha,\mathrm{sphr}} |\dot{u}^{\alpha}_{l}\rangle + \dot{\hat{H}}^{\alpha,\mathrm{sphr}} |u^{\alpha}_{l}\rangle = E_{l} |\dot{u}^{\alpha}_{l}\rangle + |u^{\alpha}_{l}\rangle, \tag{5.24}$$

where we once again neglect the very small $\dot{\hat{H}}^{\alpha,\mathrm{sphr}} |u^{\alpha}_{l}\rangle$ term. With these relations we can write down the associated contributions to the Hamilton matrix as

$$\begin{aligned} H^{\boldsymbol{k},\alpha,\mathrm{sphr}}_{ij} &= \left\langle \phi^{\alpha}_{\boldsymbol{k}i} \middle| \hat{H}^{\alpha,\mathrm{sphr}} \middle| \phi^{\alpha}_{\boldsymbol{k}j} \right\rangle \\ &= \sum_{L} E^{\alpha}_{l} \left(a^{L\alpha}_{\boldsymbol{k}i} \right)^{*} a^{L\alpha}_{\boldsymbol{k}j} + \frac{1}{2} \left[\left(a^{L\alpha}_{\boldsymbol{k}i} \right)^{*} b^{L\alpha}_{\boldsymbol{k}j} + \left(b^{L\alpha}_{\boldsymbol{k}i} \right)^{*} a^{L\alpha}_{\boldsymbol{k}j} \right] + E^{\alpha}_{l} \left(b^{L\alpha}_{\boldsymbol{k}i} \right)^{*} b^{L\alpha}_{\boldsymbol{k}j} \left\langle \dot{u}^{\alpha}_{l} \middle| \dot{u}^{\alpha}_{l} \right\rangle \\ &= \sum_{l} E^{\alpha}_{l} S^{l\alpha}_{ij}(\boldsymbol{k}) + \frac{1}{2} \sum_{L} \left(a^{L\alpha}_{\boldsymbol{k}i} \right)^{*} b^{L\alpha}_{\boldsymbol{k}j} + \left(b^{L\alpha}_{\boldsymbol{k}i} \right)^{*} a^{L\alpha}_{\boldsymbol{k}j}, \end{aligned} \tag{5.25}$$

where we already averaged over the application of the Hamilton operator to the left and to the right basis function to obtain a hermitian matrix.

In the calculation of the corresponding contributions to $S^{\boldsymbol{k},\alpha}_{\boldsymbol{G}\boldsymbol{G}'}$ and $H^{\boldsymbol{k},\alpha,\mathrm{sphr}}_{\boldsymbol{G}\boldsymbol{G}'}$ for LAPW basis functions discussed in section 3.2.3.2, one can analytically perform the summation over the m quantum number. As we have seen, this reduces the required time to perform these calculations by a factor of about 10. Unfortunately this procedure is strongly bound to the interstitial representation of the LAPWs which are simple plane waves. It cannot reasonably be translated to an equivalent elimination of the m summation in the case of (LA)^{2}PWs. Thus, we end up with a scaling behavior

for the required runtime to calculate these contributions of $\mathcal{O}\left((l_{\max}+1)^2 N_{\text{atom}} N_{\text{bas}}^2\right)$, which is a cubic scaling with respect to the size of the unit cell.

The MT contributions to the Hamilton matrix due to the nonspherical part of the effective potential are calculated in analogy to section 3.2.3.3 by first calculating the integrals (cf. equation (3.61))

$$t_{LL'}^{\alpha[\circ][\diamond]} = \left\langle {}^{[\circ]}u_l^{\alpha} Y_L \middle| \hat{H}^{\alpha,\text{nsphr}} \middle| {}^{[\diamond]}u_l^{\alpha} Y_{L'} \right\rangle, \tag{5.26}$$

where $[\circ]$ and $[\diamond]$ either denote u or $\dot{u}$, respectively. The Hamilton matrix contributions $H_{ij}^{\boldsymbol{k},\alpha,\text{nsphr}}$ then become

$$\begin{aligned}
H_{ij}^{\boldsymbol{k},\alpha,\text{nsphr}} &= \left\langle \phi_{\boldsymbol{k}i}^{\alpha} \middle| \hat{H}^{\alpha,\text{nsphr}} \middle| \phi_{\boldsymbol{k}j}^{\alpha} \right\rangle \\
&= \sum_{LL'} \left(a_{\boldsymbol{k}i}^{L\alpha}\right)^* t_{LL'}^{\alpha[\,][\,]} a_{\boldsymbol{k}j}^{L'\alpha} + \left(a_{\boldsymbol{k}i}^{L\alpha}\right)^* t_{LL'}^{\alpha[\,][\cdot]} b_{\boldsymbol{k}j}^{L'\alpha} \\
&\quad + \left(b_{\boldsymbol{k}i}^{L\alpha}\right)^* t_{LL'}^{\alpha[\cdot][\,]} a_{\boldsymbol{k}j}^{L'\alpha} + \left(b_{\boldsymbol{k}i}^{L\alpha}\right)^* t_{LL'}^{\alpha[\cdot][\cdot]} b_{\boldsymbol{k}j}^{L'\alpha} \\
&= \sum_{L} \left(a_{\boldsymbol{k}i}^{L\alpha}\right)^* \left(\sum_{L'} t_{LL'}^{\alpha[\,][\,]} a_{\boldsymbol{k}j}^{L'\alpha} \right) + \left(a_{\boldsymbol{k}i}^{L\alpha}\right)^* \left(\sum_{L'} t_{LL'}^{\alpha[\,][\cdot]} b_{\boldsymbol{k}j}^{L'\alpha} \right) \\
&\quad + \left(b_{\boldsymbol{k}i}^{L\alpha}\right)^* \left(\sum_{L'} t_{LL'}^{\alpha[\cdot][\,]} a_{\boldsymbol{k}j}^{L'\alpha} \right) + \left(b_{\boldsymbol{k}i}^{L\alpha}\right)^* \left(\sum_{L'} t_{LL'}^{\alpha[\cdot][\cdot]} b_{\boldsymbol{k}j}^{L'\alpha} \right).
\end{aligned} \tag{5.27}$$

For the LAPW basis this part of the matrix setup dominates the runtime of the overall matrix setup. However, in comparison to the previously discussed MT contributions, the LAPW basis has no advantages over the (LA)^{2}PW basis in this case. Thus, an efficient (LA)^{2}PW basis profits directly from its smaller basis set size, as the runtime for this part of the setup scales with $\mathcal{O}\left((l_{\max}^{\text{nsphr}}+1)^2 N_{\text{atom}} N_{\text{bas}}^2\right)$.

5.4 Vacuum contributions to the overlap and Hamilton matrices

Similarly to the discussion on the vacuum contributions for the LAPW basis in section 3.2.4, we split the contributions to the Hamilton matrix into a part originating from the averaged effective potential $H_{ij}^{\boldsymbol{k},\text{vac,avg}}$ and a part due to the deviations from this averaged potential $H_{ij}^{\boldsymbol{k},\text{vac,dev}}$. We start, however, with the discussion on the contributions to the overlap matrix.

In the vacuum regions the (LA)^{2}PW basis functions have the form

$$\phi_{\boldsymbol{k}_\parallel j}^{\text{vac}}(\boldsymbol{r}) = \sum_{\boldsymbol{G}_\parallel} \left[a_{\boldsymbol{k}_\parallel j}^{\boldsymbol{G}_\parallel,\text{vac}} u_{\boldsymbol{k}_\parallel \boldsymbol{G}_\parallel}^{\text{vac}}(z, E^{\text{vac}}) + b_{\boldsymbol{k}_\parallel j}^{\boldsymbol{G}_\parallel,\text{vac}} \dot{u}_{\boldsymbol{k}_\parallel \boldsymbol{G}_\parallel}^{\text{vac}}(z, E^{\text{vac}}) \right] \frac{1}{\sqrt{A}} e^{i(\boldsymbol{k}_\parallel + \boldsymbol{G}_\parallel)\boldsymbol{r}_\parallel}. \tag{5.28}$$

Considering the orthogonality relation between the different 2D plane waves in this equation and the orthogonality relation between $u^{\mathrm{vac}}_{\boldsymbol{k}_\parallel \boldsymbol{G}_\parallel}(z, E^{\mathrm{vac}})$ and $\dot{u}^{\mathrm{vac}}_{\boldsymbol{k}_\parallel \boldsymbol{G}_\parallel}(z, E^{\mathrm{vac}})$ we can directly write down the contributions to the overlap matrix in analogy to equation (3.69) as

$$S_{ij}^{\boldsymbol{k},\mathrm{vac}} = \sum_{\boldsymbol{G}_\parallel} \left[\left(a_{\boldsymbol{k}_\parallel i}^{\boldsymbol{G}_\parallel,\mathrm{vac}} \right)^* a_{\boldsymbol{k}_\parallel j}^{\boldsymbol{G}_\parallel,\mathrm{vac}} + \langle \dot{u}^{\mathrm{vac}}_{\boldsymbol{k}_\parallel \boldsymbol{G}_\parallel} | \dot{u}^{\mathrm{vac}}_{\boldsymbol{k}_\parallel \boldsymbol{G}_\parallel} \rangle_{\mathrm{vac}} \left(b_{\boldsymbol{k}_\parallel i}^{\boldsymbol{G}_\parallel,\mathrm{vac}} \right)^* b_{\boldsymbol{k}_\parallel j}^{\boldsymbol{G}_\parallel,\mathrm{vac}} \right]. \tag{5.29}$$

The contributions due to the averaged effective potential and the kinetic energy operator are obtained by making use of the relations

$$\hat{H}^{\mathrm{vac,avg}} | u^{\mathrm{vac}}_{\boldsymbol{k}_\parallel \boldsymbol{G}_\parallel} \rangle = E^{\mathrm{vac}} | u^{\mathrm{vac}}_{\boldsymbol{k}_\parallel \boldsymbol{G}_\parallel} \rangle \tag{5.30}$$

and

$$\hat{H}^{\mathrm{vac,avg}} | \dot{u}^{\mathrm{vac}}_{\boldsymbol{k}_\parallel \boldsymbol{G}_\parallel} \rangle = E^{\mathrm{vac}} | \dot{u}^{\mathrm{vac}}_{\boldsymbol{k}_\parallel \boldsymbol{G}_\parallel} \rangle + | u^{\mathrm{vac}}_{\boldsymbol{k}_\parallel \boldsymbol{G}_\parallel} \rangle. \tag{5.31}$$

In a hermitian form these contributions become

$$\begin{aligned} H_{ij}^{\boldsymbol{k},\mathrm{vac,avg}} &= \left\langle \phi^{\mathrm{vac}}_{\boldsymbol{k}_\parallel i} \middle| \hat{H}^{\mathrm{vac,avg}} \middle| \phi^{\mathrm{vac}}_{\boldsymbol{k}_\parallel j} \right\rangle \\ &= \sum_{\boldsymbol{G}_\parallel} \left\{ E^{\mathrm{vac}} \left[\left(a_{\boldsymbol{k}_\parallel i}^{\boldsymbol{G}_\parallel,\mathrm{vac}} \right)^* a_{\boldsymbol{k}_\parallel j}^{\boldsymbol{G}_\parallel,\mathrm{vac}} + \langle \dot{u}^{\mathrm{vac}}_{\boldsymbol{k}_\parallel \boldsymbol{G}_\parallel} | \dot{u}^{\mathrm{vac}}_{\boldsymbol{k}_\parallel \boldsymbol{G}'_\parallel} \rangle_{\mathrm{vac}} \left(b_{\boldsymbol{k}_\parallel i}^{\boldsymbol{G}_\parallel,\mathrm{vac}} \right)^* b_{\boldsymbol{k}_\parallel j}^{\boldsymbol{G}_\parallel,\mathrm{vac}} \right] \right. \\ &\qquad \left. + \frac{1}{2} \left[\left(a_{\boldsymbol{k}_\parallel i}^{\boldsymbol{G}_\parallel,\mathrm{vac}} \right)^* b_{\boldsymbol{k}_\parallel j}^{\boldsymbol{G}_\parallel,\mathrm{vac}} + \left(b_{\boldsymbol{k}_\parallel i}^{\boldsymbol{G}_\parallel,\mathrm{vac}} \right)^* a_{\boldsymbol{k}_\parallel j}^{\boldsymbol{G}_\parallel,\mathrm{vac}} \right] \right\}. \end{aligned} \tag{5.32}$$

Finally, in the calculation of the contributions to the Hamilton matrix due to the deviations from the averaged potential we again make use of the $t^{\mathrm{vac}[\circ][\diamond]}_{\boldsymbol{k}_\parallel \boldsymbol{G}_\parallel \boldsymbol{G}'_\parallel}$ coefficient defined in equation (3.71). We end up with the expression

$$\begin{aligned} H_{ij}^{\boldsymbol{k},\mathrm{vac,dev}} &= \left\langle \phi^{\mathrm{vac}}_{\boldsymbol{k}_\parallel i} \middle| V^{\mathrm{vac,dev}}_{\mathrm{eff}}(\boldsymbol{r}) \middle| \phi^{\mathrm{vac}}_{\boldsymbol{k}_\parallel j} \right\rangle \\ &= \sum_{\boldsymbol{G}_\parallel} \sum_{\boldsymbol{G}'_\parallel} \left(a_{\boldsymbol{k}_\parallel i}^{\boldsymbol{G}_\parallel,\mathrm{vac}} \right)^* t^{\mathrm{vac}[\ ][\ ]}_{\boldsymbol{k}_\parallel \boldsymbol{G}_\parallel \boldsymbol{G}'_\parallel} a_{\boldsymbol{k}_\parallel j}^{\boldsymbol{G}'_\parallel,\mathrm{vac}} + \left(a_{\boldsymbol{k}_\parallel i}^{\boldsymbol{G}_\parallel,\mathrm{vac}} \right)^* t^{\mathrm{vac}[\ ][\cdot]}_{\boldsymbol{k}_\parallel \boldsymbol{G}_\parallel \boldsymbol{G}'_\parallel} b_{\boldsymbol{k}_\parallel j}^{\boldsymbol{G}'_\parallel,\mathrm{vac}} \\ &\qquad + \left(b_{\boldsymbol{k}_\parallel i}^{\boldsymbol{G}_\parallel,\mathrm{vac}} \right)^* t^{\mathrm{vac}[\cdot][\ ]}_{\boldsymbol{k}_\parallel \boldsymbol{G}_\parallel \boldsymbol{G}'_\parallel} a_{\boldsymbol{k}_\parallel j}^{\boldsymbol{G}'_\parallel,\mathrm{vac}} + \left(b_{\boldsymbol{k}_\parallel i}^{\boldsymbol{G}_\parallel,\mathrm{vac}} \right)^* t^{\mathrm{vac}[\cdot][\cdot]}_{\boldsymbol{k}_\parallel \boldsymbol{G}_\parallel \boldsymbol{G}'_\parallel} b_{\boldsymbol{k}_\parallel j}^{\boldsymbol{G}'_\parallel,\mathrm{vac}}. \end{aligned} \tag{5.33}$$

By precalculating the factor $\sum_{\boldsymbol{G}'_\parallel} t^{\mathrm{vac}[\ ][\ ]}_{\boldsymbol{k}_\parallel \boldsymbol{G}_\parallel \boldsymbol{G}'_\parallel} a_{\boldsymbol{k}_\parallel j}^{\boldsymbol{G}'_\parallel,\mathrm{vac}}$ and its 3 associated terms in the other summands for each $\boldsymbol{G}_\parallel$, the time requirements for the calculation of this matrix scale with $\mathcal{O}(N_{\mathrm{bas}}^2 N_{\mathrm{PW2D}})$. Under the assumption of the proportionality $N_{\mathrm{PW2D}} \propto N_{\mathrm{PW}}^{2/3}$ this scaling behavior is better than the cubical scaling required to solve the generalized eigenvalue problem.

5.5 Representation of the eigenfunctions and construction of the valence density

In a typical FLAPW calculation most of the steps succeeding the diagonalization, performed to solve the generalized eigenvalue problem, are not very time-consuming. Thus, to simplify the integration of the $(LA)^2PW$ basis into an existing FLAPW code it is desirable to use the existing FLAPW code for these parts of the calculation. However, after solving the generalized eigenvalue problem for the $(LA)^2PW$ overlap and Hamilton matrices the eigenfunctions are given by linear combinations of $(LA)^2PW$s as

$$\psi_{\boldsymbol{k}}^{\nu}(\boldsymbol{r}) = \sum_{j} z_{\boldsymbol{k}j}^{\nu} \phi_{\boldsymbol{k}j}(\boldsymbol{r}), \tag{5.34}$$

where $z_{\boldsymbol{k}j}^{\nu}$ is the expansion coefficient of the ν-th eigenfunction into the j-th $(LA)^2PW$. To come into a position where we can reuse the FLAPW code for the succeeding calculation steps we have to transform this representation into the corresponding LAPW form (cf. equation (3.76)).

One exception to this approach is the calculation of the MT matching coefficients of the eigenfunctions (cf. equations (3.78) and (3.79)). The calculation of these coefficients is the most time consuming step after the diagonalization and its efficiency can easily be increased by performing the calculation with the $(LA)^2PW$ representation of the eigenfunctions. In detail, we calculate the matching coefficients directly with the equations

$$A_{\boldsymbol{k}\nu}^{L\alpha} = \sum_{j} z_{\boldsymbol{k}j}^{\nu} a_{\boldsymbol{k}j}^{L\alpha} \tag{5.35}$$

and

$$B_{\boldsymbol{k}\nu}^{L\alpha} = \sum_{j} z_{\boldsymbol{k}j}^{\nu} b_{\boldsymbol{k}j}^{L\alpha}, \tag{5.36}$$

where the matching coefficients for the basis functions $a_{\boldsymbol{k}j}^{L\alpha}$ and $b_{\boldsymbol{k}j}^{L\alpha}$ are once again calculated on the fly by solving the equation system (5.6).

For every other part of the self-consistency loop succeeding the diagonalization we transform the representation of the eigenfunctions back into LAPW form. We realize that such a transformation can be performed by only considering the interstitial part of the basis functions as the space spanned by the $(LA)^2PW$ basis is a subspace of the space spanned by the LAPW basis. Thus, projecting the eigenfunctions from an $(LA)^2PW$ representation onto an LAPW representation does not yield any loss of information but is pointwise exact. Obtaining this pointwise exact representation in the interstitial region is enough since the matching conditions at the MT sphere boundaries and the vacuum boundaries can be obtained from this representation, such that pointwise exact representations are also implied for the other regions.

We start by replacing the $(LA)^2PW$s by their interstitial parts extended over the whole unit cell $\tilde{\phi}_{\boldsymbol{k}j}(\boldsymbol{r})$ (cf. equation (5.13)) and do the same for the LAPWs to obtain

$\tilde{\phi}_{\boldsymbol{k}\boldsymbol{G}}(\boldsymbol{r})$. Also here the space spanned by the $\tilde{\phi}_{\boldsymbol{k}j}(\boldsymbol{r})$ is a subspace of the space spanned by the plane waves $\tilde{\phi}_{\boldsymbol{k}\boldsymbol{G}}(\boldsymbol{r})$.

For a given eigenfunction ν the transformation is then given by

$$\sum_{\boldsymbol{G}} z^{\nu}_{\boldsymbol{k}\boldsymbol{G}} \left|\tilde{\phi}_{\boldsymbol{k}\boldsymbol{G}}\right\rangle = \sum_{\boldsymbol{G}} \left|\tilde{\phi}_{\boldsymbol{k}\boldsymbol{G}}\right\rangle \sum_{\boldsymbol{G}'} \left(\tilde{S}^{-1}_{\boldsymbol{k}}\right)_{\boldsymbol{G}\boldsymbol{G}'} \sum_{j} \left\langle \tilde{\phi}_{\boldsymbol{k}\boldsymbol{G}'} \middle| z^{\nu}_{\boldsymbol{k}j} \middle| \tilde{\phi}_{\boldsymbol{k}j} \right\rangle, \tag{5.37}$$

where $\left(\tilde{S}^{-1}_{\boldsymbol{k}}\right)_{\boldsymbol{G}\boldsymbol{G}'}$ is the inverse of the overlap matrix between different plane waves. Due to the normalization of the plane waves with respect to the unit cell volume and the orthogonality relations between the plane waves this is an identity matrix. As a consequence the expression can be further simplified to

$$\sum_{\boldsymbol{G}} z^{\nu}_{\boldsymbol{k}\boldsymbol{G}} \left|\tilde{\phi}_{\boldsymbol{k}\boldsymbol{G}}\right\rangle = \sum_{\boldsymbol{G}} \left|\tilde{\phi}_{\boldsymbol{k}\boldsymbol{G}}\right\rangle \sum_{j} \left\langle \tilde{\phi}_{\boldsymbol{k}\boldsymbol{G}} \middle| z^{\nu}_{\boldsymbol{k}j} \middle| \tilde{\phi}_{\boldsymbol{k}j} \right\rangle, \tag{5.38}$$

which can be calculated for the eigenfunctions of all occupied states in a runtime scaling with $\mathcal{O}(N_{\mathrm{LAPW}} N_{\mathrm{bas}} N_{\mathrm{occ}})$. Finally, the expansion coefficients are plugged into the LAPW representation to obtain

$$\psi^{\nu}_{\boldsymbol{k}}(\boldsymbol{r}) = \sum_{\boldsymbol{G}} z^{\nu}_{\boldsymbol{k}\boldsymbol{G}} \phi_{\boldsymbol{k}\boldsymbol{G}}(\boldsymbol{r}). \tag{5.39}$$

The succeeding calculation steps are then performed as sketched in chapter 3.

6 A BASIS FROM EARLY EIGENFUNCTIONS

Contents

The idea of an (LA)^{2}PW basis presented in the preceding chapter is decoupled from the construction of the basis. Indeed, it is just a way of representing basis functions. In the general form of the (LA)^{2}PW basis functions,

$$\phi_{\boldsymbol{k}j}(\boldsymbol{r}) = \begin{cases} \frac{1}{\sqrt{\Omega}} \sum_{\boldsymbol{G}} o_{\boldsymbol{k}j}^{\boldsymbol{G}} e^{i(\boldsymbol{k}+\boldsymbol{G})\boldsymbol{r}} & \text{for } \boldsymbol{r} \in \text{IR} \\ \sum_{L} \left[a_{\boldsymbol{k}j}^{L\alpha} u_l^{\alpha}(r_\alpha, E_l^{\alpha}) + b_{\boldsymbol{k}j}^{L\alpha} \dot{u}_l^{\alpha}(r_\alpha, E_l^{\alpha}) \right] Y_L(\hat{\boldsymbol{r}}_{\boldsymbol{\alpha}}) & \text{for } \boldsymbol{r} \in \text{MT}^{\alpha} \end{cases}, \tag{6.1}$$

the plane wave expansion coefficients $o_{\boldsymbol{k}j}^{\boldsymbol{G}}$ are not yet determined. Of course, one can think of many different construction schemes for these coefficients. Here, we present a scheme that features a high description efficiency of the basis functions such that one obtains highly precise results with only very few basis functions and hence in a fraction of the required runtime of equivalent FLAPW calculations.

For the construction of the $o_{\boldsymbol{k}j}^{\boldsymbol{G}}$ coefficients we remark that we have already seen in chapter 4.2.2 that the changes of the effective potential in the MT spheres throughout the iterations of the self-consistency loop are very limited. As the MT spheres cover a large part of the unit cell and most of the charge within the unit cell, this translates to equivalently small changes of the overall wave functions in the whole unit cell. Indeed, we have also seen in chapter 4.2.3 that most of the interstitial part of the wave

functions of the self-consistent solution is already described by the associated wave functions obtained in the first iteration on the basis of the starting density, which is a superposition of atomic densities.

With this foundation we assume that the lowest eigenfunctions obtained in the first iteration of the self-consistency loop of a conventional FLAPW calculation should provide proper plane wave expansion coefficients for a highly efficient (LA)^{2}PW basis. Thus, we perform a single FLAPW iteration on top of the starting density to obtain eigenfunctions of the kind

$$\psi_{\boldsymbol{k}}^{\nu}(\boldsymbol{r}) = \sum_{\boldsymbol{G}} z_{\boldsymbol{kG}}^{\nu} \phi_{\boldsymbol{kG}}(\boldsymbol{r}). \tag{6.2}$$

For the other iterations of the self-consistency loop we use an (LA)^{2}PW basis with expansion coefficients

$$o_{\boldsymbol{kj}}^{\boldsymbol{G}} = z_{\boldsymbol{kG}}^{\nu}, \tag{6.3}$$

where $\nu = j$.

This approach of a *basis from early eigenfunctions* (BEE) is partly also motivated by a calculation scheme by Wu and Freeman [137] who repeatedly perform a single FLAPW iteration followed by several iterations with a basis of FLAPW eigenfunctions. This scheme uses very tiny basis sets for the iterations with the FLAPW eigenfunctions. The disadvantage of this approach is that each time a full FLAPW calculation is performed, one observes a large change in the electron density, such that considerably more iterations have to be performed to obtain a self consistent solution. On the other side this approach has the advantage that the solution is identical to the solution of a conventional FLAPW calculation. We go a different way in that we only perform a single conventional FLAPW iteration and then keep the plane wave expansion coefficients fixed. Thus, we allow deviations from the FLAPW calculation results. Such an approach was also sketched by Wu, though he did not provide any test results on such calculations. We add that we use larger basis sets than Wu and the calculation speedup that we show in the following sections strongly relies on the implementation of the matrix setup which in our case includes the precomputation and storage of certain quantities. Thus, it is connected to fixed $o_{\boldsymbol{kj}}^{\boldsymbol{G}}$ which is a condition that is not exploited in Wu's approach.

We also find in practice that a hybrid approach, in which only half of the (LA)^{2}PWs is constructed from the first conventional FLAPW iteration and the other half are conventional LAPWs with small wave vectors, is even more efficient than a basis that is solely constructed from early eigenfunctions. In the following a BEE-(LA)^{2}PW basis with N_{bas} functions denotes such a hybrid basis consisting of $N_{\text{bas}}/2$ basis functions from the first FLAPW iteration and also $N_{\text{bas}}/2$ LAPWs. The LAPWs in this basis are dealt with like every other (LA)^{2}PW, with the exception that several expressions given in chapter 5 are simplified whenever an LAPW is involved. We exploit such situations to further increase the efficiency. In detail, especially equations (5.19) and (5.20) reduce to simple products when an LAPW is on the left hand side of the

scalar product. Furthermore, to reduce the storage requirements we do not store the plane wave expansion coefficients and MT matching coefficients for LAPWs.

In the following we analyze the BEE-(LA)^{2}PW basis in detail. In section 6.1 we evaluate the accuracy of the BEE-F(LA)^{2}PW approach, before we investigate the obtained speedup in section 6.2. Next, in order to further speed up the calculations we develop and evaluate an approach to reduce the $l_{\max}$ requirements for the setup of the matrices in section 6.3. Finally, we provide some concluding remarks on the new basis in section 6.4.

6.1 Accuracy of the BEE-F(LA)^{2}PW approach

To gain confidence in the description efficiency of the new BEE-(LA)^{2}PW basis we perform BEE-F(LA)^{2}PW calculations on a couple of materials with strongly differing properties and investigate quantities that are highly sensitive to the precision of the calculation results. We especially concentrate on materials with different bonding mechanisms. For this we perform calculations on the already known metallically bonded fcc Cu, zinc blende SiC, and NaCl in rock-salt structure. Beyond these three materials we also perform calculations on the magnetically ordered compound FeRh in bcc B2 CsCl structure, where we especially observe the energy differences between different magnetic configurations. Finally, to evaluate the BEE-(LA)^{2}PW basis also for a thin film system, we perform a similar investigation on a strained 5 layer $CoPt_3$ film.

In F(LA)^{2}PW calculations the basis set size is controlled by the parameter N_{bas}, while the reciprocal plane wave cutoff $K_{\max}$, which controls the basis set size in the case of an LAPW basis, is a cutoff that controls to what precision the (LA)^{2}PW basis functions correspond to the idea of their construction principle. In this chapter we compare BEE-F(LA)^{2}PW to FLAPW calculations and vary both parameters, N_{bas} and $K_{\max}$, to get experience in the efficiency of the BEE-(LA)^{2}PW basis in contrast to LAPWs. Note that for same $K_{\max}$ parameters, FLAPW results are a precision limit for F(LA)^{2}PW calculations, since in such a case the (LA)^{2}PW basis spans a subspace of the space spanned by the LAPWs. Furthermore, in the limit of identical basis set sizes for F(LA)^{2}PW and FLAPW calculations with same $K_{\max}$ parameters, one ends up with identical results as the basis sets span the same space. Of course, an exception to this rule is the case in which one of function sets becomes linearly dependent. Besides these theoretical considerations we claim that the construction principle of the BEE-(LA)^{2}PW basis yields calculation results that come very near to FLAPW results, even for very small N_{bas} parameters.

To demonstrate this property of the BEE-F(LA)^{2}PW approach we determine for Cu, SiC, and NaCl the number of basis functions N_{bas} required to obtain total energies that differ by less than 25 μHtr per atom ($\sim$ 0.68 meV/atom or 0.016 kcal/mol[1]) from

[1] In this context the unit mole quantifies the number of atoms, not the number of formular units and also not the number of unit cells.

Table 6.1.: Calculational parameters for the evaluation of the BEE-(LA)^{2}PW basis. First, the table lists for each of the five investigated materials the XC functional, the crystal structure, the lattice constant, and the number of atoms in the unit cell. Next it shows the used MT radii, $l^{\alpha}_{\max}$, $l^{\alpha,\mathrm{nsphr}}_{\max}$, the number of $\boldsymbol{k}$ points in the IBZ, and the semicore states that are described with additional LOs in the valence framework. The table neither lists $K_{\max}$ nor N_{bas} as these parameters will be varied in the calculations.

parameter	Cu	SiC (Si, C)	NaCl (Na, Cl)	FeRh (Fe,Rh)	$CoPt_3$ (Co,Pt)
XC functional	PBE-GGA	PBE-GGA	PBE-GGA	PBE-GGA	PBE-GGA
crystal structure	fcc	zinc blende	rock-salt	CsCl	
lattice constant (a_0)[2]	6.831	8.238	10.620	5.66	$a = 7.68$, $c = 22.8$
atoms / unit cell	1	2	2	8	10
R_{MT} (a_0)	2.35	2.22, 1.25	2.52, 2.52	2.38, 2.38	2.4, 2.4
$l^{\alpha}_{\max}$	8	10, 8	8, 8	8, 8	10, 10
$l^{\alpha,\mathrm{nsphr}}_{\max}$	6	6, 4	6, 6	6, 6	8, 8
$\boldsymbol{k}$ points in IBZ	182	220	28	385	561
semicore LOs			2s,2p (Na)	4p (Rh)	5s (Pt)

the corresponding FLAPW result with same $K_{\max}$ and relate the respective basis set sizes to each other. Furthermore we repeat these calculations for different $K_{\max}$ to put the additional error due to the limited N_{bas} convergence in the case of the BEE-(LA)^{2}PW basis in context to typically accepted imprecisions due to the also limited $K_{\max}$ convergence in the corresponding FLAPW calculations.

The standard configuration of the materials taken under scrutiny is shown in table 6.1. Unless otherwise stated the calculations are performed with these parameters. Note that in this configuration the calculations are highly converged with respect to $l^{\alpha}_{\max}$ and on the other hand for Cu, SiC, and NaCl they are slightly underconverged with respect to $l^{\alpha,\mathrm{nsphr}}_{\max}$. As the setup of the spherical contributions to the matrices is more expensive for (LA)^{2}PWs than it is for conventional LAPWs, such a parametrization is a slight disadvantage for the BEE-(LA)^{2}PW basis. We consciously accept this disadvantage to avoid an overestimation of the speedup obtained with the BEE-(LA)^{2}PW basis.

Beyond the calculations on the total energy we also perform calculations on experimentally accessible quantities and compare the precision obtainable with different N_{bas} and $K_{\max}$ parameters for BEE-F(LA)^{2}PW and FLAPW calculations. In detail, we consider the calculation of equilibrium lattice constants and bulk moduli. The applied N_{bas} parameters are obtained through two different criteria. The first criterion is the already calculated number of basis functions required to obtain a precision of the total energy corresponding to a deviation from the FLAPW result of less than

[2] The experimental lattice constants for Cu, SiC, and NaCl were taken from [133], [134], and [135], respectively.

25 μHtr per atom. The other criterion considers for each atom in the unit cell the maximal l quantum number l^{α}_{phys} in the occupied states of the associated isolated atom. In analogy to typical basis set sizes of basis sets with numerically determined atomic orbitals we then use a basis set with two basis functions per (l, m) channel up to $l^{\alpha}_{\text{phys}} + 1$ to end up with a basis set size of $N_{\text{bas}} = 2\sum_{\alpha}(l^{\alpha}_{\text{phys}} + 2)^2$.

Depending on the respective material we extend the set of observed quantities with further tests, which are sensitive to small imprecisions in calculation results.

6.1.1 Metallic test system: fcc and hcp Cu

Figure 6.1 displays the results of the total energy calculations on fcc Cu. Depending on the K_{max} cutoff we obtain different LAPW basis set sizes. Averaged over the number of $\boldsymbol{k}$ points we obtain 58 LAPWs for $K_{\text{max}} = 3.5\ a_0^{-1}$, 86 for $K_{\text{max}} = 4.0\ a_0^{-1}$, 123 for $K_{\text{max}} = 4.5\ a_0^{-1}$, and 168 for the reference result with $K_{\text{max}} = 5.0\ a_0^{-1}$. For the BEE-F(LA)^{2}PW approach the figure clearly shows that even for very small N_{bas} cutoffs the calculations reproduce the respective FLAPW results with very high precision. Independent of the K_{max} parameter the criterion of less than 25 μHtr/atom deviation from the FLAPW results is met for BEE-(LA)^{2}PW basis set sizes with $N_{\text{bas}} \geq 20$. For $K_{\text{max}} = 4.0\ a_0^{-1}$ or less this is an additional error of less than 6 % of the error due to the incomplete K_{max} convergence. This means that even for small N_{bas} parameters the error is mainly controlled by K_{max}. This is an important fact that will help us to put the measurements on the obtained speedup below into context. Finally, we note that the angular momentum criterion for the determination of the basis set size corresponds to $N_{\text{bas}} = 32$. For such a basis set the deviation of the BEE-F(LA)^{2}PW results from the FLAPW results is less than 5 μHtr/atom.

In table 6.2 we show results for the equilibrium lattice constant and bulk modulus of fcc Cu, both obtained through Murnaghan fits to sets of 11 total energy calculations for different test lattice constants. The table also shows calculations on the binding energy difference between fcc and hcp Cu, which is very small since both structures only differ by the stacking of the second nearest neighbor atoms. Thus, it is a highly sensitive test on the precision of the different basis sets. In the table we consider BEE-LA^{2}PW basis sets of 20 (BEE-LA^{2}PW-20) and 32 (BEE-LA^{2}PW-32) basis functions per atom, according to the two mentioned basis set size criteria.

Independent of the concrete basis, the BEE-FLA^{2}PW results for the equilibrium lattice constant reproduce the corresponding FLAPW results with a deviation of less than 0.003 %. In contrast to these very small deviations, the FLAPW results with $K_{\text{max}} = 3.5\ a_0^{-1}$ differ by 0.166 % from the results with $K_{\text{max}} = 4.5\ a_0^{-1}$. With a K_{max} of $4.0\ a_0^{-1}$ this deviation from the most precise result is still 0.054 %. Nevertheless, we consider the FLAPW result with $K_{\text{max}} = 4.0\ a_0^{-1}$ to be converged. A similar picture can be observed for the bulk modulus. While the deviations of less than 0.69 GPa (0.07 GPa) between the BEE-FLA^{2}PW-20(32) results and the corresponding FLAPW results are tiny, the different values of K_{max} make a larger difference. With respect to the best FLAPW result with $K_{\text{max}} = 4.5\ a_0^{-1}$ we observe a deviation of 3.42 GPa

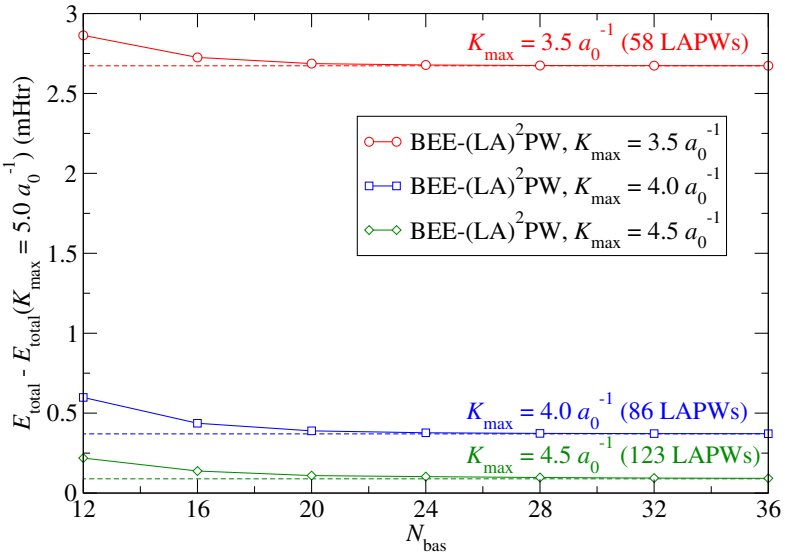

Figure 6.1.: Total energy calculations on fcc Cu. For each evaluated K_{max} the results obtained with different BEE-(LA)^{2}PW basis sets are shown by open symbols connected by solid lines. The associated results for the conventional LAPW basis sets are shown as horizontal dashed lines to which the BEE-F(LA)^{2}PW results converge with increasing number of basis functions N_{bas}. For each dashed line the figure also shows the $\boldsymbol{k}$ point averaged number of LAPW basis functions corresponding to the respective K_{max}. The total energies are given relative to the result obtained by the conventional FLAPW calculation with K_{max} = 5.0 a_0^{-1}. For $N_{bas} \geq 20$ the additional error introduced by the BEE-LA^{2}PW approach is less than 25 μHtr/atom.

for K_{max} = 3.5 a_0^{-1} and 1.16 GPa for K_{max} = 4.0 a_0^{-1}. Again, we consider the result with K_{max} = 4.0 a_0^{-1} to be converged. Finally, we discuss the precision of the binding energy difference between fcc and hcp Cu, where the fcc configuration is energetically more favorable. Again, we observe that the BEE-FLA^{2}PW results nearly stick to their FLAPW counterparts, with deviations of maximally 0.03 meV. On the other hand, the FLAPW results for different K_{max}, feature deviations up to 0.38 meV, which is an order of magnitude larger.

We also demonstrate the capability of the BEE-F(LA)^{2}PW approach to obtain accurate energies of the lowest unoccupied bands. For this, we compare the band structure calculated with the BEE-(LA)^{2}PW-20 basis to the one calculated with the conventional LAPW basis in figure 6.2. We observe that for energies up to about 30 eV above the Fermi level E_F the two band structures lie on top of each other. Beyond this energy, deviations between the two band structures can be observed. We note that the number of bands that can accurately be reproduced by the BEE-(LA)^{2}PW-20 basis corresponds to the 10 BEE-constructed basis functions within this basis set. This is a typical feature of BEE-F(LA)^{2}PW band structures that also implies that the num-

Table 6.2.: Convergence of physical quantities of fcc Cu. The number X in PW-X indicates the number of basis functions per atom in the respective basis set. BEE-(LA)^{2}PW-20(32) denotes the basis set determined according to the 25 μHtr/atom (angular momentum) criterion.

basis set	lattice constant a/a_{exp}	bulk modulus GPa	binding energy difference to hcp Cu meV/atom
$K_{\text{max}} = 3.5\ a_0^{-1}$			
LAPW-58	1.00316	143.55	8.73
BEE-(LA)^{2}PW-20	1.00314	143.51	8.71
BEE-(LA)^{2}PW-32	1.00316	143.55	8.73
$K_{\text{max}} = 4.0\ a_0^{-1}$			
LAPW-86	1.00428	141.29	8.42
BEE-(LA)^{2}PW-20	1.00425	141.41	8.39
BEE-(LA)^{2}PW-32	1.00427	141.36	8.42
$K_{\text{max}} = 4.5\ a_0^{-1}$			
LAPW-123	1.00483	140.13	8.35
BEE-(LA)^{2}PW-20	1.00483	140.82	8.38
BEE-(LA)^{2}PW-32	1.00483	140.20	8.33

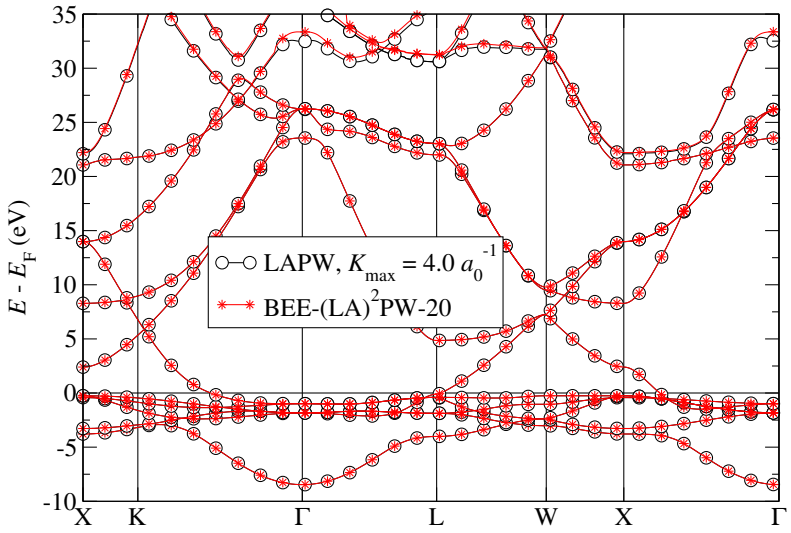

Figure 6.2.: Comparison of Cu band structures obtained with the conventional LAPW basis and the BEE-(LA)^{2}PW-20 basis, respectively. Both calculations use a reciprocal plane wave cutoff of $K_{\text{max}} = 4.0\ a_0^{-1}$.

ber of accurately reproduced bands can systematically be converged. Note however that the calculation of precise band energies far above the Fermi energy, also requires the extension of the basis with adequate LOs in the MT spheres. This was not done for the here presented comparison.

6.1.2 Covalent test system: Zinc blende SiC

The second test system is zinc blende SiC. The covalent bonds in this material are spatially directed and develop during the self-consistency cycle. This implies the development of inhomogeneities in the interstitial charge density and the potential. Thus, it is questionable if the eigenstates from the first iteration are adequate to describe every important property of the self consistent solution.

For a first estimation of the BEE-(LA)^{2}PW description efficiency for this material we show the results of total energy calculations with the BEE-F(LA)^{2}PW approach in comparison to the FLAPW method in figure 6.3. Depending on the $K_{\max}$ parameter, the FLAPW calculations use LAPW basis sets of 108 ($K_{\max} = 4.5\ a_0^{-1}$), 148 ($K_{\max} = 5.0\ a_0^{-1}$), 196 ($K_{\max} = 5.5\ a_0^{-1}$), or 255 ($K_{\max} = 6.0\ a_0^{-1}$) basis functions per atom, averaged over all $\boldsymbol{k}$ points. Similar to the picture observed for Cu, we find that even with very small N_{bas} parameters the BEE-F(LA)^{2}PW approach reproduces the corresponding FLAPW result with high precision. Independent of the $K_{\max}$ parameter as few as 48 basis functions (24 basis functions per atom) are enough to meet the convergence criterion of less than 25 μHtr/atom deviation from the FLAPW result. With the angular momentum criterion one obtains a basis set of 36 functions (18 functions per atom). The deviations from the FLAPW results with this smaller basis are still limited to 85 μHtr/atom. By relating the additional error due to the usage a BEE-(LA)^{2}PW basis to the error due the limited $K_{\max}$ convergence, we find that also for this material the remaining error is mainly controlled by $K_{\max}$.

Table 6.3 shows the results of the calculations on the equilibrium lattice constant and the bulk modulus for this material. For the lattice constant the BEE-F(LA)^{2}PW results deviate by no more than 0.002 % from their FLAPW counterparts, independent of the concrete BEE-(LA)^{2}PW basis set size. On the other hand, the deviations between FLAPW calculations with different $K_{\max}$ cutoffs are much larger. Here, the deviation between the largest and the smallest calculated equilibrium lattice constant is of the order of 0.109 %. For the bulk modulus the maximal deviations between the BEE-F(LA)^{2}PW results and their respective FLAPW counterparts are 0.15 GPa. The different $K_{\max}$ cutoffs make a larger difference. By increasing this value we observe oscillations of the calculated bulk modulus with deviations of more than 2 GPa between consecutive results. Obviously this quantity is not yet completely converged with respect to $K_{\max}$.

Finally, we also compare the band structure obtained with the BEE-F(LA)^{2}PW approach to the one obtained by an FLAPW calculation. Figure 6.4 shows that these two band structures lie on top of each other up to energies of more than 40 eV above the Fermi level E_{F}. Again, the number of accurate eigenenergies corresponds to the

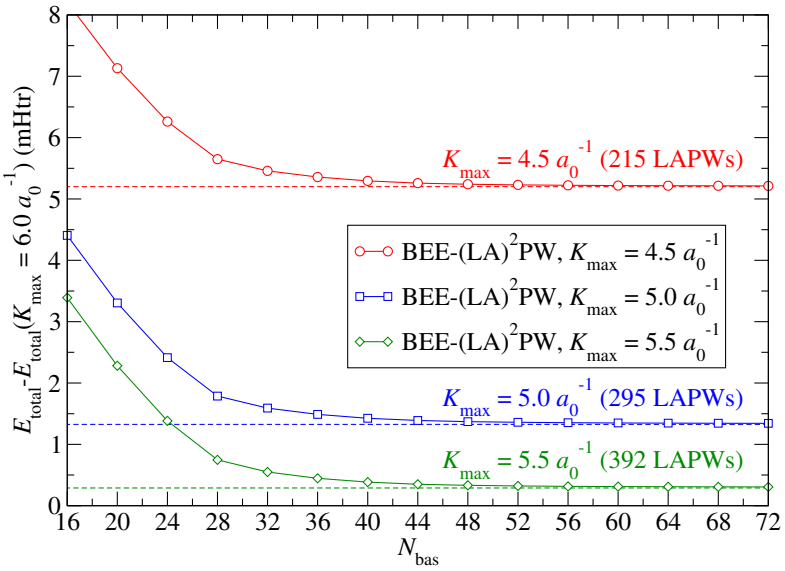

Figure 6.3.: Total energy calculations on SiC in zinc blende structure with 2 atoms in the unit cell. The total energies are given relative to the result from a conventional FLAPW calculation with $K_{max} = 6.0\ a_0^{-1}$. For $N_{bas} \geq 48$ the additional error due to the BEE-(LA)^{2}PW approach is less than 25 μHtr/atom. For explanations of symbols and lines, see caption of Fig. 6.1.

Table 6.3.: Convergence of physical quantities of SiC. BEE-(LA)^{2}PW-24(18) is a basis set determined according to the 25 μHtr/atom (angular momentum) criterion. For more details see Table 6.2.

basis set cutoff type	basis set kind	lattice constant a/a_{exp}	bulk modulus GPa
$K_{max} = 4.5\ a_0^{-1}$	LAPW-108	1.00811	215.07
	BEE-(LA)^{2}PW-18	1.00813	215.03
	BEE-(LA)^{2}PW-24	1.00811	215.09
$K_{max} = 5.0\ a_0^{-1}$	LAPW-148	1.00706	217.75
	BEE-(LA)^{2}PW-18	1.00707	217.62
	BEE-(LA)^{2}PW-24	1.00706	217.73
$K_{max} = 5.5\ a_0^{-1}$	LAPW-196	1.00701	215.69
	BEE-(LA)^{2}PW-18	1.00700	215.83
	BEE-(LA)^{2}PW-24	1.00699	215.84

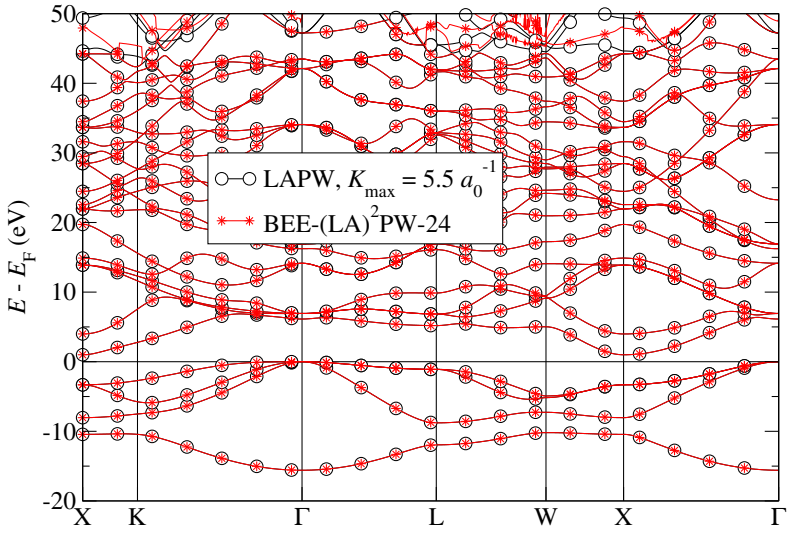

Figure 6.4.: Comparison of SiC band structures obtained with the conventional LAPW basis and the BEE-(LA)^{2}PW-24 basis, respectively. Both calculations use a reciprocal plane wave cutoff of $K_{max} = 5.5\ a_0^{-1}$.

number $N_{bas}/2$ of BEE-(LA)^{2}PW basis functions constructed by the BEE principle. Above the lowest $N_{bas}/2$ wave functions deviations between the two band structures can be significant. We especially observe that the BEE-F(LA)^{2}PW band structure exhibits discontinuities far above the Fermi level. This is due to the asymmetric cutoff for the $N_{bas}/2$ basis functions that are actually LAPWs. By using a symmetric reciprocal cutoff parameter for these basis functions these artifacts of the BEE-F(LA)^{2}PW band structure can be eliminated.

6.1.3 Ionic test system: Rock-salt NaCl

The third material under inspection is NaCl in rock-salt structure. As it is typical for ionically bonded materials, one can observe a charge transfer in this material taking place in the first iterations of the self-consistency cycle. This implies a challenge for the BEE-F(LA)^{2}PW approach as the BEE-(LA)^{2}PW basis is constructed in the very first iteration, based on a setup with a superposition of atomic densities. Again it is not clear if such a basis is adequate to describe the Kohn-Sham wave functions of the self-consistent solution.

The results of the total-energy calculations on this material are shown in figure 6.5. Averaged over the $\boldsymbol{k}$ points, the FLAPW calculations use LAPW basis sets of 69 ($K_{max} = 3.0\ a_0^{-1}$), 108 ($K_{max} = 3.5\ a_0^{-1}$), 162 ($K_{max} = 4.0\ a_0^{-1}$), or 231 ($K_{max} = 4.5\ a_0^{-1}$) basis functions per atom. The energies obtained with the FLAPW calculations are reproduced to within 25 μHtr/atom by the corresponding BEE-F(LA)^{2}PW calculations

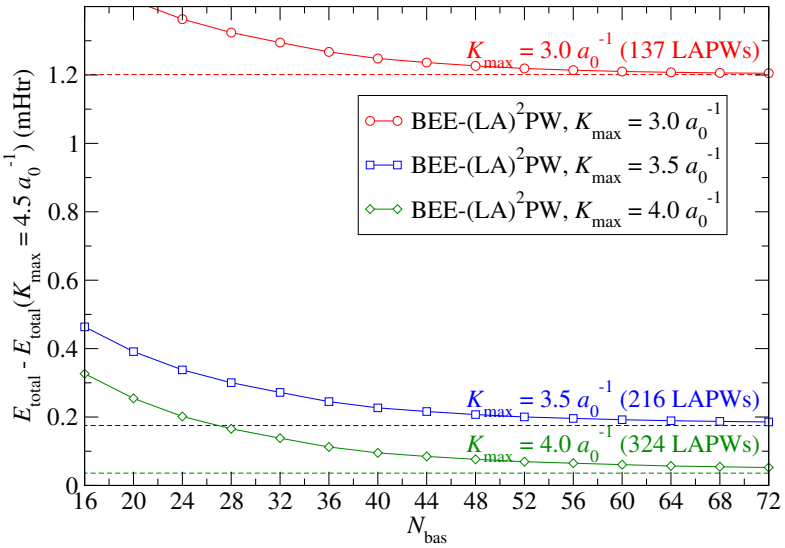

Figure 6.5.: Total energy calculations on NaCl in rock salt structure with 2 atoms in the unit cell. The total energies are given relative to the result from a conventional FLAPW calculation with K_{max} = 4.5 a_0^{-1}. For $N_{bas} \geq 44$ the additional error due to the BEE-(LA)^{2}PW approach is less than 25 μHtr/atom. For explanations of symbols and lines, see caption of Fig. 6.1.

with at least 44 basis functions (22 basis functions per atom). With the angular momentum criterion one ends up with a BEE-(LA)^{2}PW basis set size of 30 functions[3]. Such a small BEE-(LA)^{2}PW basis set still yields an agreement to the FLAPW results with deviations of less than 58 μHtr/atom, independent of K_{max}. However, beyond this very good agreement between the BEE-F(LA)^{2}PW and FLAPW total energies, we note that the LAPW basis already offers a very efficient description of this material, so that in this case the benefits of using a BEE-(LA)^{2}PW basis are limited.

Beyond the charge transfer, NaCl has another property that imposes a challenge on the BEE-F(LA)^{2}PW approach. This is its very small bulk modulus, which, according to the most precise FLAPW result in table 6.4, is only 23.6 GPa. Due to this property the determination of the lattice constant is highly sensitive to any deviations in the calculated total energies. This is visible in the results obtained for the equilibrium lattice constant in table 6.4. We find that the deviations of the BEE-F(LA)^{2}PW results from the FLAPW results are an order of magnitude larger than observed for the previously discussed materials. In detail, the BEE-(LA)^{2}PW-22 basis yields a maximal deviation of 0.030 % from the FLAPW results, while the BEE-(LA)^{2}PW-15 basis increases this value to 0.049 %. On the other hand, the maximal deviation between

[3]The 30 basis functions are 4 basis functions for the semicore states in Na, 8 basis functions for the l_{phys} of Na, and 18 basis functions for the l_{phys} of Cl.

Table 6.4.: Convergence of physical quantities of NaCl. BEE-(LA)^{2}PW-22(15) is a basis set determined according to the 25 μHtr/atom (angular momentum) criterion. For more details see Table 6.2.

basis set cutoff type	basis set kind	lattice constant a/a_{exp}	bulk modulus GPa
	LAPW-69	1.01439	24.06
$K_{\mathrm{max}} = 3.0\ a_0^{-1}$	BEE-(LA)^{2}PW-15	1.01396	24.26
	BEE-(LA)^{2}PW-22	1.01424	24.13
	LAPW-108	1.01488	23.74
$K_{\mathrm{max}} = 3.5\ a_0^{-1}$	BEE-(LA)^{2}PW-15	1.01439	23.95
	BEE-(LA)^{2}PW-22	1.01458	23.92
	LAPW-162	1.01488	23.60
$K_{\mathrm{max}} = 4.0\ a_0^{-1}$	BEE-(LA)^{2}PW-15	1.01438	23.81
	BEE-(LA)^{2}PW-22	1.01465	23.70

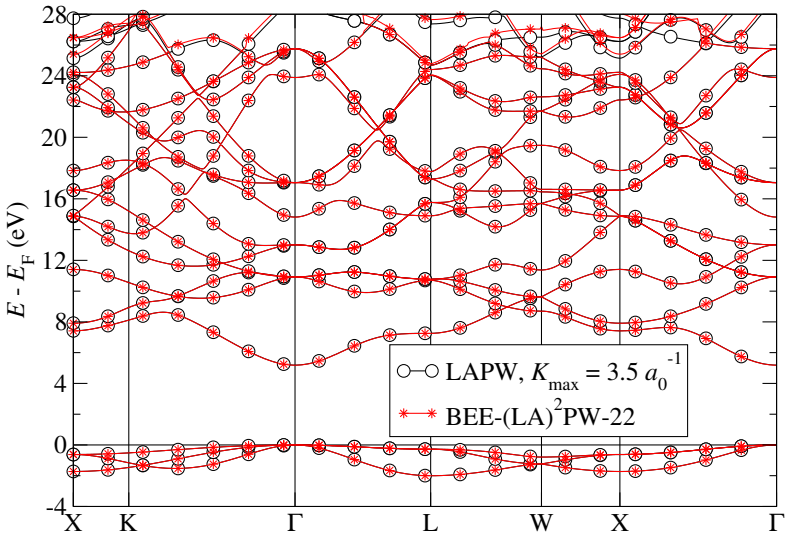

Figure 6.6.: Comparison of NaCl band structures obtained with the conventional LAPW basis and the BEE-(LA)^{2}PW-22 basis, respectively. Both calculations use a reciprocal plane wave cutoff of $K_{\mathrm{max}} = 3.5\ a_0^{-1}$.

the different FLAPW results is less than 0.048 %. Thus, in this case the additional error due to the usage of the BEE-(LA)^{2}PW basis is not orders of magnitude smaller than the error due to the limited $K_{\max}$ convergence. The results for the bulk modulus are slightly more in advantage of the BEE-F(LA)^{2}PW approach. Here, the maximal deviation from the corresponding FLAPW results for the BEE-(LA)^{2}PW-15 basis is 0.21 GPa and for the BEE-(LA)^{2}PW-22 basis it is only 0.18 GPa. The FLAPW calculations, on the other hand, deviate by maximally 0.46 GPa. We conclude that although the additional errors due to the usage of the BEE-F(LA)^{2}PW approach are larger, even for this challenging material the method still yields highly precise results with very small basis set sizes.

Finally, we compare the band structures obtained with the BEE-F(LA)^{2}PW and FLAPW methods in figure 6.6. For both calculations we use a $K_{\max}$ of 3.5 a_0^{-1}. Furthermore we use the BEE-(LA)^{2}PW-22 basis. The picture looks similar in comparison to the previously discussed band structures. Up to an energy of about 25 eV above the Fermi level the two band structures lie on top of each other. Above this energy we observe considerable deviations between both band structures. The number of bands that are accurately represented by the BEE-(LA)^{2}PW basis once again coincides with the number of basis functions that are constructed by the BEE principle.

6.1.4 Magnetic test system: Magnetically ordered compound FeRh in CsCl structure

We test the capability of the BEE-F(LA)^{2}PW approach to describe magnetic materials on the example of FeRh, which crystallizes in the bcc B2 CsCl structure with two atoms in the unit cell. Depending on the lattice constant, the ground state of this material exhibits different magnetic configurations [138]. We choose a lattice constant of $a_{\text{lat}} = 5.66\ a_0$. However, to compare the different magnetic configurations of the material we employ a larger tetragonal unit cell with $a = \sqrt{2}a_{\text{lat}}$ and $c = 2 \cdot a_{\text{lat}}$ comprising 8 atoms. As sketched in figure 6.7, the structure of the material in this unit cell can be seen as alternating layers of Fe and Rh atoms in c-direction. The Fe layers are found at $z = 0.0\ c$, at $z = 0.5\ c$, and at $z = 1.0\ c$. Each of these layers consists of an atom at each edge of the unit cell along the c-direction and another atom in the center. The Rh layers, on the other hand, are located at $z = 0.25\ c$ and at $z = 0.75\ c$. Here, atoms are found in the centers of each unit cell face.

For the chosen lattice constant FeRh possesses an antiferromagnetic ground state AFM2 in which the Fe layers couple antiferromagnetically and within each of these layers one finds a checkerboard arrangement of the magnetic up and down moments. What makes FeRh an interesting test system is the fact that two other magnetic configurations (cf. figure 6.7), the ferromagnetic configuration FM and another antiferromagnetic configuration AFM1 with ferromagnetic layers of Fe atoms that couple antiferromagnetically, exhibit total energies in the close vicinity to the ground state. We analyze to what extend the BEE-F(LA)^{2}PW approach is capable to precisely reproduce the energy differences between these different magnetic configurations with

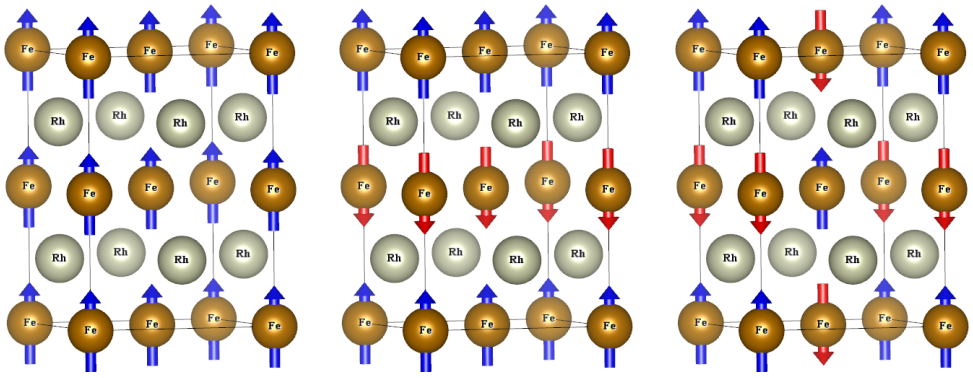

Figure 6.7.: Structure and magnetic configurations of FeRh. From left to right: ferromagnetic FM configuration, antiferromagnetic configuration AFM1, antiferromagnetic configuration AFM2. The arrows denote the magnetic moments at the respective atoms.

respect to the results obtained from corresponding FLAPW calculations.

Figure 6.8 shows for different $K_{\max}$ the energy differences between the different magnetic configurations as obtained with different BEE-(LA)^{2}PW basis sets in comparison to FLAPW results. Averaging over the $\boldsymbol{k}$ points the LAPW basis sets consist of 480, 671, and 906 basis functions for a $K_{\max}$ of 3.4 a_0^{-1}, 3.8 a_0^{-1}, and 4.2 a_0^{-1}, respectively. The considered BEE-(LA)^{2}PW basis sets with 128 to 288 basis functions are much smaller. We observe that for the smaller energy difference between the FM and AFM1 configurations BEE-(LA)^{2}PW basis sets with at least 160 basis functions are already enough to reproduce the respective FLAPW results with a deviation of about 0.1 meV. Considering 8 atoms in the unit cell, such a basis set of 160 functions consists of 10 BEE functions and 10 conventional LAPWs per atom. When we compare the deviations of the BEE-F(LA)^{2}PW from the FLAPW results we find that the error due to the limited $K_{\max}$ convergence dominates for $K_{\max} = 3.4\ a_0^{-1}$. For $K_{\max} = 3.8\ a_0^{-1}$ this error source is still larger than the additional error due to the BEE-F(LA)^{2}PW approach, though we consider the associated result to be converged. For the larger energy difference between the FM and AFM2 configurations we observe a similar picture. Here, each considered BEE-(LA)^{2}PW basis set deviates by no more than about 0.2 meV from the corresponding FLAPW result. On the other hand, the differences between the different FLAPW calculations are larger.

We also observe that a convergence beyond these already very small deviations between the BEE-F(LA)^{2}PW approach with small basis sets and the FLAPW results to an even higher agreement between the two approaches is very slow. Although we know that for equal basis set sizes we obtain identical results, the calculations show that one indeed has to use basis set sizes that come near to this limit if the last 0.1 meV or 0.2 meV deviations have to be eliminated. The reason for this problematic convergence behavior probably is a difference in the demands on the basis set in the

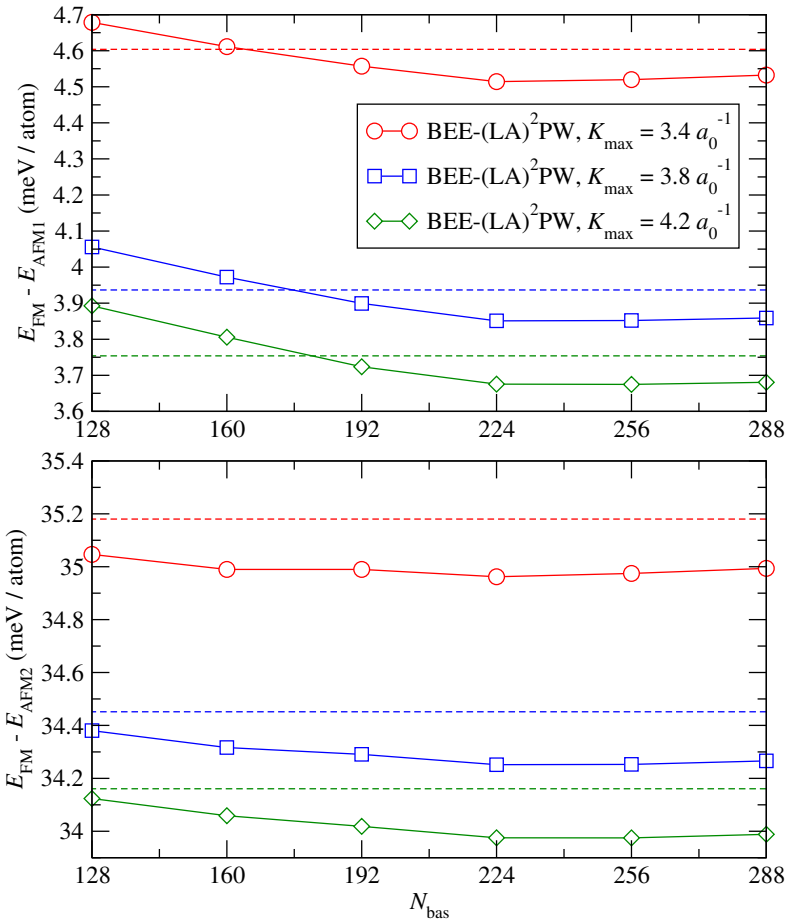

Figure 6.8.: Energy differences between different magnetic configurations of FeRh. The upper graph demonstrates the agreement between conventional FLAPW calculations and the BEE-F(LA)^{2}PW approach for the energy difference between the FM and the AFM1 configurations. The lower graph draws a similar picture for the difference between the FM and AFM2 configurations. For explanations of symbols and lines, see caption of Fig. 6.1. For the different K_{max} the $\boldsymbol{k}$ point averaged number of LAPWs in the FLAPW calculations is 480 (K_{max} = 3.4 a_0^{-1}), 671 (K_{max} = 3.8 a_0^{-1}), and 906 (K_{max} = 4.2 a_0^{-1}), respectively.

Table 6.5.: Magnetic moments of FeRh in the three configurations FM, AFM1, and AFM2. The given values are the moments inside the MT spheres associated with the respective atoms.

basis set	mag. moments (FM) Fe / Rh	mag. moments (AFM1) Fe / Rh	mag. moments (AFM2) Fe / Rh
	μ_B	μ_B	μ_B
$K_{max} = 3.4\ a_0^{-1}$			
LAPW-60	3.2092 / 1.0561	±3.1815 / 0.0000	±3.1602 / 0.0000
BEE-(LA)^{2}PW-24	3.2089 / 1.0547	±3.1807 / 0.0001	±3.1595 / 0.0000
$K_{max} = 3.8\ a_0^{-1}$			
LAPW-84	3.2149 / 1.0582	±3.1884 / 0.0000	±3.1671 / 0.0000
BEE-(LA)^{2}PW-24	3.2147 / 1.0567	±3.1875 / 0.0001	±3.1662 / 0.0001
$K_{max} = 4.2\ a_0^{-1}$			
LAPW-113	3.2166 / 1.0587	±3.1903 / 0.0000	±3.1689 / 0.0000
BEE-(LA)^{2}PW-24	3.2164 / 1.0572	±3.1894 / 0.0001	±3.1680 / 0.0001

two spin channels. It may be the case that one of the spin channels possesses an occupied state that has very high demands on the description flexibility of the basis set, while the other spin channel does not feature such a state. The construction of the BEE-(LA)^{2}PW basis does not adapt to such situations by considering different basis set sizes for the spin-up and spin-down channels. Instead, the basis set size for both spin channels is equal. Another aspect may be the changes of the wave functions during the iterations of the self-consistency cycle. These can by different for the two spin channels, which also implies a slight asymmetry in the description capabilities of the BEE-(LA)^{2}PW basis for such a material. Besides these balancing issues for the BEE-(LA)^{2}PW basis, we note that similar aspects can also yield an equivalent asymmetry in the description by the LAPW basis. We also remark that with respect to the corresponding FLAPW result, the deviations of the BEE-F(LA)^{2}PW calculations are limited to the deviations between the total energy results. Here, we saw that we obtain a rapid convergence with respect to the BEE-(LA)^{2}PW basis set size. In units of meV the 25 μHtr/atom criterion, that we considered in previous calculations, is a deviation of 0.68 meV/atom.

Another quantity that is appropriate to evaluate the precision of the BEE-F(LA)^{2}PW calculations are the magnetic moments inside the MT spheres in each of the magnetic configurations. Table 6.5 lists these moments as they are obtained by the different FLAPW calculations and the corresponding values obtained with the arbitrarily chosen BEE-(LA)^{2}PW-24 basis ($N_{bas} = 192$). With respect to the best results with $K_{max} = 4.2\ a_0^{-1}$ the other FLAPW calculations deviate by maximally 0.0088 μ_B for $K_{max} = 3.4\ a_0^{-1}$ and 0.0019 μ_B for $K_{max} = 3.8\ a_0^{-1}$. In comparison to this, the maximal deviation with the BEE-(LA)^{2}PW-24 basis from the corresponding FLAPW results is with 0.0015 μ_B smaller. Thus, again the BEE-F(LA)^{2}PW results stick to their FLAPW counterparts and we can reasonably reduce the number of basis functions by a large

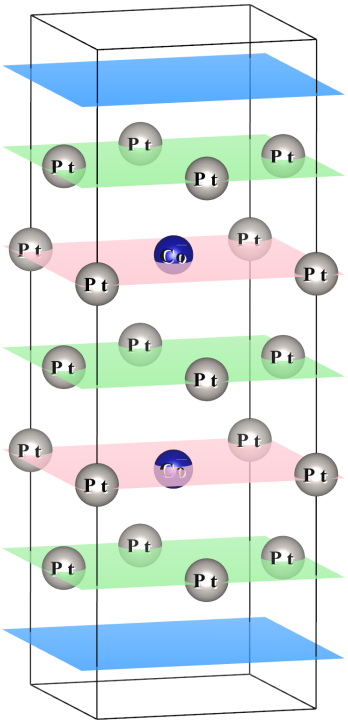

Figure 6.9.: CoPt3 unit cell. The unit cell is periodically repeated in x and y direction. The 5 layers are marked in green for layers with only Pt atoms and red for layers with both, Co and Pt atoms. The blue planes mark the boundaries to the vacuum regions.

amount by switching from the FLAPW to the BEE-F(LA)^{2}PW method.

6.1.5 Thin film test system: 5 layers of strained $CoPt_3$

The last material to be taken under scrutiny is an unsupported but laterally strained 5 layer $CoPt_3$ film. This material is a promising candidate for multiferroics applications since it features an out of plane magnetization that strongly depends on structural properties like strain and film thickness [139]. For the calculations performed in this work we consider an in plane strain such that the lattice constant fits to a $BaTiO_3$ substrate. Under these preconditions the atom positions are optimized to minimize the total energy.

With these structural properties FLAPW calculations predict a ground state with an antiferromagnetic coupling (AFM) between the two Co atoms in the unit cell. On the other hand, with respect to the total energy the ferromagnetic configuration (FM) is very close to this ground state. We evaluate to what precision the BEE-F(LA)^{2}PW

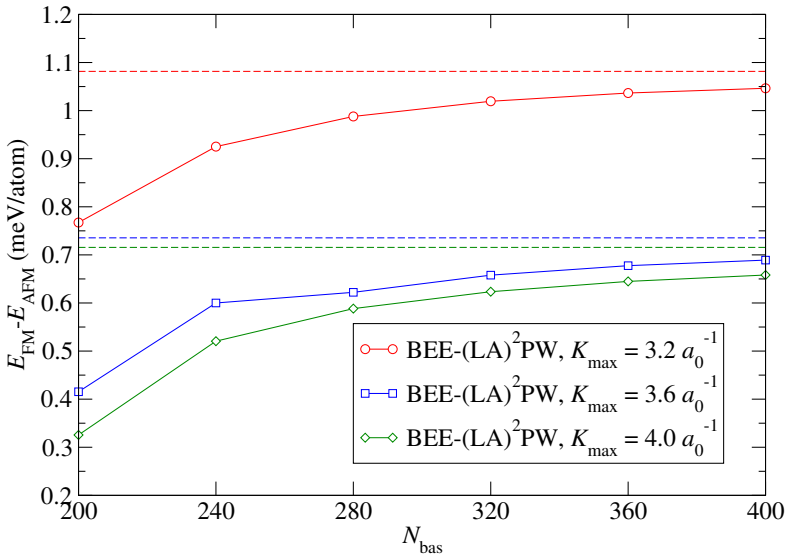

Figure 6.10.: Total energy difference between the FM and AFM configurations of the 5 layer CoPt3 film per atom. For explanations of symbols and lines, see caption of Fig. 6.1.

approach reproduces this very small energy difference.

Figure 6.9 shows the tetragonal 10 atom unit cell with $a = 7.68\ a_0$ and $c = 22.8\ a_0$. In this unit cell the vacuum boundary is located at $z_{vac} = \pm 9.6 a_0$. The positions of the Co atoms are $(0, 0, \pm 3.66 a_0)$ and the Pt atoms are located at $(a/2, a/2, \pm g)$, $(a/2, 0, 0)$, $(0, -a/2, 0)$, $(a/2, 0, \pm h)$, and $(0, -a/2, \pm h)$ with $g = 3.47\ a_0$, and $h = 6.89\ a_0$.

We plot the energy difference between the AFM and FM configurations as obtained with different BEE-(LA)^{2}PW basis sets and LAPW basis sets with different K_{max} cutoffs in figure 6.10. Averaged over the $\boldsymbol{k}$ points the different FLAPW calculations use LAPW basis sets of 745, 1061, and 1455 basis functions for a K_{max} of 3.2 a_0^{-1}, 3.6 a_0^{-1}, and 4.0 a_0^{-1}, respectively. For BEE-(LA)^{2}PW basis set sizes of $N_{bas} \geq 240$ the energy difference between the FM and AFM configuration is reproduced by the BEE-F(LA)^{2}PW approach with a precision of 0.2 meV/atom. For basis set sizes with at least 320 basis functions this maximal deviation is reduced to 0.1 meV/atom. We note however that the FM-AFM energy difference is already well converged for $K_{max} = 3.6\ a_0^{-1}$, such that the additional error due to the very small BEE-(LA)^{2}PW basis set dominates the imprecision in this case. For the smaller K_{max} of 3.2 a_0^{-1} the opposite is the case.

We also investigate the magnetic moments in the Co MT spheres in both magnetic configurations. Table 6.6 shows the values for the FLAPW calculations and for BEE-F(LA)^{2}PW calculations with arbitrarily chosen basis set sizes of 28 and 36 functions per atom. In the case of the FLAPW calculations we observe maximal deviations of 0.0214 μ_B (0.0046 μ_B) for $K_{max} = 3.2\ a_0^{-1}$ ($K_{max} = 3.6\ a_0^{-1}$) with respect to the best

Table 6.6.: Magnetic moments within the Co MT spheres in the FM and AFM configurations of the $CoPt_3$ film.

basis set	mag. moments (FM) Co μ_B	mag. moments (AFM) Co μ_B
$K_{max} = 3.2\, a_0^{-1}$		
LAPW-75	2.1822	±2.1629
BEE-(LA)^{2}PW-28	2.1852	±2.1654
BEE-(LA)^{2}PW-36	2.1830	±2.1635
$K_{max} = 3.6\, a_0^{-1}$		
LAPW-106	2.1990	±2.1777
BEE-(LA)^{2}PW-28	2.2020	±2.1802
BEE-(LA)^{2}PW-36	2.1997	±2.1782
$K_{max} = 4.0\, a_0^{-1}$		
LAPW-146	2.2036	±2.1823
BEE-(LA)^{2}PW-28	2.2066	±2.1848
BEE-(LA)^{2}PW-36	2.2043	±2.1827

result with $K_{max} = 4.0\ a_0^{-1}$. On the other hand the BEE-F(LA)^{2}PW results obtained with 28 (36) basis functions per atom deviate by no more than 0.0030 μ_B (0.0008 μ_B) from the corresponding FLAPW calculations. This means that for this quantity the incomplete K_{max} convergence with $K_{max} = 3.6\ a_0^{-1}$ still dominates the error in the calculations, while the BEE-F(LA)^{2}PW approach implies a smaller additional error.

After demonstrating the precision of the BEE-F(LA)^{2}PW approach, we conclude that with an adequately chosen BEE-(LA)^{2}PW basis set the additional imprecisions in comparison to conventional FLAPW calculations are small and in many cases negligible. In none of the here investigated materials and quantities the BEE-F(LA)^{2}PW approach implies a considerable precision disadvantage. For Cu, SiC, and NaCl the FLAPW total energy was reproduced with less than 25 μHtr/atom deviation for basis sets with 20 to 24 functions per atom. Such basis set sizes are on the same order of magnitude as basis sets obtained with the angular momentum criterion of $N_{bas} = 2\sum_\alpha (l^\alpha_{phys} + 2)^2$. However, depending on the material the angular momentum criterion yields basis sets that are either slightly larger or slightly smaller than the 25 μHtr/atom criterion basis sets.

Furthermore, we saw that even with very small BEE-(LA)^{2}PW basis sets the FLAPW results for many experimentally accessible quantities were reproduced with very high precision. The lattice constants were reproduced with an imprecision of less than 0.05 %. For the bulk moduli this maximal additional error was less than 0.7 GPa (and mostly less than 0.25 GPa). Energy differences between different structural configurations were reproduced with a higher precision than 0.1 meV per atom. The FLAPW and BEE-F(LA)^{2}PW band structures for the lowest $N_{bas}/2$ bands were indis-

tinguishable, at least on the energy scale of such band structures. Energy differences between different magnetic configurations were reproduced with a precision of about 0.2 meV per atom and, finally, the determination of the magnetic moments was also in high agreement to the FLAPW results with deviations of up to only 0.0030 μ_B.

6.2 F(LA)^{2}PW runtime performance

Both, the FLAPW method and the BEE-F(LA)^{2}PW approach, perform an iteration of the self-consistency cycle in a runtime that scales cubically with the system size, at least for large unit cells. However, in this section we show that the prefactor to this scaling is considerably smaller for BEE-F(LA)^{2}PW calculations, such that using this method instead of the conventional FLAPW approach yields a large reduction in the required amount of time.

To analyze the obtainable speedup associated with the BEE-F(LA)^{2}PW approach we compare the runtime of BEE-F(LA)^{2}PW and FLAPW calculations on Cu, SiC, and NaCl for different unit cell sizes. For small unit cells we expect that the total runtime is dominated by parts of the calculation that feature a more friendly (lower exponent) scaling behavior than the dominating cubic scaling for large unit cells. Thus, the speedup obtained by using the BEE-F(LA)^{2}PW approach will increase with growing unit cell sizes and approach an asymptotic constant for large unit cells. The speedup obtained for large unit cells is our main interest. Materials with such unit cells are associated with very large computational demands and thus a large speedup can make the difference whether DFT calculations on the system are feasible or not.

In the results presented below, the overall calculation runtimes are determined for calculations with 20 iterations of the self-consistency cycle. For the BEE-F(LA)^{2}PW method this includes the first iteration, which uses a conventional FLAPW approach. Furthermore, the second iteration is included. Here, a number of values are precomputed to increase the speedup obtained with a BEE-(LA)^{2}PW basis (cf. chapter 5 for details). 20 iterations are more or less the number of iterations required to obtain a converged charge density for the investigated materials. More complex unit cells often require much more iterations to obtain a self-consistent charge density. In such a case the calculation speedup obtained by using the BEE-F(LA)^{2}PW method approaches the larger iteration speedup of iterations that are not linked to the construction of the basis set or the precomputation of auxiliary quantities. The previously investigated $CoPt_3$ film is an example for such a material. Here, more than 100 iterations are required to obtain a self-consistent charge density. The also investigated FeRh needs about 30 iterations. Note that both methods, FLAPW and BEE-F(LA)^{2}PW, show about the same convergence behavior with respect to the required number of iterations.

Before presenting the runtime results we also mention in passing that the additional error per atom due to the usage of the BEE-F(LA)^{2}PW approach is basically independent of the unit cell size as long as the number of basis functions per atom

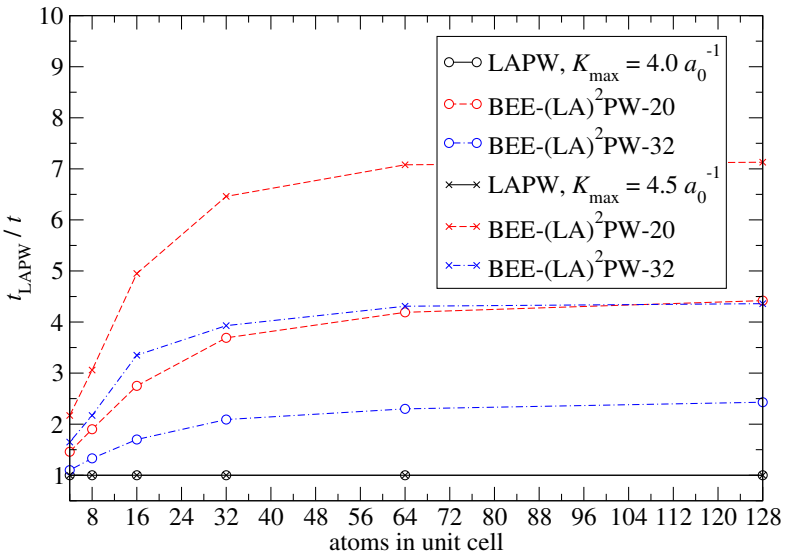

Figure 6.11.: Overall calculation speedup for fcc Cu as a function of the number of atoms per unit cell. The measured values are the ratios between the overall runtimes t_{LAPW} and t, employing the conventional LAPW and the BEE-(LA)^{2}PW basis, respectively. Each calculation consists of 20 self-consistency iterations. The values marked by circles (crosses) are determined with a K_{max} cutoff of 4.0 a_0^{-1} (4.5 a_0^{-1}).

remains unchanged. Thus, the statements on the description efficiency of the BEE-(LA)^{2}PW basis made for the small unit cells in the previous sections are also valid for larger unit cells.

We start the runtime performance discussion with the investigations on fcc Cu. The speedup results obtained for this material in different unit cells consisting of 4 to 128 atoms are shown in figure 6.11. The first observation we make in this graph is that the BEE-F(LA)^{2}PW speedup over FLAPW becomes larger as K_{max} grows. This is easily understandable since this parameter directly controls the LAPW basis set size, while the BEE-(LA)^{2}PW basis set size does not depend on it. Thus, to make reasonable statements on the BEE-F(LA)^{2}PW speedup it is important to relate the speedup to the precision of the results obtained with the respective basis sets. Here, we consider K_{max} values of 4.0 a_0^{-1} and 4.5 a_0^{-1}. At least for the smaller of these values we showed in the previous chapter that the additional error due to BEE-F(LA)^{2}PW approach is considerably smaller than the error due to the incomplete K_{max} convergence. This is the case for both, the BEE-(LA)^{2}PW-20 and the BEE-(LA)^{2}PW-32 basis set. On the other hand we also showed that a K_{max} of at least 4.0 a_0^{-1} is required to obtain reasonable results from an FLAPW calculation on this material. Thus, we focus on the speedup obtained with the BEE-(LA)^{2}PW-20 and a plane wave cutoff of K_{max} =

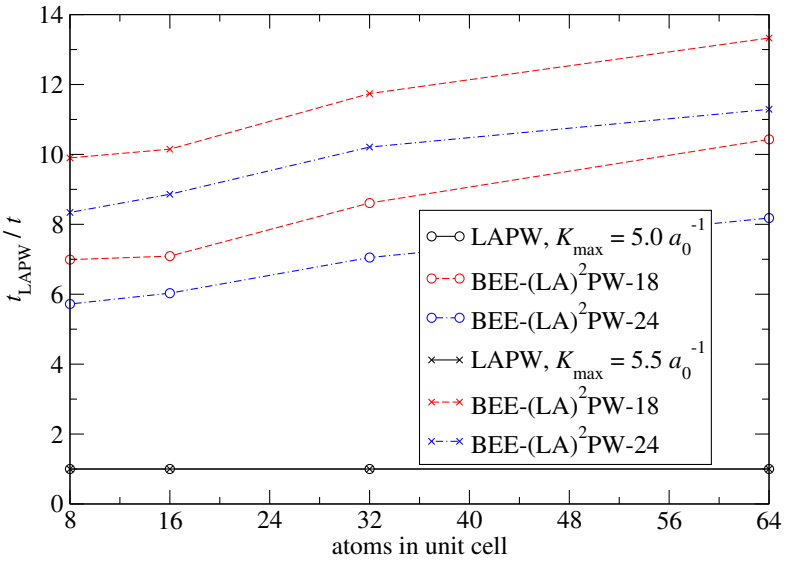

Figure 6.12.: Overall calculation speedup for zinc blende SiC as a function of the number of atoms per unit cell. The measured values are the ratios between the overall runtimes t_{LAPW} and t, employing the conventional LAPW and the BEE-(LA)^{2}PW basis, respectively. Each calculation consists of 20 self-consistency iterations. The values marked by circles (crosses) are determined with a $K_{\max}$ cutoff of 5.0 a_0^{-1} (5.5 a_0^{-1}).

4.0 a_0^{-1} over the corresponding FLAPW calculation. Here, the figure shows that for a large unit cell a speedup of 4.4 is realistic for such a material. With the larger BEE-(LA)^{2}PW-32 basis this speedup becomes smaller, though it is still about 2.4. When going to the larger $K_{\max}$ cutoff to enter the regime in which the error may actually be dominated by the restrictions due to the small BEE-(LA)^{2}PW basis sets, we obtain speedups of more than 7 for the BEE-(LA)^{2}PW-20 basis and about 4.4 for the BEE-(LA)^{2}PW-32 basis. We also note that these speedups are already nearly saturated for unit cell sizes of 64 atoms. Thus, even for such medium size unit cells one can take full advantage of the BEE-F(LA)^{2}PW approach.

The second material to be taken under scrutiny is zinc blende SiC. For this material we increase the unit cell size from 8 to 64 atoms. Results for the associated speedups are displayed in figure 6.12. We have seen that at least a $K_{\max}$ of 5.0 a_0^{-1} is required to obtain reasonable results for this material. For the bulk modulus the larger $K_{\max}$ of 5.0 a_0^{-1} seems to be even more adequate. On the other hand both of the here discussed BEE-(LA)^{2}PW basis sets, BEE-(LA)^{2}PW-18 and BEE-(LA)^{2}PW-24 reproduced the respective FLAPW results with very high precision. Thus, for this material it is reasonable to compare the BEE-(LA)^{2}PW-18 calculation with $K_{\max}$ = 5.0 a_0^{-1} to its FLAPW counterpart. For the largest unit cell with 64 atoms these two calculations

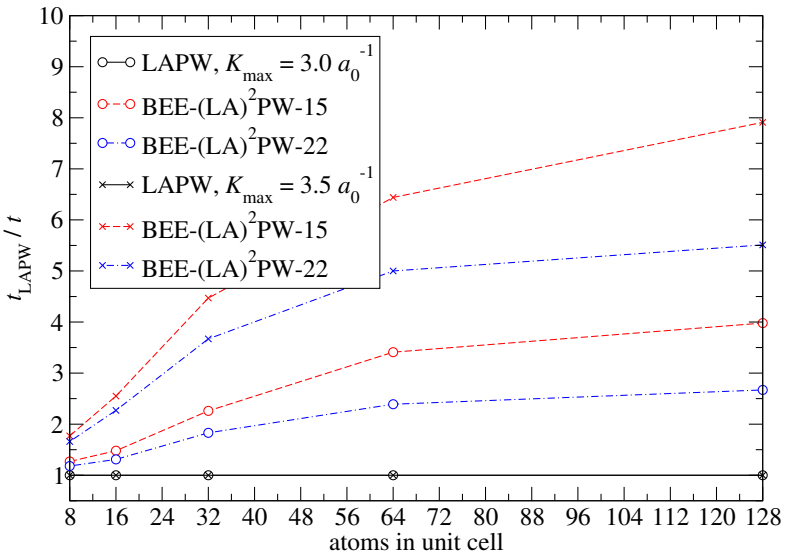

Figure 6.13.: Overall calculation speedup for rock salt NaCl as a function of the number of atoms per unit cell. The measured values are the ratios between the overall runtimes t_{LAPW} and t, employing the conventional LAPW and the BEE-(LA)^{2}PW basis, respectively. Each calculation consists of 20 self-consistency iterations. The values marked by circles (crosses) are determined with a $K_{\max}$ cutoff of 3.0 a_0^{-1} (3.5 a_0^{-1}).

are associated with a speedup of a factor of 10.4 for the BEE-F(LA)^{2}PW approach in comparison to FLAPW. But even the larger BEE-(LA)^{2}PW-24 basis yields a speedup of about 8.2. For the larger $K_{\max}$ of 5.5 a_0^{-1} these speedups become 13.3 and 11.3 for the BEE-(LA)^{2}PW-18 and BEE-(LA)^{2}PW-24 basis, respectively. We also observe that these speedups did not yet reach their asymptotic value, even for unit cells with 64 atoms. Thus, one can expect to see even larger speedups for larger unit cells. On the other hand, we also observe a large speedup of at least a factor of 5.7 for small unit cells. We conclude that for open systems like SiC the large fraction of the interstitial region with respect to the whole unit cell implies the demand for a large amount of LAPW basis functions to obtain reasonably converged FLAPW results. On the other hand, the required BEE-(LA)^{2}PW basis set size does not directly depend on this material property. Thus, the move to the BEE-F(LA)^{2}PW method for such open systems is linked to an enormous reduction in the required basis set size and therefore also with a large speedup.

The last material used for the investigations on the calculation speedup associated with the BEE-F(LA)^{2}PW approach is NaCl in rock salt structure. For unit cells comprising 8 to 128 atoms and $K_{\max}$ cutoffs of 3.0 a_0^{-1} and 3.5 a_0^{-1} the speedups are displayed in figure 6.13. Since FLAPW calculation results for this material fea-

ture a rapid convergence with respect to $K_{\max}$ we focus on the results obtained for $K_{\max} = 3.0\ a_0^{-1}$. Here, we obtain speedups of up to 4 and 2.7 for the BEE-(LA)^{2}PW-15 and BEE-(LA)^{2}PW-22 basis sets, respectively. For the larger $K_{\max}$ of $3.5\ a_0^{-1}$ these speedups become 7.9 and 5.5. For the BEE-(LA)^{2}PW-22 basis the speedups are nearly saturated for unit cells with 64 atoms. On the other hand, the smaller BEE-(LA)^{2}PW-15 benefits from even larger unit cells.

After inspecting the speedups for the different materials we note that open systems like SiC exhibit the largest benefits due to the usage of the BEE-F(LA)^{2}PW approach. For metals we saw that a speedup between 4 and 5 is reasonable and even for the challenging NaCl we saw a speedup between 2.7 and 4 for adequate $K_{\max}$ cutoffs and BEE-(LA)^{2}PW basis set sizes. Averaging over the materials we remark that one can associate the BEE-F(LA)^{2}PW approach with a typical speedup of about 5, though this speedup is exposed to large material dependent variations. We have not seen a single material in which the usage of an adequate BEE-(LA)^{2}PW basis is associated with a disadvantage in the calculation runtime.

We have also observed that the obtained speedup strongly depends on the $K_{\max}$ cutoff. For higher $K_{\max}$ cutoffs we obtain larger speedups. As mentioned this is reasonable as $K_{\max}$ directly affects the LAPW basis set size, while in the BEE-F(LA)^{2}PW approach it considerably only affects the first iteration, in which the BEE-(LA)^{2}PW basis is constructed. Beyond the basis construction $K_{\max}$ only affects the representation of the BEE-(LA)^{2}PW basis functions. However, the precomputation of the matching coefficients at the MT boundaries decouples the computational demands from this representation to a large extent. In the end, the number of plane waves N_{PW}, determined by $K_{\max}$, only enters linearly in the scaling of the runtime of the interstitial contributions to the matrices and the runtime of the backtransformation of the wave functions into the LAPW representation. Furthermore, it enters with the exponent 2/3 in the runtime of the vacuum region setup.

To obtain a starting point to further speed up the F(LA)^{2}PW approach we proceed by analyzing the time requirements of each step of BEE-F(LA)^{2}PW calculations in detail. For this, figure 6.14 resolves the runtime t_{iter} of each iteration of the self-consistency cycle with the BEE-F(LA)^{2}PW approach in relation to the minimal iteration runtime of the respective calculation. For each of the 3 materials Cu, SiC, and NaCl the figure displays the data of a representative calculation for the largest investigated unit cell.

We find that the first iteration, in which the BEE-(LA)^{2}PW basis is constructed, is a limiting aspect for the runtime of the respective calculation. Depending on the material, this iteration takes 3.2 to 25.5 times as much runtime than one of the last 18 conventional BEE-F(LA)^{2}PW iterations. Thus, the construction of an (LA)^{2}PW basis in terms of eigenfunctions to an operator obtained on the basis of LAPWs is computationally so expensive that for the next (LA)^{2}PW basis beyond the BEE-(LA)^{2}PW approach one has to consider a construction principle with less computational demands.

The second iteration also requires considerably more runtime than the respective BEE-F(LA)^{2}PW reference iteration. This is due to the precomputations performed

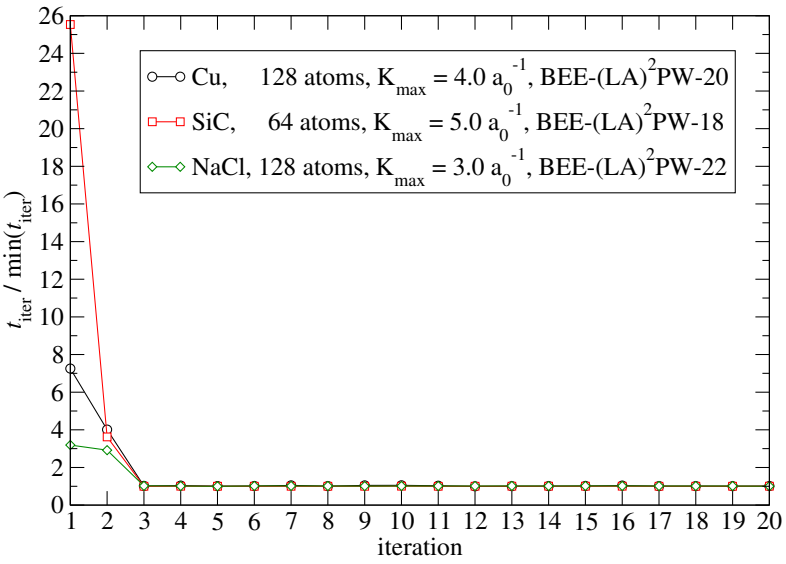

Figure 6.14.: Runtimes t_{iter} required for each iteration given relative to the minimal iteration runtime within the respective calculation for the three example systems employing unit cells of 128 atoms for Cu and NaCl, respectively, and 64 atoms for SiC.

in this iteration. Here, the calculation of the matching conditions at the MT sphere boundaries is the most time-consuming part. It typically requires about 60 to 70 percent of the total runtime of this iteration and scales with $\mathcal{O}((l_{\text{max}}+1)^2 N_{\text{atom}} N_{\text{bas}} N_{\text{PW}})$. A basis set that solves this problem either has to require a smaller angular momentum cutoff l_{max} or has to be localized, such that each basis function is only extended into a limited number of MT spheres.

The figure also shows the already mentioned fact that the BEE-F(LA)^{2}PW approach benefits from calculations requiring more than the 20 iterations for the here tested example materials. With a growing number of required iterations the calculation speedup approaches the iteration speedup, which can approximately be estimated as the speedup of the reference iteration in comparison to the very first iteration in figure 6.14.

Beyond the iteration dependent time consumption we analyze the BEE-F(LA)^{2}PW runtime consumption of each step within an iteration in table 6.7. We first observe that the most time-consuming step is the calculation of $S_{ij}^{\boldsymbol{k},\alpha}$ and $H_{ij}^{\boldsymbol{k},\alpha,\text{sphr}}$ which takes between 31 and 44 percent of the runtime of an iteration. The computational demands for this step scale with $\mathcal{O}((l_{\text{max}}+1)^2 N_{\text{atom}} N_{\text{bas}}^2)$such that it is especially sensitive to high l_{max} cutoffs. Also other steps within an iteration exhibit such a sensitivity on the angular momentum cutoffs. For example, the runtime for the determination of the MT matching coefficients for the eigenfunctions also depends quadratically on

Table 6.7.: Runtime for the different computation steps t_{step} of a BEE-F(LA)^{2}PW iteration (i.e. for $iter \geq 3$ in Fig. 6.14) relative to the total time of the iteration t_{iter} for the three example systems employing unit cells of 128 atoms for Cu and NaCl, respectively, and 64 atoms for SiC.

step	Cu	SiC	NaCl
	$t_{\text{step}}/t_{\text{iter}}$	$t_{\text{step}}/t_{\text{iter}}$	$t_{\text{step}}/t_{\text{iter}}$
potential setup	0.04	0.06	0.11
interstitial matrix setup			
calculating $\xi_{\boldsymbol{k}j}^{[\theta V\phi]}(\boldsymbol{r})$	0.06	0.09	0.04
calculating $\langle\tilde{\phi}_{\boldsymbol{k}i}\|\xi_{\boldsymbol{k}j}^{[\theta V\phi]}\rangle$	0.03	0.03	0.02
MT matrix setup			
calculating $S_{ij}^{\boldsymbol{k},\alpha}$ and $H_{ij}^{\boldsymbol{k},\alpha,\text{sphr}}$	0.36	0.44	0.31
calculating $H_{ij}^{\boldsymbol{k},\alpha,\text{nsphr}}$	0.11	0.09	0.10
eigenvalue problem			
diagonalization	0.09	0.07	0.09
transform to LAPW basis	0.11	0.03	0.05
constructing new density	0.18	0.16	0.24
rest	0.02	0.03	0.04

this cutoff and consumes most of the runtime of the construction of the new density, which is the second largest point in table 6.7. Another time-consuming part of the construction of the new density is the correction for the core tails which are extended beyond a MT sphere boundary and reach into another MT sphere (cf. chapter 3.3.6). However, due to a better scaling behavior this step will become a less important part of the runtime of calculations on materials with even larger unit cells.

With respect to the time requirements of the interstitial matrix setup we note that the calculation of the $\xi_{\boldsymbol{k}j}^{[\theta V\phi]}(\boldsymbol{r})$, which consumes most of the time in the associated section of the table, actually features a better scaling than the cubical scaling for the calculation of the matrix elements $\langle\tilde{\phi}_{\boldsymbol{k}i}|\xi_{\boldsymbol{k}j}^{[\theta V\phi]}\rangle$. Thus, for larger unit cells the calculation of the $\xi_{\boldsymbol{k}j}^{[\theta V\phi]}(\boldsymbol{r})$ will become a less dominant part of the matrix setup.

The last aspect of table 6.7 to be discussed is the runtime for the transformation of the eigenfunctions from the (LA)^{2}PW representation back to LAPWs. Though this is not a dominant step within an iteration we note that it is not necessary. The elimination of this step may provide another small addition to the performance advantage of the F(LA)^{2}PW approach. However, eliminating this step makes the integration of the F(LA)^{2}PW approach into an existing FLAPW program more expensive, such that we keep this step at the moment.

6.3 Reducing the angular momentum cutoff for the matrix setup

In table 6.7 we have seen that a large part of the runtime of a conventional F(LA)^{2}PW iteration is used to calculate the MT contributions to the overlap matrix $S_{ij}^{\boldsymbol{k},\alpha}$ and the spherical MT contributions to the Hamilton matrix $H_{ij}^{\boldsymbol{k},\alpha,\mathrm{sphr}}$. We also know that these time requirements scale with $\mathcal{O}\left((l_{\max}+1)^2 N_{\mathrm{atom}} N_{\mathrm{bas}}^2\right)$. In this section we will evaluate several approaches to reduce the $l_{\max}$ cutoff in this part of the calculation to further reduce the overall iteration runtime.

The starting point for the development of approaches to reduce $l_{\max}$ are the investigations on the properties of the basis functions and the wave functions in section 4.2. There, we have seen that the changes of the respective Kohn-Sham problem in each iteration of the self-consistency loop are rather small. As a consequence we assumed that the solution to the problem obtained in the first iteration should already be very similar to the self-consistent solution in the last iteration. The development of the BEE-F(LA)^{2}PW approach is based on this assumption. Of course, this means that just like the Kohn-Sham wave functions of the self-consistent solution also the BEE-(LA)^{2}PW basis functions possess matching conditions in which the higher l channels are strongly suppressed. Thus, the contributions of these channels to the matrices are also considerably smaller than in the case of LAPWs.

Furthermore, we have seen that the spherical potential and the radial functions $u_l^\alpha(r_\alpha, E_l^\alpha)$ and $\dot{u}_l^\alpha(r_\alpha, E_l^\alpha)$ for high l quantum numbers nearly do not change throughout the iterations of the self-consistency cycle. The strongest changes in this context were the energy parameters that shifted in accordance with the small changes of the spherical part of the potential in the near of the MT boundary.

Thus, we observe small contributions from the higher l channels that are only exposed to very small changes over the different iterations of the self-consistency loop. To benefit from these circumstances, we divide the l channels into two groups. The first group are the lower l channels from $l = 0$ to an additional cutoff parameter $l_{\max}^{\mathrm{exact},\alpha}$ and the other group are the higher l channels from $l_{\max}^{\mathrm{exact},\alpha} + 1$ to $l_{\max}^{\alpha}$. For the lower l channels we do not change anything in the calculations. This means that the contributions to the matrices due to these channels are calculated in an exact way in each iteration of the self-consistency loop. For the higher l channels, on the other hand, we evaluate three different approaches to efficiently obtain approximations to the contributions that replace the exact values.

The first approach only relies on the fact that the contributions from the higher l channels are small in comparison to the case of LAPW basis functions. To exploit this property of the basis functions we just neglect the contributions due to the higher l channels by setting them to 0.

The second approach goes one step further and uses the fact that the changes of the radial functions $u_l^\alpha(r_\alpha, E_l^\alpha)$ and $\dot{u}_l^\alpha(r_\alpha, E_l^\alpha)$ for the higher l quantum numbers over the

iterations are negligible and the energy parameters only exhibit very small changes. Here, the changes in the energy parameters are neglected, such that the contributions to the matrices can be precalculated and stored in the 2nd iteration of the self-consistency loop when the matrices for the BEE-$(LA)^2$PW are set up for the first time. In detail, in this case the overlap and Hamilton matrices are given by

$$S_{ij}^{\boldsymbol{k},\alpha} = \left(\sum_{l=0}^{l_{\max}^{\text{exact},\alpha}} S_{ij}^{\boldsymbol{k},\alpha,l} \right) + \left(\sum_{l=l_{\max}^{\text{exact},\alpha}+1}^{l_{\max}} S_{ij}^{\boldsymbol{k},\alpha,l,\text{iter}=2} \right) \tag{6.4}$$

and

$$H_{ij}^{\boldsymbol{k},\alpha} = \left(\sum_{l=0}^{l_{\max}^{\text{exact},\alpha}} H_{ij}^{\boldsymbol{k},\alpha,l} \right) + \left(\sum_{l=l_{\max}^{\text{exact},\alpha}+1}^{l_{\max}} H_{ij}^{\boldsymbol{k},\alpha,l,\text{iter}=2} \right), \tag{6.5}$$

where $S_{ij}^{\boldsymbol{k},\alpha,l,\text{iter}=2}$ and $H_{ij}^{\boldsymbol{k},\alpha,l,\text{iter}=2} = [E_l^\alpha S_{ij}^{\boldsymbol{k},\alpha,l} + \frac{1}{2}\sum_m \left(a_{\boldsymbol{k}i}^{L\alpha}\right)^* b_{\boldsymbol{k}j}^{L\alpha} + \left(b_{\boldsymbol{k}i}^{L\alpha}\right)^* a_{\boldsymbol{k}j}^{L\alpha}]^{\text{iter}=2}$ denote the respective contributions in the 2nd iteration.

In the last approach we additionally try to compensate for the changes of the energy parameters that affect only the contributions to the Hamilton matrix. This could be done in a very accurate way by precalculating $S_{ij}^{\boldsymbol{k},\alpha,l,\text{iter}=2}$ and scaling it with the iteration dependent energy parameters E_l^α. However, this is not feasible as it would require the precalculation of N_{atom} matrices and thus cubically scaling storage requirements. As an alternative that is less accurate we approximate the changes of the spherical potential in the outer parts of the MT spheres and hence also the changes of the energy parameters by the changes of the averaged interstitial potential $V_{\text{IR}}^{\text{ave}}$. With this approximation we precalculate the sum of the contributions from all atoms and multiply it with the difference of the averaged interstitial potential in the 2nd iteration and the current iteration. This gives us an additional term to the Hamilton matrix of

$$H_{ij}^{\boldsymbol{k},\text{IR correction}} = \left(V_{\text{IR}}^{\text{ave}} - V_{\text{IR}}^{\text{ave,iter}=2}\right) \sum_\alpha \sum_{l=l_{\max}^{\text{exact},\alpha}+1}^{l_{\max}} S_{ij}^{\boldsymbol{k},\alpha,l,\text{iter}=2}. \tag{6.6}$$

Note that the first two approaches do not imply additional storage requirements. For the first approach this is obvious, for the second approach we just combine the precalculated matrices with the already stored interstitial contributions to the matrices. The last approach requires additional memory as the additional contribution to the Hamilton matrix has to be stored explicitly.

For the evaluation of the three approaches we again perform calculations on fcc Cu, zinc blende SiC, and rock-salt NaCl. The different dominating bonding mechanisms in these systems provide us with representative results for a wide class of materials.

Figure 6.15 shows for fcc Cu the dependence of the total energy and the lattice constant on the reduced angular momentum cutoff parameter $l_{\max}^{\text{exact},\alpha}$. We observe

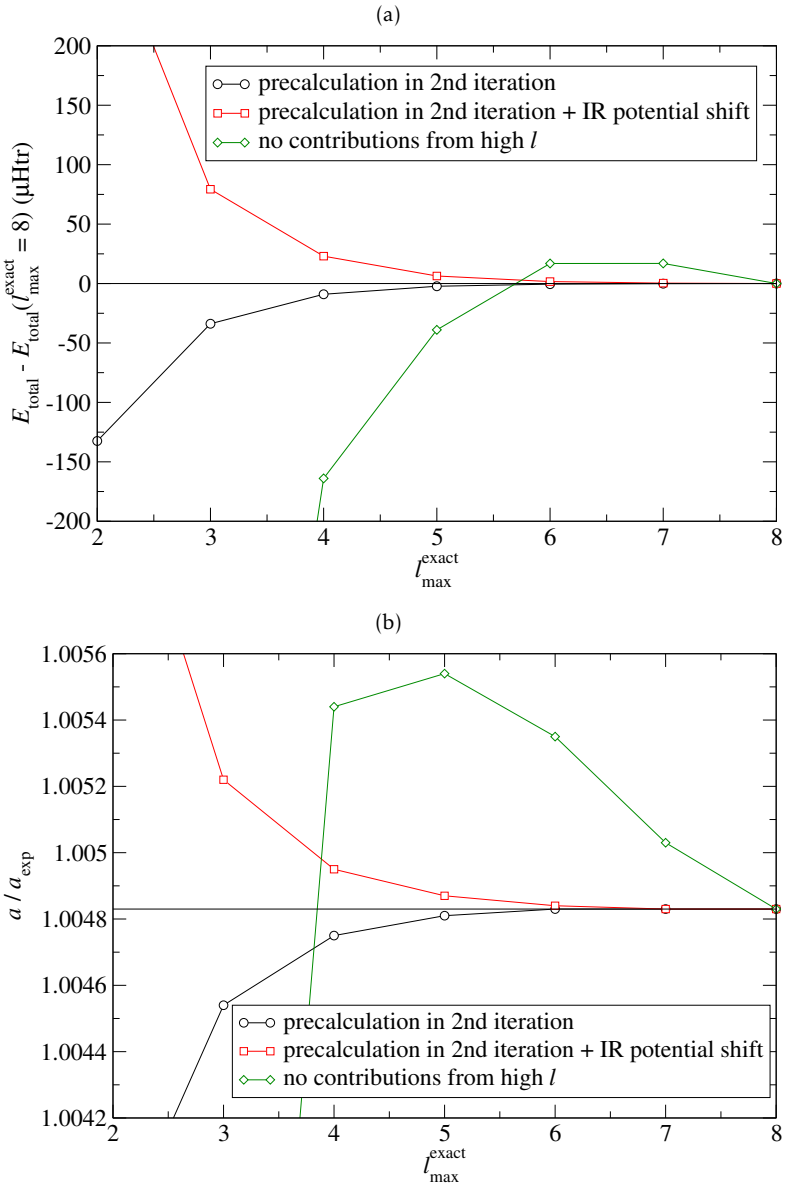

Figure 6.15.: Dependence of (a) total energy and (b) lattice constant for fcc Cu on the reduction of the angular momentum cutoff $l_{\max}^{\text{exact},\alpha}$. The figures show the results for the three different approaches to treat the higher l channels beyond $l_{\max}^{\text{exact},\alpha}$. The calculations were performed with a BEE-(LA)^{2}PW basis set size of $N_{\text{bas}} = 20$ and a reciprocal plane wave cutoff of $K_{\max} = 4.5\ a_0^{-1}$. All other parameters are in accordance to table 6.1.

that with the two approaches that include an approximate precalculation of the matrix contributions the $l_{\max}^{\text{exact},\alpha}$ cutoff can reasonably be greatly reduced. For both approaches, even with an $l_{\max}^{\text{exact},\alpha}$ of 4 the total energy deviates by no more than 25 μHtr/atom from the reference result with $l_{\max}^{\text{exact},\alpha} = 8$. Also the lattice constants for this reduced $l_{\max}^{\text{exact},\alpha}$ deviate by less than 0.02 % from the reference result. For both quantities the approach including the corrections for the changes of the energy parameters yields slightly worse results than the method without these corrections. This is directly understandable if one notes that the energy parameters for the higher l channels shift by 0.005 Htr between the 2nd iteration and the last one, while the averaged interstitial potential changes by 0.0145 Htr. Thus, in this material the changes of the averaged interstitial potential are nearly three times as large than the changes of the spherical potential near the MT sphere boundaries and thus also larger than the changes of the energy parameters. The correction on the basis of the average interstitial potential therefore overcompensates the changes of the energy parameters and finally yields a worse result than the uncorrected approach. The last approach to be discussed is the neglection of the contributions coming from the higher l channels. This approximation yields considerably worse results than the other two approaches and does not allow a significant reduction of the $l_{\max}^{\text{exact},\alpha}$ cutoff.

The results after reducing the $l_{\max}^{\text{exact},\alpha}$ in SiC are presented in figure 6.16. Here, we basically observe a similar picture in comparison to fcc Cu. However, in this case the approach that also considers the changes of the energy parameters yields the best results. We again have a closer look at the actual numbers. From the 2nd to the last iteration the energy parameters for the higher l channels in Si (C) shift by 0.0098 Htr (0.0997 Htr). With changes of the average interstitial potential of 0.0078 Htr this is very well approximated by the method involving the associated correction term. For both methods it is again reasonable to reduce the $l_{\max}^{\text{exact},\alpha}$ cutoffs to 4 as it keeps the total energy within 25 μHtr/atom of the reference result and yields deviations from the reference lattice constant of less than 0.01 %. For the approach including the extra correction to the Hamilton matrix it is even reasonable to reduce the angular momentum cutoff to 3, though in this case the lattice constant deviates by nearly 0.02 % from the reference result. The neglection of the contributions due to the higher l channels does not allow for such a large reduction of the angular momentum cutoff.

Finally, we discuss the results obtained for rock-salt NaCl, shown in figure 6.17. For this material, it is indeed reasonable to reduce the $l_{\max}^{\text{exact},\alpha}$ cutoffs to 5 by neglecting the matrix contributions originating from the higher l channels. However, the two approaches including the approximate precalculations again outperform this simple idea. With the approach neglecting the changes of the energy parameters a reduction of the $l_{\max}^{\text{exact},\alpha}$ to 4 is reasonable. With the more sophisticated approach the approximation of the changes of the high l energy parameters between the 2nd and the last iteration of 0.0286 Htr (0.0095 Htr) in Na (Cl) by the changes of the average interstitial potential of 0.0225 Htr is very good. As a consequence it is reasonable to reduce the $l_{\max}^{\text{exact},\alpha}$ cutoffs to 3 with this method. In each of these cases the total energy is

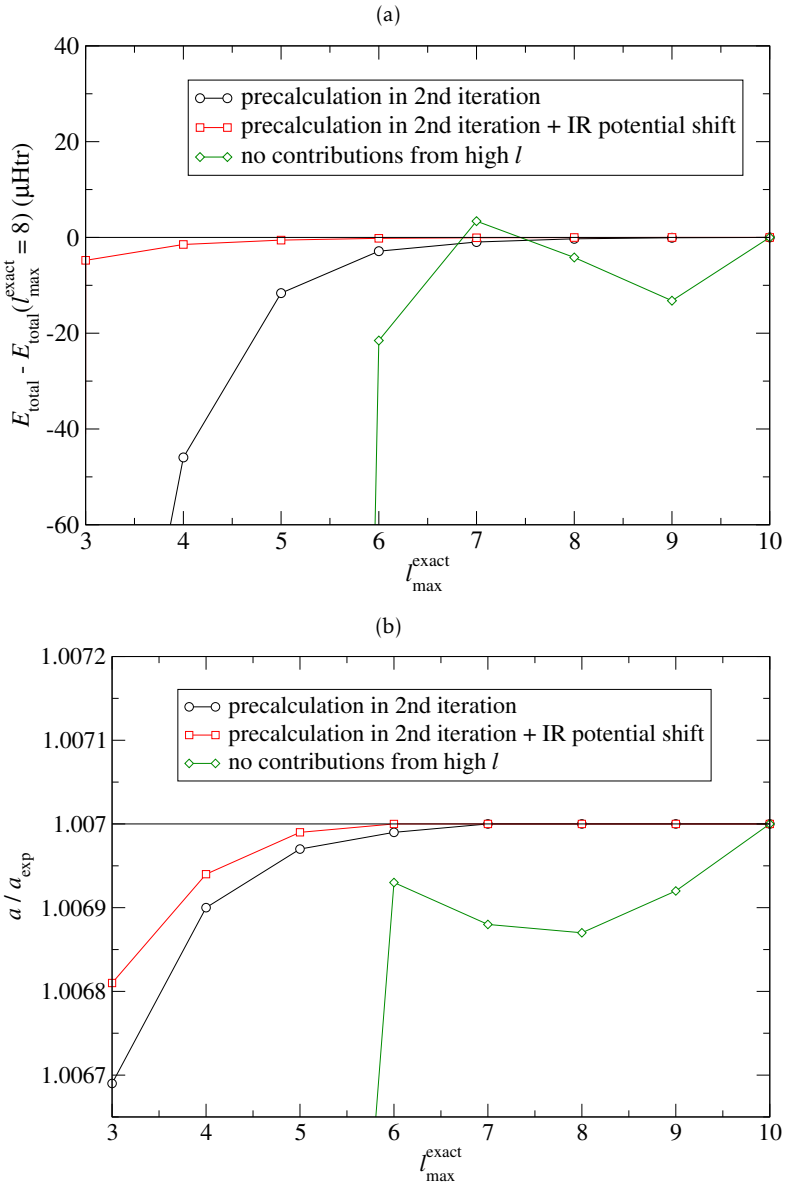

Figure 6.16.: Dependence of (a) total energy and (b) lattice constant for zinc blende SiC on the reduction of the angular momentum cutoff $l_{max}^{exact,\alpha}$, which is determined as $l_{max}^{exact,\alpha} = min\{l_{max}^{\alpha}, l_{max}^{exact}\}$ The figures show the results for the three different approaches to treat the higher l channels beyond $l_{max}^{exact,\alpha}$. The calculations were performed with a BEE-(LA)^{2}PW basis set size of N_{bas} = 36 and a reciprocal plane wave cutoff of K_{max} = 5.5 a_0^{-1}. All other parameters are in accordance to table 6.1.

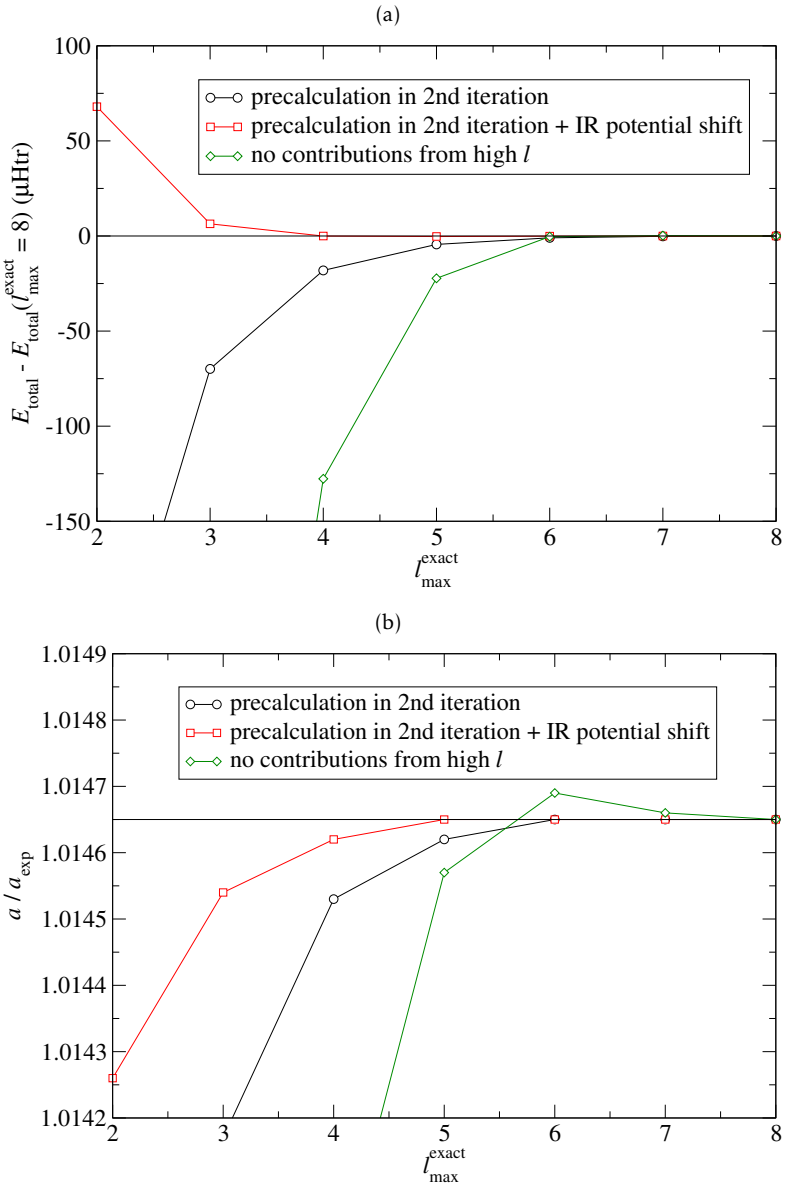

Figure 6.17.: Dependence of (a) total energy and (b) lattice constant for rock-salt NaCl on the reduction of the angular momentum cutoff $l_{\max}^{\text{exact},\alpha}$, which is determined as $l_{\max}^{\text{exact},\alpha} = min\{l_{\max}^{\alpha}, l_{\max}^{\text{exact}}\}$ The figures show the results for the three different approaches to treat the higher l channels beyond $l_{\max}^{\text{exact},\alpha}$. The calculations were performed with a BEE-(LA)^{2}PW basis set size of $N_{\text{bas}} = 44$ and a reciprocal plane wave cutoff of $K_{\max} = 4.0\ a_0^{-1}$. All other parameters are in accordance to table 6.1.

within a range of 25 μHtr/atom to the reference result and also the lattice constant deviates by no more than 0.02 % from the case with $l_{\mathrm{max}}^{\mathrm{exact},\alpha} = 8$.

We subsume these observations by noting that although the contributions from the higher l channels are small, they are still relevant and should not simply be neglected. On the other hand they can be precomputed in an approximate way, which has the potential to greatly reduce the $l_{\mathrm{max}}^{\mathrm{exact},\alpha}$ cutoffs. The changes of the energy parameters for the higher l channels are very small. As a consequence the two methods including the precomputation perform qualitatively similar, though one may argue that the method including the approximate averaged compensation to the changes of the energy parameters performs slightly better. With a more sophisticated approximation scheme to the changes of the energy parameters it may be possible to reduce the $l_{\mathrm{max}}^{\mathrm{exact},\alpha}$ cutoffs even further.

The reasonable reduction of the $l_{\mathrm{max}}^{\mathrm{exact},\alpha}$ cutoffs to 4 as we have shown it, has the potential to speed up the setup of $S_{ij}^{\boldsymbol{k},\alpha}$ and $H_{ij}^{\boldsymbol{k},\alpha,\mathrm{sphr}}$ by a factor of 3 to 4, yielding a reduction of the iteration runtime t_{iter} by 20 to 30 percent. As this only affects the conventional BEE-F(LA)^{2}PW iterations after the 2nd iteration, this especially affects the calculation runtime for materials that require many iterations to obtain a self-consistent solution and materials for which the iteration speedup of the BEE-F(LA)^{2}PW method in comparison to FLAPW is small.

6.4 Concluding remarks

In this chapter we developed and evaluated a first construction principle for (LA)^{2}PW basis functions, which is based on a single diagonalization of the FLAPW Hamiltonian for the initial density which is a superposition of atomic densities. With this starting point we composed a basis from early eigenfunctions (BEE) out of the $N_{\mathrm{bas}}/2$ energetically lowest eigenfunctions and also $N_{\mathrm{bas}}/2$ conventional LAPWs. We found that this basis function construction principle yields a basis set with a very high description efficiency, such that the basis set size in comparison to reasonable LAPW basis set sizes can considerably be reduced while maintaining the precision of the LAPW basis. This means that even with very small BEE-(LA)^{2}PW basis sets the remaining imprecision is mainly controlled by the reciprocal plane wave cutoff K_{max} that also controls the LAPW basis set size in the case of conventional FLAPW calculations.

By relating the tiny additional imprecision of the BEE-F(LA)^{2}PW approach to the imprecision due to the incomplete K_{max} convergence in associated FLAPW calculations we determined for each material a reasonable combination of the BEE-(LA)^{2}PW basis set size N_{bas} and the plane wave cutoff K_{max} for which we then measured the speedup of calculations with different unit cell sizes. We found that depending on the material, for large unit cells the BEE-F(LA)^{2}PW approach yields a calculation speedup between a factor 3 and more than 10.

To obtain a starting point for further improvements we then analyzed which steps

of BEE-F(LA)^{2}PW calculations are still time demanding. We found that the basis construction in the first DFT iteration is one of the steps that still requires a lot of time. A basis construction principle beyond the basis from early eigenfunctions has to address this issue, i.e., the required computational resources for the construction of the basis should be reduced. Another computationally expensive step is the calculation of the MT contributions to the overlap matrix and the spherical MT contributions to the Hamilton matrix. We addressed this issue by realizing that contributions associated to high l quantum numbers can reasonably be approximated. Indeed, we showed that it is possible to precalculate approximate contributions from these l channels in the 2nd iteration of the self-consistency loop and reuse them in every succeeding iteration without obtaining a significant impact on the precision. With this approach it is reasonable to further speed up BEE-F(LA)^{2}PW iterations by 20 to 30 percent.

7 Conclusions and outlook

In condensed matter physics, materials physics and materials science, the importance of materials specific theory has risen tremendously and is nowadays an invaluable tool in the investigation and design of new materials. There are two factors that contribute to the rise of this type of theory and simulation: (i) *Density functional theory* (DFT) together with the successful establishment of powerful approximations to the exchange and correlation functional and (ii) *electronic structure methods* implementing DFT and providing highly successful and dynamical approaches to numerically calculate properties of materials. The ever refining development of the theoretical and practical aspects of these methods together with the growing capacity of available computing power leads to an increasing number of application fields in which the methods are used.

One of the most accurate and wide-spread numerical implementations of DFT in terms of an electronic structure method is the *all-electron full-potential linearized augmented plane-wave* (FLAPW) method. To further extend the application domains of this method, we investigated one of its main aspects in detail: The *linearized augmented plane-wave* (LAPW) basis set, which is used to represent the Kohn-Sham wave functions. This basis is founded on a partitioning of space into so-called muffin-tin (MT) spheres centered at the atomic nuclei and the interstitial region between the spheres. In the MT spheres the basis consists of a linear combination of two types of radial functions times spherical harmonics. For predetermined angular-momentum dependent energy parameters E_l^α the first type of radial functions are solutions $u_l^\alpha(r_\alpha, E_l^\alpha)$ to the scalar-relativistic approximation to the radial Dirac equation employing the spherical potential in the given MT sphere of atom α. The second type of radial functions are the energy derivatives $\dot{u}_l^\alpha(r_\alpha, E_l^\alpha)$ of the former functions. In the interstitial region, LAPWs consist of plane waves. Continuity and differentiability of the wave functions are imposed on the level of the basis functions, i.e., at the MT sphere boundaries the MT form of the basis is matched in value and slope to the interstitial representation.

We started the investigation on the LAPW basis by analyzing the impact of the implicit linearization error on calculational results. We showed that for certain materials, e.g., materials with very broad valence bands or materials consisting of atoms with large atomic radii, this error is relevant and has to be considered. In clear words, we demonstrated that the error affects calculated total energies, equilibrium lattice constants, and Kohn-Sham band gaps. It also makes calculation results dependent on

method specific numerical parameters that cannot be converged, i.e., the energy parameters and the MT sphere radii. We evaluated several approaches to eliminate the error by adding local orbitals to the basis and found that the extension of the basis by local orbitals employing the second energy derivative $\ddot{u}_l^\alpha(r_\alpha, E_l^\alpha)$, which we call higher derivative local orbitals (HDLOs), performs best and reduces the linearization error by orders of magnitude. Indeed, with this approach the linearization error becomes so small that in any practical context the remaining rest can be neglected. We also found that the extension of the LAPW basis by HDLOs yields a decoupling of the MT and interstitial region representation of the basis functions. This decoupling implies that the addition of HDLOs goes hand in hand with reduced demands on the number of conventional LAPWs, such that the addition of HDLOs may effectively reduce the required basis set size.

We proceeded by comparing the actual matching conditions of LAPW basis functions at the MT sphere boundaries to those of the Kohn-Sham wave functions. Here, we found that LAPWs with large wave vectors possess significant contributions from high angular momentum channels. For the wave functions this is not the case since the form of the effective potential considerably deviates from a constant potential to which plane waves are solutions. Depending on the actual electronic state, certain angular momentum channels are strongly emphasized and dominate the matching conditions at the MT sphere boundaries. This is especially visible for localized atomic states and states associated with directed bonds. We recognized this discrepancy between the basis functions and the wave functions as an opportunity to develop a new basis set that is even more problem-adapted than the LAPW basis. To further explore the requirements on such a new basis we performed several additional tests that focused on the changes of the Kohn-Sham problem throughout the different iterations of the DFT self-consistency cycle. We found that these changes are small. Indeed, in the MT spheres we saw that the spherical potential only exhibits very small changes in the outer parts of the sphere. The nonspherical parts are exposed to larger relative changes, though the qualitative behavior of these functions remains unchanged. Of course, these small changes in the potential imply similarly small changes of the radial functions $u_l^\alpha(r_\alpha, E_l^\alpha)$ and $\dot{u}_l^\alpha(r_\alpha, E_l^\alpha)$, especially for high l channels. Finally, we investigated the changes of the wave functions in the interstitial region and found that these changes are also rather small: The wave functions obtained in the very first iteration can represent a large part of the associated wave functions in later iterations.

Motivated by the findings from these tests, we generalized the analytical form of the LAPWs to become a new type of basis functions, which we call *linearized augmented lattice-adapted plane-waves* (abbreviated as (LA)^{2}PWs or LA^2PWs). In these functions the plane waves in the interstitial region are replaced by a more general linear combination of plane waves. The idea is that the plane wave expansion in the interstitial region provides the freedom to adapt the basis functions in this region to the actual crystal lattice. We then developed an efficient implementation of such a basis into an existing FLAPW code.

The concept of (LA)^{2}PW basis functions is decoupled from their construction. Our first idea of how to construct a lattice-adapted basis was again motivated by the pre-

viously performed tests, especially on the observation that the changes of the Kohn-Sham problem throughout the iterations of the self-consistency cycle are small. We proposed to construct one half of the basis set in terms of the LAPW expansion coefficients of the eigenfunctions obtained by a single FLAPW iteration and take conventional LAPWs for the other half of the basis set. We then evaluated the *description efficiency* of this *basis from early eigenfunctions* (BEE) for a test set of materials with different properties and a wide array of physical quantities to obtain a picture that is representative for solid state physics and materials science. In these tests the BEE-$(LA)^2$PW basis showed a stunning performance. It reproduced the FLAPW results with very high precision, while also reducing the required basis set size to a small fraction. We then measured the obtainable speedup through the use of this new basis and found that on average results for systems with unit cells of about 100 or more atoms can be obtained 4 to 5 times as fast. Relating this speedup to the growth of available computing power of supercomputers, which is nearly a doubling each year [140], we conclude that the usage of the BEE-$(LA)^2$PW basis allows calculations on complex materials that would be infeasible for the conventional FLAPW method for another 2 or more years. In practice, this advantage is even larger since the parallelizability of matrix diagonalization algorithms is limited so that the benefits of the smaller BEE-$(LA)^2$PW matrices are greater. Nevertheless, we did not stop at this point but investigated in detail which parts of the calculations take most of the runtime. We found that the construction of the basis set is one of these steps. Another step is the setup of the MT part of the Hamilton and overlap matrices. Based on these observations we then addressed the costs of the matrix setup by developing an approximation for the higher l channels which still yields precise results but reduces the time requirements of a BEE-F$(LA)^2$PW iteration by 20 % to 30 %.

As a final outlook, we remark that we believe that it is possible to construct a localized $(LA)^2$PW basis set with a high description efficiency in a computationally less demanding way. The development of such a basis would provide another considerable speedup of the calculations and is therefore highly desirable. We also note that we developed a prototype program that does not yet feature the full functionality of a well-established FLAPW program like the FLEUR code. The development of a full production code requires a reformulation of several physical properties in terms of the $(LA)^2$PW basis instead of the LAPW basis.

A Atomic orbital $(LA)^2PW$ basis sets

Contents

We have seen that the BEE-$(LA)^2PW$ basis features a very high description efficiency. However, a drawback of this approach is that the construction of the basis is computationally expensive as it requires a complete FLAPW iteration. For some types of materials this single iteration can take a very large part of the overall calculation runtime. Thus, to further speed up the calculations, we want to develop another construction principle for $(LA)^2PW$ basis sets that is computationally less expensive. Of course, a prerequisite for such a development is the identification of the required ingredients.

What we already know is that everything we need to construct an efficient basis is already present in the starting density, which is a superposition of atomic densities. But as we want to eliminate the time requirements associated with the setup of the matrices and the diagonalization of the problem in terms of the LAPW basis, we test approaches to construct a basis in a way that does not require these steps. The first idea that comes to mind is the usage of atomic orbitals[1] or other types of radial functions times spherical harmonics that are efficiently constructible. Partly, this is also motivated by the approach of Kotani *et al.* [111] to fuse the LMTO and LAPW basis sets. Especially for calculations that do not require a very high precision, this approach considerably reduces the required basis set size. For very high precision requirements, e.g., the 25 μHtr/atom criterion that we have imposed for the BEE-$(LA)^2PW$ basis, the differences between this LMTO+LAPW approach and the conventional LAPW basis becomes smaller.

We denote an $(LA)^2PW$ basis consisting of atomic orbitals as atomic orbital $(LA)^2PW$ (AO-$(LA)^2PW$) basis. In this appendix we shortly sketch the construction of an example for such a basis in section A.1 and also provide results on the obtained description efficiency in section A.2. Finally, we conclude the appendix in section A.3.

[1] Here, we use a very broad definition of *atomic orbital* that only means that the functions are constructed by using some kind of spherical potential and that the functions vanish for very large radii.

A.1 Construction

For the construction of atomic orbitals and their expansion into plane waves in the IR we follow a simple recipe:

Recipe for the construction of atomic orbital (LA)^{2}PWs

1. Construct the functions in a spherical coordinate system. The function center of mass is at the origin.
2. Replace the part of the function that is inside the MT sphere of the associated atom by a smooth function to enable a fast converging Fourier expansion
3. Expand the function in terms of plane waves.
4. Move the function to the position of the associated atom.

For the two examples, AO-(LA)^{2}PW-A and AO-(LA)^{2}PW-B, that we discuss in this appendix, we choose the atomic orbitals in the following way. First, we use the occupied atomic states of the respective isolated atoms above the core electron states, as we have empirically observed that this is a good starting point. Next, we consider the spherical potential in the MT spheres of the respective atoms in the actual crystal and extrapolate it beyond the MT sphere by matching the function

$$f(r_\alpha) = \frac{A}{r_\alpha} + \frac{B}{r_\alpha^2} + V_{\mathrm{IR}}^{\mathrm{ave}} \tag{A.1}$$

at the MT boundary in value and slope to the spherical potential in the sphere. The coefficients A and B are obtained through this matching condition. Asymptotically, the potential obtained through this extension approaches the averaged interstitial potential $V_{\mathrm{IR}}^{\mathrm{ave}}$. After extending the spherical potential in this way beyond the MT sphere boundary, we also add a confining potential

$$V^{\mathrm{conf}}(r_\alpha) = \begin{cases} 0\ \mathrm{Htr} & \text{for } r_\alpha \leq 20\ a_0 \\ 0.005\ \frac{\mathrm{Htr}}{a_0^2}(r_\alpha - 20\ a_0)^2 & \text{for } r_\alpha > 20\ a_0 \end{cases} . \tag{A.2}$$

With the conventional energy parameters E_l^α we then calculate solutions to this spherical problem with regular behavior at $r_\alpha = \infty$. For the first approach, AO-(LA)^{2}PW-A, we take all solutions up to l_{phys}^α, and for AO-(LA)^{2}PW-B we take the solutions up to $l_{\mathrm{phys}}^\alpha + 1$. The third type of (LA)^{2}PWs entering these basis sets are once again conventional LAPWs. We add LAPWs until the desired basis set size N_{bas} is reached.

Note that the details of this construction principle are to some extent arbitrary. However, this statement can also be made for most DFT codes employing localized basis sets. In such approaches, the construction scheme is typically optimized to yield

a basis set with a high description efficiency for a prototype system or a set of prototype systems. Of course, we varied the details of the construction and performed numerous tests with different potentials and energy parameters. The result of these tests is that the two presented basis sets can be considered to be qualitatively representative. Note that we also tested Hankel functions to compare to the LMTO+LAPW fusion by Kotani *et al.* [111] as well as smoothed Hankel functions [141] as an ingredient for an (LA)^{2}PW basis. Basis sets including such functions also show a similar behavior to those presented in this appendix.

Based on the now determined atomic orbitals $\overset{\circ}{\phi}{}^{\alpha}_{Lj}(\boldsymbol{r}) = \overset{\circ}{\phi}{}^{\alpha}_{lj}(r_\alpha)Y_L(\hat{\boldsymbol{r}}_\alpha)$, where the angular momentum l and magnetic m quantum numbers, as well as the atom α, are directly given by the index of the function j, we now construct a smooth function $\tilde{\phi}^{\alpha}_{Lj}$ that is identical to $\overset{\circ}{\phi}{}^{\alpha}_{Lj}$ in the IR but differs in the MT sphere of atom α. This construction follows a recipe proposed by K. M. Rappe *et al.* [142]. To ensure a fast convergence of the Fourier expansion of $\tilde{\phi}^{\alpha}_{Lj}$ we consider the cutoff parameter $K_{\max}$ for the expansion and minimize the kinetic energy connected to those Fourier components that are beyond the cutoff.

In detail, we calculate the kinetic energy once in real space on the radial mesh and once by the Fourier expansion and minimize the difference between these two calculations. Formally, this difference is

$$\Delta E_{\text{kin}} = -\frac{1}{2}\int \left(\tilde{\phi}^{\alpha}_{Lj}\right)^*(\boldsymbol{r})\nabla^2\tilde{\phi}^{\alpha}_{Lj}(\boldsymbol{r})d^3r - \frac{1}{2}\int\limits_{|\boldsymbol{K}|<K_{\max}} |\boldsymbol{K}|^2|\tilde{\phi}^{\alpha}_{Lj}(\boldsymbol{K})|^2 d^3K. \tag{A.3}$$

To minimize ΔE_{kin} we first have to define the set of functions in which the minimization takes place. Rappe proposes to construct the smooth function in the MT spheres in terms of a linear combination of spherical Bessel functions associated with different wave vectors K_i. We stick to this approach and thus the smooth atomic orbitals have the form

$$\tilde{\phi}^{\alpha}_{Lj}(\boldsymbol{r}) = \tilde{\phi}^{\alpha}_{lj}(r_\alpha)Y_L(\hat{\boldsymbol{r}}_\alpha) = \begin{cases} \sum\limits_i \gamma_i j_l(K_i r_\alpha)Y_L(\hat{\boldsymbol{r}}_\alpha) & \text{for } r_\alpha \le R_{\text{MT}^\alpha} \\ \overset{\circ}{\phi}{}^{\alpha}_{lj}(r_\alpha)Y_L(\hat{\boldsymbol{r}}_\alpha) & \text{for } r_\alpha > R_{\text{MT}^\alpha} \end{cases}, \tag{A.4}$$

where γ_i are the expansion coefficients for the i-th spherical Bessel function. A requirement that has to be fulfilled by the smooth atomic orbital is that it is continuous in value, slope, and curvature. An optimization problem of this type is a special form of a so-called quadratic programming problem. As it only exhibits equality constraints and no inequality constraints it is solvable with the method of Lagrange multipliers.

The third step in the construction of an AO-(LA)^{2}PW basis is the expansion of the $\tilde{\phi}^{\alpha}_{Lj}(\boldsymbol{r})$ in plane waves. We directly expand these functions in plane waves including the Bloch factor, $\frac{1}{\sqrt{\Omega}}e^{i(\boldsymbol{k}+\boldsymbol{G})\boldsymbol{r}}$, by performing the Fourier transformation on the radial

mesh. For this, we expand the plane waves in terms of radial Bessel functions to obtain

$$\phi^{\mathrm{PW}}_{\boldsymbol{kG}}(\boldsymbol{r}) = \frac{1}{\sqrt{\Omega}} e^{i(\boldsymbol{k}+\boldsymbol{G})\boldsymbol{r}} = \frac{1}{\sqrt{\Omega}} \sum_{L} 4\pi i^l j_l(|\boldsymbol{k}+\boldsymbol{G}|r) Y_L^*(\widehat{\boldsymbol{k}+\boldsymbol{G}}) Y_L(\hat{\boldsymbol{r}}). \tag{A.5}$$

As the atomic orbital vanishes for each but a single L channel, the Fourier expansion of $\tilde{\phi}^{\alpha}_{Lj}(\boldsymbol{r})$ is then given by the simple integral over the whole space,

$$\langle \phi^{\mathrm{PW}}_{\boldsymbol{kG}} | \tilde{\phi}^{\alpha}_{Lj} \rangle = \frac{1}{\sqrt{\Omega}} 4\pi i^l \int r^2 j_l(|\boldsymbol{k}+\boldsymbol{G}|r) Y_L(\widehat{\boldsymbol{k}+\boldsymbol{G}}) \tilde{\phi}^{\alpha}_{lj}(r) dr. \tag{A.6}$$

Note that the integration over the whole space does not only yield the atomic orbital from the actual atom, but a superposition of atomic orbitals that includes the orbitals from equivalent atoms in the neighboring unit cells, multiplied with the Bloch factor.

Finally, we have to move the center of the function to the actual atom position by multiplying it with the associated translation factor in reciprocal space. With this we obtain the plane wave expansion coefficients of the AO-(LA)^{2}PW basis functions as

$$o^{\boldsymbol{G}}_{\boldsymbol{k}j} = e^{-i(\boldsymbol{k}+\boldsymbol{G})\tau_\alpha} \langle \phi^{\mathrm{PW}}_{\boldsymbol{kG}} | \tilde{\phi}^{\alpha}_{Lj} \rangle, \tag{A.7}$$

where τ_α is the atom position. Note that the construction of such a basis is more efficient than the construction of the BEE-(LA)^{2}PW basis as its time requirements only scale with $\mathcal{N}_{\mathrm{bas}}\mathcal{N}_{\mathrm{PW}}$.

A.2 Precision

We test the precision of the two considered AO-(LA)^{2}PW basis sets on two materials, fcc Cu and zinc blende SiC, and for three quantities, i.e., the total energy, the equilibrium lattice constant, and the bulk modulus. Unless otherwise noted, the calculation parameters are identical to those presented in table 6.1.

For Cu, the convergence behavior for the total energy is presented in figure A.1. We observe that the two AO-(LA)^{2}PW basis sets yield a very similar convergence, which is better than the convergence with the conventional LAPW basis, but on the other hand worse than the convergence for the BEE-(LA)^{2}PW basis. Indeed, for the same number of basis functions the error in the total energy of the BEE-(LA)^{2}PW basis is nearly two orders of magnitude smaller than the one for the AO-(LA)^{2}PW basis sets.

For the convergence of the equilibrium lattice constant presented in figure A.2 the picture looks similar. The AO-(LA)^{2}PW basis sets do not feature such a high description efficiency as the BEE-(LA)^{2}PW basis, but the convergence in comparison to the conventional LAPW basis is much faster. The AO-(LA)^{2}PW values obtained with rather small basis set sizes of 30 or more basis functions are quite usable as they deviate by less than 0.01 % from the associated FLAPW result. We note, however, that the convergence beyond this deviation is slow.

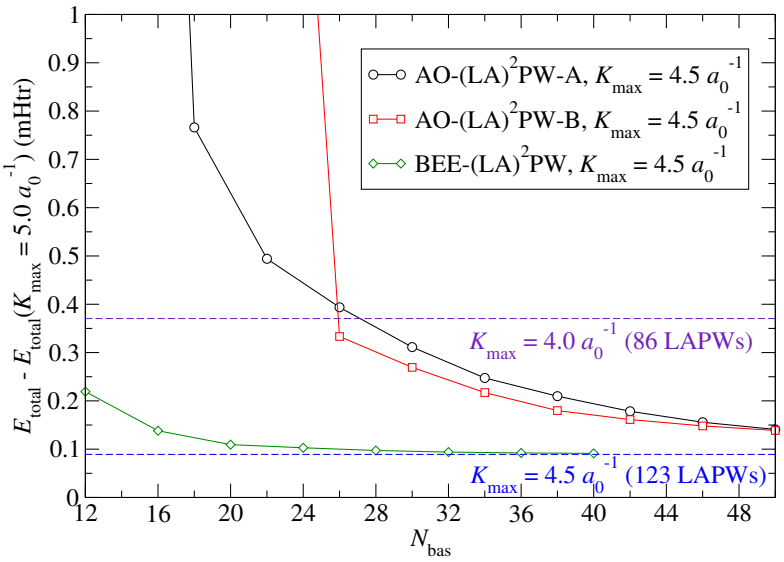

Figure A.1.: Convergence behavior of the total energy for fcc Cu obtained with the two AO-(LA)^{2}PW basis sets, the BEE-(LA)^{2}PW basis, and the conventional FLAPW method. The dashed lines show the results obtained with the conventional FLAPW method and the given $K_{\max}$ parameters.

Figure A.3 shows the convergence of the bulk modulus. Here, we observe that the error associated with the AO-(LA)^{2}PW basis sets is larger, though this quantity still converges faster than with the conventional LAPW basis. Again the BEE-(LA)^{2}PW basis yields by far the highest description efficiency.

For SiC the convergence of the total energy is displayed in figure A.4. We observe that the additional error associated with the two AO-(LA)^{2}PW basis sets is considerably larger in comparison to the previously discussed fcc Cu. However, also the FLAPW method yields a slower convergence for this material, so that the AO-(LA)^{2}PW approach still allows to significantly reduce the basis set size. On the other hand, the BEE-(LA)^{2}PW basis does not suffer from the challenges in the description of this material and again yields a considerably faster convergence. For same basis set sizes the error associated with this basis in comparison to the AO-(LA)^{2}PW basis sets is once again smaller by nearly two orders of magnitude.

Figure A.5 shows the convergence for the equilibrium lattice constant, where the so far drawn picture is once again confirmed. Though the AO-(LA)^{2}PW basis sets yield a faster convergence than the conventional LAPW basis, they are by far not as good as the BEE-(LA)^{2}PW basis. In comparison to the very nice agreement of the AO-(LA)^{2}PW lattice constants for fcc Cu, in this case a basis set size of 60 basis function, i.e., 30 basis functions per atom, yields larger deviations to the FLAPW reference result. Nevertheless, it these deviations are still smaller than 0.1 %

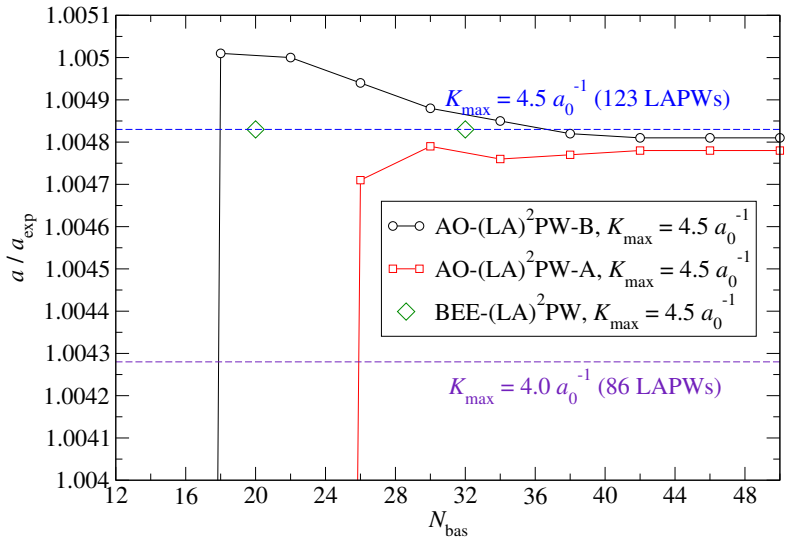

Figure A.2.: Convergence behavior of the equilibrium lattice constant a for fcc Cu obtained with the two AO-(LA)^{2}PW basis sets, the BEE-(LA)^{2}PW basis, and the conventional FLAPW method. The dashed lines show the results obtained with the conventional FLAPW method and the given K_{max} parameters.

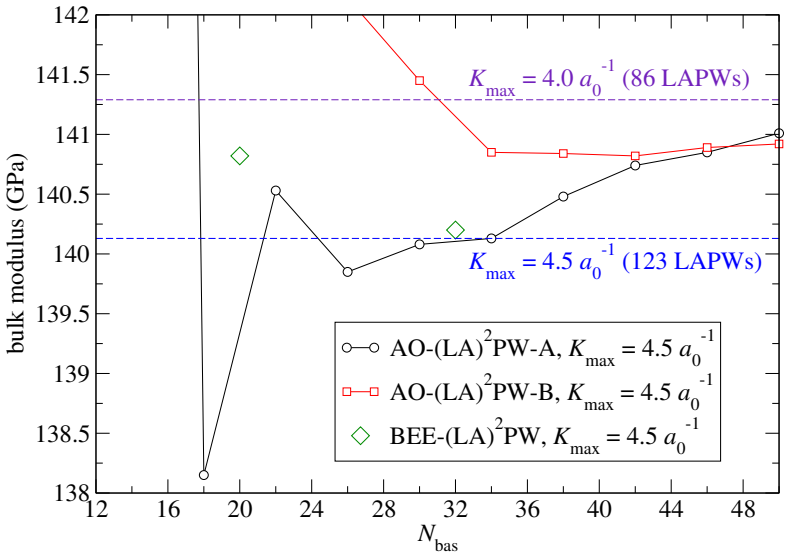

Figure A.3.: Convergence behavior of the bulk modulus for fcc Cu obtained with the two AO-(LA)^{2}PW basis sets, the BEE-(LA)^{2}PW basis, and the conventional FLAPW method. The dashed lines show the results obtained with the conventional FLAPW method and the given K_{max} parameters.

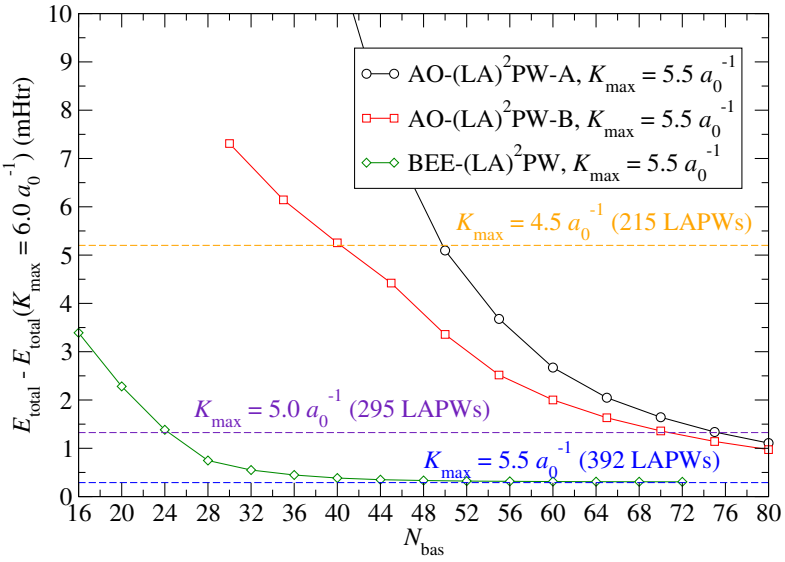

Figure A.4.: Convergence behavior of the total energy for zinc blende SiC obtained with the two AO-(LA)^{2}PW basis sets, the BEE-(LA)^{2}PW basis, and the conventional FLAPW method. The dashed lines show the results obtained with the conventional FLAPW method and the given K_{max} parameters.

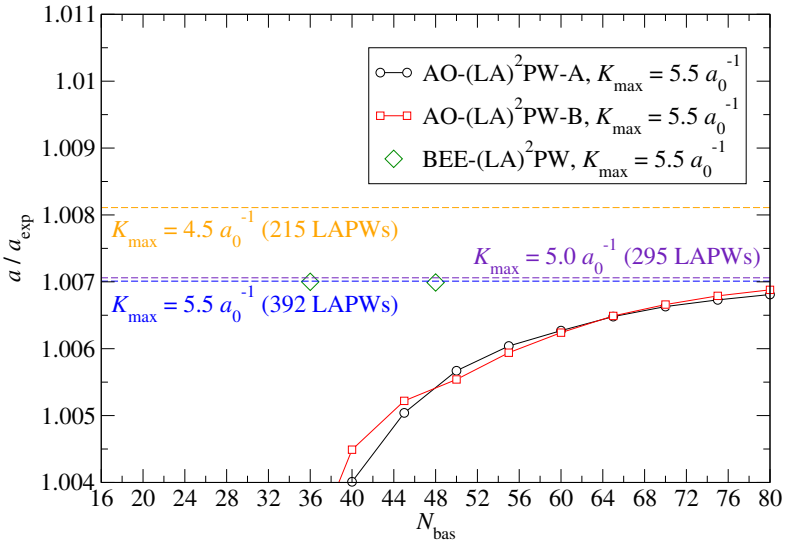

Figure A.5.: Convergence behavior of the equilibrium lattice constant a for zinc blende SiC obtained with the two AO-(LA)^{2}PW basis sets, the BEE-(LA)^{2}PW basis, and the conventional FLAPW method. The dashed lines show the results obtained with the conventional FLAPW method and the given K_{max} parameters.

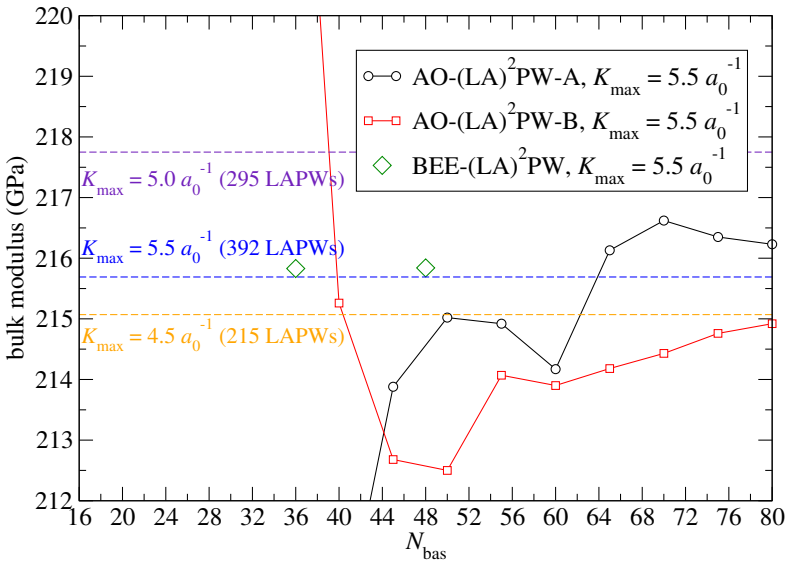

Figure A.6.: Convergence behavior of the bulk modulus for zinc blende SiC obtained with the two AO-(LA)^{2}PW basis sets, the BEE-(LA)^{2}PW basis, and the conventional FLAPW method. The dashed lines show the results obtained with the conventional FLAPW method and the given $K_{\max}$ parameters.

Finally, the convergence of the bulk modulus for SiC is presented in figure A.6. Here we observe a rather slow convergence with the AO-(LA)^{2}PW basis sets. The BEE-F(LA)^{2}PW results, on the other hand, stick to their FLAPW counterpart.

A.3 Concluding remarks

We have seen that the convergence obtained with the AO-(LA)^{2}PW basis sets is more efficient in comparison to the convergence with the LAPW basis but also much slower than the one obtained with the BEE-(LA)^{2}PW basis. As this is connected to larger required basis sets it is questionable if a considerable speedup can be obtained with an AO-(LA)^{2}PW approach. Judging from the results we have obtained in this appendix, the convergence behavior of the AO-(LA)^{2}PW basis sets is similar to the convergence of the fused LMTO+LAPW method, though in the original publication on this method [111] other example materials have been used to test the convergence. The 25 μHtr/atom criterion is not reachable with small AO-(LA)^{2}PW basis sets and it is probable that we have to add many conventional LAPWs to the basis sets to comply with this criterion.

The BEE-(LA)^{2}PW basis has the advantage that its plane wave expansion coefficients $o_{\boldsymbol{kj}}^{\boldsymbol{G}}$ are very well adapted to the actual crystal, especially the coefficients for

the larger wave vectors are a very good choice. This implies that the matching conditions to the MT spheres are also very well adapted to the physics of the respective system, even for high angular momentum quantum numbers l. As a consequence, a few conventional LAPWs and a few BEE-constructed functions are sufficient to reproduce the associated FLAPW results with very high precision. Obviously this is not the case for the AO-(LA)^{2}PW basis sets. Here, additional LAPWs with larger wave vectors are a relevant extension of the basis and thus the obtained convergence behavior is worse. On the other hand it is a significant step forward in comparison to the LAPW basis as we have seen that for a mediocre precision the basis set size can be reduced with the AO-(LA)^{2}PW approach. We stress that this is evidence that the construction of AO-(LA)^{2}PWs is a step into the right direction, but an important ingredient is missing.

One promising candidate for such an ingredient is the inclusion of the nonspherical part of the potential in the construction of the AOs. While each AO-(LA)^{2}PW is associated to a single L channel, we have seen in chapter 6.3 that the matching conditions of the wave functions at the MT sphere boundaries have contributions from a broad range of L channels. The inclusion of the nonspherical part of the potential in the construction yields basis functions that feature nonvanishing contributions in such a range of L channels and may thus provide a chance to obtain fitting matching conditions at the MT sphere boundaries, even for high angular momentum quantum numbers. We assume that this would considerably reduce the demands for additional LAPWs with large wave vectors.

List of abbreviations

AEP	atomic energy parameter
AO	atomic orbital
AFM	antiferromagnetic
APW	augmented plane-wave
B3LYP	Becke, 3 parameter, Lee-Yang-Parr
BEE	basis from early eigenfunctions
cRPA	constrained random phase approximation
DFT	density functional theory
DOS	density of states
ECM	energy center of mass
ELAPW	extended linearized augmented plane-wave
EXX	exact exchange
FFT	fast Fourier transform
F(LA)^{2}PW	full-potential linearized augmented lattice-adapted plane-wave
FLAPW	full-potential linearized augmented plane-wave
FM	ferromagnetic
GEA	gradient expansion approximation
GGA	generalized gradient approximation
HDLO	higher derivative local orbital
HELO	higher energy local orbital
HSE	Heyd-Scuseria-Ernzerhof
IBZ	irreducible wedge of the Brillouin zone
IR	interstitial region
KKR	Korringa-Kohn-Rostoker
(LA)^{2}PW	linearized augmented lattice-adapted plane-wave
LAPW	linearized augmented plane-wave
LCAO	linear combination of atomic orbitals
LDA	local density approximation
LMTO	linearized muffin-tin orbitals
LO	local orbital
LSDA	local spin density approximation
MAPW	modified augmented plane-wave
MBPT	many-body perturbation theory

MT	muffin-tin
OEP	optimized effective potential
PAW	projector augmented wave
PBE	Perdew-Burke-Ernzerhof
PW	plane-wave
PZ	Perdew-Zunger
QAPW	quadratically augmented plane-wave
r2PT	renormalized second order perturbation theory
RPA	random phase approximation
rSE	renormalized single excitation
SAPW	spline augmented plane-wave
SOSEX	second order screened exchange
SRA	scalar-relativistic approximation
VR	vacuum region
XC	exchange and correlation

Bibliography

[1] G. E. Moore, *Cramming More Components Onto Integrated Circuits*, Proceedings of the IEEE **86** (1998), 82–85.

[2] P. Hohenberg and W. Kohn, *Inhomogeneous Electron Gas*, Phys. Rev. **136** (1964), B864–B871.

[3] W. Kohn and L. J. Sham, *Self-Consistent Equations Including Exchange and Correlation Effects*, Phys. Rev. **140** (1965), A1133–A1138.

[4] *Materials Project*, `https://materialsproject.org/`.

[5] *Web of Knowledge*, `http://wokinfo.com/`.

[6] O. K. Andersen, *Linear methods in band theory*, Phys. Rev. B **12** (1975), 3060–3083.

[7] E. Wimmer, H. Krakauer, M. Weinert, and A. J. Freeman, *Full-potential self-consistent linearized-augmented-plane-wave method for calculating the electronic structure of molecules and surfaces:* O_2 *molecule*, Phys. Rev. B **24** (1981), 864–875.

[8] J. C. Slater, *Wave Functions in a Periodic Potential*, Phys. Rev. **51** (1937), 846–851.

[9] D. Singh, *Ground-state properties of lanthanum: Treatment of extended-core states*, Phys. Rev. B **43** (1991), 6388–6392.

[10] E. E. Krasovskii, A. N. Yaresko, and V. N. Antonov, *Theoretical study of ultraviolet photoemission spectra of noble metals*, Journal of Electron Spectroscopy and Related Phenomena **68** (1994), 157–166.

[11] E. E. Krasovskii and W. Schattke, *The extended-LAPW-based* $\boldsymbol{k}\cdot\boldsymbol{p}$ *method for complex band structure calculations*, Solid State Communications **93** (1995), 775–779.

[12] E. E. Krasovskii, *Accuracy and convergence properties of the extended linear augmented-plane-wave method*, Phys. Rev. B **56** (1997), 12866–12873.

[13] E. E. Krasovskii, V. V. Nemoshkalenko, and V. N. Antonov, *On the accuracy of the wavefunctions calculated by LAPW method*, Zeitschrift für Physik B Condensed Matter **91** (1993), 463–466.

[14] E. Sjöstedt, L. Nordström, and D. J. Singh, *An alternative way of linearizing the augmented plane-wave method*, Solid State Communications **114** (2000), 15–20.

[15] G. K. H. Madsen, P. Blaha, K. Schwarz, E. Sjöstedt, and L. Nordström, *Efficient linearization of the augmented plane-wave method*, Phys. Rev. B **64** (2001), 195134.

[16] F. Bultmark, K. Dewhurst, D. J. Singh, and L. Nordström, *Tests of the efficiency of an augmented distorted planewave basis in electronic structure calculations*, Journal of Physics: Condensed Matter **20** (2008), 235241.

[17] *The Jülich FLEUR project*, `http://www.flapw.de/`.

[18] P. Kurz, *Non-Collinear Magnetism at Surfaces and in Ultrathin Films*, Ph.D. thesis, RWTH Aachen, 2000.

[19] M. Betzinger, *Orbital-dependent exchange-correlation functionals in density-functional theory realized by the FLAPW method*, Ph.D. thesis, RWTH Aachen, 2011.

[20] K. Capelle, *A bird's-eye view of density-functional theory*, arXiv:cond-mat/0211443v5 (2006).

[21] R. M. Martin, *Electronic Structure - Basic Theory and Practical Methods*, Cambridge, 2004.

[22] M. Born and R. Oppenheimer, *Zur Quantentheorie der Molekeln*, Annalen der Physik **389** (1927), 457–484.

[23] W. Kohn, *Nobel Lecture: Electronic structure of matter¯wave functions and density functionals*, Rev. Mod. Phys. **71** (1999), 1253–1266.

[24] M. Levy, *Electron densities in search of Hamiltonians*, Phys. Rev. A **26** (1982), 1200–1208.

[25] R. G. Parr, R. A. Donnelly, M. Levy, and W. E. Palke, *Electronegativity: The density functional viewpoint*, The Journal of Chemical Physics **68** (1978), 3801–3807.

[26] M. Levy, *Universal variational functionals of electron densities, first-order density matrices, and natural spin-orbitals and solution of the v-representability problem*, Proceedings of the National Academy of Sciences **76** (1979), 6062–6065.

[27] W. Kohn, A. D. Becke, and R. G. Parr, *Density Functional Theory of Electronic Structure*, The Journal of Physical Chemistry **100** (1996), 12974–12980.

[28] U. von Barth and L. Hedin, *A local exchange-correlation potential for the spin polarized case: I*, Journal of Physics C: Solid State Physics **5** (1972), 1629.

[29] D. M. Ceperley and B. J. Alder, *Ground State of the Electron Gas by a Stochastic Method*, Phys. Rev. Lett. **45** (1980), 566–569.

[30] S. H. Vosko, L. Wilk, and M. Nusair, *Accurate spin-dependent electron liquid correlation energies for local spin density calculations: a critical analysis*, Canadian Journal of Physics **58** (1980), 1200–1211.

[31] J. P. Perdew and A. Zunger, *Self-interaction correction to density-functional approximations for many-electron systems*, Phys. Rev. B **23** (1981), 5048–5079.

[32] F. Herman, J. P. Van Dyke, and I. B. Ortenburger, *Improved Statistical Exchange Approximation for Inhomogeneous Many-Electron Systems*, Phys. Rev. Lett. **22** (1969), 807–811.

[33] P. S. Svendsen and U. von Barth, *Gradient expansion of the exchange energy from second-order density response theory*, Phys. Rev. B **54** (1996), 17402–17413.

[34] S.-K. Ma and K. A. Brueckner, *Correlation Energy of an Electron Gas with a Slowly Varying High Density*, Phys. Rev. **165** (1968), 18–31.

[35] A. D. Becke, *Density-functional exchange-energy approximation with correct asymptotic behavior*, Phys. Rev. A **38** (1988), 3098–3100.

[36] J. P. Perdew and Y. Wang, *Accurate and simple analytic representation of the electron-gas correlation energy*, Phys. Rev. B **45** (1992), 13244–13249.

[37] J. P. Perdew, K. Burke, and M. Ernzerhof, *Generalized Gradient Approximation Made Simple*, Phys. Rev. Lett. **77** (1996), 3865–3868.

[38] Y. Zhang and W. Yang, *Comment on "Generalized Gradient Approximation Made Simple"*, Phys. Rev. Lett. **80** (1998), 890–890.

[39] V. I. Anisimov, J. Zaanen, and O. K. Andersen, *Band theory and Mott insulators: Hubbard U instead of Stoner I*, Phys. Rev. B **44** (1991), 943–954.

[40] V. I. Anisimov, F. Aryasetiawan, and A. I. Lichtenstein, *First-principles calculations of the electronic structure and spectra of strongly correlated systems: the LDA + U method*, Journal of Physics: Condensed Matter **9** (1997), 767.

[41] J. Hubbard, *Electron Correlations in Narrow Energy Bands. IV. The Atomic Representation*, Proceedings of the Royal Society of London. Series A. Mathematical and Physical Sciences **285** (1965), 542–560.

[42] F. Aryasetiawan, M. Imada, A. Georges, G. Kotliar, S. Biermann, and A. I. Lichtenstein, *Frequency-dependent local interactions and low-energy effective models from electronic structure calculations*, Phys. Rev. B **70** (2004), 195104.

[43] F. Aryasetiawan, K. Karlsson, O. Jepsen, and U. Schönberger, *Calculations of Hubbard U from first-principles*, Phys. Rev. B **74** (2006), 125106.

[44] T. Miyake and F. Aryasetiawan, *Screened Coulomb interaction in the maximally localized Wannier basis*, Phys. Rev. B **77** (2008), 085122.

[45] T. Miyake, F. Aryasetiawan, and M. Imada, *Ab initio procedure for constructing effective models of correlated materials with entangled band structure*, Phys. Rev. B **80** (2009), 155134.

[46] E. Şaşıoğlu, C. Friedrich, and S. Blügel, *Effective Coulomb interaction in transition metals from constrained random-phase approximation*, Phys. Rev. B **83** (2011), 121101.

[47] A. D. Becke, *Density-functional thermochemistry. III. The role of exact exchange*, The Journal of Chemical Physics **98** (1993), 5648–5652.

[48] P. J. Stephens, F. J. Devlin, C. F. Chabalowski, and M. J. Frisch, *Ab Initio Calculation of Vibrational Absorption and Circular Dichroism Spectra Using Density Functional Force Fields*, The Journal of Physical Chemistry **98** (1994), 11623–11627.

[49] C. Lee, W. Yang, and R. G. Parr, *Development of the Colle-Salvetti correlation-energy formula into a functional of the electron density*, Phys. Rev. B **37** (1988), 785–789.

[50] J. Heyd, G. E. Scuseria, and M. Ernzerhof, *Hybrid functionals based on a screened Coulomb potential*, The Journal of Chemical Physics **118** (2003), 8207–8215.

[51] B. G. Janesko, T. M. Henderson, and G. E. Scuseria, *Screened hybrid density functionals for solid-state chemistry and physics*, Phys. Chem. Chem. Phys. **11** (2009), 443–454.

[52] D. C. Langreth and J. P. Perdew, *The exchange-correlation energy of a metallic surface*, Solid State Communications **17** (1975), 1425–1429.

[53] D. C. Langreth and J. P. Perdew, *Exchange-correlation energy of a metallic surface: Wave-vector analysis*, Phys. Rev. B **15** (1977), 2884–2901.

[54] O. Gunnarsson and B. I. Lundqvist, *Exchange and correlation in atoms, molecules, and solids by the spin-density-functional formalism*, Phys. Rev. B **13** (1976), 4274–4298.

[55] D. Bohm and D. Pines, *A Collective Description of Electron Interactions. I. Magnetic Interactions*, Phys. Rev. **82** (1951), 625–634.

[56] D. Pines and D. Bohm, *A Collective Description of Electron Interactions: II. Collective* vs *Individual Particle Aspects of the Interactions*, Phys. Rev. **85** (1952), 338–353.

[57] D. Bohm and D. Pines, *A Collective Description of Electron Interactions: III. Coulomb Interactions in a Degenerate Electron Gas*, Phys. Rev. **92** (1953), 609–625.

[58] D. Pines, *A Collective Description of Electron Interactions: IV. Electron Interaction in Metals*, Phys. Rev. **92** (1953), 626–636.

[59] M. Gell-Mann and K. A. Brueckner, *Correlation Energy of an Electron Gas at High Density*, Phys. Rev. **106** (1957), 364–368.

[60] X. Ren, P. Rinke, C. Joas, and M. Scheffler, *Random-phase approximation and its applications in computational chemistry and materials science*, Journal of Materials Science **47** (2012), 7447–7471 (English).

[61] A. Heßelmann and A. Görling, *Random-phase approximation correlation methods for molecules and solids*, Molecular Physics **109** (2011), 2473–2500.

[62] K. S. Singwi, M. P. Tosi, R. H. Land, and A. Sjölander, *Electron Correlations at Metallic Densities*, Phys. Rev. **176** (1968), 589–599.

[63] S. Kurth and J. P. Perdew, *Density-functional correction of random-phase-approximation correlation with results for jellium surface energies*, Phys. Rev. B **59** (1999), 10461–10468.

[64] Z. Yan, J. P. Perdew, and S. Kurth, *Density functional for short-range correlation: Accuracy of the random-phase approximation for isoelectronic energy changes*, Phys. Rev. B **61** (2000), 16430–16439.

[65] J. Paier, B. G. Janesko, T. M. Henderson, G. E. Scuseria, A. Gruneis, and G. Kresse, *Hybrid functionals including random phase approximation correlation and second-order screened exchange*, The Journal of Chemical Physics **132** (2010), 094103.

[66] D. L. Freeman, *Coupled-cluster expansion applied to the electron gas: Inclusion of ring and exchange effects*, Phys. Rev. B **15** (1977), 5512–5521.

[67] A. Grüneis, M. Marsman, J. Harl, L. Schimka, and G. Kresse, *Making the random phase approximation to electronic correlation accurate*, The Journal of Chemical Physics **131** (2009), 154115.

[68] X. Ren, A. Tkatchenko, P. Rinke, and M. Scheffler, *Beyond the Random-Phase Approximation for the Electron Correlation Energy: The Importance of Single Excitations*, Phys. Rev. Lett. **106** (2011), 153003.

[69] X. Ren, P. Rinke, G. E. Scuseria, and M. Scheffler, *Renormalized second-order perturbation theory for the electron correlation energy: Concept, implementation, and benchmarks*, Phys. Rev. B **88** (2013), 035120.

[70] S. Blügel and G. Bihlmayer, *Full-Potential Linearized Augmented Planewave Method*, NIC Series, vol. 31, pp. 85–129, John von Neumann Institute for Computing, Jülich, 2006.

[71] H. J. F. Jansen, *Magnetic anisotropy in density-functional theory*, Phys. Rev. B **38** (1988), 8022–8029.

[72] A. H. MacDonald and S. H. Vosko, *A relativistic density functional formalism*, Journal of Physics C: Solid State Physics **12** (1979), 2977.

[73] A. K. Rajagopal, *Inhomogeneous relativistic electron gas*, Journal of Physics C: Solid State Physics **11** (1978), L943.

[74] D. D. Koelling and B. N. Harmon, *A technique for relativistic spin-polarised calculations*, Journal of Physics C: Solid State Physics **10** (1977), 3107.

[75] T. Takeda, *The scalar relativistic approximation*, Zeitschrift für Physik B Condensed Matter **32** (1978), 43–48 (English).

[76] N. Troullier and J. L. Martins, *Efficient pseudopotentials for plane-wave calculations*, Phys. Rev. B **43** (1991), 1993–2006.

[77] D. R. Hamann, M. Schlüter, and C. Chiang, *Norm-Conserving Pseudopotentials*, Phys. Rev. Lett. **43** (1979), 1494–1497.

[78] L. Kleinman and D. M. Bylander, *Efficacious Form for Model Pseudopotentials*, Phys. Rev. Lett. **48** (1982), 1425–1428.

[79] D. Vanderbilt, *Soft self-consistent pseudopotentials in a generalized eigenvalue formalism*, Phys. Rev. B **41** (1990), 7892–7895.

[80] W. J. Hehre, R. F. Stewart, and J. A. Pople, *Self-Consistent Molecular-Orbital Methods. I. Use of Gaussian Expansions of Slater-Type Atomic Orbitals*, The Journal of Chemical Physics **51** (1969), 2657–2664.

[81] J. C. Slater, *Atomic Shielding Constants*, Phys. Rev. **36** (1930), 57–64.

[82] B. Delley, *An all-electron numerical method for solving the local density functional for polyatomic molecules*, The Journal of Chemical Physics **92** (1990), 508–517.

[83] K. Koepernik and H. Eschrig, *Full-potential nonorthogonal local-orbital minimum-basis band-structure scheme*, Phys. Rev. B **59** (1999), 1743–1757.

[84] V. Blum, R. Gehrke, F. Hanke, P. Havu, V. Havu, X. Ren, K. Reuter, and M. Scheffler, *Ab initio molecular simulations with numeric atom-centered orbitals*, Computer Physics Communications **180** (2009), 2175–2196.

[85] P. E. Blöchl, *Projector augmented-wave method*, Phys. Rev. B **50** (1994), 17953–17979.

[86] J. Korringa, *On the calculation of the energy of a Bloch wave in a metal*, Physica **13** (1947), 392–400.

[87] W. Kohn and N. Rostoker, *Solution of the Schrödinger Equation in Periodic Lattices with an Application to Metallic Lithium*, Phys. Rev. **94** (1954), 1111–1120.

[88] B. Drittler, M. Weinert, R. Zeller, and P. H. Dederichs, *Vacancy formation energies of fcc transition metals calculated by a full potential green's function method*, Solid State Communications **79** (1991), 31–35.

[89] M. Ogura and H. Akai, *The full potential Korringa-Kohn-Rostoker method and its application in electric field gradient calculations*, Journal of Physics: Condensed Matter **17** (2005), 5741.

[90] J. L. Beeby, *The Density of Electrons in a Perfect or Imperfect Lattice*, Proceedings of the Royal Society of London. Series A. Mathematical and Physical Sciences **302** (1967), 113–136.

[91] T. H. Dupree, *Electron scattering in a crystal lattice*, Annals of Physics **15** (1961), 63–78.

[92] H. Bross, *Ein neues Verfahren zur Berechnung von Einelektronenzuständen in Kristallen*, Physik der kondensierten Materie **3** (1964), 119–138 (German).

[93] H. Bross, *Verallgemeinerung der MAPW-Methode für ein beliebiges Potential*, Helv. Phys. Acta **41** (1968), 717–722.

[94] H. Bross, G. Bohn, G. Meister, W. Schubö, and H. Stöhr, *New Version of the Modified Augmented-Plane-Wave Method*, Phys. Rev. B **2** (1970), 3098–3103.

[95] H. Bross and G. M. Fehrenbach, *The spline augmented plane wave method*, Zeitschrift für Physik B Condensed Matter **81** (1990), 233–243.

[96] H. L. Skriver, *The LMTO method*, Springer, 1983.

[97] G. A. J. Bihlmayer, *Berechnung der Gesamtenergien und elastischen Konstanten-von NiTi- und PdTi-Phasen*, Ph.D. thesis, Universität Wien, 1994.

[98] D. J. Singh and L. Nordström, *Planewaves, Pseudopotentials, and the LAPW Method*, 2nd edition ed., Springer, 2005.

[99] H. Krakauer, M. Posternak, and A. J. Freeman, *Linearized augmented plane-wave method for the electronic band structure of thin films*, Phys. Rev. B **19** (1979), 1706–1719.

[100] Y. Mokrousov, G. Bihlmayer, and S. Blügel, *Full-potential linearized augmented plane-wave method for one-dimensional systems: Gold nanowire and iron monowires in a gold tube*, Phys. Rev. B **72** (2005), 045402.

[101] L. Smrčka, *Linearized augmented plane wave method utilizing the quadratic energy expansion of radial wave functions*, Czechoslovak Journal of Physics **34** (1984), 694–704.

[102] J. Petrů and L. Smrčka, *Quadratic augmented plane wave method for self-consistent band structure calculations*, Czechoslovak Journal of Physics **35** (1985), 62–71.

[103] M. Betzinger, C. Friedrich, S. Blügel, and A. Görling, *Local exact exchange potentials within the all-electron FLAPW method and a comparison with pseudopotential results*, Phys. Rev. B **83** (2011), 045105.

[104] L. Hedin, *New Method for Calculating the One-Particle Green's Function with Application to the Electron-Gas Problem*, Phys. Rev. **139** (1965), A796–A823.

[105] N. Hamada, M. Hwang, and A. J. Freeman, *Self-energy correction for the energy bands of silicon by the full-potential linearized augmented-plane-wave method: Effect of the valence-band polarization*, Phys. Rev. B **41** (1990), 3620–3626.

[106] F. Aryasetiawan, *Self-energy of ferromagnetic nickel in the GW approximation*, Phys. Rev. B **46** (1992), 13051–13064.

[107] W. Ku and A. G. Eguiluz, *Band-Gap Problem in Semiconductors Revisited: Effects of Core States and Many-Body Self-Consistency*, Phys. Rev. Lett. **89** (2002), 126401.

[108] M. Usuda, N. Hamada, T. Kotani, and M. van Schilfgaarde, *All-electron* GW *calculation based on the LAPW method: Application to wurtzite ZnO*, Phys. Rev. B **66** (2002), 125101.

[109] C. Friedrich, S. Blügel, and A. Schindlmayr, *Efficient implementation of the GW approximation within the all-electron FLAPW method*, Phys. Rev. B **81** (2010), 125102.

[110] C. Friedrich, A. Schindlmayr, S. Blügel, and T. Kotani, *Elimination of the linearization error in GW calculations based on the linearized augmented-plane-wave method*, Phys. Rev. B **74** (2006), 045104.

[111] T. Kotani and M. van Schilfgaarde, *Fusion of the LAPW and LMTO methods: The augmented plane wave plus muffin-tin orbital method*, Phys. Rev. B **81** (2010), 125117.

[112] J. M. Soler and A. R. Williams, *Simple formula for the atomic forces in the augmented-plane-wave method*, Phys. Rev. B **40** (1989), 1560–1564.

[113] M. Weinert, E. Wimmer, and A. J. Freeman, *Total-energy all-electron density functional method for bulk solids and surfaces*, Phys. Rev. B **26** (1982), 4571–4578.

[114] A. B. Shick, A. I. Liechtenstein, and W. E. Pickett, *Implementation of the LDA+U method using the full-potential linearized augmented plane-wave basis*, Phys. Rev. B **60** (1999), 10763–10769.

[115] M. Betzinger, C. Friedrich, and S. Blügel, *Hybrid functionals within the all-electron FLAPW method: Implementation and applications of PBE0*, Phys. Rev. B **81** (2010), 195117.

[116] M. Schlipf, M. Betzinger, C. Friedrich, M. Ležaić, and S. Blügel, *HSE hybrid functional within the FLAPW method and its application to GdN*, Phys. Rev. B **84** (2011), 125142.

[117] P. Pulay, *Ab initio calculation of force constants and equilibrium geometries in polyatomic molecules*, Molecular Physics **17** (1969), 197–204.

[118] R. Yu, D. Singh, and H. Krakauer, *All-electron and pseudopotential force calculations using the linearized-augmented-plane-wave method*, Phys. Rev. B **43** (1991), 6411–6422.

[119] D. A. Klüppelberg, M. Betzinger, and S. Blügel, *Atomic force calculations within the all-electron FLAPW method: Treatment of core states and discontinuities at the muffin-tin sphere boundary*, Phys. Rev. B **91** (2015), 035105.

[120] M. Betzinger, C. Friedrich, A. Görling, and S. Blügel, *Precise response functions in all-electron methods: Application to the optimized-effective-potential approach*, Phys. Rev. B **85** (2012), 245124.

[121] M. Betzinger, C. Friedrich, and S. Blügel, *Precise response functions in all-electron methods: Generalization to nonspherical perturbations and application to NiO*, Phys. Rev. B **88** (2013), 075130.

[122] C. Li, A. J. Freeman, H. J. F. Jansen, and C. L. Fu, *Magnetic anisotropy in low-dimensional ferromagnetic systems: Fe monolayers on Ag(001), Au(001), and Pd(001) substrates*, Phys. Rev. B **42** (1990), 5433–5442.

[123] M. Heide, G. Bihlmayer, and S. Blügel, *Describing DzyaloshinskiiMoriya spirals from first principles* , Physica B: Condensed Matter **404** (2009), 2678–2683.

[124] P. Kurz, F. Förster, L. Nordström, G. Bihlmayer, and S. Blügel, *Ab initio treatment of noncollinear magnets with the full-potential linearized augmented plane wave method*, Phys. Rev. B **69** (2004), 024415.

[125] F. Freimuth, Y. Mokrousov, D. Wortmann, S. Heinze, and S. Blügel, *Maximally localized Wannier functions within the FLAPW formalism*, Phys. Rev. B **78** (2008), 035120.

[126] B. Hardrat, N.-P. Wang, F. Freimuth, Y. Mokrousov, and S. Heinze, *One-dimensional ballistic transport with FLAPW Wannier functions*, Phys. Rev. B **85** (2012), 245412.

[127] G. Michalicek, M. Betzinger, C. Friedrich, and S. Blügel, *Elimination of the linearization error and improved basis-set convergence within the FLAPW method*, Computer Physics Communications **184** (2013), 2670 – 2679.

[128] H. Ott, *Die Strukturen von Mn O, Mn S, Ag F, Ni S, Sn I4, Sr Cl2, Ba F2, Praezisionsmessungen einiger Alkalihalogenide.*, Zeitschrift für Kristallographie, Kristallgeometrie, Kristallphysik, Kristallchemie **63** (1926), 222–230.

[129] D. G. Henshaw, *Atomic Distribution in Liquid and Solid Neon and Solid Argon by Neutron Diffraction*, Phys. Rev. **111** (1958), 1470–1475.

[130] B. M. Vasyutinskiy, G. N. Kartmazov, Y. M. Smirnov, and V. A. Finkel, *High-temperature crystalline structure of niobium and vanadium*, Phys. Met. Metall. **21** (1966), 134–135.

[131] F. Murnaghan, *The Compressibility of Media under Extreme Pressures*, Proc. Nat. Acad. Sci. USA **30** (1944), 244–247.

[132] C. Friedrich, M. C. Müller, and S. Blügel, *Band convergence and linearization error correction of all-electron GW calculations: The extreme case of zinc oxide*, Phys. Rev. B **83** (2011), 081101.

[133] M. E. Straumanis and L. S. Yu, *Lattice parameters, densities, expansion coefficients and perfection of structure of Cu and of Cu–In α phase*, Acta Crystallographica Section A **25** (1969), 676–682.

[134] A. Taylor and R. Jones, *in 'Silicon Carbide - A High Temperature Semiconductor'*, p. 147, Pergamon Press, Oxford, London, New York, Paris, 1960.

[135] M. Straumanis and A. Ieviņš, *Die Drehkristallmethode als Präzisionsverfahren und deren Vergleich mit der Pulvermethode*, Zeitschrift für Physik **109** (1938), 728–743 (German).

[136] E. Di Napoli, S. Blügel, and P. Bientinesi, *Correlations in sequences of generalized eigenproblems arising in Density Functional Theory*, Computer Physics Communications **183** (2012), 1674–1682.

[137] R. Wu and A. Freeman, *An efficient step-forward way to solve the Schrödinger eigenvalue equation in self-consistent calculations*, Computer Physics Communications **76** (1993), 58–62.

[138] V. L. Moruzzi and P. M. Marcus, *Antiferromagnetic-ferromagnetic transition in FeRh*, Phys. Rev. B **46** (1992), 2864–2873.

[139] L. Xu, K. Rushchanskii, P. Mavropoulos, M. Lezaic, and S. Blügel, *to be published*.

[140] *TOP500 Supercomputer Sites*, `http://www.top500.org/`.

[141] E. Bott, M. Methfessel, W. Krabs, and P. C. Schmidt, *Nonsingular Hankel functions as a new basis for electronic structure calculations*, Journal of Mathematical Physics **39** (1998), 3393–3425.

[142] A. M. Rappe, K. M. Rabe, E. Kaxiras, and J. D. Joannopoulos, *Optimized pseudopotentials*, Phys. Rev. B **41** (1990), 1227–1230.

Publikationen

Wir haben einige Teile dieser Doktorarbeit bereits in Fachzeitschriften veröffentlicht und streben dies für weitere Teile in Kürze an:

1. Die Inhalte von Kapitel 4.1 haben wir bereits veröffentlicht in

   G. Michalicek, M. Betzinger, C. Friedrich und S. Blügel, *Elimination of the linearization error and improved basis-set convergence within the FLAPW method*, Computer Physics Communications **184** (2013), 2670-2679

2. Die Hauptteile der Kapitel 5 und 6 werden in Kürze eingereicht werden in

   G. Michalicek und S. Blügel, *The full-potential linearized augmented lattice-adapted plane-wave method*, in preparation.

Danksagung

Einige Personen haben mich während meiner Promotionszeit begleitet und waren mir oft eine große Hilfe. An dieser Stelle möchte ich mich hierfür explizit bedanken:

- Ich danke Prof. Dr. Stefan Blügel, der mich in dieser Zeit betreut hat und die Arbeit begutachtet. Durch Stefans Enthusiasmus, physikalischem Sachverstand und Hilfsbereitschaft habe ich viel gelernt und wurde immer wieder motiviert.
- Ich danke Prof. Dr. Eugene Krasovskii, der mich in einigen für mich sehr wertvollen Gesprächen an seinem enormen Verständnis der FLAPW Methode teilhaben ließ, konstruktive Verbesserungsvorschläge eingebracht hat und sich bereit erklärt hat, das Zweitgutachten zu dieser Arbeit anzufertigen.
- Ich danke Prof. Dr. Stefan Wessel, der sich bereit erklärt hat, das Drittgutachten zu dieser Arbeit anzufertigen und so einen weiteren Blickwinkel in die Begutachtung einzubringen.
- Ich danke Dr. Christoph Friedrich, der mich dazu gebracht hat, die entstehende Ungenauigkeit durch die Linearisierung in der FLAPW Methode detailliert zu analysieren. Durch Christoph's Qualitätsansprüche habe ich vieles wesentlich detaillierter betrachtet und habe eine Menge gelernt.
- Ich danke Dr. Gustav Bihlmayer und Dr. Daniel Wortmann, die mir in vielen Gesprächen die Details der FLAPW Methode und im Speziellen des FLEUR Codes beigebracht haben.
- Ich danke Dr. Markus Betzinger, von dessen Detailwissen und systematischer, wissenschaftlicher Arbeitsweise ich sehr profitiert habe. Markus hat Teile der Arbeit korrekturgelesen und sehr hilfreiche Verbesserungsvorschläge gemacht.
- Ich danke meinen Bürokollegen, die immer für eine tolle Arbeitsatmosphäre gesorgt haben und mit denen ich viele interessante, motivierende, hilfreiche und auch lustige Gespräche geführt habe. Dies betrifft insbesondere die Bürokollegen mit denen ich das Büro über einen sehr langen Zeitraum geteilt habe: Dr. Martin Schlipf und Aaron Klüppelberg.
- Ich bedanke mich bei meinen Eltern und meinen Geschwistern, die mir immer den benötigten Halt gegeben haben.

Band / Volume 88
Multiscale Multimodel Simulation of Micromagnetic Singularities
C. Andreas (2014), xix, 188 pp
ISBN: 978-3-89336-983-6

Band / Volume 89
***Ab initio* description of transverse transport due to impurity scattering in transition-metals**
B. C. Zimmermann (2014), 164 pp
ISBN: 978-3-89336-985-0

Band / Volume 90
Ladungstransport durch Graphenschichten und GaAs-Nanodrähte untersucht mit einem Multispitzen-Rastertunnelmikroskop
S. Korte (2014), 96 pp
ISBN: 978-3-89336-990-4

Band / Volume 91
6th Georgian-German School and Workshop in Basic Science
A. Kacharava (Ed.) (2014), CD
ISBN: 978-3-89336-991-1

Band / Volume 92
Ab initio investigations of π-conjugated-molecule-metal interfaces for molecular electronics and spintronics
M. Callsen (2014), viii, 155 pp
ISBN: 978-3-89336-992-8

Band / Volume 93
Ladungstransportmessungen an Si(111) Oberflächen mit einem Multispitzen-Rastertunnelmikroskop
M. Blab (2014), iv, 132, X pp
ISBN: 978-3-89336-997-3

Band / Volume 94
Functional Soft Matter
Lecture Notes of the 46th IFF Spring School 2015
23 February – 06 March, 2015 Jülich, Germany
ed. by J. Dhont, G. Gompper, G. Meier, D. Richter, G. Vliegenthart, R. Zorn
(2015), ca. 600 pp
ISBN: 978-3-89336-999-7

Band / Volume 95
2-Steps in 1-pot: enzyme cascades for the synthesis of chiral vicinal amino alcohols
T. Sehl (2014), XIV, 167 pp
ISBN: 978-3-95806-001-2

Band / Volume 96
Immunohistochemical and electrophysiological characterization of the mouse model for Retinitis Pigmentosa, *rd10*
S. Biswas (2014), XII, 119 pp
ISBN: 978-3-95806-011-1

Band / Volume 97
Single molecule localization microscopy: Imaging of cellular structures and a new three-dimensional localization technique
X. Fan (2014), XII, 92 pp
ISBN: 978-3-95806-014-2

Band / Volume 98
Cryogenic Break-Junction Characterization of Single Organic Molecules
T. Grellmann (2014), VI, 86 pp
ISBN: 978-3-95806-015-9

Band / Volume 99
Interacting Interactions: A Study on the Interplay of Molecule-Molecule and Molecule-Substrate Interactions at Metal-Organic Interfaces
M. Willenbockel (2014), IX, 245 pp
ISBN: 978-3-95806-018-0

Band / Volume 100
Microwire crossbar arrays for chemical, mechanical, and thermal stimulation of cells
P. Rinklin (2015), xii, 184 pp
ISBN: 978-3-95806-022-7

Band / Volume 101
Modification and characterization of potential bioelectronic interfaces
K. Greben (2015), 76 pp
ISBN: 978-3-95806-028-9

Band / Volume 102
Extending the precision and efficiency of the all-electron full-potential linearized augmented plane-wave density-functional theory method
G. Michalicek (2015), 195 pp
ISBN: 978-3-95806-031-9

Weitere ***Schriften des Verlags im Forschungszentrum Jülich*** unter
http://wwwzb1.fz-juelich.de/verlagextern1/index.asp

Schlüsseltechnologien /
Key Technologies
Band / Volume 102
ISBN 978-3-95806-031-9